

8-3-2023 2:00 PM

Novel Magnetic Resonance Imaging-Compatible Mechatronic Needle Guidance System for Prostate Focal Laser Ablation Therapy

Eric R. Knull, *Western University*

Supervisor: Fenser, Aaron, *The University of Western Ontario*

A thesis submitted in partial fulfillment of the requirements for the Doctor of Philosophy degree in Biomedical Engineering

© Eric R. Knull 2023

Follow this and additional works at: <https://ir.lib.uwo.ca/etd>



Part of the [Bioimaging and Biomedical Optics Commons](#), and the [Biomedical Devices and Instrumentation Commons](#)

Recommended Citation

Knull, Eric R., "Novel Magnetic Resonance Imaging-Compatible Mechatronic Needle Guidance System for Prostate Focal Laser Ablation Therapy" (2023). *Electronic Thesis and Dissertation Repository*. 9462. <https://ir.lib.uwo.ca/etd/9462>

This Dissertation/Thesis is brought to you for free and open access by Scholarship@Western. It has been accepted for inclusion in Electronic Thesis and Dissertation Repository by an authorized administrator of Scholarship@Western. For more information, please contact wlsadmin@uwo.ca.

Abstract

Advances in prostate cancer (PCa) screening techniques have led to diagnosis of many cases of low-grade and highly localized disease. Conventional whole-gland therapies often result in overtreatment in such cases and debate still surrounds the optimal method of oncologic control. MRI-guided prostate focal laser ablation (FLA) is a minimally invasive treatment option, which has demonstrated potential to destroy localized lesions while sparing healthy prostatic tissue, thereby reducing treatment-related side effects. Many challenges still exist in the development of FLA, including patient selection; tumour localization, visualization, and characterization; needle guidance; and evaluation of treatment efficacy. The objective of this thesis work was to advance and enhance techniques for needle guidance in MRI-guided focal laser ablation (FLA) therapy of PCa.

Several steps were taken in achieving this goal. Firstly, we evaluated the overlap between identified lesions and MRI-confirmed ablation regions using conventional needle guidance. Non-rigid thin-plate spline registration of pre-operative and intra-operative images was performed to align lesions with ablation boundaries and quantify the degree of coverage. Complete coverage of the lesion with the ablation zone is a clinically important metric of success for FLA therapy and we found it was not achieved in many cases. Therefore, our next step was to develop an MRI-compatible, remotely actuated mechatronic system for transperineal FLA of prostate cancer. The system allows physicians in the MRI scanner control room to accurately target lesions through 4 degrees of freedom while the patient remains in the scanner bore. To maintain compatibility with the MRI environment, piezoelectric motors were used to actuate the needle guidance templates, the device was constructed from non-ferromagnetic materials, and all cables were shielded from electromagnetic interference. The MR compatibility and needle placement accuracy of the device were evaluated with virtual and phantom targets.

The system should next be validated for accuracy and usefulness in a clinical trial where more complex tissue properties and potential patient motion will be encountered. Future advances in modeling the tissue properties and compensating for deformation of the prostate, as

well as predicting needle deflection, will further bolster the potential of FLA as option for the management of PCa.

Keywords: prostate cancer, magnetic resonance imaging, MRI, image-guided intervention, MRI-guided intervention, transperineal prostate intervention, focal therapy, laser ablation, thermal ablation, mechatronic system, needle guidance, image registration, image segmentation, thin plate spline, tissue-mimicking phantoms

Summary for Lay Audience

Prostate cancer (PCa) is the most common non-skin cancer in Canadian men, but many cases are low-grade, meaning they are unlikely to cause death. Often, the side effects of typical treatments such as surgery or radiation are worse than the symptoms of the cancer itself. Focal laser ablation (FLA) is an alternative treatment option which can be used to treat low-grade PCa with fewer side effects than traditional treatments. FLA uses needles inserted through the skin and into the prostate to heat and destroy tumours from the inside. The needles are guided using magnetic resonance images (MRI), which are created using powerful magnetic fields that can “see” inside the body. The overall goal of this work was to improve the accuracy and useability of MRI-guided FLA for PCa.

The first step was to compare ablation zones (regions of tissue destroyed by FLA) with the locations of the tumours that were to be destroyed. To do this, MRI images where the tumours were visible were aligned with images where the ablation zones were visible. In many cases, the ablation zone did not completely overlap the tumour, which meant part of the tumour may have been left untreated. Therefore, the next step was to develop a robot which could more accurately place needles for FLA.

This robot was constructed using specialized motors and materials which would not be affected by the strong magnetic fields of the MRI scanner. The robot can adjust both the angle and position of a needle before it penetrates the skin. A series of tests were done to verify the robot’s MRI-compatibility and then the accuracy with which it could place needles was measured in artificial prostate models. It was shown that the robot can place needles within 4.13 mm of an intended target 95% of the time. This is a high enough level of accuracy for FLA therapy, and it can be accomplished while the physician is outside of the MRI scanner room. The next step for the robot is to be used in clinical trials, where its safety and effectiveness can be demonstrated in real patients.

Co-Authorship Statement

This thesis is presented in an integrated article format, the chapters of which are based on the following journal publications:

Chapter 2: Knull, E., Oto, A., Eggener, S., Tessier, D., Guneyli, S., Chatterjee, A., & Fenster, A. (2019). Evaluation of tumor coverage after MR-guided prostate focal laser ablation therapy. *Medical Physics*, 46(2), 800–810.

I created the affine and non-rigid registration algorithms, performed data analysis, wrote the main manuscript text, and prepared all figures. A. Oto was the radiologist on clinical trials and segmented tumours. S. Eggener was the urologist on clinical trials. D. Tessier performed segmentation of prostates. S. Guneyli performed segmentation of ablation zones. A. Chatterjee assisted with data analysis and corresponded with physicians. A. Fenster conceived the experiment. All authors reviewed the final manuscript.

Chapter 3: Knull, E., Bax, J. S., Park, C. K. S., Tessier, D., & Fenster, A. (2021). Design and validation of an MRI-compatible mechatronic system for needle delivery to localized prostate cancer. *Medical Physics*, 48(9), 5283-5299.

I implemented all electronics and wiring, wrote motor control and registration software, performed open-air accuracy measurement experiments, assisted in collecting MRI scans, performed data analysis, wrote the main manuscript text, and prepared figures for the results section. J. Bax created the mechanical designs and CAD figures, and assisted in collecting MRI scans. C.K. Park contributed to the manuscript discussion and prepared figures for the methods section. D. Tessier collected MR scans and provided technical support. A. Fenster conceived the experiment and the system. All authors reviewed the final manuscript.

Chapter 4: Knull, E., Park, C. K. S., Bax, J., Tessier, D., & Fenster, A. (2023). Toward mechatronic MRI-guided focal laser ablation of the prostate: Robust registration for improved needle delivery. *Medical Physics*, 50(3), 1259–1273.

I conceived the new registration fiducial assembly and experiments, wrote and implemented

the new registration and segmentation software, fabricated tissue-mimicking phantoms, collected MRI scans, performed data analysis, wrote the main manuscript text, and prepared figures for the results section. C.K. Park contributed to data analysis, the manuscript methods and discussion, assisted in phantom preparation, and prepared figures for the methods section. J. Bax created the mechanical designs and CAD models, and assisted in collected of MRI scans. D. Tessier assisted in collection of MRI scans and provided technical support. A. Fenster conceived the overall system. All authors reviewed the final manuscript.

Acknowledgements

There are many people who offered their guidance, mentorship, companionship, and inspiration to me throughout the course of my graduate school program, without whom this work would not have been possible.

First and foremost, I would like to express my sincere gratitude to my supervisor, Dr. Aaron Fenster, for his invaluable mentorship and endless patience throughout my PhD program. His expertise and encouragement helped me to complete this research, and his positive guidance and cheerful attitude always made me feel confident in my ability to tackle difficult problems. And of course, I would never have been able to find the best smoked meat deli in Montreal without him. I would also like to thank Dr. Rob Bartha and Dr. Eugene Wong for serving on my thesis committee and providing critical feedback and suggestions to improve the direction of my work, as well as helping me to prepare for oral examinations.

I am grateful to the Engineering Faculty at the University of Western Ontario and the Robarts Research Institute for providing me with the opportunity to conduct my research and for all of the resources and support they provided. I would like to extend a special thanks to Dr. James Lacefield, who went above and beyond to guide me through the program requirements and deadlines. I also commend Dr. Quazi Rahman and Dr. Ken McIsaac for being engaging professors and inspiring me to pursue higher education in the field of Engineering.

There are many people in the Fenster lab group who deserve recognition for their contributions to this work. Special recognition goes to Claire Park who is, without a doubt, the greatest peer one could hope to encounter during their studies. Ever since the day she insisted on joining our intramural soccer team, she has been instrumental in all aspects of this thesis, from mixing condensed milk for phantoms to preparing manuscripts for conferences and journals. She has my eternal gratitude for her encouragement and camaraderie. I must also thank Dr. Jeff Bax for contributing the mechanical designs and manufacturing for this thesis, and endlessly iterating

on them with me. Dr. David Tessier provided much appreciated expertise for designing electronic systems and operating the 3T MRI scanner. The other members of Dr. Fenster's lab and the community at Robarts deserve recognition for their intelligent discussions, contributions of expertise, and editorial feedback: Igor Gyackov, Lori Gardi, Dr. Jeremy Cepek, Jacques Montreuil, David Reese, Dr. Terry Peters, Dr. Derek Cool, Dr. Nirmal Kikani, Chandima Edirisinghe, Kevin Barker, Dr. Jessica Rodgers, Dr. Derek Gillies, Dr. Nathan Orlando, Dr. Jessica Kishimoto, Dr. Tom Hrinivich, Sam Papernick, Justin Michael, Dr. Kamyar Abhari, and Matt Gravett.

I am forever thankful to my friends and family for their love and support during this process. Without them, this journey would not have been possible. My parents, Ron and Darcie, and my sister Jennie, have supported me unconditionally through any endeavour I wished to pursue, and picked me up whenever I stumbled. My Oma, Helene Knull, was a loving role model whose perseverance and kindness were inspirational. My youth soccer coach, Bob Gravett, not only connected me with my supervisor and opened the door to graduate studies for me, but also instilled in me the values of discipline and teamwork and a life-long love of soccer along with his co-coach, Richard Braiden. More thanks go to Adem Boussaad, Justin Szoke-Sieswerda, Adam Vandenakker, Mark Dawidek, Ruben Campos, and Jon Tingey for sharing many laughs and helping me keep my sanity throughout my education. Finally, words cannot express my gratitude to Shauna Malek for her unwavering faith in my success and for giving me the strength to carry on.

Sources of funding that have supported me personally include the National Sciences and Engineering Research Council of Canada, the Cancer Research and Technology Transfer Trainee Award, and the Western Graduate Research Scholarship.

Contents

Abstract	ii
Summary for Lay Audience	iv
Co-Authorship Statement	v
Acknowledgements	vii
List of Figures	xiii
List of Tables	xviii
List of Appendices	xix
List of Abbreviations, Symbols, and Nomenclature	xx
1 Introduction	1
1.1 Prostate Anatomy and Function	1
1.2 Prostate Cancer	4
1.3 Prostate Cancer Diagnosis	5
1.3.1 The Prostate Specific Antigen Test	5
1.3.2 Digital Rectal Examination	6
1.3.3 Biopsy	8
Targeted Biopsy	9
1.3.4 Imaging	11
Ultrasound	11
Magnetic Resonance Imaging	12
1.4 Prostate Cancer Treatment	14
1.4.1 Conventional Treatments	15
1.4.2 Focal Therapies	16
Focal Laser Ablation Therapy	17
1.5 Challenges in Using MRI-Guidance for Needle Delivery in Prostate Interventions	20
1.5.1 Effects of MRI on Devices	20
1.5.2 Effects of Devices on MRI	21
1.6 Existing MRI-Guided Prostate Needle Delivery Devices and Techniques	22
1.6.1 Conventional Techniques	23
1.6.2 Mechatronic or Robotic Systems	23

1.7	Thesis Hypothesis and Objectives	26
1.7.1	Specific Objectives	27
1.8	Thesis Outline	27
1.8.1	Chapter 2: Evaluation of Tumour Coverage after MR-Guided Prostate Focal Laser Ablation Therapy	28
1.8.2	Chapter 3: Design and Validation of an MRI-Compatible Mechatronic System for Needle Delivery to Localized Prostate Cancer	29
1.8.3	Chapter 4: Toward Mechatronic MRI-Guided Focal Laser Ablation of the Prostate: Robust Registration for Improved Needle Delivery	30
1.8.4	Chapter 5: Conclusions and Future Work	32
	Bibliography	33
2	Evaluation of Tumour Coverage after MR-Guided Prostate Focal Laser Ablation Therapy	52
2.1	Introduction	52
2.2	Methods	54
2.2.1	Materials	54
2.2.2	Registration Pipeline	56
	Surface Segmentation	56
	Linear Registration	57
	Equal Angle Parameterization	58
	Deformable Surface Registration	59
	Consensus Surfaces	61
	Evaluation Metrics	61
	Data Availability	62
2.3	Results	63
2.4	Discussion	68
2.5	Conclusion	74
	Bibliography	76
3	Design and Validation of an MRI-Compatible Mechatronic System for Needle Delivery to Localized Prostate Cancer	81
3.1	Introduction	81
3.2	Methods	84
3.2.1	Mechatronic System Design	84
	Mechanical Design	85
	Electrical Components	87
	User Interface	87
	Clinical Workflow Integration	88
3.2.2	MRI Compatibility Testing	89
	Effects of MRI on System	90
	Effects of System on Images	91
3.2.3	Open-air Targeting Accuracy	92
	Registration of Mechatronic System and Optical Tracker Coordinate Systems	93

	Needle Guidance Accuracy Evaluation	95
3.2.4	MRI Targeting Accuracy	97
	Registration of Mechatronic System and Scanner Coordinate Systems .	100
	Needle Guidance Accuracy Testing	101
3.3	Results	102
3.3.1	MRI Compatibility	102
3.3.2	Open Air Accuracy	104
3.3.3	Needle Guidance Error in the MRI Bore	104
3.4	Discussion	107
3.5	Conclusion	110
3.6	Acknowledgements	111
3.7	Conflict of interest	111
3.8	Data Availability Statement	111
	Bibliography	112
4	Toward Mechatronic MRI-Guided Focal Laser Ablation of the Prostate: Robust Registration for Improved Needle Delivery	117
4.1	Introduction	117
4.2	Methods	119
4.2.1	Mechatronic System Description	119
4.2.2	Graphical User Interface	120
4.2.3	MR Image Acquisition	121
4.2.4	Registration of the Mechatronic System and MR Images	123
	Registration Fiducial Assembly	123
	Fiducial Localization	124
	Transform	126
4.2.5	Phantom Design	127
4.2.6	Needle Track Segmentation	128
	Validation of Semi-Automatic Segmentation	130
4.2.7	Needle Targeting Accuracy	130
	Comparison with Previous Registration Method	132
4.2.8	Statistical Analysis	132
4.3	Results	134
4.3.1	Needle Targeting Accuracy	134
4.3.2	Comparison with Previous Registration Method	134
4.3.3	Validation of Semi-Automatic Needle Segmentation	136
4.4	Discussion	137
4.5	Conclusion	141
4.6	Acknowledgments	142
	Bibliography	143
5	Conclusions and Future Work	151
5.1	Limitations and Future Work	152
	Bibliography	155

A Mechatronic System Kinematics	157
B Permissions	161
B.1 Permission to reproduce previously published material in Chapters 2, 3, and 4 .	161
Curriculum Vitae	180

List of Figures

1.1	Location and surrounding structures of the prostate. (Image by Canadian Cancer Society)	3
1.2	Zonal anatomy of the prostate in a young healthy male. (Image by Mikael Haggstrom, MD. Public Domain CC0 1.0. 2019.)	3
1.3	Age standardized incidence rates of prostate cancer in Canada (solid line). (Image taken from [17])	7
1.4	Age standardized mortality rates of prostate cancer in Canada (solid line). (Image taken from [17])	7
1.5	Example cell structure used in Gleason's grading system. With increasing grade, cells become more spread out and glandular architecture is lost. (Image by National Institutes of Health)	10
2.1	Diagram of steps used to compare tumours and ablation zones. Dashed lines indicate clinical processes.	56
2.2	Distributions of (a) prostate volumes segmented from pre-operative images, (b) prostate volumes segmented from post-ablative images, (c) tumour volumes, and (d) ablation zone volumes.	64
2.3	Histogram (left axis) and CDF (right axis) of margins between mean registered tumours and ablation zones.	64
2.4	Histogram of minimum margins between registered tumours and ablation zones. Error bars indicate the 95% confidence interval of bin value.	65
2.5	Average minimum margin for each tumour versus shortest distance to either prostate capsule or urethra (whichever was closer to the tumour) (n=23).	66
2.6	Histogram of treated tumour volume calculated using consensus tumour surfaces. The 95% confidence intervals for each bin value are plotted as vertical error bars (n=12).	67
2.7	Axial view of five different registered tumour surfaces (yellow) with consensus surface (green), ablation zone (blue) and prostate (red).	68
2.8	Slices of registered tumour (green), ablation zone (blue), and prostate boundary (red) overlaid on MRI. Each row is a different patient. Images in the left column are pre-operative T2 images, and images in the right column are DCE images. The tumour in the top row was partially ablated, and the tumours in the second and third rows were completely ablated.	69

3.1	Computer-aided design (CAD) isometric model of the MRI-compatible mecha- tronic needle guidance system for prostate focal laser ablation (FLA) needle in- tervention. Encoders are identified by purple casings. Motors are hidden inside the device. Red arrows indicate where the needles are inserted: first through the guide at the rear of the system, then through the rest of the needle guides, and finally into the perineum.	84
3.2	(a) Side View. The trajectory of the needle as it passes through the guides is determined by the poses of the front and rear arms. The arms are controlled using piezoelectric motors and the position is measured using optical encoders (two motor/encoder pairs are hidden in the top of the system). Each arm is counterbalanced to aid the motors against gravity. (b) Reverse Side View. The alignment handle and lock knob allow for manual positioning and locking of the needle guides. Electrical connections are shielded against RF interference using an aluminum junction box and copper tape.	86
3.3	Three orthogonal surfaces used for registering the system with the optical tracker's coordinate system. Points for the set P_{plane} were collected by tracing the stylus over the green surface, P_{line} was collected from the red surface, and P_{point} was collected from the blue surface. The three surfaces intersect at the point O' , which is a fixed displacement from the system's origin at O	94
3.4	NDI Medical Polaris Vicra Optical Tracking System. (a) Arrangement of stereo cameras tuned to the same infrared frequency emitted by the infrared illumina- tor. (b) Tracking stylus contains three reflective spheres. The position of the tip can be calculated based on the tracked positions of the spheres and the known geometry of the stylus, as long as all three spheres are facing both cameras and are not occluded.	98
3.5	Attachable fiducial component containing four MR-visible spheres arranged in two orthogonal lines. The component can be quickly interchanged with the needle templates to perform system registration before procedures.	99
3.6	Axial gradient-echo image of fluid-filled spheres used in the attachable regis- tration fiducial. (a) Original image of horizontal fiducials. (b) Original image of vertical fiducials. (c) Filtered image with the region of interest thresholded. Localized centroid delineated by a cross.	100
3.7	Low bandwidth (195 Hz/pixel) T1w gradient-echo images acquired during the distortion test. Absolute difference images (b)-(d) are subtracted from baseline image (a). (a) System absent. (b) System present. (c) System connected. (d) System powered. The window of intensities for each image has a range of 1,000. 103	
3.8	3D plane fitted to the horizontal component of error in the position of the front arm generated from the set of 85 trajectories used for bias compensation. The equation of the plane along with a plane similarly fitted to the vertical com- ponent of error was used to determine and compensate for the systematic bias present in the system. The same procedure was used to compensate for bias in the rear arm.	105

3.9	Targeting error from open-air experiment measured using 40 trajectories. (a) Components of the error separated into horizontal and vertical directions, where the origin corresponds to the target point for each trajectory at a depth of 10 cm calculated using the forward kinematics. Dashed circles are shown to indicate error magnitudes of 0.5, 1.0, and 1.5 mm. (b) Cumulative distribution of targeting error, representing the percentage of trajectories with the error less than E_{max} .	106
3.10	Cumulative distribution of angular error from an open-air experiment on 40 trajectories, representing the percentage of trajectories with the error less than A_{max} .	106
3.11	Targeting error from MRI virtual targeting experiment using 25 trajectories. a) Components of error separated into left-right and superior-inferior directions, where the origin corresponds to the target point for each trajectory at a depth of 10 cm calculated using the forward kinematics. Dashed circles are shown to indicate error magnitudes of 0.5, 1.0, and 1.5 mm. b) Cumulative distribution of targeting error, representing the percentage of trajectories with error less than E_{max} .	107
3.12	Cumulative distribution of angular error from MRI virtual targeting experiment on 25 trajectories, representing the percentage of trajectories with error less than A_{max} .	108
4.1	Isometric (a) and top-down (b) views of computer-aided design (CAD) model of the previously developed MRI-compatible mechatronic system for prostate focal laser ablation (FLA) needle guidance. The system's front (identified by the needle guides arrow) is placed against the patient's perineum. After alignment with chosen targets, needles are inserted through the needle guides, starting at the back of the system and into the perineum.	121
4.2	Screenshot of the Python scripted module created within Slicer software. The panel on the left is divided into three sections. The first section is used to control the motors, the second is used for segmenting fiducials and needle tracks, and the third is used to register the image with the mechatronic system's coordinate system using the segmented fiducials. The visualization panels show, clockwise from the top right: 3D view of the orthogonal imaging planes, coronal imaging plane, sagittal imaging plane, axial imaging plane. The images have been overlayed with lines created using VTK (Visualization ToolKit), which show the current needle trajectory, the targeted needle trajectory, and the needle trajectory segmented from the image. The motors can also be moved by adjusting the targeted needle trajectory on the image.	122
4.3	a) Previous four-sphere fiducial assembly (in blue) shown attached to the rest of the system. Note that the assembly takes the place of the needle templates, making it difficult to attach and detach as part of the clinical workflow. b) Close-up view of the previous fiducial assembly. The use of only four spheres limits the registration accuracy.	124

4.4	a) Improved multi-fiducial structure (in blue) shown attached to the rest of the system. The needle template remains in place, making it less disruptive to the clinical workflow. b) Close-up view of one layer of the improved multi-fiducial design. The layer contains twelve hollowed-out spheres filled with MR-visible fluid, and two more layers are stacked on top.	125
4.5	a) Tissue-mimicking prostate phantom. An agar and condensed milk prostate moulded from anatomical data is embedded in agar background material. The phantom has similar T1 and T2 relaxation times and stiffness characteristics to human prostate tissue. b) Custom tungsten trocar and PEEK catheter used for all needle insertion tests.	128
4.6	Example axial (a) and coronal (b) images of air tracks left behind after withdrawing the needle assembly from the tissue-mimicking prostate phantom. The air tracks were clearly visible for all insertions. The semi-automatic segmentation of one of the needle tracks is shown overlayed in green.	129
4.7	Cumulative distribution functions of needle guidance errors in tissue-mimicking prostate phantoms measured using 44 trajectories. The CDF plots the percentage of trajectories with error less than the value on the x-axis. (a) CDF of E_{total} , representing the shortest Euclidean distance between the measured needle trajectory and the targeted point. 50% of the errors were less than 1.0 mm. (b) CDF of A_{total} , representing the angle between the intended needle trajectory and the measured needle trajectory. 61% of the errors were less than 0.01 rad.	135
4.8	Spatial components of targeting error in prostate phantoms measured using 44 trajectories. E_{total} was separated into left-right and anterior-posterior directions, where the origin corresponds to the target point for each trajectory at a depth of 10 cm calculated using the forward kinematics. Dashed circles are shown to indicate error magnitudes in steps of 1 mm. The 95% confidence ellipsoid represents the area which is 95% likely to contain the the true value of the means of the components of needle guidance error.	135
4.9	Comparison of the left-right and anterior-posterior components of targeting error using the new and previous registration fiducial arrangements on 7 trajectories. The origin corresponds to the target point for each trajectory at a depth of 10 cm calculated using the forward kinematics. Dashed circles are shown to indicate error magnitudes in steps of 1 mm. ‘+’ marks indicate errors using the new registration method, and ‘o’ marks indicate errors using the previous registration method.	136
4.10	Comparison of the left-right and anterior-posterior components of targeting error using manual and semi-automatic needle track segmentation on 26 trajectories. The origin corresponds to the target point for each trajectory at a depth of 10 cm calculated using the forward kinematics. Dashed circles are shown to indicate error magnitudes in steps of 1 mm. ‘+’ marks indicate errors using semi-automatic segmentation, and ‘o’ marks indicate errors using manual segmentation.	137

A.1	System kinematics. a Variables used in the kinematic equations. θ_1 and θ_2 are the angles of the links, measured by encoders on each arm, used to calculate the pose, (p^n) and (\hat{v}^n) , of the needle guide in the forwards kinematics. Conversely, in the inverse kinematics, the pose of the needle guide is used to calculate the angles of the links. O is the origin of the system's coordinate system. b Simplified diagram of the two-link 2D kinematic chain. The origin (x_0, y_0) is placed at the location of (x_2, y_2) in the “base” pose (both θ_1 and θ_2 are zero), so that the kinematics provide the displacement of the end effector from the base pose. h_x , h_y , and h_z are the fixed displacements of the hole in the needle guide from the end-effector of the front arm.	160
-----	--	-----

List of Tables

2.1	Median and interquartile range (IQR) of prostate, tumour, and ablation zone volumes and tumour diameters (n=23). Pre-operative volumes and diameters were measured on T2 diagnostic MR images taken several months before ablation, and post-ablative volumes were measured on T1 intra-operative DCE MR images immediately after ablation. Tumour diameter was defined as the largest dimension of the tumour visible on axial images.	63
3.1	Image acquisition parameters for distortion and SNR measurements. A 3T Discovery MR750 scanner by GE Healthcare (Chicago, IL) was used.	90
3.2	Summary of distortion measurements. Voxel dimensions 1.17 mm × 1.17 mm × 0.94 mm in the T1w image and 1.17 mm × 1.17 mm × 0.94 mm in the T2w and DWI images.	103
3.3	Summary of SNR measurements.	104
4.1	Acquisition parameters for images of the registration fiducials and prostate phantom, acquired on 3T Discovery MR750 scanner by GE Healthcare (Chicago, IL).	123

List of Appendices

Appendix A Mechatronic System Kinematics	157
Appendix B Permissions	161

List of Abbreviations, Symbols, and Nomenclature

2D	Two-Dimensional
3D	Three-Dimensional
ADC	Apparent Diffusion Coefficient
ADT	Androgen Deprivation Therapy
AFS	Anterior Fibromuscular Stroma
API	Application Programming Interface
AS	Active Surveillance
ASIR	Age Standardized Incidence Rate
ASMR	Age Standardized Mortality Rate
ASTM	American Society for Testing and Materials
AUASS	American Urological Association Symptom Score
BPH	Benign Prostatic Hyperplasia
CAD	Computer-Aided Design
CDF	Cumulative Distribution Function
CEUS	Contrast-Enhanced Ultrasound
CT	Computed Tomography
CZ	Central Zone
DCE	Dynamic Contrast-Enhanced
DIL	Dominant Index Lesion
DOF	Degree-of-Freedom
DRE	Digital Rectal Examination
DWI	Diffusion-Weighted Imaging
EBRT	External Beam Radiation Therapy
EDTA	Ethylenediaminetetraacetic Acid Tetrasodium
FLE	Fiducial Localization Error
FTP	File Transfer Protocol
GRE	Gradient Recalled Echo
GUD	Genitourinary Diaphragm
GUI	Graphical User Interface
HIFU	High-Intensity Focused Ultrasound
HRQOL	Health-Related Quality of Life
IPSS	International Prostate Symptom Score
IQR	Interquartile Range
ITK	Insight Toolkit
MIRP	Minimally Invasive Radical Prostatectomy
mpMRI	Multi-Parametric Magnetic Resonance Imaging
MRI	Magnetic Resonance Imaging
MRSI	Magnetic Resonance Spectroscopic Imaging
Na-MRI	Sodium Magnetic Resonance Imaging
NEMA	National Electrical Manufacturers Association
NVB	Neurovascular Bundles

PCa	Prostate Cancer
PCA	Principal Component Analysis
PCSM	Prostate Cancer-Specific Mortality
PDT	Photodynamic Therapy
PEEK	Polyetheretherketone
PET	Positron Emission Tomography
PI-RADS	Prostate Imaging Reporting & Data System
PIVOT	Prostate Cancer Intervention Versus Observation Trial
PK	Pharmacokinetic
PSA	Prostate Specific Antigen
PYLL	Potential Years of Life Lost
PZ	Peripheral Zone
QALY	Quality-Adjusted Life-Years
RF	Radiofrequency
RMS	Root Mean Square
ROI	Region of Interest
RRP	Retropubic Radical Prostatectomy
SHIM	Sexual Health Inventory for Men
SNR	Signal-to-Noise Ratio
SPECT	Single Positron Emission Computed Tomography
SPGR	Spoiled Gradient Echo
SVD	Singular Value Decomposition
T1W	T1-Weighted
T2W	T2-Weighted
TE	Echo Time
TPS	Thin Plate Spline
TR	Repetition Time
TRUS	Transrectal Ultrasound
TRUS-GB	Transrectal Ultrasound Guided Biopsy
TSC	Tissue Sodium Concentration
TZ	Transition Zone
US	Ultrasound
USB	Universal Serial Bus
VTK	Visualization Toolkit

Chapter 1

Introduction

Focal therapy for the treatment of localized prostate cancer (PCa) is an ongoing area of research with the goal of maintaining effective oncologic control while reducing treatment-related side effects. Many different energy modalities have been developed for the ablation of prostate tissue, but there is not yet a clinical consensus on which modality most successfully meets the goals of focal therapy. A meaningful comparison between different energies requires each to be optimized with regards to guidance and delivery techniques. Therefore, the bulk of this thesis is dedicated to improving the accuracy and workflow of magnetic resonance imaging (MRI)-guided prostate focal laser ablation (FLA) therapy needle delivery. This will allow future clinical trials of FLA therapy to achieve more successful outcomes and provide greater insight into the efficacy of this energy modality as a tool for the management of PCa.

1.1 Prostate Anatomy and Function

The prostate is a small gland comprised mainly of muscle and glandular tissue, which is located anterior to the rectum and inferior to the bladder in men (see Fig. 1.1). [1] Its volume is roughly 30 cc in a healthy young adult and increases with age and disease. [2] The base of the prostate makes up its superior surface adjacent to the bladder wall, and the gland tapers distally towards its apex where it meets the genitourinary diaphragm (GUD). [3] The urethra courses inferiorly through the prostate from its origin at the bladder neck and preprostatic sphincter to

its termination at the membranous urethra. The urethra kinks anteriorly at the verumontanum where ducts from the seminal vesicles flow into the urethra. [4] The prostatic sphincter extends from the verumontanum to the apex, and the external urethral sphincter is located in the GUD continuous with the apex. [5] The prostate is divided into four main zones contained within a common capsule (see Fig. 1.2): [6, 7, 4, 8]

- **Peripheral zone (PZ):** The PZ is the largest zone of the healthy prostate, which makes up its posterior and lateral aspects from the prostatic apex to the base and constitutes approximately 70% of its mass. It is the most common site for carcinomas to be found.
- **Central zone (CZ):** Comprising 25% of the prostate's mass, the CZ forms the base of the prostate and surrounds the ejaculatory ducts along their course to the urethra. Less than 5% of prostate cancers arise in this zone. [9]
- **Transition zone (TZ):** The TZ consists of two independent lobes surrounding the urethra as it enters the prostate from the bladder. It is the smallest portion of the gland in young adults, however, it expands with age and is the principal zone affected by benign prostatic hyperplasia (BPH). Approximately 20% of prostate cancers are found in this zone. [9]
- **Anterior fibromuscular stroma (AFS):** The AFS is a sheath of smooth muscle cells and fibrous tissue, which covers the anteromedial surface of the prostate from the bladder neck to the prostate apex.

The prostate plays important roles in male fertility and urinary continence. The primary function of the prostate is to secrete an alkaline fluid, which makes up approximately 20-30% of the semen volume. [10] The fluid contains enzymes such as prostate specific antigen (PSA), which decreases seminal viscosity in order to promote sperm motility. [11] The sphincters in the prostate regulate the flow of urine and semen in the urethra, with the preprostatic sphincter responsible for preventing retrograde ejaculation. [5] Neurovascular bundles (NVB) run posterolaterally to the prostatic capsule and adjacent to the peripheral zone, and they carry neural

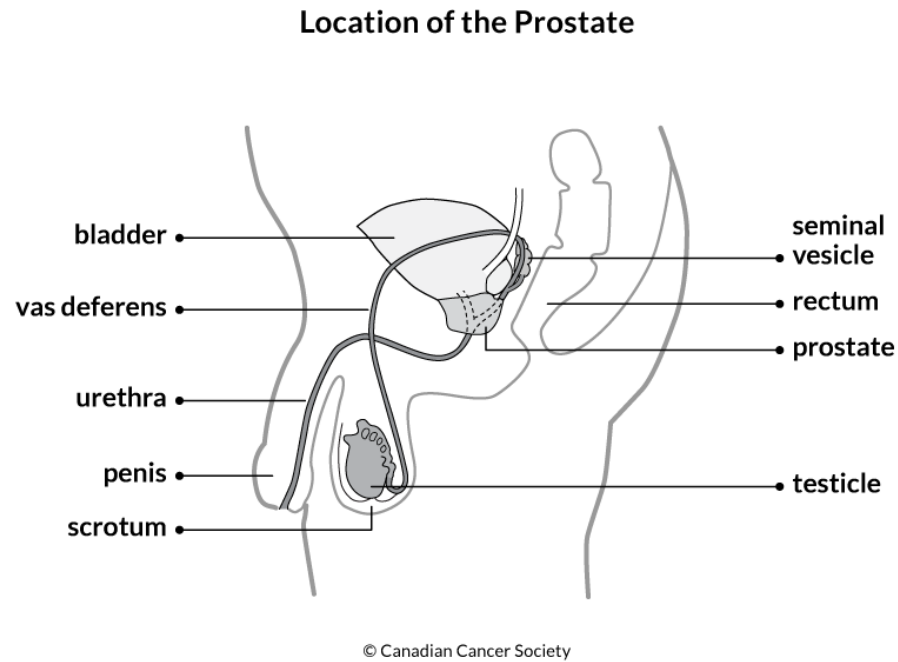


Figure 1.1: Location and surrounding structures of the prostate. (Image by Canadian Cancer Society)

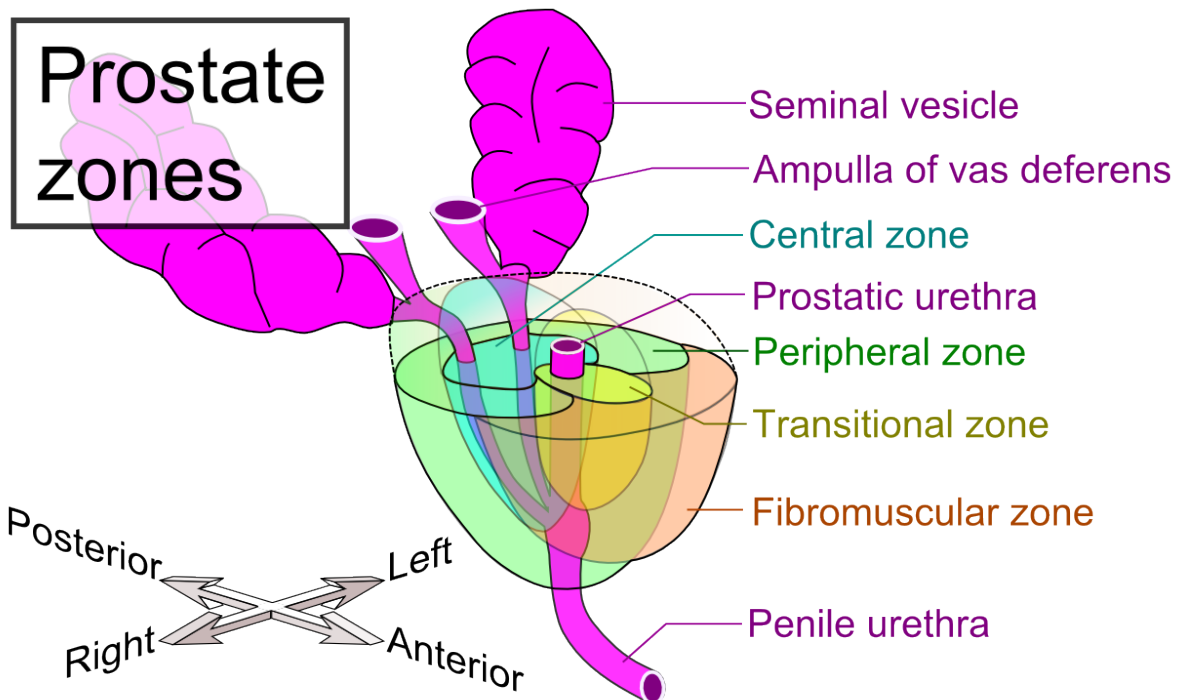


Figure 1.2: Zonal anatomy of the prostate in a young healthy male. (Image by Mikael Hagstrom, MD. Public Domain CC0 1.0. 2019.)

impulses to the cavernosal tissue responsible for erectile expansion. [12] Finally, the prostate metabolizes testosterone into dihydrotestosterone, its biologically active form. [13]

1.2 Prostate Cancer

In Canada, cancer continues to be the largest contributor to potential years of life lost (PYLL) in men, with an average of 743,800 PYLL yearly between 2010 to 2012. [14] Prostate cancer (PCa) was the most commonly diagnosed cancer among Canadian men in 2020 (excluding nonmelanoma skin cancers), with an estimated 23,300 new cases. [15] This figure represents 20% of all new male cancer diagnoses, and corresponds to an approximately 11.1% chance of a man being diagnosed with PCa at some point during his lifetime. The age-standardized incidence rate of PCa in Canada has been trending downward since 2011 (see Figure 1.3), [15] reflecting modifications to screening guidelines, which now recommend against PSA testing, particularly in men less than 55 and greater than 75 years of age. [16] PCa was the cause of 4,200 deaths in 2020, or about 10% of all male cancer deaths in Canada, and a man has an approximately 3.4% chance of dying from it. The average yearly PYLL due to PCa between 2010 to 2012 was 23,500, exceeded only by lung (192,700 PYLL) and colorectal (81,100 PYLL) cancers. The age-standardized mortality rate (ASMR) of PCa has been declining in Canada for the past two decades, reflecting improvements in therapeutic techniques (see Figure 1.4). Prognosis of PCa is now generally favourable, with a 10-year relative survival ratio of 95%, the highest among all cancers in Canadian men. [17]

Living with PCa also has negative implications for a patient's health-related quality of life (HRQOL). A study of American PCa patients over the age of 65 found a clinically meaningful decline in physical, mental, and social aspects of health within the first six months after diagnosis compared with a healthy control group, despite reporting similar health status pre-diagnosis. [18] PCa progression and treatment impact HRQOL specific to the disease domain (e.g. urinary, sexual, and bowel function) as well as general HRQOL factors (e.g. bodily pain,

loss of energy, or role-performance), [19] however general HRQOL tends to restore within a year of treatment. [18, 19] A Finnish study found that patients with metastatic disease experienced larger deficits in all aspects of HRQOL compared to patients with localized disease or patients in remission. [20] The risk of suicide and of cardiovascular death are both elevated in the first three months following diagnosis, particularly if metastatic disease is present, which is attributed to the psychological stress of receiving such a diagnosis. [21] Providing effective options for the management of PCa while maintaining HRQOL across all domains remains an ongoing area of research. [22]

1.3 Prostate Cancer Diagnosis

The use of prostate specific antigen testing, magnetic resonance imaging, and advances in prostate biopsy have resulted in earlier and more accurate detection of PCa, [23] particularly of small, highly localized, and low-grade tumours. [24] While detecting and treating cancer early is critical for cancer control, [25] many of the non-lethal or indolent tumours are unnecessarily treated. [26] The main screening tool for PCa is the PSA test, however, widespread screening is no longer recommended [27] in order to balance the benefits of early detection with the harms of screening, which include false-positive results, complications of biopsy, and overdiagnosis. [16, 28]

1.3.1 The Prostate Specific Antigen Test

After it was discovered that PSA was detectable in the bloodstream, [29, 30, 31] serum PSA levels were found to correlate with PCa stage [32] and with tumour volume. [33] This correlation is a result of disruption of the normal glandular structure in the prostate [34] and led to the use of PSA testing as a screening tool for PCa. The adoption of the PSA test led to a steep increase in the diagnosis rate of PCa (see Figure 1.3), with peaks in 1993 and 2001 corresponding to intensified use in Canada. [35] Rising diagnosis rates also saw a rise in overdiagnosis

and overtreatment of PCa, as much of the disease now being detected was low-grade and may have caused no change in HRQOL, even without treatment. [36, 37] This is supported by the observation that there was no corresponding major drop in PCa mortality rate following the introduction of PSA screening (see Figure 1.4). Although the ASMR of PCa has been declining since 1994, this is more likely due to improvements in treatment such as hormone therapy for early and advanced stage disease [38, 39] or advances in radiation therapy, [40] and not a result of PSA screening. [17]

Exacerbating the problem of overdiagnosis, PSA tests have a low specificity to PCa. There are many potential causes of a false positive result, such as BPH, prostatitis, urethral instrumentation, prostate biopsy, vigorous digital rectal examination (DRE), or recent ejaculation. [34] A high serum PSA level may lead to a patient receiving unnecessary biopsy, which carries risks such as hematuria or infection, or it may alter a physician's interpretation of biopsy results. [41] Measurement of PSA kinetics such as velocity, nadir level, or time to nadir [42] have attempted to improve the specificity to PCa, however they have not been associated with an improvement in the prediction of clinically significant cancer despite leading to increases in additional biopsies. [43]

Recognizing these issues, cancer screening guidelines in Canada were modified in 2014 to advise against performing PSA tests in asymptomatic men, as screening among the general population was only found to reduce PCa mortality by 0.1%. [16] The test remains an elective procedure for men aged 55-70, acknowledging that some men may value the small reduction in risk of death over the potential harms of the test. Following the modifications to the guidelines, incidence rates of PCa began to decline without an increase in mortality or diagnosis of late stage tumours. [17, 44]

1.3.2 Digital Rectal Examination

During a digital rectal examination, the physician manually palpates the prostate through the rectum, looking for hardening tissue and lateral differences between lobes. This test detects

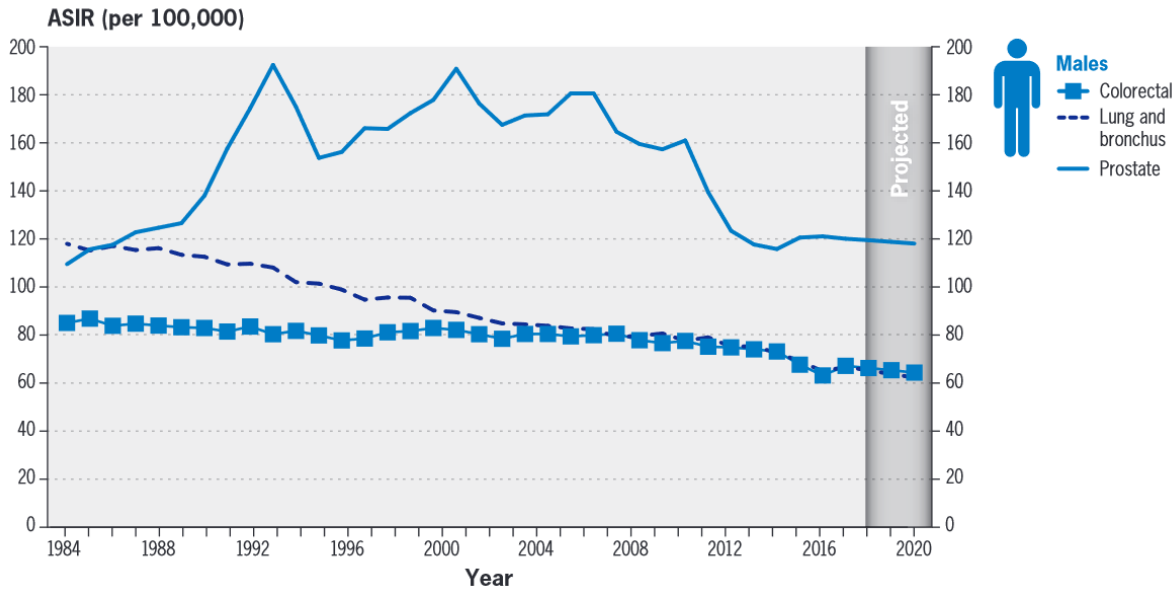


Figure 1.3: Age standardized incidence rates of prostate cancer in Canada (solid line). (Image taken from [17])

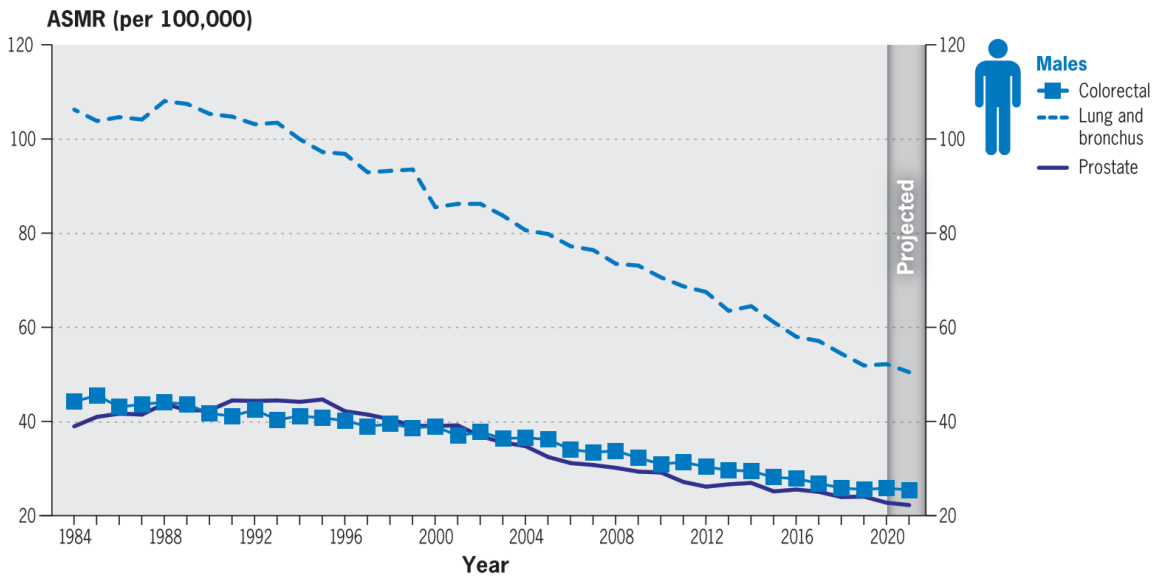


Figure 1.4: Age standardized mortality rates of prostate cancer in Canada (solid line). (Image taken from [17])

cancer in the PZ (adjacent to rectal wall), and is unreliable at detecting tumours in other zones of the prostate. In general, DRE suffers from low sensitivity to PCa, [45, 46] especially in patients with low PSA ranges (< 4 ng/mL). [47] Therefore, DRE must be combined with other more sensitive tests, usually PSA level, in order to exclude the presence of PCa. As a result of this shortcoming, DRE is no longer recommended as a screening tool in Canada. [16]

1.3.3 Biopsy

During biopsy, a pathologist examines the appearance of glands and cells in histopathological tissue samples under a microscope. The appearance is ranked against a standard reference (see Figure 1.5) to quantify the amount and grade of cancer present in the biopsy sample. Gleason scores are assigned by ranking the aggression of the most prevalent and second most prevalent types of cancer cells observed by the pathologist, and adding the two ranks together. [48] Gleason scores are used for PCa prognosis, as they have been shown to correlate strongly with PCa-specific mortality (PCSM). [49] An accurate prognosis is important to provide patients with realistic expectations and to administer an appropriate treatment strategy. [50] A pathologist's assignment of a Gleason score is considered the gold standard in the diagnosis of PCa. [51] Despite this, Gleason scores are subject to some sources of error. Interpretation bias may be caused by pathologists hesitating to characterize small amounts of high grade cancer cells in an otherwise low grade sample. [48] Furthermore, sampling errors when obtaining biopsy cores may cause an underestimate of the number of lesions or may miss more aggressive cancer, [52] and a robust sampling strategy is critical for achieving an accurate Gleason score.

Transrectal ultrasound (TRUS) guided biopsy (TRUS-GB) is the most common method of obtaining biopsy samples. During TRUS-GB, the patient lays in the lateral decubitus position as biopsy needles are inserted transrectally or transperineally into the prostate to obtain cores of sample tissue. The biopsy needles and prostates are imaged through the rectal wall via an ultrasound probe inserted through the anus. A grid template is used to evenly sample regions of the prostate where cancer is most likely to develop (i.e. the PZ). Sextant biopsy is the standard

biopsy scheme, but extended biopsy schemes, which obtain up to 12 biopsy cores improve the prediction value of the underlying pathologic Gleason score for PCa [53]. However, even the extended biopsy schemes carry a 1 in 5 chance of clinically meaningful underestimation of cancer grade [50] and repeat samples may suffer from the same errors as initial samples or may resample previously sampled areas. [54] Additionally, more samples increases the chances of adverse biopsy-related events such as infection, hematuria, rectal bleeding, or voiding difficulties. [55] In general, systematic TRUS-GB has difficulty sampling the anterior, midline, and apex regions of the prostate. [56]

Targeted Biopsy

Targeted biopsy schemes aim to reduce the sampling errors of systematic biopsy by using MR imaging of PCa to select the best regions for biopsy. MRI has demonstrated effectiveness in detecting, localizing, and grading cancer directly, and its diagnostic potential is further enhanced when combined with biopsy. [57] Analysing MRI for suspicious regions to target with biopsy increases the likelihood of accurately determining the extent and stage of any disease present. [56] In one study, MRI was found to have a sensitivity of 83% and specificity of 61% for detecting biopsy-confirmed PCa, suggesting the potential for MRI to be useful in targeted biopsies. [58] The study found a targeted biopsy detection rate of 78% compared to extended biopsy detection rate of 96%. However, further analysis revealed that the cancers missed by targeted biopsy were mostly clinically insignificant, and targeted biopsy detected cancer in the anterior regions of the prostate, which extended biopsy was unable to reach. Another study found significantly higher cancer detection rates when 3T MR diagnostic images were used to inform TRUS-GB. [59] A systematic review of image-guided biopsy using MRI-derived targets found cancer was detected in 30% of all cores sampled using targeted biopsy, compared to only 7% of cores from systematic biopsy. [56]. Therefore, targeted biopsy may enable fewer cores to achieve the same probability of cancer detection and reduce morbidity. Larger studies are still required to validate the efficacy of targeted biopsy.

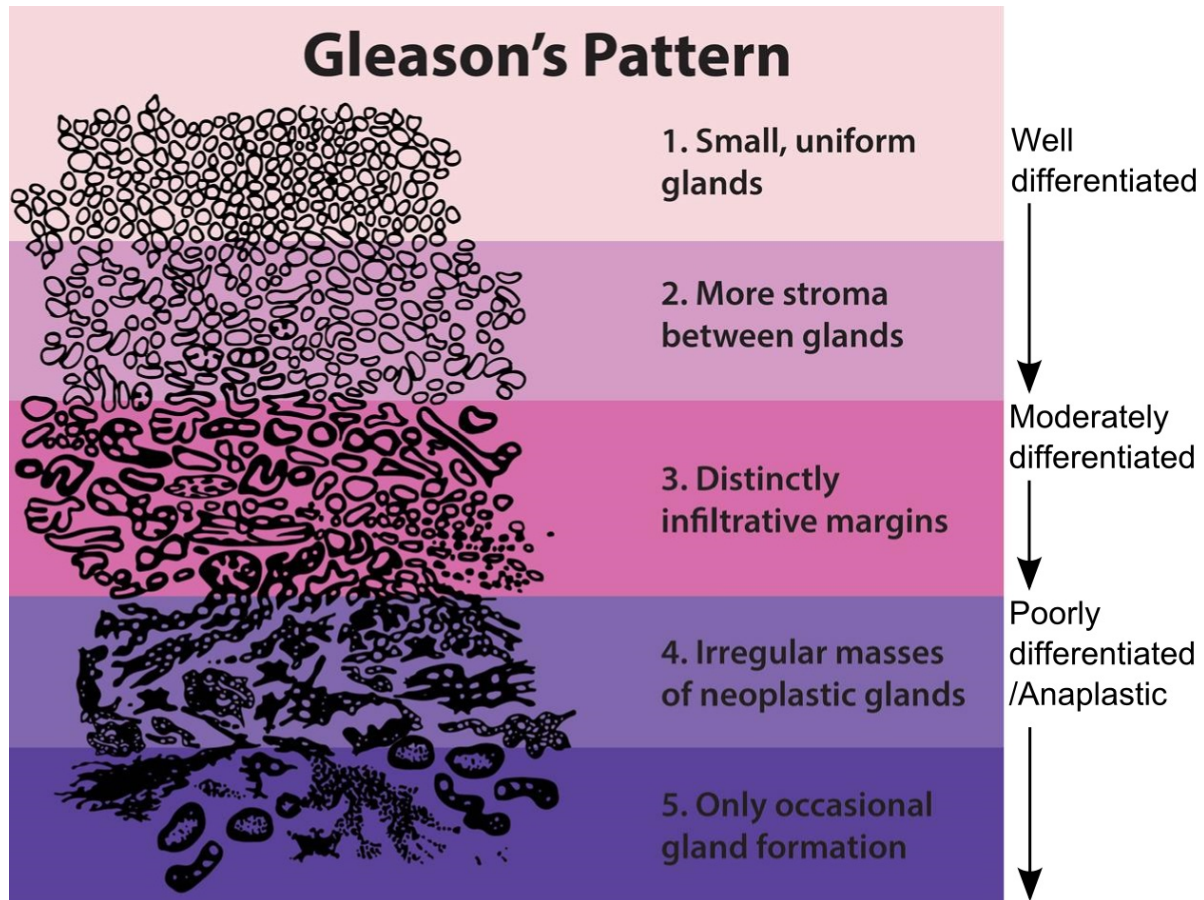


Figure 1.5: Example cell structure used in Gleason's grading system. With increasing grade, cells become more spread out and glandular architecture is lost. (Image by National Institutes of Health)

1.3.4 Imaging

Ultrasound (US) and MRI are most common modalities for diagnosis of PCa and image-guided interventions in the prostate. Other modalities such as computed tomography (CT), positron emission tomography (PET), and single positron emission computed tomography (SPECT) are usually limited to ancillary roles of imaging related structures and are generally not involved in evaluating localized PCa. This section will discuss the roles of US and MRI in PCa diagnosis.

Ultrasound

Ultrasound is the most common modality for imaging of the prostate owing mainly to its relatively low cost, portability, and real time imaging capabilities. [60] Transrectal US provides close access to the prostate via the rectal wall and is able to distinguish the zonal anatomy of the prostate and PCa, although it is not highly sensitive or specific to prostate carcinomas. [61] TRUS especially has difficulty with identifying the dominant cancer location in patients with low-grade PCa, [62] and with identifying tumours in the TZ or CZ, which are further from the rectal wall. [63] Nevertheless, TRUS has demonstrated useful capabilities for PCa management. One such use is its ability to calculate prostate volume, an important metric for predictive nomograms and for calculating PSA density. [64] Additionally, several techniques have improved the ability of TRUS to directly visualize tumours.

Contrast agents are intravenously injected substances, which contain tiny, gas-filled microbubbles that are highly echogenic. Contrast-enhanced US (CEUS) can improve sensitivity to larger, higher grade lesions, which are more vascular than healthy background tissue and thus take up contrast agents more readily. [60] The hypervascularity and uncontrolled angiogenesis of tumours are also leveraged in the power doppler ultrasound technique, which can measure the amplitude of blood flowing perpendicular to the US transducer within the imaging volume. Irregular or asymmetrical blood flow detected using these techniques may indicate the present of prostate cancer, [65] but other studies found that biopsies targeted using these techniques were negative in 20% of cases where systematic biopsy returned a positive result. [66, 67]

US elastography aims to detect regions of prostate tissue with increased stiffness, which is correlated to the disordered growth and increased cell density found in PCa. [66] Low-frequency vibrations are applied to the tissue and real-time US imaging of the vibrations is used to generate a map of estimated tissue stiffness. [68] Although elastography images provided superior contrast for visualizing prostate anatomy compared to traditional US images, [69] the performance of elastography for guiding biopsy is comparable to Doppler US and CEUS. [70, 66, 71] The technique may be useful for guidance of brachytherapy or laproscopic radical prostatectomy. [72]

Magnetic Resonance Imaging

Despite being more expensive and less portable than ultrasound imaging systems, MRI offers several advantages, which have proven useful for the detection and localization of carcinomas within the prostate. [64, 73, 74] With sub-millimeter resolution and high soft-tissue contrast available, the zonal anatomy of the prostate and some lesions are clearly distinguishable, even on T2-weighted (T2W) images alone. [75, 76] Many studies have compared MR prostate images with histopathologic images of PCa. [77, 78, 79] The sensitivity of MRI to PCa and its ability to stage PCa depends on many factors, such as the definition of clinically significant, the location of cancer in the gland, field strength of the scanner and the type of radiofrequency (RF) coil or MR sequence used. [80] Multi-parametric MRI (mpMRI) supplements MRI with other techniques such as dynamic contrast-enhanced MRI, diffusion weighted imaging, and MR spectroscopy to further increase the sensitivity and specificity of MRI to a wide range of prostate carcinomas. MR imaging has seen steadily increasing use in clinical practice, most commonly for detecting cancer or guiding targeted biopsy. [81]

T2-weighted images perform best for detecting PCa in the PZ. On T2W images, intensity of the signal in regions of PCa decreases correlated with increasing Gleason grade and contrasts with the relatively bright healthy PZ tissue. [82] Prostatitis, scarring, and hemorrhage also present as regions of hypointensity on T2W images, leading to poor specificity when using

T2W images alone for the detection of PCa. [75] T2W images are still useful for detecting disease in prostate regions difficult to reach with biopsy and in nearby structures such as the NVB, seminal vesicles, or lymph nodes. [64]

Dynamic contrast-enhanced (DCE) MRI is a functional imaging technique in which a contrast agent is injected into the patient's bloodstream, and a temporal series of rapid T1-weighted (T1W) three-dimensional (3D) spoiled gradient echo (SPGR) MR images are acquired as the gland uptakes and then washes out the contrast agent. [83] The dye appears earlier in cancerous regions, which exhibit increased angiogenesis and permeability compared with healthy tissue. [64, 84] In order to reduce the inter-observer variability that is inherent to a qualitative analysis of DCE MRI, pharmacokinetic (PK) parameters are calculated from signal-vs-time curves, such as the initial or wash-out slopes, time-to-peak, or maximum signal enhancement. [57] DCE MRI was reported to have a similar sensitivity and specificity to PCa as T2W imaging, with prostatitis and BPH potentially appearing as false positive results. [75] DCE images suffer from poor spatial resolution, which is a concession made in order to achieve the higher temporal imaging resolution required to observe the appearance of the contrast agent. Further research is required to settle on standards for optimal acquisition and analysis protocols for the use of DCE in PCa detection.

Diffusion-weighted imaging (DWI) is another functional MR imaging technique, which uses specialized gradients to encode the motion of protons in water as it diffuses through membranes in the gland. Acquiring multiple images with different levels of diffusion weighting allows mapping of the apparent diffusion coefficient (ADC) throughout the prostate [75] Since prostate tumours display restricted diffusion, [60] lower ADC values have been shown to correlate with regions of PCa, and combining DWI with T2W images resulted in a sensitivity of 81% and specificity of 84% for detecting cancerous lesions in the prostate. [85] DWI can be acquired faster than DCE images and without using a contrast agent, however both techniques suffer from poor spatial resolution.

MR spectroscopic imaging (MRSI) is a molecular imaging technique, which measures 3D

spectral profiles of protons in different metabolites. In the prostate, the dominant peaks in these profiles are from protons in citrate, creatine, and choline compounds. Altered metabolism in cancerous regions will cause a reduction in the synthesis of citrates and increase of choline compounds, [86, 87] the ratios of which can be used as biomarkers for PCa. [88] Whole-gland MRSI with sufficient signal-to-noise ratio (SNR) and spatial resolution for cancer detection can be acquired in 10-15 minutes. [89] Due to the varying normal ratios of metabolites throughout the prostate or disturbances caused by other pathology, as well as a strong susceptibility to magnetic field distortions, MRSI requires specialized knowledge and training for proper interpretation. [75] Despite this, MRSI has been demonstrated good sensitivity for detection of lesions in the transition zone, and may even outperform biopsy when detecting recurrent disease. [80] MRSI continues to develop as a complementary technique for MR imaging of PCa. [90, 91] Sodium MRI (Na-MRI) is a specific type of MRSI, which allows for higher resolution images since sodium is more easily distinguishable from the resonances of other atoms in the prostate. [92] Na-MRI has shown to be useful for characterization of PCa [93] since cancerous lesions demonstrate a significantly higher tissue sodium concentration (TSC) over normal glandular tissue. [94] The TSC correlates well with Gleason score. [95]

Achieving the optimal detection, localization, and characterization of PCa likely requires a multi-parametric approach, which combines T2W, functional, and molecular imaging. [75, 96, 97, 98, 99, 100, 101, 102] This approach outperforms results from any single technique, especially when considering specificity and distinguishing PCa from hemorrhage, prostatitis, or other pathologies. [75, 80]

1.4 Prostate Cancer Treatment

This section briefly introduces the most common clinical therapies for management of PCa as well as their associated side effects. An overview of focal therapy and its various energy modalities will also be given. Since this thesis is based on focal laser ablation therapy, this

modality will receive the bulk of the discussion.

1.4.1 Conventional Treatments

Conventional interventions for gland-confined prostate cancer are typically whole- or half-gland treatments, such as retropubic radical prostatectomy (RRP), external beam radiation therapy (EBRT), brachytherapy, or androgen deprivation therapy (ADT). These treatments provide excellent oncologic control but present risks to delicate structures such as the urethra, rectum, NVB, or bladder, which are critical for normal genitourinary function. [103] Damage to these structures can cause complications such as incontinence, erectile dysfunction, and rectal toxicity, [104, 105, 106, 107, 108] which negatively impacts post-treatment HRQOL. [19, 103, 109, 110, 111] In particular, Parker *et al.* found urinary and sexual function did not recover to pre-operative baseline at 5 year followup after RRP for localized PCa. [112] Of all the conventional treatment options, RRP had the highest rates of associated urinary incontinence [18, 111] and impotence. [113] Minimally invasive radical prostatectomy (MIRP) was found to reduce surgical complications and length of stay, but resulted in higher rates of genitourinary complication, incontinence, and erectile dysfunction at follow-up compared with conventional open RRP. [114] Another study of RRP and MIRP found sexual and social functioning remained poor at 12 month follow-up, although other HRQOL domains recovered to baseline levels. [115] EBRT was associated with adverse bowel function [111] and decline in sexual function, [113] and ADT led to fatigue, muscle weakness, and weight gain. [116] Bergius *et al.* found the number of quality-adjusted life-years (QALY) during a 2-year follow-up was lowest among patients who received ADT versus patients who received RRP, EBRT, or no treatment. [117]

The risk of treatment-related morbidity, weighed against the high 10-year survival rates of low-grade PCa, indicates men with localized low- to intermediate-risk PCa (PSA levels less than 15 ng/ml, Gleason scores 7 or less, and 25% or less tumour involvement in biopsies) are overtreated by whole gland therapy, and the risk of treatment-related side effects may out-

weigh the benefit of treatment. [118] In these cases, patients may undergo watchful waiting or active surveillance (AS), [119] in which disease progression is monitored and intervention is delayed until the tumour volume or risk increases. [119, 120, 121] The Prostate Cancer Intervention Versus Observation Trial (PIVOT) [122] randomized 731 men under the age of 75 with clinically localized PCa to either RRP or AS groups, with a follow-up after a median of 10 years. There was no significant difference in rates of PCSM between the two groups, but significantly higher rates of urinary incontinence and erectile dysfunction were reported in the RRP group. [123] A similar trial found an absolute reduction in risk of prostate cancer death of 5.3% in the RRP group over the AS group after 10-year follow-up, [124] however the AS group experienced a 10.2% higher cumulative incidence of distant metastasis and a 25.1% higher cumulative incidence of local disease progression at 10-year follow up. Therefore, watchful waiting may be considered undertreatment and it may be advantageous to begin controlling disease while it remains low-grade and localized. AS also may lead to decreased HRQOL as a result of the psychological burden of living with untreated disease, leading men to seek definitive treatment even without clinical indicators of disease progression. [21, 125, 126]

1.4.2 Focal Therapies

The optimal treatment for localized low- to intermediate-risk PCa, which balances oncologic control and treatment-related morbidity, is not yet well understood. Focal therapies are emerging as an alternative interventional option to bridge the gap between whole gland therapy and active surveillance. [127, 128, 129, 130, 131] The focal therapy concept is motivated by research that suggests a single dominant index lesion (DIL) is the most likely origin of other lesions in the prostate as well as metastases. [132] Treatment of the DIL while sparing the rest of the gland may adequately control disease while preserving nearby critical structures to minimize treatment-related side effects. [133] Several energy modalities have the capability to ablate a small, well-defined region of tissue within the prostate, including high-intensity focused ultrasound (HIFU), cryotherapy, photodynamic therapy (PDT), and FLA, [23] but there

is not yet a consensus as to which modality is optimal for focal therapy or which patients are the best candidates for this treatment option. [134, 23]

Focal Laser Ablation Therapy

FLA is an attractive energy modality due to its ability to completely ablate a targeted region, [135] and particularly in the prostate, its precise control over the extent of ablation, owing to prostatic tissue's ideal optical absorption rate without excess vascularity. [136] During FLA therapy, laser energy is delivered via diffuser-tipped needle fibers inserted transperineally through a needle guided by a template to the tumour site. [137] The tissue surrounding the needle tip is heated to 60 °C with the intention of ablating the tumour as well as a 5 mm margin of healthy tissue where possible (i.e., avoiding functional structures). [138] However, recent research suggests that healthy tissue margins of at least 10 mm around lesions contoured on MRI must also be ablated in order to ensure complete eradication of cancerous cells, as mpMRI tends to underestimate the extent of PCa. [139, 140, 141]

Although the optimal patient selection criteria for FLA therapy is an ongoing area of research, candidates are generally selected based on having disease confined to one half of the prostate or less, low PSA levels, Gleason score 7 or less, and MRI-visible lesions concordant with positive biopsy locations. Patients undergo a pre-operative mpMRI examination, during which T2W, DCE, and DWI (see Sec. 1.3.4) images are acquired. [142, 143] The images are interpreted by a radiologist to identify and localize the index lesion. The sextant (i.e. left/right and apex/mid-gland/base) where the lesion is located is recorded, along with the length of its largest dimension. A typical measurement range of lesions targeted for FLA therapy is 4-12 mm [24] with some studies targeting lesions up to 20 mm. [144] Cancer with a volume of less than 0.5 mL is not considered clinically significant. [145] During the procedure information about the lesion size and location is aligned with intra-operative images, either mentally by the physician [24] or using automated software, [146] in order to guide needles to the correct location.

The first reported treatment of localized PCa with FLA occurred in 1984, using a 1064 nm laser to ablate prostate tissue with a combined transurethral and suprapubic approach in 47 patients without causing damage to the rectal wall. [147] In 1993, Amin *et al.* performed interstitial laser coagulation of a focal abnormality in a patient with PCa using a transperineal approach without complications. [148] Colour Doppler and b-mode US were used for real-time temperature monitoring. Although tissue necrosis was biopsy-confirmed in the ablation regions, follow-up biopsy found residual cancer.

Advancements in image guidance led to a phase I trial evaluating photothermal ablation on twelve patients with low-risk PCa using intra-operative US guidance to MRI-identified targets. [149, 146] CEUS was used for treatment monitoring and a modified brachytherapy template was for used for needle guidance. The authors reported no significant decrease in erectile or urinary function, however a six-month follow up found 33% patients had positive post-treatment biopsies in the targeted regions, possibly due to inaccuracies when registering pre-operative MR and intra-operative US images and difficulties localizing small tumours on MRI. [146]

To avoid the problem of MR-US registration, Raz *et al.* performed FLA therapy on 2 patients using direct MRI-guidance. [137] MR imaging was used pre-operatively to plan a treatment region on T2W and DWI MR images. Intraoperatively, MRI was used for guidance of needles during insertion, and for real-time temperature monitoring during energy application using MR thermometry. Temperature profiles at each voxel were used to estimate the ablation zone based on an Arrhenius rate process model. [150, 151] Post-operative DCE MRI was used to confirm devascularization of the ablation zone, and was found to correlate well with the region predicted by MR thermometry. [152, 153] DCE MR images, where the immediate devascularization of ablated tissue presents as a hypo-intense signal void, have also been shown to correlate well with ablation regions measured using whole-mount histopathology. [154, 155, 156]

In 2013 and 2014, 21 patients were treated using MRI-guided FLA at the NYULMC

Smilow and Sperling Prostate Cancer Centres. [157] In 13 patients who underwent subsequent targeted biopsy of the ablation region, 12 showed no cancer in the biopsy samples. No significant changes in the American Urological Association Symptom Score (AUASS), International Prostate Symptom Score (IPSS), or Sexual Health Inventory for Men (SHIM) scores were reported. Oto *et al.* performed a phase I clinical trial of MRI-guided FLA on nine patients and found no cancer in biopsy samples of the ablation zone of seven patients at six month follow-up. [24] A phase II trial at the same centre on 27 patients found residual cancer in the ablation zones of one patient at three month follow-up and three patients at twelve month follow-up. [138] Both trials reported acceptable treatment-related morbidity for all patients. J. Bomers *et al.* performed FLA on five patients using MRI guidance and a fixed template, followed three weeks later by total prostatectomy. [158] Post-ablative T1W MRI scans found a strong correlation with histopathology when measuring ablative volume, but no correlation was found between the damage estimation maps and histopathology. A phase I clinical trial of FLA using T2W images to confirm laser applicator position was successfully performed in 8 subjects with minimal adverse events. [159] Follow-up biopsy at 6 months detected cancer in the ablation zone in 3 men and outside the treatment margin in 6 men, confirming that larger treatment margins should be planned when performing MR-guided FLA. [159] These studies demonstrate that FLA is capable of destroying the DIL with minimal patient morbidity, and reinforce that MRI is the most desirable image guidance modality.

While the techniques for planning, guidance, delivery, and monitoring of FLA procedures have improved considerably from the first clinical trial, modern trials studying FLA therapy continue to report detection of residual cancer on post-treatment biopsies or recurrence of cancer at follow-up. The success of FLA is dependent on proper patient selection criteria, [133, 160] diligent treatment planning, [160] and accurate needle guidance. [161] Continuing to develop the techniques used in MRI-guided FLA therapy is necessary to improve its ability to provide localized cancer control in the prostate.

1.5 Challenges in Using MRI-Guidance for Needle Delivery in Prostate Interventions

MRI offers many advantages for the guidance of prostate FLA, [143] but it also presents several challenges for integration with an interventional workflow. An MRI scanner is a large, complicated system, which typically occupies several rooms - a shielded examination room in which the MR scanner is located, an equipment room, which contains amplification and measuring equipment, and a control room, which contains a console for operating the scanner. A movable bed is used to position the imaging subject at the isocenter of the magnetic field within the bore of the MR scanner, which is typically 1-2 meters in length and about half a meter in diameter. The limited confines of the scanner bore limits access to the patient without first withdrawing the bed.

Strong electromagnetic fields are a unique feature of MRI systems compared with other imaging modalities, and are not compatible with typical mechatronic systems. The American Society for Testing and Materials (ASTM) defines the MR-environment as the volume of space encompassed by the 5-Gauss line of an MR system. Since the examination room is shielded, a penetration panel is located between the examination and control rooms as a means of passing cables into the MR environment. When designing any device meant to be used within the MRI environment, considerations must be made for the effects that the electromagnetic fields will have on the device, and for the effects that the device will have on the acquisition of MR images.

1.5.1 Effects of MRI on Devices

A variety of magnetic fields are present in the bore of an MRI scanner. Clinical scanners generate an always-on, strong static magnetic field in the order of several Tesla. This field will apply strong forces and torques to any nearby ferromagnetic materials, potentially turning them into dangerous projectiles as well as causing unwanted motion in guidance devices constructed

from these materials. [162, 163] The concern for interaction with the magnetic field limits the use of common materials used in mechatronic systems and requires the use of specialized materials, which may be more difficult to fabricate. [164]

MR scanners also generate time-varying magnetic field gradients to perform spatial encoding of voxels during image acquisitions. These fields have the potential to develop eddy currents in conductive materials inside the scanner bore, and those currents can lead to motion that opposes the magnetic field, or that heats the material. [164, 165] RF signals generated by the scanner can also induce currents in conductive materials. The largest currents are induced in objects that are long, have a large surface area, or form loops, especially when they are placed near the gradient coils. [163] This means that needles especially should be carefully chosen to ensure MRI compatibility and wiring needs to be properly shielded so as to avoid noise being introduced into circuits.

1.5.2 Effects of Devices on MRI

Even though a device may be safe to bring into the MR environment, it still has the potential to degrade the quality of acquired images by introducing magnetic field inhomogeneities or RF noise. Any object placed in the scanner's bore will cause distortions of the magnetic fields proportional to the magnetic susceptibility of the materials used to construct the object. [162] Eddy currents or intentional electrical currents passed through the device will also distort the magnetic fields. To mitigate distortions, ideally foreign objects should be withdrawn from the bore during image acquisition. Devices that must remain in the scanner bore should be constructed of materials that have a magnetic susceptibility close to air if placed near the image volume, or a magnetic susceptibility close to human tissue if placed within the image volume. [164] Magnetic field distortions manifest as spatial distortions in acquired images, causing voxels to be encoded into the wrong slice, or distorting the shape of anatomy within the slices. [166, 167] Using stronger magnetic field gradients can reduce the magnitude of image distortions, but a strong gradient causes a larger spread of resonance frequencies and requires a wider RF re-

ceiver bandwidth to capture those frequencies, thus increasing the SNR of the image. [167] Because of this penalty and because gradient strength is often not a parameter selected manually by the operator, appropriate material selection is the preferred way of limiting image distortion.

Electrical currents in the actuators or sensors used in mechatronic devices can also emit RF noise that will degrade image quality. An RF signal emitted in a narrow frequency range will cause a bright line artifact to appear in the image at the location associated with the same frequency used for the spatial encoding. [166] Conversely, RF noise emitted across a wide frequency range will degrade the overall SNR of the acquired images. As alluded to earlier, SNR can be improved with a lower gradient field strength, but that will increase the magnitude of spatial distortions caused by magnetic field inhomogeneity. Therefore, RF noise should be mitigated as much as possible by properly shielding electrical components in the device, and using the appropriate connections in the control room's penetration panel.

1.6 Existing MRI-Guided Prostate Needle Delivery Devices and Techniques

A wide range of systems have been developed for MRI-guidance of needles to the prostate for procedures such as biopsy, brachytherapy, or focal therapy. Most systems use either a transrectal or transperineal approach to access the prostate, and can be strictly mechanical, electronically monitored, or fully mechatronic with remote actuation capabilities. As the transrectal approach conveys a higher risk of adverse clinical consequences, such as sepsis and rectal bleeding, compared with a transperineal approach, [168, 169] this section will provide an overview of systems and techniques that have been previously developed for transperineal MRI-guided prostate needle delivery.

1.6.1 Conventional Techniques

A fixed grid template containing regularly spaced holes for needle insertion is the standard clinical method of transperineal needle guidance to the prostate. For image guidance, a TRUS probe can also be mounted to the grid template, providing a fixed relationship between the holes of the template and the imaging plane, which enables physicians to select the correct hole to reach a target identified on the US images. This approach was adapted for the first MRI-guided prostate interventions by attaching a set of MR-visible fiducials to the template in order to register it with the MRI coordinate system. [170]

The first MRI-guided interstitial prostate brachytherapy was reported in 1998, using an open 0.5 T MRI scanner and pelvic coil with a perineal template for needle insertion in 9 patients. [170] To deposit the sources in their planned locations, an iterative approach was implemented whereby catheters were imaged during insertion and this information was used to adjust their position accordingly. A median minimum dosimetric coverage of 94% of the clinical target volume was achieved with minimal acute morbidity. Two years later, the same approach was used to perform a targeted biopsy of suspicious lesions on a patient ineligible for TRUS-guided biopsy. [171] MR-guided biopsy confirmed the presence of adenocarcinoma, where all six cores obtained from random sextant biopsy were negative.

Hata *et al.* also performed MRI-guided prostate biopsy on two patients in an open scanner with a grid template, using optical tracking for registration with the MRI coordinate system. [172] In one of the patients, core samples obtained from targeted biopsy of suspicious lesions were positive where all sextant biopsy core samples were negative. This study also highlighted the advantages of MRI-guidance for biopsy in patients where the prostate's shape has been altered by BPH.

1.6.2 Mechatronic or Robotic Systems

Although the studies mentioned in the previous section demonstrated the potential advantages of MRI-guidance for prostate interventions, they also revealed the shortcomings of conven-

tional techniques and the need for more advanced systems specifically designed for the challenges of the MR environment. Open-bore MRI scanners, while providing easier access to the patient on the imaging bed, suffer from reduced image quality compared to closed-bore scanners. [173] Closed-bore MRI scanners are able to generate higher magnetic field strengths and are also more widely available in clinical settings. Unfortunately, the restricted access to the patient in a closed-bore scanner makes MRI-guided prostate interventions even more challenging on top the presence of strong magnetic field gradients. Some studies attempted to register higher quality pre-operative images from closed-bore scanners to intra-operative images from open-bore scanners in order to maintain easy access to the patient, but the deformable nature of the prostate posed challenges as the patient was moved between scanners. [174, 175]

Another trial of 10 brachytherapy procedures attempted to work within the confines of a 1.5 T scanner bore by placing the patient in the lateral decubitus position instead of the standard lithotomy position, [173] using a custom integrated grid template and endorectal coil attached to a positioning arm designed for prostate biopsy and brachytherapy. [176]. While the high-resolution images enabled them to achieve good needle placement accuracy and a mean minimum dosage coverage of 94% of the targeted volume, they reported longer procedure times and difficulties with prostate stability in the lateral decubitus position. Additionally, patients were withdrawn from the bore to perform needle insertions, introducing a further elevated risk of prostate motion. This suggests that a robotic needle guidance system may be able to improve the clinical workflow of MRI-guided prostate interventions in closed-bore scanners.

Several MRI-compatible mechatronic systems have been previously reported in the literature. Since standard motors cannot be used in the presence of the MRI scanner's strong magnetic fields, pneumatically actuated systems have proven a popular alternative. Stoianovici *et al.* developed a remotely actuated robot, which they dubbed "MRI Stealth" and showed to have adequate MRI compatibility and targeting accuracy in tissue-mimicking phantoms and canine models. [177, 178, 179] The robot employed specially developed stepped pneumatic motors and light-based encoders [180] to facilitate high precision and easily controllable mo-

tion, which is usually not available using pneumatics. The group demonstrated a workflow for translation of their system to clinical trials, which have yet to be reported. [181] However, this system required patients to lie in the lateral decubitus position, again providing less stability to the prostate than the standard lithotomy position. The INNOMOTION system is an MRI- and CT-compatible pneumatically actuated 5 degree-of-freedom (DOF) robotic system for positioning instruments inside the bore of an MRI, which could be used to guide FLA needles. The system meets European standards for safety and sterilizability and has begun clinical trials. [182] Van den Bosch *et al.* developed a system that used hydraulics and pneumatics for template positioning and needle insertion, respectively. [183] Song *et al.* developed a 4 DOF pneumatically actuated parallel robot for prostate biopsy and brachytherapy. [184] All of these pneumatically or hydraulically actuated devices require a bulky network of pumps and hoses to be placed either at an appropriate distance from the scanner inside the same room, or to be connected externally in the MRI control room.

Other actuation methods that have been verified as MRI-compatible include a series of embedded binary pneumatic actuators made from molded polymers [185], a bistable manipulator comprised of dielectric elastomer actuators, [186] and a polyethylene cable-driven needle positioning mechanism for prostate cryoablation. [187] Piezoelectric motors generate motion using piezoelectric materials that change their shape when an electric field is applied, instead of using magnetic fields as a traditional electric motor does. These motors are capable of very precise movements and have demonstrated compatibility with the MRI environment.

Goldenberg *et al.* developed an ultrasonic motor-driven robot for prostate ablations including remote control of trocar penetration and retraction. [188, 189, 190] However, the fully robotic design eliminated haptic feedback for the physician, made the system more difficult to sterilize, and complicated the insertion process since motors must be deactivated during imaging. Shang *et al.* developed a tele-operation system for percutaneous interventional procedures which employed a master-slave control scheme and used piezoelectric motors for actuation and custom fiber optic force sensors for haptic feedback. [191] Su *et al.* also presented a feasibility

study of a concentric tube 6 DOF manipulator driven by piezoelectric motors for guidance of a curved, steerable cannula. The authors reported a loss of less than 2% SNR while the motors were active during 3T scans while achieving a root mean square (RMS) needle tip position error of 1.0 mm at depths of up to 50 mm. [192] However, Fischer *et al.* reported some noise in MRI scans acquired while piezoelectric motors were active in the scanner bore. [177]

Cepek *et al.* developed a manually actuated, position encoded device, which allows the needle guide to be positioned inside the scanner bore with the patient in the lithotomy position using external manipulator arms. [193] Manual actuation avoids the problem of requiring complicated, specialized actuators while still maintaining a high level of accuracy by using encoders to provide position feedback. A clinical trial was performed on ten patients and a median needle accuracy of 3.5 mm was measured with a median needle delivery time of 9 minutes. [194] However, the physician was still required to partially enter the confines of the bore to perform needle insertion, and was not able to view guidance images while operating the system.

1.7 Thesis Hypothesis and Objectives

Based on the review above, the need remains for a system capable of accurately delivering needles transperineally to the prostate, that allows for remote adjustment of the needle trajectory without restricting access to the patient. The system should be unobtrusive in order to provide a clear view and access to the perineum, and should retain manual needle insertion in order to improve patient safety and ease of sterilization. The overarching hypothesis of this thesis is that a remotely actuated mechatronic needle guidance system with manual needle insertion is capable of accurately and consistently delivering needles to MRI-identified targets within tissue-mimicking phantoms, while not significantly degrading the quality of MR images acquired while it is inside the scanner's bore. Our vision is that the system will proceed to clinical FLA trials where it will be able to accurately guide needles to lesions in the

prostate, reduce focal laser ablation procedure times, and maintain patient safety. This system will provide an important step towards the clinical evaluation of FLA as a technique for the control of localized prostate cancer with minimal treatment-related side effects, allowing it to be meaningfully compared with competing energy modalities for focal therapy.

1.7.1 Specific Objectives

The specific objectives of this thesis each correspond to one of the major chapters presented in the next section.

1. Develop a deformable image registration method that can be used to compensate for prostate deformation between pre-operative and post-operative MR images, and use the method to compare target volumes with ablation regions to determine whether adequate treatment coverage was obtained or not.
2. Develop an MRI-compatible, remotely actuated, mechatronic needle guidance system that fits inside the scanner bore. Verify the MRI-compatibility and evaluate the accuracy of the system in guiding needles to virtual targets.
3. Improve the accuracy of the procedure for registering the coordinate systems of the MR images and the mechatronic system, and develop a graphical user interface (GUI) to facilitate the system's integration with the clinical workflow. Quantify improvement of the needle placement accuracy of the new procedure in tissue-mimicking phantoms.

1.8 Thesis Outline

This section provides summaries of the remaining chapters in this thesis.

1.8.1 Chapter 2: Evaluation of Tumour Coverage after MR-Guided Prostate Focal Laser Ablation Therapy

Prostate cancer is the most common non-cutaneous cancer among men in Canada. Focal laser thermal ablation has the potential to control small tumours while preserving urinary and erectile function by leaving the neurovascular bundles and urethral sphincters intact. Accurate needle guidance is critical to the success of FLA. Multi-parametric magnetic resonance images can be used to identify targets, guide needles, and assess treatment outcomes. In this chapter, we evaluated the location of ablation zones relative to targeted lesions in 23 patients who underwent FLA therapy in a phase II trial. The ablation zone margins and unablated tumour volume were measured to determine whether complete coverage of each tumour was achieved, which would be considered a clinically successful ablation.

Pre-operative mpMRI were acquired for each patient two to three months preceding the procedure and the prostate and lesion(s) were manually contoured on 3T T2-weighted axial images. The prostate and ablation zone(s) were also manually contoured on post-ablation 1.5T T1-weighted contrast-enhanced axial images acquired immediately after the procedure intra-operatively. The lesion surface was non-rigidly registered to the post-ablation image using an initial affine registration followed by non-rigid thin-plate spline registration of the prostate surfaces. The margins between the registered lesion and ablation zone were calculated using a uniform spherical distribution of rays, and the volume of intersection was also calculated. Each prostate was contoured five times to determine the segmentation variability and its effect on intersection of the lesion and ablation zone.

We showed that the boundaries of the segmented tumour and ablation zone were close. Of the 23 lesions that were analyzed, eleven were completely covered by the ablation zone and twelve were partially covered. A shift of 1.0, 2.0, and 2.6 mm would result in 19, 21, and all tumours completely covered by the ablation zone, respectively. The median unablated tumour volume across all tumours was 0.1 mm^3 with an IQR of 3.7 mm^3 , which was 0.2% of the median tumour volume (46.5 mm^3 with an IQR of 46.3 mm^3). The median extension of the

tumours beyond the ablation zone, in cases which were partially ablated, was 0.9 mm (IQR of 1.3 mm), with the furthest tumour extending 2.6 mm.

In all cases the boundary of the tumour was close to the boundary of the ablation zone and in some cases the boundary of the ablation zone did not completely enclose the tumour. Our results suggest that some of the ablations were not clinically successful and that there is a need for more accurate needle tracking and guidance methods. Limitations of the study include errors in the registration and segmentation methods used, as well as different voxel sizes and contrast between the registered T2 and T1 MRI sequences and asymmetric swelling of the prostate post-procedurally. Results from this chapter directly motivated the work of the next two chapters.

1.8.2 Chapter 3: Design and Validation of an MRI-Compatible Mechatronic System for Needle Delivery to Localized Prostate Cancer

Accurate needle guidance is critical to the success of FLA. Multi-parametric magnetic resonance images can be used to identify targets, guide needles, and assess treatment outcomes. The purpose of this chapter was to design and evaluate the accuracy of an MR-compatible mechatronic system for in-bore transperineal guidance of FLA ablation needles to localized lesions in the prostate.

The mechatronic system was constructed entirely of non-ferromagnetic materials, with actuation controlled by piezoelectric motors and optical encoders. The needle guide hangs between independent front and rear two-link arms, which allows for horizontal and vertical translation as well as pitch and yaw rotation of the guide with a 6.0 cm range of motion in each direction. Needles are inserted manually through a chosen hole in the guide, which has been aligned with the target in the prostate. Open-air positioning error was evaluated using an optical tracking system (0.25 mm RMS accuracy) to measure 125 trajectories in free space. Correction of systematic bias in the system was performed using 85 of the trajectories, and the remaining 40 were used to estimate the residual error. The error was calculated as the hori-

zontal and vertical displacement between the axis of the desired and measured trajectories at a typical needle insertion depth of 10 cm. MR-compatibility was evaluated using a grid phantom to assess image degradation due to the presence of the system, and induced force, heating, and electrical interference in the system were assessed qualitatively. In-bore positioning error was evaluated on 25 trajectories.

Open-air mean positioning error at the needle tip was 0.80 ± 0.36 mm with a one-sided 95% confidence interval of 1.40 mm. The mean deviation of needle trajectories from the planned direction was $0.14 \pm 0.06^\circ$. In the MR bore, the mean positioning error at the needle tip was 2.11 ± 1.05 mm with a one-sided 95% prediction interval of 3.84 mm. The mean angular error was $0.49 \pm 0.26^\circ$. The system was found to be compatible with the MR environment under the specified gradient-echo sequence parameters used in this study.

A complete system for delivering needles to localized prostate tumours was developed and described in this chapter, and its compatibility with the MR environment was demonstrated. In-bore MRI positioning error was sufficiently small for targeting small localized prostate tumours.

1.8.3 Chapter 4: Toward Mechatronic MRI-Guided Focal Laser Ablation of the Prostate: Robust Registration for Improved Needle Delivery

Multi-parametric MRI is an effective tool for detecting and staging prostate cancer, guiding interventional therapy, and monitoring PCa treatment outcomes. MRI-guided focal laser ablation therapy is an alternative, minimally invasive treatment method to conventional therapies, which has been demonstrated to control low-grade, localized PCa while preserving patient quality of life. The therapeutic success of FLA depends on the accurate placement of needles for adequate delivery of ablative energy to the target lesion. In the previous chapter, we developed an MR-compatible mechatronic system for prostate FLA needle guidance and evaluated its per-

formance in open-air and clinical 3T in-bore experiments using virtual targets. The purpose of this chapter is to develop a robust MRI-to-mechatronic system registration method and evaluate its in-bore MR-guided needle delivery accuracy in tissue-mimicking prostate phantoms.

The improved registration multi-fiducial assembly houses thirty-six aqueous gadolinium-filled spheres distributed over a 7.3 x 7.3 x 5.2 cm volume. MRI-guided needle guidance accuracy was quantified in agar-based tissue-mimicking prostate phantoms on trajectories ($N = 44$) to virtual targets covering the mechatronic system's range of motion. 3T gradient recalled echo (GRE) MRI images were acquired after needle insertions to each target, and the air-filled needle tracks were segmented. Needle guidance error was measured as the shortest Euclidean distance between the target point and the segmented needle trajectory, and angular error was measured as the angle between the targeted trajectory and the segmented needle trajectory. These measurements were made using both the previously-designed four-sphere registration fiducial assembly on trajectories ($N = 7$) and compared with the improved multi-fiducial assembly using a Mann Whitney U test.

The median needle guidance error of the system using the improved registration fiducial assembly at a depth of 10 cm was 1.02 mm with an interquartile range (IQR) of 0.42 - 2.94 mm. The upper limit of the one-sided 95% prediction interval of needle guidance error was 4.13 mm. The median (IQR) angular error was 0.0097 rad (0.0057 - 0.015 rad) with a one-sided 95% prediction interval upper limit of 0.022 rad. The median (IQR) positioning error using the previous four-sphere registration fiducial assembly was 1.87 mm (1.77 - 2.14 mm). This was found to be significantly different ($p=0.0012$) from the median (IQR) positioning error of 0.28 mm (0.14 - 0.95 mm) using the new registration fiducial assembly on the same trajectories. No significant difference was detected between the medians of the angular errors ($p=0.26$).

This chapter presents an improved registration method and evaluation in tissue-mimicking phantoms of our remotely actuated MR-compatible mechatronic system for delivery of prostate FLA needles. Accounting for the effects of needle deflection, the system was demonstrated to be capable of needle delivery with an error of 4.13 mm or less in 95% of cases under ideal

conditions, which is a statistically significant improvement over the previous method.

1.8.4 Chapter 5: Conclusions and Future Work

This chapter summarizes the conclusions of the previous three major chapters of the thesis, and discusses limitations of the thesis that warrant further study.

Bibliography

- [1] M. W. Dunn and M. W. Kazer, "Prostate Cancer Overview," *Seminars in Oncology Nursing*, vol. 27, no. 4, pp. 241–250, 2011.
- [2] J. Bosch, K. Tilling, A. M. Bohnen, C. H. Bangma, and J. L. Donovan, "Establishing normal reference ranges for prostate volume change with age in the population-based Krimpen-study: Prediction of future prostate volume in individual men," *The Prostate*, vol. 67, pp. 1816–1824, dec 2007.
- [3] P. W. McLaughlin, C. Evans, M. Feng, and V. Narayana, "Radiographic and Anatomic Basis for Prostate Contouring Errors and Methods to Improve Prostate Contouring Accuracy," *International Journal of Radiation Oncology*Biophysics*, vol. 76, no. 2, pp. 369–378, 2010.
- [4] P. W. McLaughlin, S. Troyer, S. Berri, V. Narayana, A. Meirowitz, P. L. Roberson, and J. Montie, "Functional anatomy of the prostate: Implications for treatment planning," *International Journal of Radiation Oncology Biology Physics*, vol. 63, no. 2, pp. 479–491, 2005.
- [5] J. Smith, S. Howards, G. Preminger, and R. Dmochowski, *Hinman's Atlas of Urologic Surgery Revised Reprint*. Elsevier, 4 ed., 2019.
- [6] J. E. McNeal, "The zonal anatomy of the prostate," *The Prostate*, vol. 2, pp. 35–49, jan 1981.
- [7] S. H. Selman, "The McNeal Prostate: A Review," *Urology*, vol. 78, no. 6, pp. 1224–1228, 2011.
- [8] J. E. McNeal, "Normal Histology of the Prostate," *The American Journal of Surgical Pathology*, vol. 12, no. 8, 1988.
- [9] J. E. McNeal, E. A. Redwine, F. S. Freiha, and T. A. Stamey, "Zonal distribution of prostatic adenocarcinoma. Correlation with histologic pattern and direction of spread," *The American journal of surgical pathology*, vol. 12, pp. 897–906, dec 1988.
- [10] B. Turner and L. Drudge-Coates, "Prostate cancer: risk factors, diagnosis and management," *Cancer Nursing Practice*, vol. 9, pp. 29–36, dec 2010.
- [11] H. Lilja and P. A. Abrahamsson, "Three predominant proteins secreted by the human prostate gland," *The Prostate*, vol. 12, no. 1, pp. 29–38, 1988.
- [12] Y. H. Park, C. W. Jeong, and S. E. Lee, "A comprehensive review of neuroanatomy of the prostate," *Prostate international*, vol. 1, no. 4, pp. 139–145, 2013.
- [13] R. S. Swerdloff, R. E. Dudley, S. T. Page, C. Wang, and W. A. Salameh, "Dihydrotestosterone: Biochemistry, Physiology, and Clinical Implications of Elevated Blood Levels," *Endocrine reviews*, vol. 38, pp. 220–254, jun 2017.

- [14] Statistics Canada, “CANSIM - 102-4309 - Mortality and potential years of life lost, by selected causes of death and sex, three-year average, Canada, provinces, territories, health regions and peer groups,” 2013.
- [15] D. R. Brenner, H. K. Weir, A. A. Demers, L. F. Ellison, C. Louzado, A. Shaw, D. Turner, R. R. Woods, and L. M. Smith, “Projected estimates of cancer in Canada in 2020,” *Canadian Medical Association Journal*, vol. 192, pp. E199 LP – E205, mar 2020.
- [16] N. Bell, S. C. Gorber, A. Shane, M. Joffres, H. Singh, J. Dickinson, E. Shaw, L. Dunfield, and M. Tonelli, “Recommendations on screening for prostate cancer with the prostate-specific antigen test,” *Canadian Medical Association Journal*, vol. 186, pp. 1225 LP – 1234, nov 2014.
- [17] Canadian Cancer Statistics Advisory Committee in collaboration with the Canadian Cancer Society, “Canadian Cancer Statistics 2021,” tech. rep., Statistics Canada and the Public Health Agency of Canada, Toronto, ON, 2021.
- [18] B. B. Reeve, A. M. Stover, R. E. Jensen, R. C. Chen, K. L. Taylor, S. B. Clauser, S. P. Collins, and A. L. Potosky, “Impact of diagnosis and treatment of clinically localized prostate cancer on health-related quality of life for older Americans: a population-based study,” *Cancer*, vol. 118, pp. 5679–5687, nov 2012.
- [19] D. T. Eton and S. J. Lepore, “Prostate cancer and health-related quality of life: a review of the literature,” *Psycho-oncology*, vol. 11, no. 4, pp. 307–326, 2002.
- [20] S. Torvinen, N. Färkkilä, H. Sintonen, T. Saarto, R. P. Roine, and K. Taari, “Health-related quality of life in prostate cancer,” *Acta Oncologica*, vol. 52, pp. 1094–1101, aug 2013.
- [21] F. Fang, N. L. Keating, L. A. Mucci, H.-O. Adami, M. J. Stampfer, U. Valdimarsdóttir, and K. Fall, “Immediate risk of suicide and cardiovascular death after a prostate cancer diagnosis: cohort study in the United States,” *Journal of the National Cancer Institute*, vol. 102, pp. 307–314, mar 2010.
- [22] M. Ahdoot, A. H. Lebastchi, B. Turkbey, B. Wood, and P. A. Pinto, “Contemporary treatments in prostate cancer focal therapy,” *Current opinion in oncology*, vol. 31, pp. 200–206, may 2019.
- [23] G. Bozzini, P. Colin, P. Nevoux, A. Villers, S. Mordon, and N. Betrouni, “Focal therapy of prostate cancer: energies and procedures,” *Urologic Oncology: Seminars and Original Investigations*, vol. 31, no. 2, pp. 155–167, 2013.
- [24] A. Oto, I. Sethi, G. Karczmar, R. J. McNichols, M. K. Ivancevic, W. M. Stadler, S. Watson, and S. E. Eggener, “MR imaging-guided focal laser ablation for prostate cancer: phase I trial,” *Radiology*, vol. 267, pp. 932–940, jun 2013.
- [25] F. Labrie, B. Candas, A. Dupont, L. Cusan, J. L. Gomez, R. E. Suburu, P. Diamond, J. Levesque, and A. Belanger, “Screening decreases prostate cancer death: first analysis

- of the 1988 Quebec prospective randomized controlled trial,” *Prostate*, vol. 38, pp. 83–91, feb 1999.
- [26] C. Parker, D. Muston, J. Melia, S. Moss, and D. Dearnaley, “A model of the natural history of screen-detected prostate cancer, and the effect of radical treatment on overall survival,” *British Journal of Cancer*, vol. 94, pp. 1361–8, may 2006.
- [27] R. A. Rendon, R. J. Mason, K. Marzouk, A. Finelli, F. Saad, A. So, P. Violette, and R. H. Breau, “Recommandations de l’Association des urologues du Canada sur le dépistage et le diagnostic précoce du cancer de la prostate,” *Canadian Urological Association journal = Journal de l’Association des urologues du Canada*, vol. 11, pp. 298–309, oct 2017.
- [28] L. D. Dunfield, D. Fitzpatrick-Lewis, A. Usman, and A. Shane, “Screening for prostate cancer with prostate specific antigen and treatment of early-stage or screen-detected prostate cancer,” 2015.
- [29] W. J. Catalona, D. S. Smith, T. L. Ratliff, K. M. Dodds, D. E. Coplen, J. J. J. Yuan, J. A. Petros, and G. L. Andriole, “Measurement of Prostate-Specific Antigen in Serum as a Screening Test for Prostate Cancer,” *New England Journal of Medicine*, vol. 324, pp. 1156–1161, apr 1991.
- [30] W. J. Catalona, D. S. Smith, T. L. Ratliff, and J. W. Basler, “Detection of Organ-Confined Prostate Cancer Is Increased Through Prostate-Specific Antigen—Based Screening,” *JAMA*, vol. 270, pp. 948–954, aug 1993.
- [31] D. S. Smith, W. J. Catalona, and J. D. Herschman, “Longitudinal Screening for Prostate Cancer With Prostate-Specific Antigen,” *JAMA*, vol. 276, pp. 1309–1315, oct 1996.
- [32] T. A. Stamey, N. Yang, A. R. Hay, J. E. McNeal, F. S. Freiha, and E. Redwine, “Prostate-specific antigen as a serum marker for adenocarcinoma of the prostate,” *The New England journal of medicine*, vol. 317, pp. 909–916, oct 1987.
- [33] A. R. Rao, H. G. Motiwala, and O. M. A. Karim, “The discovery of prostate-specific antigen,” *BJU international*, vol. 101, pp. 5–10, jan 2008.
- [34] J. I. Izawa, L. Klotz, D. R. Siemens, W. Kassouf, A. So, J. Jordan, M. Chetner, and A. E. Iansavichene, “Prostate cancer screening: Canadian guidelines 2011,” *Canadian Urological Association journal = Journal de l’Association des urologues du Canada*, vol. 5, pp. 235–240, aug 2011.
- [35] A. G. LeBlanc, A. Demers, and A. Shaw, “Recent trends in prostate cancer in Canada,” *Health reports*, vol. 30, pp. 12–17, apr 2019.
- [36] A. L. Potosky, B. A. Miller, P. C. Albertsen, and B. S. Kramer, “The Role of Increasing Detection in the Rising Incidence of Prostate Cancer,” *JAMA*, vol. 273, pp. 548–552, feb 1995.

- [37] R. Etzioni, D. F. Penson, J. M. Legler, D. di Tommaso, R. Boer, P. H. Gann, and E. J. Feuer, “Overdiagnosis Due to Prostate-Specific Antigen Screening: Lessons From U.S. Prostate Cancer Incidence Trends,” *JNCI: Journal of the National Cancer Institute*, vol. 94, pp. 981–990, jul 2002.
- [38] M. R. Cooperberg, G. D. Grossfeld, D. P. Lubeck, and P. R. Carroll, “National practice patterns and time trends in androgen ablation for localized prostate cancer,” *Journal of the National Cancer Institute*, vol. 95, pp. 981–989, jul 2003.
- [39] M. V. Meng, G. D. Grossfeld, N. Sadetsky, S. S. Mehta, D. P. Lubeck, and P. R. Carroll, “Contemporary patterns of androgen deprivation therapy use for newly diagnosed prostate cancer,” *Urology*, vol. 60, pp. 2–7, sep 2002.
- [40] P. A. Kupelian, J. C. Buchsbaum, M. A. Elshaikh, C. A. Reddy, and E. A. Klein, “Improvement in relapse-free survival throughout the PSA era in patients with localized prostate cancer treated with definitive radiotherapy: year of treatment an independent predictor of outcome,” *International journal of radiation oncology, biology, physics*, vol. 57, pp. 629–634, nov 2003.
- [41] J. B. Eifler, Z. Feng, B. M. Lin, M. T. Partin, E. B. Humphreys, M. Han, J. I. Epstein, P. C. Walsh, B. J. Trock, and A. W. Partin, “An updated prostate cancer staging nomogram (Partin tables) based on cases from 2006 to 2011,” *BJU international*, vol. 111, pp. 22–29, jan 2013.
- [42] A. Afriansyah, A. R. A. H. Hamid, C. A. Mochtar, and R. Umbas, “Prostate specific antigen (PSA) kinetic as a prognostic factor in metastatic prostate cancer receiving androgen deprivation therapy: systematic review and meta-analysis,” *F1000Research*, vol. 7, p. 246, 2018.
- [43] A. J. Vickers, C. Till, C. M. Tangen, H. Lilja, and I. M. Thompson, “An empirical evaluation of guidelines on prostate-specific antigen velocity in prostate cancer detection,” *Journal of the National Cancer Institute*, vol. 103, pp. 462–469, mar 2011.
- [44] R. L. Siegel, K. D. Miller, H. E. Fuchs, and A. Jemal, “Cancer Statistics, 2021,” *CA: A Cancer Journal for Clinicians*, vol. 71, pp. 7–33, jan 2021.
- [45] A. Hoogendam, F. Buntinx, and H. C. de Vet, “The diagnostic value of digital rectal examination in primary care screening for prostate cancer: a meta-analysis,” *Family practice*, vol. 16, pp. 621–626, dec 1999.
- [46] L. Naji, H. Randhawa, Z. Sohani, B. Dennis, D. Lautenbach, O. Kavanagh, M. Bawor, L. Banfield, and J. Profetto, “Digital Rectal Examination for Prostate Cancer Screening in Primary Care: A Systematic Review and Meta-Analysis,” *The Annals of Family Medicine*, vol. 16, pp. 149 LP – 154, mar 2018.
- [47] F. H. Schröder, P. van der Maas, P. Beemsterboer, A. B. Kruger, R. Hoedemaeker, J. Rietbergen, and R. Kranse, “Evaluation of the digital rectal examination as a screening test for prostate cancer. Rotterdam section of the European Randomized Study of Screening

- for Prostate Cancer.,” *Journal of the National Cancer Institute*, vol. 90, pp. 1817–1823, dec 1998.
- [48] D. F. Gleason, “Histologic grading of prostate cancer: A perspective,” *Human Pathology*, vol. 23, no. 3, pp. 273–279, 1992.
- [49] J. L. Wright, C. A. Salinas, D. W. Lin, S. Kolb, J. Koopmeiners, Z. Feng, and J. L. Stanford, “Prostate cancer specific mortality and Gleason 7 disease differences in prostate cancer outcomes between cases with Gleason 4 + 3 and Gleason 3 + 4 tumors in a population based cohort.,” *The Journal of urology*, vol. 182, pp. 2702–2707, dec 2009.
- [50] C. R. King, J. E. McNeal, H. Gill, and J. C. J. Presti, “Extended prostate biopsy scheme improves reliability of Gleason grading: implications for radiotherapy patients.,” *International journal of radiation oncology, biology, physics*, vol. 59, pp. 386–391, jun 2004.
- [51] J. Gordetsky and J. Epstein, “Grading of prostatic adenocarcinoma: current state and prognostic implications,” *Diagnostic Pathology*, vol. 11, no. 1, p. 25, 2016.
- [52] G. L. Andriole, “Pathology: the lottery of conventional prostate biopsy.,” apr 2009.
- [53] F. Schröder, L. Denis, M. Roobol, and ECRPC, “The story of the european randomized study of screening for prostate cancer,” *BJU international*, vol. 92, pp. 1–13, 2003.
- [54] D. W. Keetch, W. J. Catalona, and D. S. Smith, “Serial Prostatic Biopsies in Men with Persistently Elevated Serum Prostate Specific Antigen Values,” *The Journal of Urology*, vol. 151, no. 6, pp. 1571–1574, 1994.
- [55] E. Klaus, H. Susanne, W. Jennifer, M. Lindsey, B. L. M., and K. Jos, “Diagnostic Value of Systematic Biopsy Methods in the Investigation of Prostate Cancer: A Systematic Review,” *Journal of Urology*, vol. 175, pp. 1605–1612, may 2006.
- [56] C. M. Moore, N. L. Robertson, N. Arsanious, T. Middleton, A. Villers, L. Klotz, S. S. Taneja, and M. Emberton, “Image-Guided Prostate Biopsy Using Magnetic Resonance Imaging–Derived Targets: A Systematic Review,” *European Urology*, vol. 63, no. 1, pp. 125–140, 2013.
- [57] J. V. Hegde, R. V. Mulkern, L. P. Panych, F. M. Fennessy, A. Fedorov, S. E. Maier, and C. M. C. Tempany, “Multiparametric MRI of prostate cancer: an update on state-of-the-art techniques and their performance in detecting and localizing prostate cancer.,” *Journal of magnetic resonance imaging : JMRI*, vol. 37, pp. 1035–1054, may 2013.
- [58] J. Haffner, L. Lemaitre, P. Puech, G.-P. Haber, X. Leroy, J. S. Jones, and A. Villers, “Role of magnetic resonance imaging before initial biopsy: comparison of magnetic resonance imaging-targeted and systematic biopsy for significant prostate cancer detection,” *BJU International*, vol. 108, pp. E171–E178, oct 2011.
- [59] B. K. Park, J. W. Park, S. Y. Park, C. K. Kim, H. M. Lee, S. S. Jeon, S. I. Seo, B. C. Jeong, and H. Y. Choi, “Prospective evaluation of 3-T MRI performed before initial transrectal ultrasound-guided prostate biopsy in patients with high prostate-specific antigen and no

- previous biopsy.," *AJR. American journal of roentgenology*, vol. 197, pp. W876–81, nov 2011.
- [60] E. K. Outwater and J. L. Montilla-Soler, "Imaging of prostate carcinoma.," *Cancer control : journal of the Moffitt Cancer Center*, vol. 20, pp. 161–176, jul 2013.
- [61] S. W. T. P. J. Heijmink, H. van Moerkerk, L. A. L. M. Kiemeney, J. A. Witjes, F. Frauscher, and J. O. Barentsz, "A comparison of the diagnostic performance of systematic versus ultrasound-guided biopsies of prostate cancer.," *European radiology*, vol. 16, pp. 927–938, apr 2006.
- [62] S. L. Washington, M. Bonham, J. M. Whitson, J. E. Cowan, and P. R. Carroll, "Transrectal ultrasonography-guided biopsy does not reliably identify dominant cancer location in men with low-risk prostate cancer," *BJU International*, vol. 110, no. 1, pp. 50–55, 2012.
- [63] R. Clements, "Ultrasonography of prostate cancer," *European Radiology*, vol. 11, no. 11, pp. 2119–2125, 2001.
- [64] H. Hricak, P. L. Choyke, S. C. Eberhardt, S. A. Leibel, and P. T. Scardino, "Imaging prostate cancer: a multidisciplinary perspective.," *Radiology*, vol. 243, pp. 28–53, apr 2007.
- [65] K. Ashi, B. Kirkham, A. Chauhan, S. M. Schultz, B. J. Brake, and C. M. Sehgal, "Quantitative colour Doppler and greyscale ultrasound for evaluating prostate cancer.," *Ultrasound (Leeds, England)*, vol. 29, pp. 106–111, may 2021.
- [66] E. J. Trabulsi, D. Sackett, L. G. Gomella, and E. J. Halpern, "Enhanced transrectal ultrasound modalities in the diagnosis of prostate cancer," *Urology*, vol. 76, no. 5, pp. 1025–1033, 2010.
- [67] R. A. Linden and E. J. Halpern, "Advances in Transrectal Ultrasound Imaging of the Prostate," *Seminars in Ultrasound, CT and MRI*, vol. 28, no. 4, pp. 249–257, 2007.
- [68] R. Zahiri Azar, A. Baghani, S. E. Salcudean, and R. Rohling, "2-D high-frame-rate dynamic elastography using delay compensated and angularly compounded motion vectors: preliminary results.," *IEEE transactions on ultrasonics, ferroelectrics, and frequency control*, vol. 57, pp. 2421–2436, nov 2010.
- [69] S. S. Mahdavi, M. Moradi, X. Wen, W. J. Morris, and S. E. Salcudean, "Evaluation of visualization of the prostate gland in vibro-elastography images," *Medical image analysis*, vol. 15, no. 4, pp. 589–600, 2011.
- [70] G. Salomon, J. Köllerman, I. Thederan, F. K. H. Chun, L. Budäus, T. Schlomm, H. Isbarn, H. Heinzer, H. Huland, and M. Graefen, "Evaluation of prostate cancer detection with ultrasound real-time elastography: a comparison with step section pathological analysis after radical prostatectomy.," *European urology*, vol. 54, pp. 1354–1362, dec 2008.

- [71] F. Aigner, L. Pallwein, D. Junker, G. Schäfer, G. Mikuz, F. Pedross, M. J. Mitterberger, W. Jaschke, E. J. Halpern, and F. Frauscher, "Value of real-time elastography targeted biopsy for prostate cancer detection in men with prostate specific antigen 1.25 ng/ml or greater and 4.00 ng/ml or less.," *The Journal of urology*, vol. 184, pp. 913–917, sep 2010.
- [72] T. Adebar, S. Salcudean, S. Mahdavi, M. Moradi, C. Ngan, and L. Goldenberg, "A Robotic System for Intra-operative Trans-Rectal Ultrasound and Ultrasound Elastography in Radical Prostatectomy BT - Information Processing in Computer-Assisted Interventions," (Berlin, Heidelberg), pp. 79–89, Springer Berlin Heidelberg, 2011.
- [73] P. Kozlowski, S. D. Chang, R. Meng, B. Mädler, R. Bell, E. C. Jones, and S. L. Goldenberg, "Combined prostate diffusion tensor imaging and dynamic contrast enhanced MRI at 3T—quantitative correlation with biopsy.," *Magnetic Resonance Imaging*, vol. 28, pp. 621–8, jun 2010.
- [74] G. Murphy, M. Haider, S. Ghai, and B. Sreeharsha, "The expanding role of MRI in prostate cancer," *American Journal of Roentgenology*, vol. 201, no. 6, pp. 1229–1238, 2013.
- [75] C. M. A. Hoeks, J. J. O. Barentsz, T. Hambrock, D. Yakar, D. M. Somford, S. W. T. P. J. Heijmink, T. W. J. Scheenen, P. C. Vos, H. Huisman, I. M. van Oort, J. A. Witjes, A. Heerschap, and J. J. Fütterer, "Prostate cancer: multiparametric MR imaging for detection, localization, and staging," *Radiology*, vol. 261, no. 1, pp. 46–66, 2011.
- [76] Ö. Algan, G. E. Hanks, and A. H. Shaer, "Localization of the prostatic apex for radiation treatment planning," *International Journal of Radiation Oncology, Biology, Physics*, vol. 33, no. 4, pp. 925–930, 1995.
- [77] E. Gibson, C. Crukley, M. Gaed, J. A. Gómez, M. Moussa, J. L. Chin, G. S. Bauman, A. Fenster, and A. D. Ward, "Registration of prostate histology images to ex vivo MR images via strand-shaped fiducials.," *Journal of magnetic resonance imaging : JMRI*, vol. 36, pp. 1402–1412, dec 2012.
- [78] A. D. Ward, C. Crukley, C. McKenzie, J. Montreuil, E. Gibson, J. A. Gomez, M. Moussa, G. Bauman, and A. Fenster, "Registration of In Vivo Prostate Magnetic Resonance Images to Digital Histopathology Images BT - Prostate Cancer Imaging. Computer-Aided Diagnosis, Prognosis, and Intervention," (Berlin, Heidelberg), pp. 66–76, Springer Berlin Heidelberg, 2010.
- [79] A. D. Ward, C. Crukley, C. A. McKenzie, J. Montreuil, E. Gibson, C. Romagnoli, J. A. Gomez, M. Moussa, J. Chin, G. Bauman, and A. Fenster, "Prostate: registration of digital histopathologic images to in vivo MR images acquired by using endorectal receive coil.," *Radiology*, vol. 263, pp. 856–864, jun 2012.
- [80] A. P. S. Kirkham, M. Emberton, and C. Allen, "How good is MRI at detecting and characterising cancer within the prostate?," *European urology*, vol. 50, pp. 1163–74; discussion 1175, dec 2006.

- [81] Y. Mazaheri, A. Shukla-Dave, A. Muellner, and H. Hricak, "MR imaging of the prostate in clinical practice.," *Magma (New York, N.Y.)*, vol. 21, pp. 379–392, nov 2008.
- [82] L. Wang, Y. Mazaheri, J. Zhang, N. M. Ishill, K. Kuroiwa, and H. Hricak, "Assessment of biologic aggressiveness of prostate cancer: correlation of MR signal intensity with Gleason grade after radical prostatectomy.," *Radiology*, vol. 246, pp. 168–176, jan 2008.
- [83] S. Verma, B. Turkbey, N. Muradyan, A. Rajesh, F. Cornud, M. A. Haider, P. L. Choyke, and M. Harisinghani, "Overview of dynamic contrast-enhanced MRI in prostate cancer diagnosis and management.," *AJR. American journal of roentgenology*, vol. 198, pp. 1277–1288, jun 2012.
- [84] H.-P. Schlemmer, J. Merkle, R. Grobholz, T. Jaeger, M. S. Michel, A. Werner, J. Rabe, and G. van Kaick, "Can pre-operative contrast-enhanced dynamic MR imaging for prostate cancer predict microvessel density in prostatectomy specimens?," *European radiology*, vol. 14, pp. 309–317, feb 2004.
- [85] M. A. Haider, T. H. van der Kwast, J. Tanguay, A. J. Evans, A.-T. Hashmi, G. Lockwood, and J. Trachtenberg, "Combined T2-weighted and diffusion-weighted MRI for localization of prostate cancer.," *AJR. American journal of roentgenology*, vol. 189, pp. 323–328, aug 2007.
- [86] C. Testa, R. Schiavina, R. Lodi, E. Salizzoni, B. Corti, M. Farsad, J. Kurhanewicz, F. Manferrari, E. Brunocilla, C. Tonon, N. Monetti, P. Castellucci, S. Fanti, M. Coe, W. F. Grigioni, G. Martorana, R. Canini, and B. Barbiroli, "Prostate cancer: sextant localization with MR imaging, MR spectroscopy, and 11C-choline PET/CT.," *Radiology*, vol. 244, pp. 797–806, sep 2007.
- [87] C. D. Petraki and C. P. Sfikas, "Histopathological changes induced by therapies in the benign prostate and prostate adenocarcinoma.," *Histology and histopathology*, vol. 22, pp. 107–118, jan 2007.
- [88] E. B. Cornel, G. A. Smits, G. O. Oosterhof, H. F. Karthaus, F. M. Deburyne, J. A. Schalken, and A. Heerschap, "Characterization of human prostate cancer, benign prostatic hyperplasia and normal prostate by in vitro 1H and 31P magnetic resonance spectroscopy.," *The Journal of urology*, vol. 150, pp. 2019–2024, dec 1993.
- [89] T. W. J. Scheenen, D. W. J. Klomp, S. A. Röhl, J. J. Fütterer, J. O. Barentsz, and A. Heerschap, "Fast acquisition-weighted three-dimensional proton MR spectroscopic imaging of the human prostate.," *Magnetic resonance in medicine*, vol. 52, pp. 80–88, jul 2004.
- [90] Y. Mazaheri, A. Shukla-Dave, D. A. Goldman, C. S. Moskowitz, T. Takeda, V. E. Reuter, O. Akin, and H. Hricak, "Characterization of prostate cancer with MR spectroscopic imaging and diffusion-weighted imaging at 3 Tesla," *Magnetic Resonance Imaging*, vol. 55, pp. 93–102, 2019.
- [91] A. Stamatelatos, T. W. J. Scheenen, and A. Heerschap, "Developments in proton MR spectroscopic imaging of prostate cancer," *Magnetic Resonance Materials in Physics, Biology and Medicine*, vol. 35, no. 4, pp. 645–665, 2022.

- [92] J. Near and R. Bartha, "Quantitative sodium MRI of the mouse prostate," *Magnetic Resonance in Medicine*, vol. 63, pp. 822–827, mar 2010.
- [93] T. Barrett, F. Riemer, M. A. McLean, J. D. Kaggie, F. Robb, A. Y. Warren, M. J. Graves, and F. A. Gallagher, "Molecular imaging of the prostate: Comparing total sodium concentration quantification in prostate cancer and normal tissue using dedicated ^{13}C and ^{23}Na endorectal coils," *Journal of Magnetic Resonance Imaging*, vol. 51, pp. 90–97, jan 2020.
- [94] T. Barrett, F. Riemer, M. A. McLean, J. Kaggie, F. Robb, J. S. Tropp, A. Warren, O. Bratt, N. Shah, V. J. Gnanapragasam, F. J. Gilbert, M. J. Graves, and F. A. Gallagher, "Quantification of Total and Intracellular Sodium Concentration in Primary Prostate Cancer and Adjacent Normal Prostate Tissue With Magnetic Resonance Imaging," *Investigative Radiology*, vol. 53, no. 8, 2018.
- [95] N. C. Broeke, J. Peterson, J. Lee, P. R. Martin, A. Farag, J. A. Gomez, M. Moussa, M. Gaed, J. Chin, S. E. Pautler, A. Ward, G. Bauman, R. Bartha, and T. J. Scholl, "Characterization of clinical human prostate cancer lesions using 3.0-T sodium MRI registered to Gleason-graded whole-mount histopathology," *Journal of Magnetic Resonance Imaging*, vol. 49, pp. 1409–1419, may 2019.
- [96] L. Dickinson, H. U. Ahmed, C. Allen, J. O. Barentsz, B. Carey, J. J. Futterer, S. W. Heijmink, P. J. Hoskin, A. Kirkham, A. R. Padhani, R. Persad, P. Puech, S. Punwani, A. S. Sohaib, B. Tombal, A. Villers, J. van der Meulen, and M. Emberton, "Magnetic Resonance Imaging for the Detection, Localisation, and Characterisation of Prostate Cancer: Recommendations from a European Consensus Meeting," *European Urology*, vol. 59, no. 4, pp. 477–494, 2011.
- [97] J. O. Barentsz, J. C. Weinreb, S. Verma, H. C. Thoeny, C. M. Tempany, F. Shtern, A. R. Padhani, D. Margolis, K. J. Macura, M. A. Haider, F. Cornud, and P. L. Choyke, "Synopsis of the PI-RADS v2 Guidelines for Multiparametric Prostate Magnetic Resonance Imaging and Recommendations for Use.," jan 2016.
- [98] A. R. Padhani, J. Weinreb, A. B. Rosenkrantz, G. Villeirs, B. Turkbey, and J. Barentsz, "Prostate Imaging-Reporting and Data System Steering Committee: PI-RADS v2 Status Update and Future Directions," *European Urology*, vol. 75, no. 3, pp. 385–396, 2019.
- [99] S. Rais-Bahrami, M. M. Siddiqui, B. Turkbey, L. Stamatakis, J. Logan, A. N. Hoang, A. Walton-Diaz, S. Vourganti, H. Truong, J. Kruecker, M. J. Merino, B. J. Wood, P. L. Choyke, and P. A. Pinto, "Utility of multiparametric magnetic resonance imaging suspicion levels for detecting prostate cancer," *Journal of Urology*, vol. 190, no. 5, pp. 1721–1727, 2013.
- [100] D. L. Langer, T. H. van der Kwast, A. J. Evans, J. Trachtenberg, B. C. Wilson, and M. A. Haider, "Prostate cancer detection with multi-parametric MRI: Logistic regression analysis of quantitative T2, diffusion-weighted imaging, and dynamic contrast-enhanced MRI," *Journal of Magnetic Resonance Imaging*, vol. 30, pp. 327–334, aug 2009.

- [101] B. Turkbey, H. Mani, V. Shah, A. R. Rastinehad, M. Bernardo, T. Pohida, Y. Pang, D. Daar, C. Benjamin, Y. L. McKinney, H. Trivedi, C. Chua, G. Bratslavsky, J. H. Shih, W. M. Linehan, M. J. Merino, P. L. Choyke, and P. A. Pinto, “Multiparametric 3T prostate magnetic resonance imaging to detect cancer: histopathological correlation using prostatectomy specimens processed in customized magnetic resonance imaging based molds,” *The Journal of urology*, vol. 186, pp. 1818–1824, nov 2011.
- [102] N. B. Delongchamps, M. Rouanne, T. Flam, F. Beuvon, M. Liberatore, M. Zerbib, and F. Cornud, “Multiparametric magnetic resonance imaging for the detection and localization of prostate cancer: combination of T2-weighted, dynamic contrast-enhanced and diffusion-weighted imaging,” *BJU International*, vol. 107, pp. 1411–1418, may 2011.
- [103] M. G. Sanda, R. L. Dunn, J. Michalski, H. M. Sandler, L. Northouse, L. Hembroff, X. Lin, T. K. Greenfield, M. S. Litwin, C. S. Saigal, A. Mahadevan, E. Klein, A. Kibel, L. L. Pisters, D. Kuban, I. Kaplan, D. Wood, J. Ciezki, N. Shah, and J. T. Wei, “Quality of life and satisfaction with outcome among prostate-cancer survivors,” *The New England journal of medicine*, vol. 358, pp. 1250–1261, mar 2008.
- [104] A. U. Frey, J. Sønksen, and M. Fode, “Neglected side effects after radical prostatectomy: A systematic review,” *The Journal of Sexual Medicine*, vol. 11, no. 2, pp. 374–385, 2014.
- [105] J. Hugosson, J. Stranne, and S. V. Carlsson, “Radical retropubic prostatectomy: A review of outcomes and side-effects,” *Acta Oncologica*, vol. 50, no. SUPPL. 1, pp. 92–97, 2011.
- [106] N. N. Stone and R. G. Stock, “Complications following permanent prostate brachytherapy,” *European Urology*, vol. 41, no. 4, pp. 427–433, 2002.
- [107] J. F. Anderson, D. A. Swanson, L. B. Levy, D. A. Kuban, A. K. Lee, R. Kudchadker, J. Phan, T. Bruno, and S. J. Frank, “Urinary Side Effects and Complications After Permanent Prostate Brachytherapy: The MD Anderson Cancer Center Experience,” *Urology*, vol. 74, no. 3, pp. 601–605, 2009.
- [108] J. L. Donovan, F. C. Hamdy, J. A. Lane, M. Mason, C. Metcalfe, E. Walsh, J. M. Blazeby, T. J. Peters, P. Holding, S. Bonnington, T. Lennon, L. Bradshaw, D. Cooper, P. Herbert, J. Howson, A. Jones, N. Lyons, E. Salter, P. Thompson, S. Tidball, J. Blaikie, C. Gray, P. Bollina, J. Catto, A. Doble, A. Doherty, D. Gillatt, R. Kockelbergh, H. Kynaston, A. Paul, P. Powell, S. Prescott, D. J. Rosario, E. Rowe, M. Davis, E. L. Turner, R. M. Martin, D. E. Neal, and P. S. Group*, “Patient-Reported Outcomes after Monitoring, Surgery, or Radiotherapy for Prostate Cancer,” *The New England journal of medicine*, vol. 375, pp. 1425–1437, oct 2016.
- [109] S. Odeo and A. Degu, “Factors affecting health-related quality of life among prostate cancer patients: A systematic review,” *Journal of Oncology Pharmacy Practice*, vol. 26, pp. 1997–2010, sep 2020.
- [110] A. Sureda, L. Fumadó, M. Ferrer, O. Garín, X. Bonet, M. Castells, M. C. Mir, J. M. Abascal, F. Vigués, L. Cecchini, and J. F. Suárez, “Health-related quality of life in

men with prostate cancer undergoing active surveillance versus radical prostatectomy, external-beam radiotherapy, prostate brachytherapy and reference population: a cross-sectional study,” *Health and Quality of Life Outcomes*, vol. 17, no. 1, p. 11, 2019.

- [111] J. T. Wei, R. L. Dunn, H. M. Sandler, P. W. McLaughlin, J. E. Montie, M. S. Litwin, L. Nyquist, and M. G. Sanda, “Comprehensive comparison of health-related quality of life after contemporary therapies for localized prostate cancer,” *Journal of clinical oncology : official journal of the American Society of Clinical Oncology*, vol. 20, pp. 557–566, jan 2002.
- [112] W. R. Parker, R. Wang, C. He, and D. P. Wood, “Five year expanded prostate cancer index composite-based quality of life outcomes after prostatectomy for localized prostate cancer,” *BJU International*, vol. 107, no. 4, pp. 585–590, 2011.
- [113] A. L. Potosky, J. Legler, P. C. Albertsen, J. L. Stanford, F. D. Gilliland, A. S. Hamilton, J. W. Eley, R. A. Stephenson, and L. C. Harlan, “Health outcomes after prostatectomy or radiotherapy for prostate cancer: results from the Prostate Cancer Outcomes Study,” *Journal of the National Cancer Institute*, vol. 92, pp. 1582–1592, oct 2000.
- [114] J. C. Hu, X. Gu, S. R. Lipsitz, M. J. Barry, A. V. D’Amico, A. C. Weinberg, and N. L. Keating, “Comparative effectiveness of minimally invasive vs open radical prostatectomy,” *Journal of the American Medical Association*, vol. 302, p. 1557, oct 2009.
- [115] D. W. Shin, S. H. Lee, T.-H. Kim, S. J. Yun, J. K. Nam, S. H. Jeon, S. C. Park, S. I. Jung, J.-H. Park, and J. Park, “Health-Related Quality of Life Changes in Prostate Cancer Patients after Radical Prostatectomy: A Longitudinal Cohort Study,” *Cancer research and treatment*, vol. 51, pp. 556–567, apr 2019.
- [116] N. Sadetsky, K. Greene, M. R. Cooperberg, A. Hubbard, P. R. Carroll, and W. Satariano, “Impact of androgen deprivation on physical well-being in patients with prostate cancer,” 2011.
- [117] S. Bergius, R. P. Roine, K. Taari, and H. Sintonen, “Health-Related Quality of Life and Survival in Prostate Cancer Patients in a Real-World Setting,” *Urologia Internationalis*, vol. 104, no. 11-12, pp. 939–947, 2020.
- [118] M. Djulbegovic, R. J. Beyth, M. M. Neuberger, T. L. Stoffs, J. Vieweg, B. Djulbegovic, and P. Dahm, “Screening for prostate cancer: systematic review and meta-analysis of randomised controlled trials,” *BMJ*, vol. 341, p. c4543, sep 2010.
- [119] L. Klotz, L. Zhang, A. Lam, R. Nam, A. Mamedov, and A. Loblaw, “Clinical results of long-term follow-up of a large, active surveillance cohort with localized prostate cancer,” *Journal of Clinical Oncology : Official Journal of the American Society of Clinical Oncology*, vol. 28, pp. 126–31, jan 2010.
- [120] M. R. Cooperberg and P. R. Carroll, “Trends in Management for Patients With Localized Prostate Cancer, 1990-2013,” *JAMA*, vol. 314, pp. 80–82, jul 2015.

- [121] P. R. Womble, J. E. Montie, Z. Ye, S. M. Linsell, B. R. Lane, and D. C. Miller, “Contemporary use of initial active surveillance among men in Michigan with low-risk prostate cancer,” *European urology*, vol. 67, pp. 44–50, jan 2015.
- [122] T. J. Wilt and M. K. Brawer, “The Prostate Cancer Intervention Versus Observation Trial: a randomized trial comparing radical prostatectomy versus expectant management for the treatment of clinically localized prostate cancer,” *The Journal of urology*, vol. 152, pp. 1910–1914, nov 1994.
- [123] T. J. Wilt, M. K. Brawer, K. M. Jones, M. J. Barry, W. J. Aronson, S. Fox, J. R. Gingrich, J. T. Wei, P. Gilhooly, B. M. Grob, I. Nsouli, P. Iyer, R. Cartagena, G. Snider, C. Roehrborn, R. Sharifi, W. Blank, P. Pandya, G. L. Andriole, D. Culkin, and T. Wheeler, “Radical prostatectomy versus observation for localized prostate cancer,” *The New England journal of medicine*, vol. 367, pp. 203–213, jul 2012.
- [124] A. Bill-Axelson, L. Holmberg, M. Ruutu, M. Häggman, S.-O. Andersson, S. Bratell, A. Spångberg, C. Busch, S. Nordling, H. Garmo, J. Palmgren, H.-O. Adami, B. J. Norlén, and J.-E. Johansson, “Radical prostatectomy versus watchful waiting in early prostate cancer,” *The New England journal of medicine*, vol. 352, pp. 1977–1984, may 2005.
- [125] B. J. Davison and S. L. Goldenberg, “Patient acceptance of active surveillance as a treatment option for low-risk prostate cancer,” *BJU international*, vol. 108, pp. 1787–1793, dec 2011.
- [126] R. Choo, L. Klotz, C. Danjoux, G. C. Morton, G. DeBoer, E. Szumacher, N. Fleshner, P. Bunting, and G. Hruby, “Feasibility study: watchful waiting for localized low to intermediate grade prostate carcinoma with selective delayed intervention based on prostate specific antigen, histological and/or clinical progression,” *The Journal of urology*, vol. 167, pp. 1664–1669, apr 2002.
- [127] M. Perera, N. Krishnananthan, U. Lindner, and N. Lawrentschuk, “An update on focal therapy for prostate cancer,” *Nature Reviews Urology*, vol. 13, no. 11, pp. 641–653, 2016.
- [128] M. Valerio, H. U. Ahmed, M. Emberton, N. Lawrentschuk, M. Lazzeri, R. Montironi, P. L. Nguyen, J. Trachtenberg, and T. J. Polascik, “The Role of Focal Therapy in the Management of Localised Prostate Cancer: A Systematic Review,” *European Urology*, vol. 66, no. 4, pp. 732–751, 2014.
- [129] A. H. Hou, K. F. Sullivan, and E. D. Crawford, “Targeted focal therapy for prostate cancer: a review,” *Current Opinion in Urology*, vol. 19, no. 3, 2009.
- [130] C. T. Iberti, N. Mohamed, and M. A. Palese, “A review of focal therapy techniques in prostate cancer: clinical results for high-intensity focused ultrasound and focal cryoablation,” *Reviews in urology*, vol. 13, no. 4, pp. 196–202, 2011.

- [131] S. Marshall and S. Taneja, "Focal therapy for prostate cancer: The current status," *Prostate International*, 2015.
- [132] H. U. Ahmed, "The index lesion and the origin of prostate cancer," *New England Journal of Medicine*, vol. 361, no. 17, pp. 1704–1706, 2009.
- [133] M. R. Abern, M. Tsivian, and T. J. Polascik, "Focal therapy of prostate cancer: evidence-based analysis for modern selection criteria," *Current urology reports*, vol. 13, no. 2, pp. 160–169, 2012.
- [134] S. Eggener, G. Salomon, P. T. Scardino, J. De la Rosette, T. J. Polascik, and S. Brewster, "Focal Therapy for Prostate Cancer: Possibilities and Limitations," *European Urology*, vol. 58, pp. 57–64, jul 2010.
- [135] S. A. van Nimwegen, H. F. L'Eplattenier, A. I. Rem, J. J. van der Lugt, and J. Kirpensteijn, "Nd:YAG surgical laser effects in canine prostate tissue: temperature and damage distribution.," *Physics in medicine and biology*, vol. 54, pp. 29–44, jan 2009.
- [136] U. Lindner, N. Lawrentschuk, and J. Trachtenberg, "Focal laser ablation for localized prostate cancer.," *Journal of endourology*, vol. 24, pp. 791–797, may 2010.
- [137] O. Raz, M. A. Haider, S. R. H. Davidson, U. Lindner, E. Hlasny, R. A. Weersink, M. R. Gertner, W. Kucharczyk, S. A. McCluskey, and J. Trachtenberg, "Real-time magnetic resonance imaging-guided focal laser therapy in patients with low-risk prostate cancer," *European Urology*, vol. 58, no. 1, pp. 173–177, 2010.
- [138] S. E. Eggener, A. Yousuf, S. Watson, S. Wang, and A. Oto, "Phase II evaluation of magnetic resonance imaging guided focal laser ablation of prostate cancer," *Journal of Urology*, vol. 196, no. 6, pp. 1670–1675, 2016.
- [139] J. Le Nobin, A. B. Rosenkrantz, A. Villers, C. Orczyk, F. M. Deng, J. Melamed, A. Mikheev, H. Rusinek, and S. S. Taneja, "Image Guided Focal Therapy for Magnetic Resonance Imaging Visible Prostate Cancer: Defining a 3-Dimensional Treatment Margin Based on Magnetic Resonance Imaging Histology Co-Registration Analysis," *Journal of Urology*, vol. 194, no. 2, pp. 364–370, 2015.
- [140] E. Gibson, G. S. Bauman, C. Romagnoli, D. W. Cool, M. Bastian-Jordan, Z. Kassam, M. Gaed, M. Moussa, J. A. Gómez, S. E. Pautler, J. L. Chin, C. Crukley, M. A. Haider, A. Fenster, and A. D. Ward, "Toward prostate cancer contouring guidelines on magnetic resonance imaging: dominant lesion gross and clinical target volume coverage via accurate histology fusion," *International Journal of Radiation Oncology, Biology, Physics*, vol. 96, no. 1, pp. 188–196, 2016.
- [141] A. Priester, S. Natarajan, P. Khoshnoodi, D. J. Margolis, S. S. Raman, R. E. Reiter, J. Huang, W. Grundfest, and L. S. Marks, "Magnetic resonance imaging underestimation of prostate cancer geometry: use of patient specific molds to correlate images with whole mount pathology," *Journal of Urology*, vol. 197, no. 2, pp. 320–326, 2017.

- [142] American College of Radiology, “PI-RADS™ Prostate Imaging – Reporting and Data System, Version 2.1,” tech. rep., American College of Radiology, 2015.
- [143] G. Sommer, D. Bouley, H. Gill, B. Daniel, K. B. Pauly, and C. Diederich, “Focal ablation of prostate cancer: four roles for magnetic resonance imaging guidance,” *The Canadian journal of urology*, vol. 20, pp. 6672–6681, apr 2013.
- [144] E. Walser, A. Nance, L. Ynalvez, S. Yong, J. S. Aoughsten, E. J. Eyzaguirre, and S. B. Williams, “Focal Laser Ablation of Prostate Cancer: Results in 120 Patients with Low-to Intermediate-Risk Disease,” *Journal of vascular and interventional radiology : JVIR*, vol. 30, pp. 401–409.e2, mar 2019.
- [145] T. A. Stamey, F. S. Freiha, J. E. McNeal, E. A. Redwine, A. S. Whittemore, and H. P. Schmid, “Localized prostate cancer. Relationship of tumor volume to clinical significance for treatment of prostate cancer,” *Cancer*, vol. 71, pp. 933–938, feb 1993.
- [146] U. Lindner, R. A. Weersink, M. A. Haider, M. R. Gertner, S. R. H. Davidson, M. Atri, B. Wilson, A. Fenster, and J. Trachtenberg, “Image guided photothermal focal therapy for localized prostate cancer: phase I trial,” *The Journal of Urology*, vol. 182, no. 4, pp. 1371–1377, 2009.
- [147] H. O. Beisland and E. Stranden, “Rectal temperature monitoring during neodymium-YAG laser irradiation for prostatic carcinoma,” *Urological research*, vol. 12, no. 5, pp. 257–259, 1984.
- [148] Z. Amin, W. R. Lees, and S. G. Bown, “Interstitial laser photocoagulation for the treatment of prostatic cancer,” *The British Journal of Radiology*, vol. 66, no. 791, pp. 1044–7, 1993.
- [149] M. Atri, M. R. Gertner, M. A. Haider, R. A. Weersink, and J. Trachtenberg, “Contrast-enhanced ultrasonography for real-time monitoring of interstitial laser thermal therapy in the focal treatment of prostate cancer,” *Canadian Urological Association Journal*, vol. 3, no. 2, pp. 125–130, 2009.
- [150] D. A. Woodrum, K. R. Gorny, L. A. Mynderse, K. K. Amrami, J. P. Felmlee, H. Bjarnason, O. I. Garcia-Medina, R. J. McNichols, T. D. Atwell, and M. R. Callstrom, “Feasibility of 3.0T Magnetic Resonance Imaging-guided Laser Ablation of a Cadaveric Prostate,” *Urology*, vol. 75, no. 6, pp. 1514.e1–1514.e6, 2010.
- [151] R. J. McNichols, A. Gowda, M. Kangasniemi, J. A. Bankson, R. E. Price, and J. D. Hazle, “MR thermometry-based feedback control of laser interstitial thermal therapy at 980 nm,” *Lasers in surgery and medicine*, vol. 34, no. 1, pp. 48–55, 2004.
- [152] R. J. Stafford, A. Shetty, A. M. Elliott, S. A. Klumpp, R. J. McNichols, A. Gowda, J. D. Hazle, and J. F. Ward, “Magnetic resonance guided, focal laser induced interstitial thermal therapy in a canine prostate model,” *The Journal of Urology*, vol. 184, pp. 1514–20, oct 2010.

- [153] J. Yuan, C.-S. Mei, L. P. Panych, N. J. McDannold, and B. Madore, “Towards fast and accurate temperature mapping with proton resonance frequency-based MR thermometry,” *Quantitative imaging in medicine and surgery*, vol. 2, no. 1, pp. 21–32, 2012.
- [154] U. Lindner, N. Lawrentschuk, R. A. Weersink, S. R. H. Davidson, O. Raz, E. Hlasny, D. L. Langer, M. R. Gertner, T. Van der Kwast, M. A. Haider, and J. Trachtenberg, “Focal laser ablation for prostate cancer followed by radical prostatectomy: validation of focal therapy and imaging accuracy,” *European Urology*, vol. 57, no. 6, pp. 1111–1114, 2010.
- [155] A. Boyes, K. Tang, M. Yaffe, L. Sugar, R. Chopra, and M. Bronskill, “Prostate tissue analysis immediately following magnetic resonance imaging guided transurethral ultrasound thermal therapy,” *The Journal of urology*, vol. 178, pp. 1080–1085, sep 2007.
- [156] H.-L. M. Cheng, M. A. Haider, M. J. Dill-Macky, J. M. Sweet, J. Trachtenberg, and M. R. Gertner, “MRI and contrast-enhanced ultrasound monitoring of prostate microwave focal thermal therapy: an in vivo canine study,” *Journal of magnetic resonance imaging : JMRI*, vol. 28, pp. 136–143, jul 2008.
- [157] T. Lee, N. Mendhiratta, D. Sperling, and H. Lepor, “Focal laser ablation for localized prostate cancer: principles, clinical trials, and our initial experience,” *Reviews in urology*, vol. 16, no. 2, pp. 55–66, 2014.
- [158] J. G. Bomers, E. B. Cornel, J. J. Fütterer, S. F. Jenniskens, H. E. Schaafsma, J. O. Barentsz, J. P. Sedelaar, C. A. Hulsbergen-van de Kaa, and J. A. Witjes, “MRI-guided focal laser ablation for prostate cancer followed by radical prostatectomy: correlation of treatment effects with imaging,” *World Journal of Urology*, vol. 35, no. 5, pp. 703–711, 2017.
- [159] S. Natarajan, S. Raman, A. M. Priester, J. Garritano, D. J. Margolis, P. Lieu, M. L. Macairan, J. Huang, W. Grundfest, and L. S. Marks, “Focal Laser Ablation of Prostate Cancer: Phase I Clinical Trial,” *Journal of Urology*, vol. 196, no. 1, pp. 68–75, 2016.
- [160] O. Rouvière, R. Souchon, R. Salomir, A. Gelet, J.-Y. Chapelon, and D. Lyonnet, “Transrectal high-intensity focused ultrasound ablation of prostate cancer: Effective treatment requiring accurate imaging,” *European Journal of Radiology*, vol. 63, pp. 317–327, sep 2007.
- [161] P. Colin, S. Mordon, P. Nevoux, M. F. Marqa, A. Ouzzane, P. Puech, G. Bozzini, B. Leroux, A. Villers, and N. Betrouni, “Focal Laser Ablation of Prostate Cancer: Definition, Needs, and Future,” *Advances in Urology*, vol. 2012, p. 589160, 2012.
- [162] N. V. Tsekos, A. Khanicheh, E. Christoforou, and C. Mavroidis, “Magnetic Resonance-Compatible Robotic and Mechatronics Systems for Image-Guided Interventions and Rehabilitation: A Review Study,” *Annual Review of Biomedical Engineering*, vol. 9, pp. 351–387, jul 2007.

- [163] J. A. Nyenhuis, S.-M. Park, R. Kamondetdacha, A. Amjad, F. G. Shellock, and A. R. Rezai, "MRI and implanted medical devices: basic interactions with an emphasis on heating," *IEEE Transactions on Device and Materials Reliability*, vol. 5, pp. 467–480, 2005.
- [164] R. Gassert, E. Burdet, and K. Chinzei, "Opportunities and Challenges in MR-Compatible Robotics," *IEEE Engineering in Medicine and Biology Magazine*, vol. 27, no. 3, pp. 15–22, 2008.
- [165] K. El Bannan, W. Handler, B. Chronik, and S. P. Salisbury, "Heating of metallic rods induced by time-varying gradient fields in MRI.," *Journal of magnetic resonance imaging : JMRI*, vol. 38, pp. 411–416, aug 2013.
- [166] K. Chinzei, R. Kikinis, and F. A. Jolesz, "MR Compatibility of Mechatronic Devices: Design Criteria BT - Medical Image Computing and Computer-Assisted Intervention – MICCAI'99," (Berlin, Heidelberg), pp. 1020–1030, Springer Berlin Heidelberg, 1999.
- [167] J. F. Schenck, "The role of magnetic susceptibility in magnetic resonance imaging: MRI magnetic compatibility of the first and second kinds," *Medical Physics*, vol. 23, no. 6, pp. 815–850, 1996.
- [168] J. Xiang, H. Yan, J. Li, X. Wang, H. Chen, and X. Zheng, "Transperineal versus transrectal prostate biopsy in the diagnosis of prostate cancer: a systematic review and meta-analysis," *World Journal of Surgical Oncology*, vol. 17, no. 1, p. 31, 2019.
- [169] J. P. Grummet, M. Weerakoon, S. Huang, N. Lawrentschuk, M. Frydenberg, D. A. Moon, M. O'Reilly, and D. Murphy, "Sepsis and 'superbugs': should we favour the transperineal over the transrectal approach for prostate biopsy?," *BJU international*, vol. 114, pp. 384–388, sep 2014.
- [170] A. V. D'Amico, R. Cormack, C. M. Tempany, S. Kumar, G. Topulos, H. M. Kooy, and C. N. Coleman, "Real-time magnetic resonance image-guided interstitial brachytherapy in the treatment of select patients with clinically localized prostate cancer.," *International Journal of Radiation Oncology, Biology, Physics*, vol. 42, no. 3, pp. 507–515, 1998.
- [171] A. V. D'Amico, C. M. Tempany, R. Cormack, N. Hata, M. Jinzaki, K. Tuncali, M. Weinstein, J. P. Richie, and P. Richie, "Transperineal magnetic resonance image guided prostate biopsy.," *The Journal of Urology*, vol. 164, no. 2, pp. 385–387, 2000.
- [172] N. Hata, M. Jinzaki, D. Kacher, R. Cormack, D. Gering, A. Nabavi, S. G. Silverman, a. V. D'Amico, R. Kikinis, F. a. Jolesz, and C. M. Tempany, "MR imaging-guided prostate biopsy with surgical navigation software: device validation and feasibility.," *Radiology*, vol. 220, no. 1, pp. 263–8, 2001.
- [173] C. Ménard, R. C. Susil, P. Choyke, G. S. Gustafson, W. Kammerer, H. Ning, R. W. Miller, K. L. Ullman, N. Sears Crouse, S. Smith, E. Lessard, J. Pouliot, V. Wright, E. McVeigh, C. N. Coleman, and K. Camphausen, "MRI-guided HDR prostate

- brachytherapy in standard 1.5T scanner,” *International Journal of Radiation Oncology Biology Physics*, vol. 59, no. 5, pp. 1414–1423, 2004.
- [174] R. A. Cormack, A. V. D’Amico, N. Hata, S. Silverman, M. Weinstein, and C. M. Tempany, “Feasibility of transperineal prostate biopsy under interventional magnetic resonance guidance,” *Urology*, vol. 56, no. 4, pp. 663–664, 2000.
 - [175] B. Fei, J. L. Duerk, D. T. Boll, J. S. Lewin, and D. L. Wilson, “Slice-to-volume registration and its potential application to interventional MRI-guided radio-frequency thermal ablation of prostate cancer,” *IEEE Transactions on Medical Imaging*, vol. 22, no. 4, pp. 515–525, 2003.
 - [176] R. C. Susil, K. Camphausen, P. Choyke, E. R. McVeigh, G. S. Gustafson, H. Ning, R. W. Miller, E. Atalar, C. N. Coleman, and C. Ménard, “System for prostate brachytherapy and biopsy in a standard 1.5 T MRI scanner,” *Magnetic Resonance in Medicine*, vol. 52, no. 3, pp. 683–687, 2004.
 - [177] G. S. Fischer, I. Iordachita, C. Csoma, J. Tokuda, S. P. DiMaio, C. M. Tempany, N. Hata, and G. Fichtinger, “MRI-compatible pneumatic robot for transperineal prostate needle placement,” *IEEE/ASME Transactions on Mechatronics*, vol. 13, no. 3, pp. 295–305, 2008.
 - [178] D. Stoianovici, D. Song, D. Petrisor, D. Ursu, D. Mazilu, M. Mutener, M. Schar, and A. Patriciu, ““MRI Stealth” robot for prostate interventions,” *Minimally Invasive Therapy and Allied Technologies*, vol. 16, no. 4, pp. 241–248, 2007.
 - [179] A. Patriciu, D. Petrisor, M. Muntener, D. Mazilu, M. Schar, and D. Stoianovici, “Automatic Brachytherapy Seed Placement Under MRI Guidance,” *IEEE Transactions on Biomedical Engineering*, vol. 54, no. 8, pp. 1499–1506, 2007.
 - [180] D. Stoianovici, A. Patriciu, D. Mazilu, L. Kavoussi, and D. Petrisor, “A New Type of Motor: Pneumatic Step Motor,” *IEEE/ASME TRANSACTIONS ON MECHATRONICS*, vol. 12, no. 1, pp. 98–106, 2007.
 - [181] J. A. Cunha, I.-C. Hsu, J. Pouliot, M. Roach III, K. Shinohara, J. Kurhanewicz, G. Reed, and D. Stoianovici, “Toward adaptive stereotactic robotic brachytherapy for prostate cancer: Demonstration of an adaptive workflow incorporating inverse planning and an MR stealth robot,” *Minimally Invasive Therapy & Allied Technologies*, vol. 19, pp. 189–202, aug 2010.
 - [182] A. Melzer, B. Gutmann, T. Remmele, R. Wolf, A. Lukoscheck, M. Bock, H. Bardenheuer, and H. Fischer, “INNOMOTION for percutaneous image-guided interventions,” *IEEE Engineering in Medicine and Biology Magazine*, vol. 27, no. 3, pp. 66–73, 2008.
 - [183] M. R. Van Den Bosch, M. R. Moman, M. Van Vulpen, J. J. Battermann, E. Duiveman, L. J. Van Schelven, H. De Leeuw, J. J. Lagendijk, and M. A. Moerland, “MRI-guided robotic system for transperineal prostate interventions: Proof of principle,” *Physics in Medicine and Biology*, vol. 55, no. 5, 2010.

- [184] S. E. Song, N. B. Cho, G. Fischer, N. Hata, C. Tempany, G. Fichtinger, and I. Iordachita, "Development of a pneumatic robot for MRI-guided transperineal prostate biopsy and brachytherapy: New approaches," in *Proceedings - IEEE International Conference on Robotics and Automation*, (Anchorage, AK, USA), pp. 2580–2585, IEEE, 2010.
- [185] G. Miron, A. Girard, J.-S. Plante, and M. Lepage, "Design and Manufacturing of Embedded Air-Muscles for a Magnetic Resonance Imaging Compatible Prostate Cancer Binary Manipulator," *Journal of Mechanical Design*, vol. 135, nov 2012.
- [186] K. Tadakuma, L. M. DeVita, J. S. Plante, Y. Shaoze, and S. Dubowsky, "The experimental study of a precision parallel manipulator with binary actuation: With application to MRI cancer treatment," in *2008 IEEE International Conference on Robotics and Automation*, pp. 2503–2508, 2008.
- [187] S. Abdelaziz, L. Esteveny, P. Renaud, B. Bayle, L. Barbé, M. De Mathelin, and A. Gangi, "Design considerations for a novel MRI compatible manipulator for prostate cryoablation," *International journal of computer assisted radiology and surgery*, vol. 6, pp. 811–819, nov 2011.
- [188] A. A. Goldenberg, J. Trachtenberg, W. Kucharczyk, Y. Yi, M. Haider, L. Ma, R. Weersink, and C. Raoufi, "Robotic system for closed-bore MRI-guided prostatic interventions," *IEEE/ASME Transactions on Mechatronics*, vol. 13, no. 3, pp. 374–379, 2008.
- [189] A. A. Goldenberg, J. Trachtenberg, Y. Yi, R. Weersink, M. S. Sussman, M. Haider, L. Ma, and W. Kucharczyk, "Robot-assisted MRI-guided prostatic interventions," *Robotica*, vol. 28, no. 2, pp. 215–234, 2010.
- [190] U. Lindner, S. A. Louis, and J. A. Colquhoun, "First robotic magnetic resonance-guided laser focal therapy for prostate cancer: A case report and review of the literature," *Interven Oncol Soc J*, vol. 1, pp. 69–77, jan 2011.
- [191] W. Shang, H. Su, G. Li, and G. S. Fischer, "Teleoperation system with hybrid pneumatic-piezoelectric actuation for MRI-guided needle insertion with haptic feedback," in *2013 IEEE/RSJ International Conference on Intelligent Robots and Systems*, pp. 4092–4098, 2013.
- [192] H. Su, D. C. Cardona, W. Shang, A. Camilo, G. A. Cole, D. C. Rucker, R. J. Webster, and G. S. Fischer, "A MRI-guided concentric tube continuum robot with piezoelectric actuation: A feasibility study," in *Proceedings - IEEE International Conference on Robotics and Automation*, (Saint Paul, MN, USA), pp. 1939–1945, IEEE, 2012.
- [193] J. Cepek, B. A. Chronik, U. Lindner, J. Trachtenberg, S. R. H. Davidson, J. Bax, and A. Fenster, "A system for MRI-guided transperineal delivery of needles to the prostate for focal therapy," *Medical Physics*, vol. 40, no. 1, p. 012304, 2013.

- [194] J. Cepek, U. Lindner, S. Ghai, A. S. Louis, S. R. H. Davidson, M. R. Gertner, E. Hlasny, M. S. Sussman, A. Fenster, and J. Trachtenberg, “Mechatronic system for in-bore MRI-guided insertion of needles to the prostate: An in vivo needle guidance accuracy study,” *Journal of Magnetic Resonance Imaging*, vol. 42, no. 1, pp. 48–55, 2015.

Chapter 2

Evaluation of Tumour Coverage after MR-Guided Prostate Focal Laser Ablation Therapy

2.1 Introduction

Prostate Cancer (PCa) is the most common non-cutaneous cancer in men in the USA with approximately 181,000 new diagnoses in 2016, and is the second leading cause of cancer death in men. [1] Use of prostate specific antigen (PSA) screening, magnetic resonance imaging (MRI), and advances in prostate biopsy have resulted in earlier and more accurate detection of PCa, [2] particularly of small, highly localized, and low grade [3] tumours. While detecting and treating cancer early is critical for cancer control, [4] many of the non-lethal tumours are unnecessarily treated. [5]

The most common treatment methods for PCa include radical prostatectomy, external beam radiation, brachytherapy, and chemotherapy. These treatments provide excellent oncologic control; however, they have many negative side effects including genitourinary complications, erectile dysfunction, incontinence, and rectal toxicity, which severely impact the quality of life for the patient. [6, 7] For low- and low-intermediate-risk tumours (PSA levels less than 15 ng/ml, Gleason scores 7 or less, and 25% or less tumour involvement in biopsies), the risk of associated side effects may outweigh the benefit of treatment. In these cases, patients may

undergo active surveillance (AS), [8] in which patients are monitored and treatment is delayed until the tumour volume or risk increases. Unfortunately, the psychological burden of living with untreated cancer causes many men to opt for surgery. [9]

Addressing the gap between surgery and AS, focal prostate therapy is emerging as a minimally invasive alternative to conventional treatment options. Prostate focal therapy is motivated by evidence that the dominant index lesion (DIL) is the most likely origin of metastases. [10] Prostate focal therapy aims to deliver localized treatment to the DIL while preserving the rest of the gland – including important functional structures such as the neurovascular bundles and urethral sphincters – thus reducing patient morbidity. Many techniques are available for focal therapy, such as cryotherapy, photodynamic therapy, high-intensity focused ultrasound (HIFU), and focal laser thermal ablation (FLA). [2] Patients in this study underwent MRI-guided FLA therapy.

During FLA therapy, a laser diffuser is inserted transperineally through a needle guided by a template to the tumour site. [11] The tissue surrounding the needle tip is heated to 60 °C with the intention of ablating the tumour as well as a 5 mm margin of healthy tissue where possible (i.e., avoiding functional structures). [12] MRI is an ideal imaging modality for focal therapy guidance because it offers excellent soft tissue contrast for identifying and localizing tumours [13] and the prostate, [14] and MRI thermometry allows for real-time temperature monitoring during ablation. [15] Additionally, dynamic contrast enhanced (DCE) MR images make it possible to visualize post-ablation tissue destruction as a hypo-intense signal void. [16] FLA is attractive due to its ability to completely ablate a targeted region, [13] and use of MRI for temperature monitoring.

Uncertainty still surrounds aspects of FLA therapy including patient selection; tumour localization, visualization, and characterization; needle guidance; and evaluation of treatment efficacy. [2] This paper aims to quantify the accuracy of ablation zone placement and burn radius during FLA therapy by measuring the overlap between ablation zones and tumours identified during treatment planning in patients who underwent prostate FLA therapy. The

measurements were performed by non-linearly registering pre-operative MR images with MR images acquired immediately after ablation. To the best of our knowledge, this is the first study to perform such a measurement.

2.2 Methods

2.2.1 Materials

A prospective, single arm, nonrandomized, unblinded phase II trial was institutional review board approved and registered at the University of Chicago. [12] 27 patients were treated by an experienced radiologist (A.O.) and urologist (S.E.) at University of Chicago Medicine using prostate FLA therapy in accordance with the clinical trial protocol (ClinicalTrials.gov NCT01792024, registered February 15, 2013) and following all relevant guidelines and regulations. All participants provided written informed consent. Patients had a median age of 62 years, mean PSA of 4.4 ng/ml (range 0.88-8.99 ng/ml), and Gleason scores of 6 in 85% of patients, 7 (3+4) in 11% of patients, and 7 (4+3) in 4% of patients. Seven of these patients were treated for two tumours, but the second ablation zones were not analysed in this study due to the potential occurrence of prostate motion during repeated needle insertions. Additionally, low volume Gleason 6 disease was identified outside the intended ablation zone(s) in seven patients.

Multi-parametric MRI (mpMRI) pre-operative images were acquired for each patient on a 3.0 T Philips Achieva MR scanner (Philips Medical Systems, Best, Netherlands) two to three months preceding their procedure. The pre-operative images [12] used in this study were axial T2-weighted turbo spin echo MRI with image dimensions 400 pixels x 397 pixels and voxel dimensions 0.3125 x 0.3125 x 3.0 mm³ (TR: 3947.87-5639.81 ms, TE: 115.0 ms, flip angle: 90.00°, bandwidth: 172.00 Hz/px). Depending on the patient, between 28 and 40 image slices were acquired. The procedures were guided by MRI using a 1.5 T Philips Achieva MR scanner (Philips Medical Systems, Best, Netherlands) with an endorectal coil. The post-ablative DCE

T1W fast field echo MRI (*THRIVE* sequence on the Philips Achieva scanner) used in this study, with image dimensions 190 x 192 x 121 voxels and voxel dimensions 0.99 x 0.99 x 2.0 mm³ (TR: 3.92 ms, TE: 1.84 ms, flip angle: 10.00°, bandwidth: 434.00 Hz/px), were acquired during the procedure after tissue was ablated and gadodiamide (Omniscan; GE Healthcare, Princeton, NJ) contrast agent was injected. The first patient was dropped from the study to avoid learning curve effects, and three patients were dropped from the study due to artefacts obscuring the ablation zones in the DCE MRI, leaving 23 tumours.

Ablation was performed using a 15 W Visualase[®] laser system while patients were consciously sedated. The 17-gauge laser applicator was introduced through a 14-gauge titanium needle with a polytetrafluoroethylene catheter. The laser was applied at a reduced power level (insufficient to cause thermal injury) for verification of placement accuracy using fast radio frequency-spoiled gradient recalled echo images, and then turned up to between 6 to 15 W, depending on the size of the intended ablation zone, for a duration of 60 to 120 seconds to complete the ablation. During the ablation, temperature changes were monitored using the proton resonance frequency shift from gradient-recalled echo pulse sequence images acquired every 5 seconds. A 90 °C control point was placed at the applicator-tissue interface to minimize the possibility of deleterious high-temperature effects (i.e., char formation, vaporization, and cavitation). Lower temperature control points (45 °C) were set near important functional structures such as the urethra and rectal wall to minimize the risk of damage. If the designated temperature at a control point was reached, ablation was automatically terminated by the system.

Tissue damage estimates were calculated by the Visualase software, which uses the Arrhenius formulation based on temperature history as follows

$$\Omega(t) = \int_0^t A \exp\left(\frac{-E_a}{RT(\tau)}\right) d\tau \quad (2.1)$$

where R is the universal gas constant, E_a is the activation energy, T is the temperature, and A is the frequency factor. This formulation has been shown to predict thermal necrosis eval-

uated on prostate histology. [17] The tissue damage maps were used in real-time to influence treatment decision-making, and tissue was considered ablated when the parameter $\Omega(t)$ reached unity in that region. The minimum targeted ablation margin was 5 mm of healthy tissue from the lesion when possible. [12]

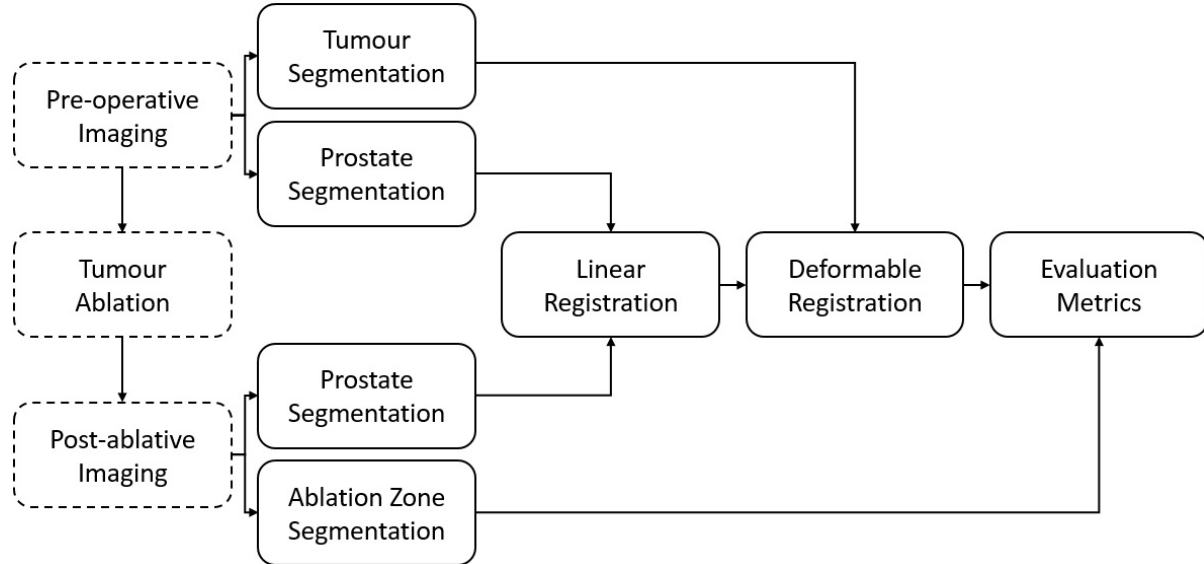


Figure 2.1: Diagram of steps used to compare tumours and ablation zones. Dashed lines indicate clinical processes.

2.2.2 Registration Pipeline

Overlap between tumours and ablation zones was compared using a deformable registration process outlined in Figure 2.1 for patients who underwent prostate FLA therapy.

Surface Segmentation

Lesions were identified on pre-operative mpMRI and outlined on pre-operative T2 images by an experienced radiologist (A.O.) as part of the procedure workflow. Ablation zones were identified as a hypo-intense void on post-ablation DCE images and outlined post-operatively by a trained operator (S.G.) under the supervision of the same radiologist. Prostates were post-operatively outlined on pre-operative T2 images and post-ablation DCE images by a trained

operator (D.T.). All structures were outlined slice-by-slice, and the outlines were converted into closed 3D surfaces. Prostate outlines were repeated five times with at least two days of separation between repetitions.

Linear Registration

Pre-operative images and post-ablation images were placed in a common co-ordinate system using an affine landmark registration with translation and anisotropic scaling. Landmarks were chosen as the maximum and minimum co-ordinates on the prostate surfaces in each of the imaging dimensions (x, y, and z), which corresponded approximately to the anatomical planes (sagittal, coronal, and axial). These landmarks are similar to the ones used by *Sun, Y. et al* [18] and described by *Mahdavi, S. et al.* [19] The landmarks L_{pre}^{max} and L_{pre}^{min} on the pre-operative image were defined using the pre-operative prostate surface $P_{pre} \subset R^3$ as

$$L_{pre}^{max} = \begin{bmatrix} \max_{x \in P_{pre}} x_1 \\ \max_{x \in P_{pre}} x_2 \\ \max_{x \in P_{pre}} x_3 \end{bmatrix}, \quad L_{pre}^{min} = \begin{bmatrix} \min_{x \in P_{pre}} x_1 \\ \min_{x \in P_{pre}} x_2 \\ \min_{x \in P_{pre}} x_3 \end{bmatrix} \quad (2.2)$$

where $x = [x_1, x_2, x_3]^T$. L_{post}^{max} and L_{post}^{min} , the landmarks on the post-ablative image, were defined similarly using the post-ablative prostate surface $P_{post} \subset R^3$. The transformation matrix A was calculated as

$$A = \begin{bmatrix} a_1 & 0 & 0 & t_1 \\ 0 & a_2 & 0 & t_2 \\ 0 & 0 & a_3 & t_3 \\ 0 & 0 & 0 & 1 \end{bmatrix} \quad (2.3)$$

$$a_i = \frac{L_{post_i}^{max} - L_{post_i}^{min}}{L_{pre_i}^{max} - L_{pre_i}^{min}}, \quad t = c_{post} - c_{pre}$$

where c_{pre} and c_{post} are the centroids of P_{pre} and P_{post} , respectively. The transform A was

applied to P_{pre} and the pre-operative tumour surface $T_{pre} \subset R^3$ to generate transformed surfaces P_{trans} and T_{trans} in the post-ablation co-ordinate space.

$$P_{trans} = AP_{pre}, \quad T_{trans} = AT_{pre} \quad (2.4)$$

The transformation A forces P_{trans} and P_{post} to have the same centroid, width, length, and height. This was important for good initialization of the deformable registration described in the next section since the dimensions of the prostates sometimes changed between image acquisitions, due to factors such as variable bladder filling, needle insertion, or rectal peristalsis.

Very little rotation was assumed as patients were lying in approximately the same supine position between scans. Any rotation present was likely around the superior-inferior axis due to side-to-side motion of the patient. Pre-operative and post-ablative images were visually inspected for signs of rotation based on anatomical landmarks (femoral head). For any suspicious cases, the pre-operative images were manually rotated ± 5 and ± 10 degrees to check for improvements in the registration.

Equal Angle Parameterization

Equal angle parameterization is a technique used to distribute control points across a closed 3D surface $S \subset R^3$. The technique leverages a bounding sphere B , which has the same centroid c as S and radius

$$r \geq \max_{x \in S} \|c - x\| \quad (2.5)$$

such that every point in S is enclosed by B . Spherical Fibonacci mapping [20] generates a nearly uniform point distribution $S F^n$ on B according to

$$sf_i^n = M(\phi_i, \theta_i) \quad (2.6)$$

$$\phi_i = 2\pi \left(\frac{i}{\Phi} - \left\lfloor \frac{i}{\Phi} \right\rfloor \right), \quad \theta_i = \cos^{-1} \left(1 - \frac{2i+1}{n} \right), \quad 0 \leq i < n$$

$$M(\phi, \theta) = (r \cos \phi \sin \theta + c_x, r \sin \phi \sin \theta + c_y, r \cos \theta + c_z)$$

where n is the number of points in the distribution, i is the point index, Φ is the golden ratio $\frac{1+\sqrt{5}}{2}$ and $\lfloor x \rfloor$ denotes the mathematical floor function. Each point $sf_i \in SF^n$ is used to generate a line segment $\mathbf{r}_i = sf_i - c$ which originates at the surface centroid. The intersection of \mathbf{r}_i with S yields the control point cp_i , and the set of all control points is defined as $CP^n = cp_i | 0 \leq i < n$. If S is star convex [21] at c , each line segment originating from c intersects with S exactly once. If S is not star convex at c , multiple intersections along each line segment are possible, and cp_i is chosen as the first point of intersection (closest to c).

Deformable Surface Registration

Deformable registration was used to align prostate interiors (and by extension, the tumours) since prostates may change shape between image acquisitions due to factors such as patient posture, variable bladder filling, needle insertion, endorectal coil inflation, rectal peristalsis, or growth of the prostate. Thin-plate splines [22] (TPS) can be used as a nonlinear surface registration technique, which models prostate tissue deformation. [23, 24] TPS interpolates between two sets of corresponding control points while minimizing the curvature of the interpolation, which is analogous to bending a thin sheet of metal. This generates a smooth deformation of one surface to match the other without ripples between control points or sharp transitions. TPS was described by *Rohr et al.* for registration of images with dimensionality three or greater. [25] The set of 512 control points CP_{pre}^{512} on pre-operative prostate surface P_{pre} and CP_{post}^{512} on post-ablative prostate surface P_{post} were selected using equal angle parameterization. Let the transformation $u : R^3 \rightarrow R^3$ represent the displacement in the x-dimension and define it as

$$u(x, y, z) = a_1 + a_2x + a_3y + a_4z + \sum_{i=1}^{512} w_i |CP_{pre_i}^{512} - (x, y, z)| \quad (2.7)$$

where a_1, a_2, a_3, a_4 and w_i for each control point are coefficients to be determined. To solve for the coefficients, the following matrices were first defined

$$K = \begin{bmatrix} |CP_{pre_1}^{512} - CP_{pre_1}^{512}| & |CP_{pre_1}^{512} - CP_{pre_2}^{512}| & \dots \\ |CP_{pre_2}^{512} - CP_{pre_1}^{512}| & |CP_{pre_2}^{512} - CP_{pre_2}^{512}| & \dots \\ \vdots & \vdots & |CP_{pre_{512}}^{512} - CP_{pre_{512}}^{512}| \end{bmatrix}$$

$$C = \begin{bmatrix} 1 & pre_x^1 & pre_y^1 & pre_z^1 \\ 1 & pre_x^2 & pre_y^2 & pre_z^2 \\ \vdots & \vdots & \vdots & \vdots \\ 1 & pre_x^{512} & pre_y^{512} & pre_z^{512} \end{bmatrix}, v = \begin{bmatrix} post_x^1 - pre_x^1 \\ post_x^2 - pre_x^2 \\ \vdots \\ post_x^{512} - pre_x^{512} \end{bmatrix}, a = \begin{bmatrix} a_1 \\ a_2 \\ a_3 \\ a_4 \end{bmatrix}, w = \begin{bmatrix} w_1 \\ w_2 \\ \vdots \\ w_{512} \end{bmatrix}$$

where $(pre_x^i, pre_y^i, pre_z^i)$ are the co-ordinates of $CP_{pre_i}^{512}$ and $(post_x^i, post_y^i, post_z^i)$ are the co-ordinates of $CP_{post_i}^{512}$. The system of linear equations

$$Kw + Ca = v \quad (2.8a)$$

$$C^T w = 0 \quad (2.8b)$$

was solved to find the coefficients of \mathbf{u} . TPS was also calculated to find transformations in the y- and z-dimensions and all three transforms were combined into the co-ordinate mapping $V : R^3 \rightarrow R^3$. \mathbf{V} was then applied to T_{trans} to generate T_{def} , which is the pre-operative tumour surface transformed into the post-ablative image co-ordinate system and corrected for tissue deformation.

Consensus Surfaces

To determine the effect of prostate intra-observer segmentation variability on registration accuracy and our evaluation metrics, a consensus tumour surface was created as follows. [26] Each of the five pairs of prostate surfaces on pre-operative and post-ablative images were used to calculate five different transforms, A^i and V^i , $1 \leq i \leq 5$. These transforms were applied to the pre-operative tumour surface to generate five potential candidates, T_{def}^i , $1 \leq i \leq 5$, for the tumour's location and shape in post-ablative image space. A consensus tumour surface was determined as follows.

The centroids of each tumour candidate were used to calculate an average centroid. The standard deviation of the centroid positions were also calculated. Equal angle parameterization (as described earlier) was applied to each surface with 512 points. For each of these points on each surface, the distance from the point to the surface's centroid was calculated. Points on the consensus surface were generated by averaging the distances from the centroids of corresponding points on the candidate surfaces (corresponding points are in the same direction from the centroid of the surface they are on). The standard deviation of the distances was also calculated. The average distance was projected from the average centroid in the same direction to create a new point. The set of 512 points on the consensus surface were used as control points to deform a candidate surface to create the consensus surface.

Evaluation Metrics

The volumes of the average tumours and ablation zones were measured and the volume of intersection between them was determined. Let V_T be the volume of tumour T , V_{AZ} be the volume of ablation zone AZ , and $V_{T \cap AZ}$ be the volume of the intersection between T and AZ . To calculate the margins of the ablation zones, 2,048 control points were found on T using equal angle parameterization and formed the set CP_T . The line segments from this parameterization were extended to find the closest point of intersection with AZ to form the set CP_{AZ} . From these data, several metrics were calculated for each tumour:

- Margins – margins between the boundaries of the tumour and ablation zone were calculated in all directions using

$$M_i = \begin{cases} |CP_T^i - CP_{AZ}^i|, & \text{if } CP_T^i \text{ contained in AZ} \\ -|CP_T^i - CP_{AZ}^i|, & \text{otherwise} \end{cases} \quad (2.9)$$

- Minimum margin – shortest distance between the tumour boundary and ablation zone boundary (closest point between the two surfaces). If the tumour extended beyond the ablation zone boundary, the furthest point of its extension was used as the minimum margin and the minimum margin was negative

$$\min_{0 \leq i < 2,048} M_i \quad (2.10)$$

- Untreated tumour volume - volume of any portion of the tumour, which does not intersect with the ablation zone

$$V_T - V_{T \cap AZ} \quad (2.11)$$

- Percentage of untreated tumour volume – untreated tumour volume as a percentage of the total tumour volume

$$\frac{V_T - V_{T \cap AZ}}{V_T} \times 100\% \quad (2.12)$$

Data Availability

The datasets analysed during the current study are not publicly available due to patient confidentiality but are available from the physicians at the University of Chicago (S.E. and A.O.) on reasonable request.

2.3 Results

Metric	Median	IQR
Pre-operative Prostate Volume (cm ³)	43.0	24.5
Post-ablative Prostate Volume (cm ³)	43.5	21.5
Pre-operative Tumour Volume (cm ³)	0.057	0.093
Pre-operative Tumour Diameter (mm)	6.0	4.7
Post-ablative Ablation Zone Volume (cm ³)	5.13	2.40

Table 2.1: Median and interquartile range (IQR) of prostate, tumour, and ablation zone volumes and tumour diameters (n=23). Pre-operative volumes and diameters were measured on T2 diagnostic MR images taken several months before ablation, and post-ablative volumes were measured on T1 intra-operative DCE MR images immediately after ablation. Tumour diameter was defined as the largest dimension of the tumour visible on axial images.

Table 2.1 shows the median and interquartile range (IQR) of volumes of the prostate glands, tumours, and ablation zones and diameters of the tumours. The median pre-operative prostate volume was very similar to the median post-ablative prostate volume. A paired t-test revealed no statistically significant difference between pre-operative and post-ablative segmented mean prostate volumes ($p=0.31$). The ablation zone volumes were significantly larger than the tumour volumes. Distributions of these values are shown in Figure 2.2. The histograms of pre-operative and post-ablative prostate volumes were nearly identical. Most of the tumour volumes fell into the range of 0.004 to 0.216 cm³, with one large tumour measuring 0.528 cm³. Ablation zone volumes ranged from 1.2 to 8.3 cm³. The solid vertical line in each graph indicates the median value shown in Table 2.1. These distributions were tested for normality using the D’Agostino-Pearson omnibus K2 test in GraphPad Prism 7 (GraphPad Software, La Jolla, USA). The pre-operative prostate volumes, post-ablative prostate volumes, and tumour volumes were each significantly different ($p<0.05$) from a normal distribution with the same mean and standard deviation. The ablation zone volumes were consistent with a normal distribution ($p=0.95$).

After inspecting images for patient rotation (see section on linear registration), eight cases were identified as being possibly mis-rotated. After manual rotation, two registration results

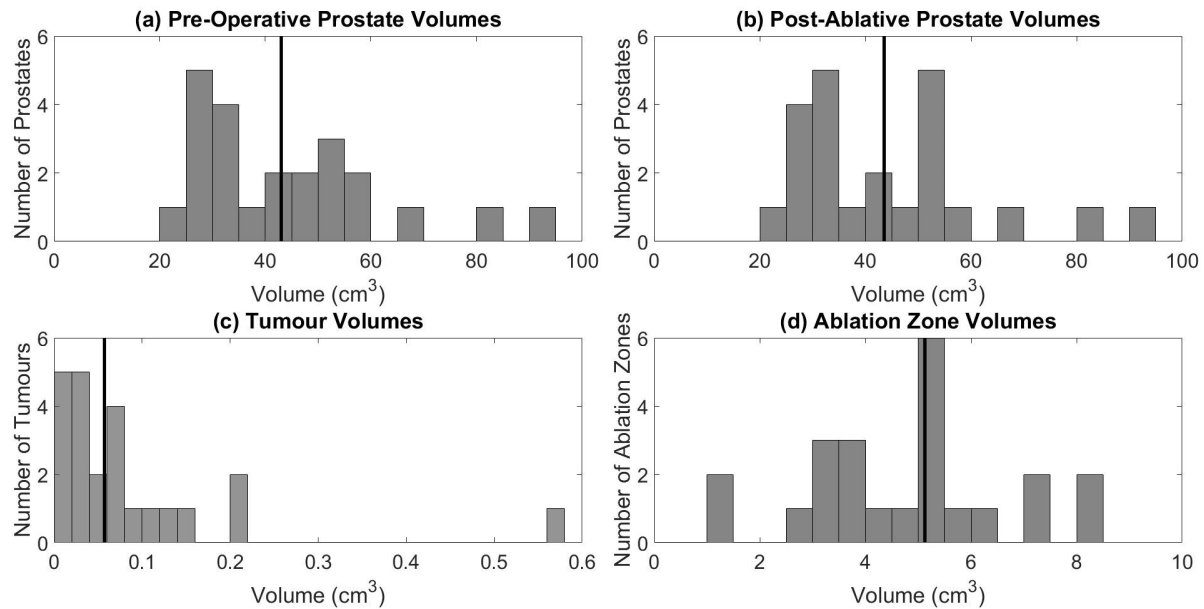


Figure 2.2: Distributions of (a) prostate volumes segmented from pre-operative images, (b) prostate volumes segmented from post-ablative images, (c) tumour volumes, and (d) ablation zone volumes.

were improved by a -10 degree rotation and one was improved by a +10 degree rotation around the superior-inferior axis. These results are included in the following figures. The other five cases saw no improvement from rotation.

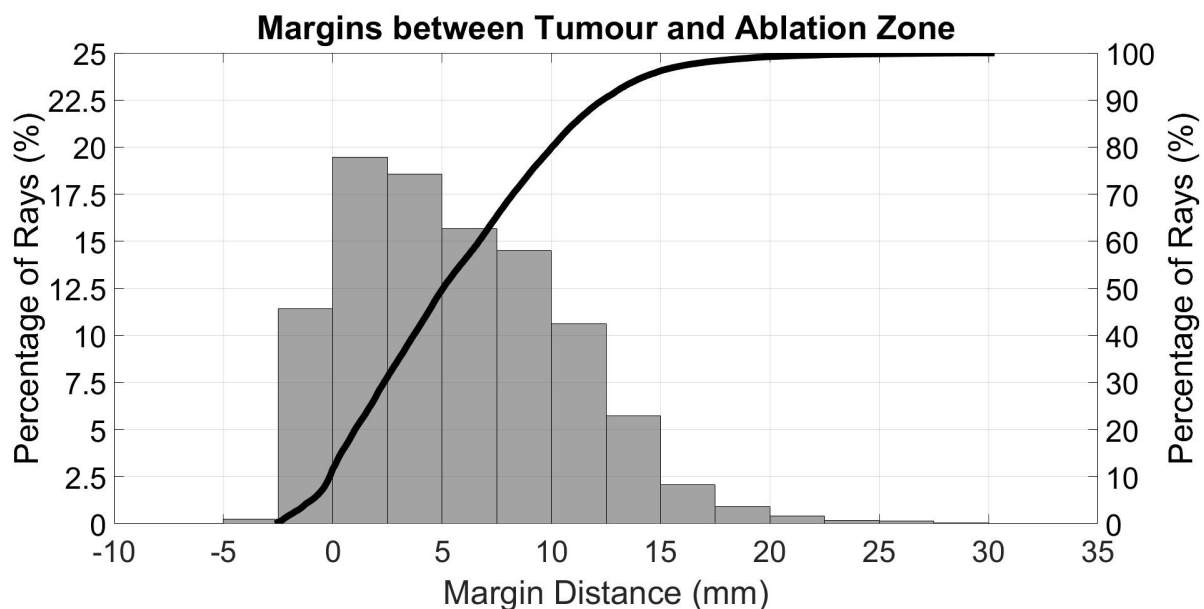


Figure 2.3: Histogram (left axis) and CDF (right axis) of margins between mean registered tumours and ablation zones.

Figure 2.3 shows the histogram and cumulative distribution function (CDF) of the margins (see Eq. 2.9) between the mean tumours and ablation zones for all of the angles generated using equal angle parameterization. Negative margins resulted from tumours extending beyond the boundary of the ablation zones. The majority of the margins (88.3%) were positive and therefore were inside the ablation zones, and 11.7% were outside the ablation zones. As can be seen on the CDF, 30.9% of margins were between -2.5 to 2.5 mm, which reflects the proximity of tumours to the boundary of the ablation zone in many cases. Large positive margins (10 to 30 mm) also resulted from tumours close to the ablation zone boundary, on the opposite side of the tumour from the small margins.

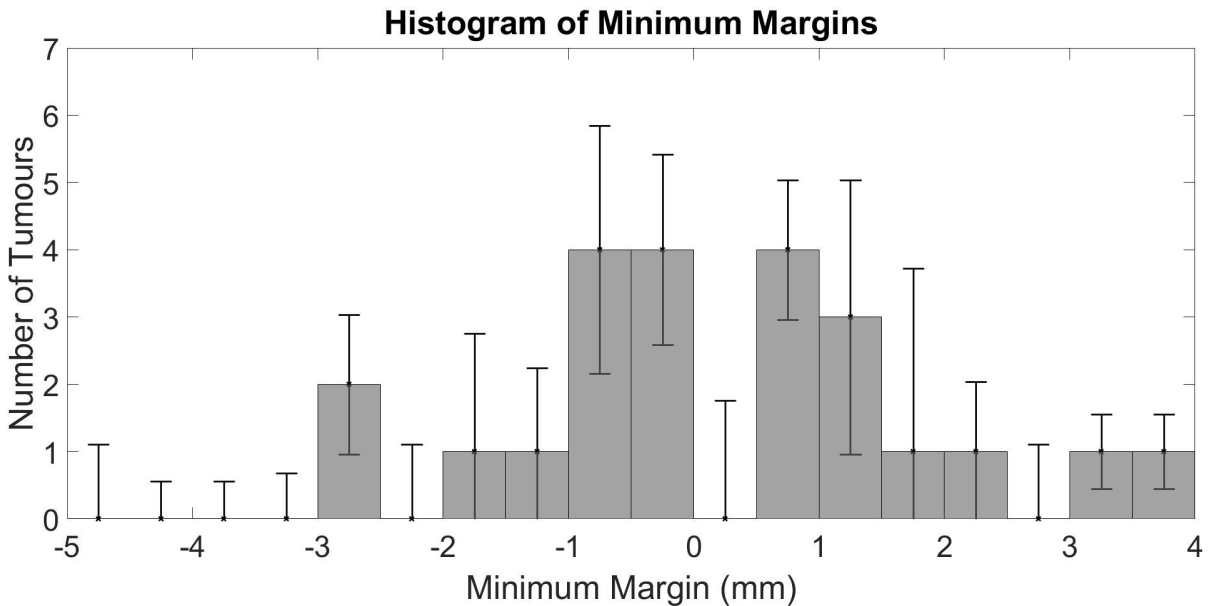


Figure 2.4: Histogram of minimum margins between registered tumours and ablation zones. Error bars indicate the 95% confidence interval of bin value.

Figure 2.4 shows the distribution of the minimum margins of the tumours (see Eq. 2.10). The minimum margin was found for the consensus tumour surface for each patient and the variability was assessed from the registrations generated by the five different prostate segmentations. In 12 cases, the tumour extended beyond the ablation zone by 0.1 to 2.6 mm. The median extension in these cases was 0.9 mm with an IQR of 1.3 mm. Completely ablated tumours were still within 3.8 mm of the ablation zone boundary. The median completely ablated

tumour had a minimum margin of 1.1 mm (IQR of 1.5 mm). The confidence interval of each bin value is plotted as a vertical error bar. The average minimum margin for each tumour was also plotted on the x-axis against the shortest distance from that tumour boundary to the closest functional structure (either the prostate capsule or the urethra) on the y-axis in Figure 2.5. Negative distances on the y-axis indicate tumours which extended beyond the prostate capsule. Since patients with T1c-T2a disease were selected, tumours outside the prostate boundary are more likely due to segmentation errors than actual extra-capsular extension. Distances to the cavernous nerves and rectum were not measured as they are outside the capsule. The small range of distances on the y-axis (-3.36 mm to +3.93 mm) reflects most tumours being located in the peripheral zone. Those tumours which were not located in the peripheral zone happened to be near the urethra.

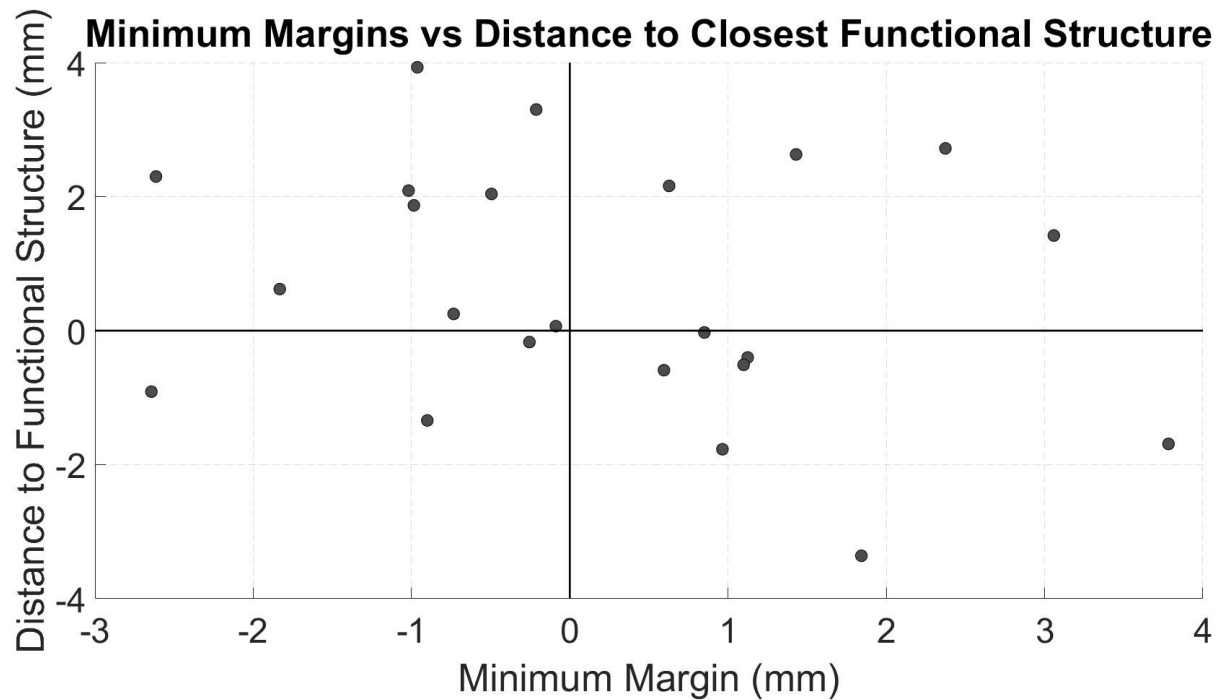


Figure 2.5: Average minimum margin for each tumour versus shortest distance to either prostate capsule or urethra (whichever was closer to the tumour) (n=23).

Figure 2.6 shows the histogram of unablated tumour volumes, which were calculated using the consensus tumour surfaces. The eleven tumours which were completely enclosed by the ablation zone were not included in the histogram. The unablated volume was less than 20 mm³

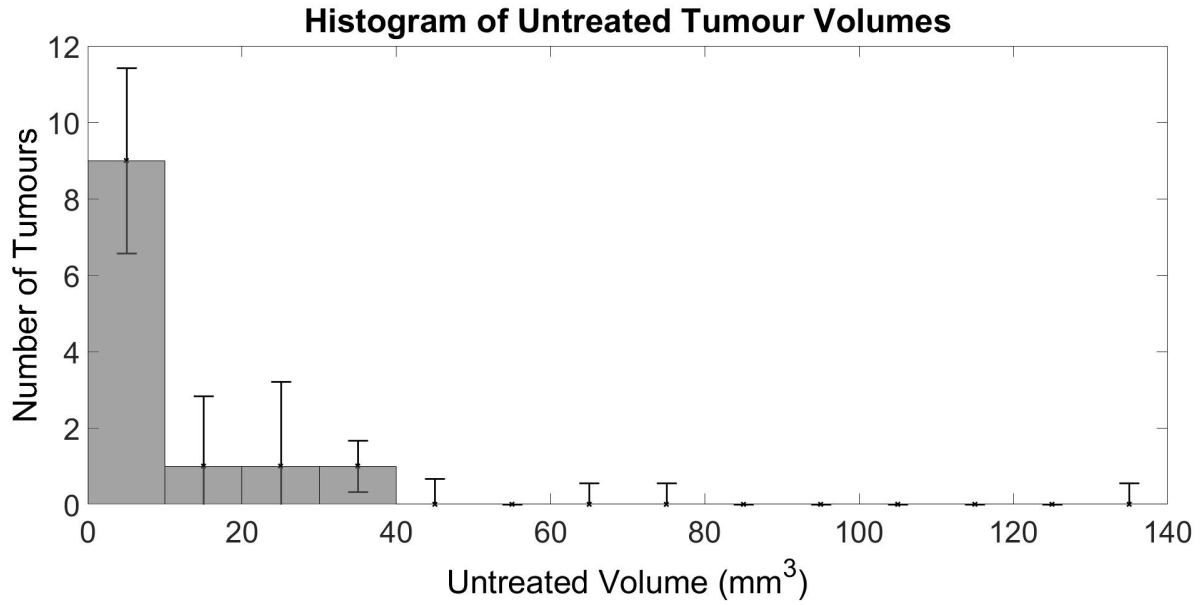


Figure 2.6: Histogram of treated tumour volume calculated using consensus tumour surfaces. The 95% confidence intervals for each bin value are plotted as vertical error bars ($n=12$).

for ten of the remaining tumours. Two tumours had between 20 and 40 mm³ of unablated volume.

An example of the consensus tumour surface created from five different tumour registrations is shown in Figure 2.7. Even though one of the candidates extended beyond the ablation zone, the other four were within the ablation zone and the consensus surface was calculated to also be within the ablation zone. Therefore, the unablated volume of this consensus tumour surface was 0 mm³ despite one of the candidates having unablated volume.

After registering tumours to the ablation zones and averaging the results across segmentations for each patient, eleven tumours completely overlapped and twelve tumours partially overlapped the corresponding ablation zones. Figure 2.8 shows examples of partial (first row) and complete (second and third rows) overlap. The median unablated tumour volume across all patients was 0.1 mm³ with an IQR of 3.7 mm³. Expressed as a percentage of the median tumour volume, the median unablated tumour volume was 0.2%.

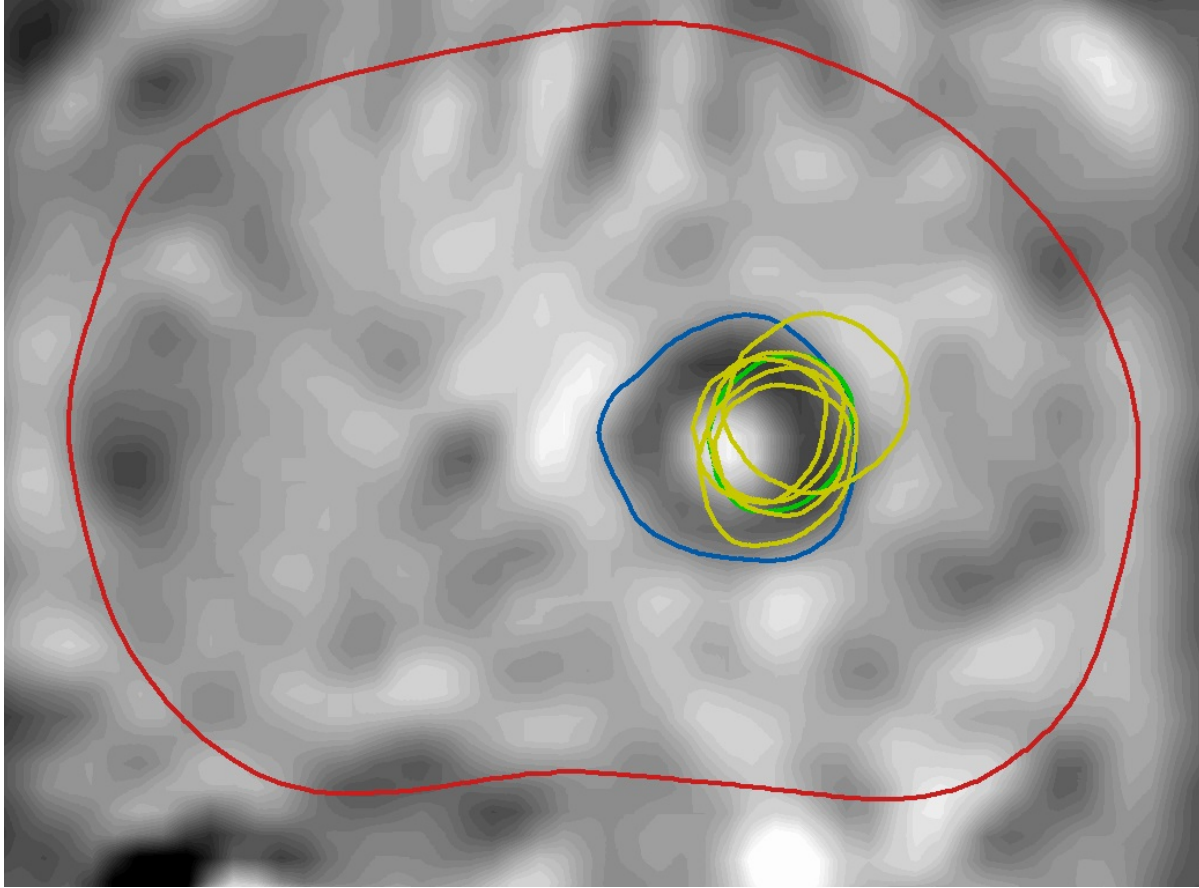


Figure 2.7: Axial view of five different registered tumour surfaces (yellow) with consensus surface (green), ablation zone (blue) and prostate (red).

2.4 Discussion

Focal ablation is an attractive option for treatment of many cancerous tumours and is being performed in many organs, such as the liver and kidney. Interest in focal ablation of prostate cancer is rising with an increasing number of reports. [3, 11, 12, 27, 28, 29] Quantitative analysis of the accuracy of ablation delivery, in addition to clinical trials focused on biochemical changes and recurrence, is needed to identify inaccuracies and variability to provide direction for improvements in the technology used to perform focal ablation on prostate tumours. To the best of our knowledge, this is the first quantitative report comparing the prostate focal ablation zone with the intended tumour target.

Since the distances between the margins of the ablation zone and the identified tumour

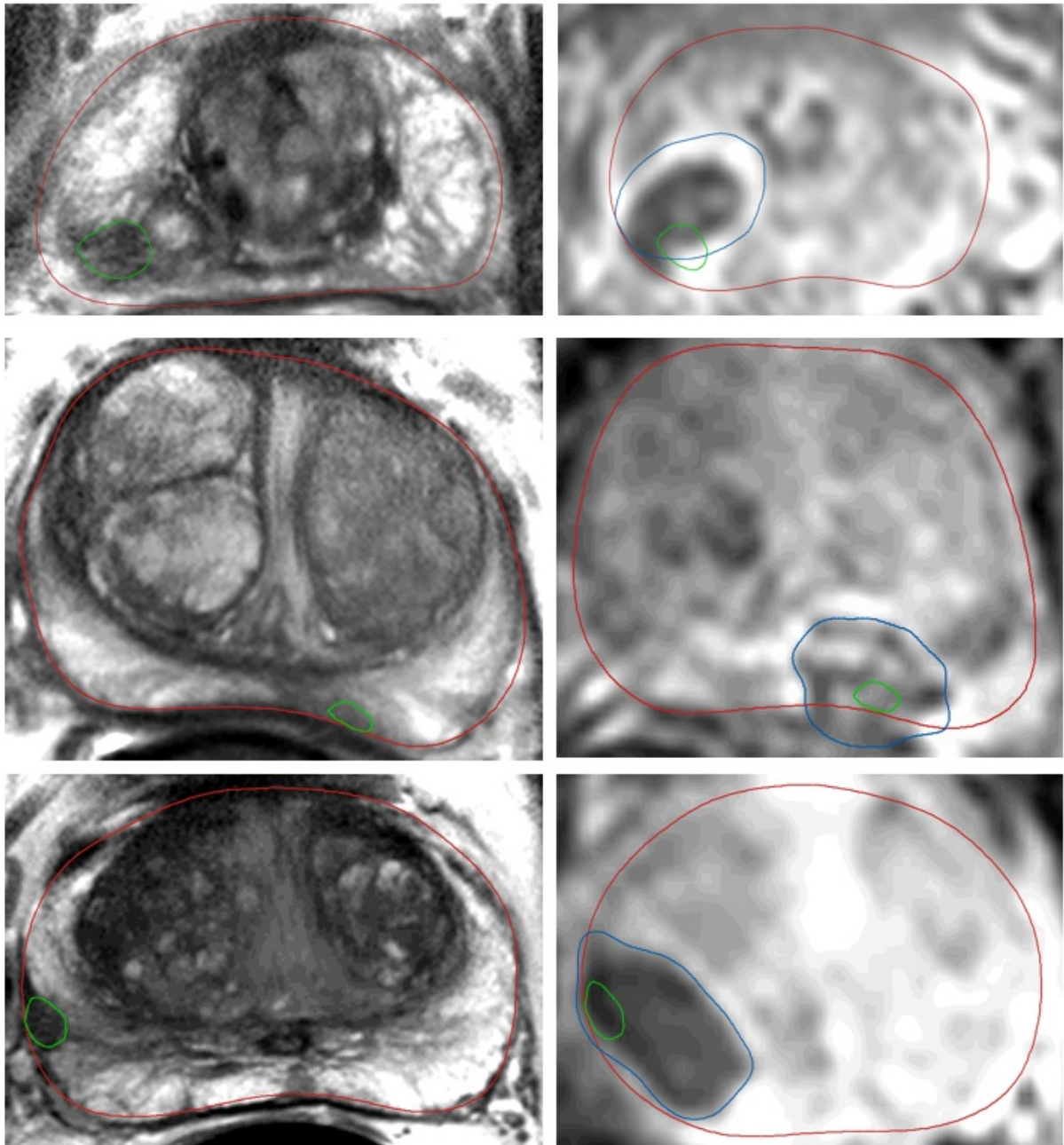


Figure 2.8: Slices of registered tumour (green), ablation zone (blue), and prostate boundary (red) overlayed on MRI. Each row is a different patient. Images in the left column are pre-operative T2 images, and images in the right column are DCE images. The tumour in the top row was partially ablated, and the tumours in the second and third rows were completely ablated.

using MRI are small, inaccuracy and variability in the analysis method will have a large impact on the results. For example, Figure 2.4 shows that a shift in tumour position of just 1 mm after registration could result in up to eight more tumours, for a total of 19, being completely within the boundaries of the ablation zone, or up to four more tumours moving partially outside of the ablation zone. A shift of 2 mm would result in 21 tumours being completely within the ablation zone, and a shift of 2.6 mm would result in all 23 tumours being completely within the ablation zone. Examining the smallest ablation zones revealed that the 1.2 cm³ ablation zone covered about 2.1% of the tumour volume; however, the next two smallest ablation zones (1.4 cm³ and 1.8 cm³) achieved 99.3% and 94.3% coverage of the tumour. Thus, it seems that small ablation zone volumes can be used as long as they are placed accurately, although this should be studied more comprehensively.

In the absence of better techniques to place ablation zones more accurately, our data suggests that the 5 mm margins used for this procedure were insufficient and should be extended 3 mm further for complete ablation of the dominant lesion in all cases. This recommendation is consistent with other reports which suggest using margins of at least 9 mm [30, 31] although they are based on segmentation variability and MR visibility of tumours. Increasing margins may not be possible if the tumour is close to a functional structure that needs to be preserved, such as the urethra or rectum, but Figure 2.5 shows that we did not observe a relationship between the margins the physician was able to achieve and the proximity to functional structures. This suggests that needle guidance accuracy is a bigger factor in achieving adequate margins than concern for preservation of functional structures, which is consistent with *Linder, U. et al* reporting no difficulties in ablation of peripheral zone tumours up to the lateral and anterior edges of the prostate and no concern for rectal injury during ablation. [16]

Different spatial resolution and anatomical contrast of the two registered MR sequences (T2 3.0 T vs DCE 1.5 T) and asymmetric deformation and swelling of the prostate on post-procedure MR images are factors that can limit the accuracy of registration. No significant difference was detected between pre-operative and post-ablative prostate volumes. Even though

some patients may experience prostate enlargement due to tumour growth or benign prostatic hyperplasia, not much is to be expected in the few months between pre-operative imaging and the operation. However, this asymmetric deformation and swelling can still affect the registration and thus we discuss the potential sources of error to provide direction for improvements in the analysis as well as the procedure. We did not compare how many tumours could be visualized at 1.5 T against 3.0 T in this study, which would be the subject of a separate study. Diagnosis was performed on 3.0 T imaging which is the recommended field strength for prostate cancer detection. [32] The tumour location was known prior to 1.5 T intra-procedural imaging and this knowledge was used to localize the tumour in the 1.5 T images based on the zonal anatomy of the prostate and the tumour's distance from the rectal wall.

Patients in this study returned for a one year follow up during which a systematic 12 core biopsy was performed with two cores MR-directed to the ablation zone. [12] Residual cancer was found inside the ablation zone in three patients and outside the ablation zone in six patients. The three patients with cancer inside the ablation zone had minimum margins of -1.0, -0.7, and 0.9 mm and tumour coverage of 93.1%, 93.5%, and 100% respectively according to our analysis. The residual cancer could be due to insufficient tissue heating leading to incomplete destruction of the tissue within the targeted area. Two of the patients in which cancer was found outside the ablation zone in the follow up had complete tumour coverage according to our analysis with minimum margins of 1.0 and 0.6 mm. These results might be due to an error in our registration process, but they could also be explained by microscopic cancer which was undetected by the biopsy or screening MRI. The other four patients which had cancer outside the ablation zone had partial tumour coverage which indicates that the ablation zones did not cover the complete tumour. Seven patients had partial tumour coverage but no cancer was found in the one year follow up. In summary, six of the twelve patients with partial coverage had positive biopsies, and three of the eleven patients with complete coverage had positive biopsies. While they are not yet available, ideally five and ten year follow up of PSA level and imaging should be performed [33] to further validate these results due to the slow-growing

nature of prostate cancer.

One limitation of this study is with surface segmentation of prostate boundaries. Segmentation began with manual slice-by-slice contouring on pre-operative and post-ablative MR images. The resolution of these images was limited, especially on the 1.5 T MRI post-ablative images, and interpolation must be performed to generate a continuous surface between contoured slices. The limited resolution resulted in poorer visualization of the prostate margins, particularly at the base and apex, and potentially resulted in less accurate segmentations. This may explain the high number of tumours seen extending beyond the prostate boundary in Figure 2.3. Since registration was surface based, these errors would propagate to errors in localization of the tumour in the post-ablative image. We have attempted to mitigate this issue by using the mean boundary of five segmentations; however, the possibility still exists that the mean boundary is not the true boundary.

Similarly, segmentation of the tumour boundary on the pre-operative image is also subject to inaccuracy and variability, but we did not account for tumour segmentation variability in our analysis. Since tumour segmentation is highly variable between clinicians, [34] with uncertainty of up to 5 mm, [35] our results would be better interpreted with knowledge of the intra- and inter-observer segmentation variability of the tumour. In our study, the same segmentations were used for targeting as for our analysis, and therefore the accuracy of the targeting can be assessed. However, a future study can focus on the impact of tumour segmentation variability on analysis of coverage of the tumour by the ablation zone. Furthermore, some studies suggest tumour boundaries extend beyond what can be seen on MRI [27, 30, 31, 35] which means our results likely underestimate the volume of the untreated tumour. Histological analysis, which was not performed in this study, would reveal the full extent of untreated tumour.

The linear step of our registration algorithm may also contribute some error to the final results. This step assumed that the extreme points of the prostates along each axis were corresponding, which may not be always true because some rotation of the prostate may have occurred between the pre-operative and post-ablative pose of the prostate. For most patients,

it was assumed that no prostate rotation occurred. However, testing with a few patient images found that small rotations (less than ten degrees) around the superior-inferior axis substantially impacted results. Also, scaling along each axis was assumed to be linear and uniform, although certain regions of the prostate are more elastic than others and will account for the majority of shape differences which may have occurred due to prostate swelling and deformation. Finally, there may be errors associated with the non-linear step of the registration method used here. Corresponding points in the prostate boundary were chosen based on intersection with a ray emanating from the prostate center, rather than anatomical correspondences. The locations of ray intersections depended strongly on the previous linear step. In addition, the non-linear TPS surface registration used for this study did not take into account the biomechanical properties of the prostate, which would have required a much more complex model. [36, 37, 38, 39] As a surface registration algorithm, TPS may incorrectly register the interior of the prostate, especially without modeling the tissue properties. The majority of tumours were near the prostate boundary so this potential source of error will be less severe, but this effect will be more severe for those tumours near the center.

Damage maps generated by the ablation planning software based on MR thermal images were not compared with post-ablation images in this study. Damage maps are used to ensure temperatures of 60 °C are reached inside the ablation zone while important functional structures are protected from high temperatures. However, these thermal images are acquired rapidly with a limited field-of-view and therefore registration based on prostate surfaces is difficult. Furthermore, we believe such comparison is redundant as ablation zone information from damage maps and from post-contrast images has been reported to have good correlation. [3]

Needle deflection by as much as 2.8 mm at a depth of 6.0 cm has been observed in prostate biopsy and brachytherapy procedures. [40] Thus, visualization of the needle and the tumour during the ablation procedure would ensure that the needle is in its correct location. However, poor visualization of the tumour and time constraints during the ablation procedure may result in errors in placing the needle at its intended location. Inaccurate placement of the needles with

respect to the tumour may lead to repeated needle insertions [41] or incomplete treatment if the error is not detected. Errors in needle placement may be reduced by the use of MRI visible needles or needle tips. [42] Inaccurate needle guidance and placement should be studied further as a source of error in ablation zone coverage of the tumour. While MR thermometry is used to monitor the ablation region, its spatial and temporal resolution limit its usefulness for real-time applications [43] and movement of tissue (e.g. rectal peristalsis) has been reported to cause artifacts in the temperature map. [3]

Prostate deformation due to forces from needle insertion, variable bladder filling, rectal peristalsis, [44, 45] or patient motion (since patients were only consciously sedated) may cause the prostate margins of the pre-operative and post-ablative images to be different; as well, the margins of the prostate during the procedure may vary, resulting in registration errors and an incorrect location of the intended target. Re-segmentation of the prostate and re-registration would mitigate this issue if identified, thus good image quality and robust segmentation and registration approaches that can be performed in a short time are required. While many investigators have developed prostate segmentation and registration methods, they are not yet integrated into routine ablation procedures.

2.5 Conclusion

This study examined the accuracy of tumour targeting during FLA therapy for treatment of PCa. Tumour surfaces were segmented on pre-operative images, transformed to the post-ablative volume using a combination of linear registration and deformable TPS registration, and then compared with the ablation zones. With the assumptions above, our results indicate that in some cases the boundary of the tumour is close to the boundary of the ablation zone. After registering 23 tumours and using our results, eleven tumours completely overlapped the ablation zone and twelve partially overlapped. A shift of 1 mm would result in 19 tumours completely overlapping the ablation zone, and a shift of 2 and 2.6 mm would result in 21 and

23 tumours completely overlapping the ablation zone, respectively. The median untreated percentage of tumour volume was 0.2%. Thus, our results suggest a need for accurate needle tracking and guidance methods to improve targeting, improved image quality of the intra-ablation images, and possibly re-segmentation and re-registration of the prostate to account for any changes in pose of the prostate. Clearly, our results are subject to the assumptions used in the analysis and variability introduced by the segmentation and registration methods used. Future studies should include analysis based on the variability of the prostate and tumour segmentation on MR images and employ a biomechanical prostate model for registration to account for possible non-uniform deformation of the prostate between the pre-operative and intra-ablative images.

Acknowledgements

The author gratefully acknowledges funding from the Imaging Translation program of the Ontario Institute of Cancer Research and the Canadian Institutes of Health Research. All software was created in C++ using ITK and VTK libraries for image processing and visualization. Contour tracing and surface generation was performed in custom software (3D Quantify) created by Igor Gyacskov.

Competing interests

The authors have no relevant conflicts of interest to disclose.

Bibliography

- [1] American Cancer Society, “Cancer Facts & Figures 2016,” *Cancer Facts & Figures 2016*, pp. 1–9, 2016.
- [2] G. Bozzini, P. Colin, P. Nevoux, A. Villers, S. Mordon, and N. Betrouni, “Focal therapy of prostate cancer: energies and procedures,” *Urologic Oncology: Seminars and Original Investigations*, vol. 31, no. 2, pp. 155–167, 2013.
- [3] A. Oto, I. Sethi, G. Karczmar, R. J. McNichols, M. K. Ivancevic, W. M. Stadler, S. Watson, and S. E. Eggener, “MR imaging–guided focal laser ablation for prostate cancer: phase I trial,” *Radiology*, vol. 267, pp. 932–940, jun 2013.
- [4] F. Labrie, B. Candas, A. Dupont, L. Cusan, J. L. Gomez, R. E. Suburu, P. Diamond, J. Levesque, and A. Belanger, “Screening decreases prostate cancer death: first analysis of the 1988 Quebec prospective randomized controlled trial,” *Prostate*, vol. 38, pp. 83–91, feb 1999.
- [5] C. Parker, D. Muston, J. Melia, S. Moss, and D. Dearnaley, “A model of the natural history of screen-detected prostate cancer, and the effect of radical treatment on overall survival,” *British Journal of Cancer*, vol. 94, pp. 1361–8, may 2006.
- [6] W. R. Parker, R. Wang, C. He, and D. P. Wood Jr, “Five year expanded prostate cancer index composite-based quality of life outcomes after prostatectomy for localized prostate cancer,” *BJU International*, vol. 107, pp. 585–590, feb 2011.
- [7] J. C. Hu, X. Gu, S. R. Lipsitz, M. J. Barry, A. V. D’Amico, A. C. Weinberg, and N. L. Keating, “Comparative effectiveness of minimally invasive vs open radical prostatectomy,” *Journal of the American Medical Association*, vol. 302, p. 1557, oct 2009.
- [8] L. Klotz, L. Zhang, A. Lam, R. Nam, A. Mamedov, and A. Loblaw, “Clinical results of long-term follow-up of a large, active surveillance cohort with localized prostate cancer,” *Journal of Clinical Oncology : Official Journal of the American Society of Clinical Oncology*, vol. 28, pp. 126–31, jan 2010.
- [9] F. Fang, N. L. Keating, L. A. Mucci, H.-O. Adami, M. J. Stampfer, U. Valdimarsdóttir, and K. Fall, “Immediate risk of suicide and cardiovascular death after a prostate cancer diagnosis: cohort study in the United States,” *Journal of the National Cancer Institute*, vol. 102, pp. 307–314, mar 2010.
- [10] H. U. Ahmed, “The index lesion and the origin of prostate cancer,” *New England Journal of Medicine*, vol. 361, no. 17, pp. 1704–1706, 2009.
- [11] O. Raz, M. A. Haider, S. R. H. Davidson, U. Lindner, E. Hlasny, R. A. Weersink, M. R. Gertner, W. Kucharczyk, S. A. McCluskey, and J. Trachtenberg, “Real-time magnetic resonance imaging-guided focal laser therapy in patients with low-risk prostate cancer,” *European Urology*, vol. 58, no. 1, pp. 173–177, 2010.

- [12] S. E. Eggener, A. Yousuf, S. Watson, S. Wang, and A. Oto, “Phase II evaluation of magnetic resonance imaging guided focal laser ablation of prostate cancer,” *Journal of Urology*, vol. 196, no. 6, pp. 1670–1675, 2016.
- [13] P. Kozlowski, S. D. Chang, R. Meng, B. Mädler, R. Bell, E. C. Jones, and S. L. Goldenberg, “Combined prostate diffusion tensor imaging and dynamic contrast enhanced MRI at 3T—quantitative correlation with biopsy,” *Magnetic Resonance Imaging*, vol. 28, pp. 621–8, jun 2010.
- [14] Ö. Algan, G. E. Hanks, and A. H. Shaer, “Localization of the prostatic apex for radiation treatment planning,” *International Journal of Radiation Oncology, Biology, Physics*, vol. 33, no. 4, pp. 925–930, 1995.
- [15] R. J. Stafford, A. Shetty, A. M. Elliott, S. A. Klumpp, R. J. McNichols, A. Gowda, J. D. Hazle, and J. F. Ward, “Magnetic resonance guided, focal laser induced interstitial thermal therapy in a canine prostate model,” *The Journal of Urology*, vol. 184, pp. 1514–20, oct 2010.
- [16] U. Lindner, N. Lawrentschuk, R. A. Weersink, S. R. H. Davidson, O. Raz, E. Hlasny, D. L. Langer, M. R. Gertner, T. Van der Kwast, M. A. Haider, and J. Trachtenberg, “Focal laser ablation for prostate cancer followed by radical prostatectomy: validation of focal therapy and imaging accuracy,” *European Urology*, vol. 57, no. 6, pp. 1111–1114, 2010.
- [17] R. J. McNichols, A. Gowda, M. Kangasniemi, J. A. Bankson, R. E. Price, and J. D. Hazle, “Mr thermometry-based feedback control of laser interstitial thermal therapy at 980 nm,” *Lasers in Surgery and Medicine*, vol. 34, no. 1, pp. 48–55, 2004.
- [18] Y. Sun, J. Yuan, W. Qiu, M. Rajchl, C. Romagnoli, and A. Fenster, “Three-dimensional nonrigid MR-TRUS registration using dual optimization,” *IEEE Transactions on Medical Imaging*, vol. 34, no. 5, pp. 1085–1095, 2015.
- [19] S. S. Mahdavi, N. Chng, I. Spadinger, W. J. Morris, and S. E. Salcudean, “Semi-automatic segmentation for prostate interventions,” *Medical Image Analysis*, vol. 15, no. 2, pp. 226–237, 2011.
- [20] B. Keinert, M. Innmann, M. Sängler, and M. Stamminger, “Spherical fibonacci mapping,” *ACM Transactions on Graphics*, vol. 34, pp. 193:1—193:7, oct 2015.
- [21] S. G. Krantz, *Convex Analysis*. CRC Press, 2014.
- [22] F. L. Bookstein, “Principal warps: thin-plate splines and the decomposition of deformations,” *IEEE Transactions on Pattern Analysis and Machine Intelligence*, vol. 11, pp. 567–585, jun 1989.
- [23] N. Venugopal, B. McCurdy, A. Hnatov, and A. Dubey, “A feasibility study to investigate the use of thin-plate splines to account for prostate deformation,” *Physics in Medicine and Biology*, vol. 50, no. 12, pp. 2871–85, 2005.

- [24] Y. Sun, W. Qiu, J. Yuan, C. Romagnoli, and A. Fenster, “Three-dimensional nonrigid landmark-based magnetic resonance to transrectal ultrasound registration for image-guided prostate biopsy,” *Journal of Medical Imaging*, vol. 2, no. 2, p. 025002, 2015.
- [25] K. Rohr, H. Stiehl, R. Sprengel, T. Buzug, J. Weese, and M. Kuhn, “Landmark-based elastic registration using approximating thin-plate splines,” *IEEE Transactions on Medical Imaging*, vol. 20, pp. 526–534, jun 2001.
- [26] B. Chiu, M. Egger, J. D. Spence, G. Parraga, and A. Fenster, “Quantification of carotid vessel wall and plaque thickness change using 3D ultrasound images,” *Medical Physics*, vol. 35, pp. 3691–3710, jul 2008.
- [27] A. Napoli, M. Anzidei, C. De Nunzio, G. Cartocci, V. Panebianco, C. De Dominicis, C. Catalano, F. Petrucci, and C. Leonardo, “Real-time magnetic resonance-guided high-intensity focused ultrasound focal therapy for localised prostate cancer: preliminary experience,” *European Urology*, vol. 63, no. 2, pp. 395–398, 2013.
- [28] H. U. Ahmed, R. G. Hindley, L. Dickinson, A. Freeman, A. P. Kirkham, M. Sahu, R. Scott, C. Allen, J. Van der Meulen, and M. Emberton, “Focal therapy for localised unifocal and multifocal prostate cancer: A prospective development study,” *The Lancet Oncology*, vol. 13, no. 6, pp. 622–632, 2012.
- [29] U. Lindner, R. A. Weersink, M. A. Haider, M. R. Gertner, S. R. H. Davidson, M. Atri, B. Wilson, A. Fenster, and J. Trachtenberg, “Image guided photothermal focal therapy for localized prostate cancer: phase I trial,” *The Journal of Urology*, vol. 182, no. 4, pp. 1371–1377, 2009.
- [30] J. Le Nobin, A. B. Rosenkrantz, A. Villers, C. Orczyk, F. M. Deng, J. Melamed, A. Mikheev, H. Rusinek, and S. S. Taneja, “Image Guided Focal Therapy for Magnetic Resonance Imaging Visible Prostate Cancer: Defining a 3-Dimensional Treatment Margin Based on Magnetic Resonance Imaging Histology Co-Registration Analysis,” *Journal of Urology*, vol. 194, no. 2, pp. 364–370, 2015.
- [31] M. Piert, P. R. Shankar, J. Montgomery, L. P. Kunju, V. Rogers, J. Siddiqui, T. Rajendiran, J. Hearn, A. George, X. Shao, and M. S. Davenport, “Accuracy of tumor segmentation from multi-parametric prostate MRI and F-choline PET / CT for focal prostate cancer therapy applications,” *European Journal of Nuclear Medicine and Molecular Imaging*, vol. 8, no. 23, pp. 1–14, 2018.
- [32] L. Dickinson, H. U. Ahmed, C. Allen, J. O. Barentsz, B. Carey, J. J. Futterer, S. W. Heijmink, P. J. Hoskin, A. Kirkham, A. R. Padhani, R. Persad, P. Puech, S. Punwani, A. S. Sohaib, B. Tombal, A. Villers, J. Van Der Meulen, and M. Emberton, “Magnetic resonance imaging for the detection, localisation, and characterisation of prostate cancer: Recommendations from a European consensus meeting,” *European Urology*, vol. 59, no. 4, pp. 477–494, 2011.
- [33] H. I. Scher, S. Halabi, I. Tannock, M. Morris, C. N. Sternberg, M. A. Carducci, M. A. Eisenberger, C. Higano, G. J. Bubley, R. Dreicer, D. Petrylak, P. Kantoff, E. Basch, W. K.

- Kelly, W. D. Figg, E. J. Small, T. M. Beer, G. Wilding, A. Martin, and M. Hussain, "Design and end points of clinical trials for patients with progressive prostate cancer and castrate levels of testosterone: Recommendations of the prostate cancer clinical trials working group," *Journal of Clinical Oncology*, vol. 26, no. 7, pp. 1148–1159, 2008. PMID: 18309951.
- [34] G. M. Villeirs, K. Van Vaerenbergh, L. Vakaet, S. Bral, F. Claus, W. J. De Neve, K. L. Verstraete, and G. O. De Meerleer, "Interobserver delineation variation using CT versus combined CT + MRI in intensity-modulated radiotherapy for prostate cancer," *Strahlentherapie und Onkologie*, vol. 181, pp. 424–430, jul 2005.
- [35] E. Gibson, G. S. Bauman, C. Romagnoli, D. W. Cool, M. Bastian-Jordan, Z. Kassam, M. Gaed, M. Moussa, J. A. Gómez, S. E. Pautler, J. L. Chin, C. Crukley, M. A. Haider, A. Fenster, and A. D. Ward, "Toward prostate cancer contouring guidelines on magnetic resonance imaging: dominant lesion gross and clinical target volume coverage via accurate histology fusion," *International Journal of Radiation Oncology, Biology, Physics*, vol. 96, no. 1, pp. 188–196, 2016.
- [36] J. M. Hensel, C. Ménard, P. W. M. Chung, M. F. Milosevic, A. Kirilova, J. L. Moseley, M. A. Haider, and K. K. Brock, "Development of multiorgan finite element-based prostate deformation model enabling registration of endorectal coil magnetic resonance imaging for radiotherapy planning," *International Journal of Radiation Oncology, Biology, Physics*, vol. 68, no. 5, pp. 1522–1528, 2007.
- [37] B. Marami, S. Sirouspour, S. Ghoul, J. Cepek, S. R. H. Davidson, D. W. Capson, J. Trachtenberg, and A. Fenster, "Elastic registration of prostate MR images based on estimation of deformation states," *Medical Image Analysis*, vol. 21, no. 1, pp. 87–103, 2015.
- [38] A. Bharatha, M. Hirose, N. Hata, S. K. Warfield, M. Ferrant, K. H. Zou, E. Suarez-Santana, J. Ruiz-Alzola, A. D'Amico, R. A. Cormack, R. Kikinis, F. A. Jolesz, and C. M. Tempany, "Evaluation of three-dimensional finite element-based deformable registration of pre- and intraoperative prostate imaging," *Medical Physics*, vol. 28, no. 12, pp. 2551–2560, 2001.
- [39] A. Mohamed, C. Davatzikos, and R. Taylor, "A combined statistical and biomechanical model for estimation of intra-operative prostate deformation," in *Medical Image Computing and Computer-Assisted Intervention — MICCAI 2002* (T. Dohi and R. Kikinis, eds.), vol. 2489, pp. 452–460, Springer, Berlin, Heidelberg, 2002.
- [40] G. Wan, Z. Wei, L. Gardi, D. B. Downey, and A. Fenster, "Brachytherapy needle deflection evaluation and correction," *Medical Physics*, vol. 32, no. 4, pp. 902–909, 2005.
- [41] J. Cepek, U. Lindner, S. Ghai, A. S. Louis, S. R. H. Davidson, M. R. Gertner, E. Hlasny, M. S. Sussman, A. Fenster, and J. Trachtenberg, "Mechatronic system for in-bore MRI-guided insertion of needles to the prostate: An in vivo needle guidance accuracy study," *Journal of Magnetic Resonance Imaging*, vol. 42, no. 1, pp. 48–55, 2015.

- [42] J. Cepek, B. A. Chronik, U. Lindner, J. Trachtenberg, S. R. H. Davidson, J. Bax, and A. Fenster, “A system for MRI-guided transperineal delivery of needles to the prostate for focal therapy,” *Medical Physics*, vol. 40, no. 1, p. 012304, 2013.
- [43] J. Yuan, C.-S. Mei, L. P. Panych, N. J. McDannold, and B. Madore, “Towards fast and accurate temperature mapping with proton resonance frequency-based mr thermometry,” *Quantitative Imaging in Medicine and Surgery*, vol. 2, no. 1, 2012.
- [44] M. van Herk, A. Bruce, A. P. G. Kroes, T. Shouman, A. Touw, and J. V. Lebesque, “Quantification of organ motion during conformal radiotherapy of the prostate by three dimensional image registration,” *International Journal of Radiation Oncology, Biology, Physics*, vol. 33, no. 5, pp. 1311–1320, 1995.
- [45] A. M. Nichol, K. K. Brock, G. A. Lockwood, D. J. Moseley, T. Rosewall, P. R. Warde, C. N. Catton, and D. A. Jaffray, “A magnetic resonance imaging study of prostate deformation relative to implanted gold fiducial markers,” *International Journal of Radiation Oncology, Biology, Physics*, vol. 67, no. 1, pp. 48–56, 2007.

Chapter 3

Design and Validation of an MRI-Compatible Mechatronic System for Needle Delivery to Localized Prostate Cancer

3.1 Introduction

Conventional treatments for prostate cancer (PCa) - such as radical prostatectomy, external beam radiation therapy, brachytherapy, or chemotherapy - present risks for detrimental side-effects such as incontinence, genitourinary complications, erectile dysfunction, and rectal toxicity [1, 2, 3, 4]. For low and intermediate-risk PCa, these treatments may severely impact the patients' quality of life. Therefore, these patients are often placed on active surveillance [5], where disease progression is monitored. However, living with untreated cancer exposes patients and their families to detrimental psychological distress [6], and it may be advantageous to begin treatment early while the disease is small and localized. Focal treatment of the PCa has emerged as a viable treatment option for men who would normally be put on active surveillance but elect for therapy, as well as a treatment option of the index lesion (the tumour that is likely to drive progression) in men with multifocal PCa [7]. Prostate focal laser ablation (FLA) is one such focal therapy with fewer genitourinary side effects than radical whole gland options.

FLA is a minimally invasive technique in which optical fibers attached to a laser generator are inserted through transperineal catheters into the prostate to ablate the dominant index lesion (DIL), which is the most likely site of generation of metastases [8]. The aim of FLA is to ablate the tumour, but spare critical anatomical structures such as the neurovascular bundles, urethral sphincter, and rectum. Clinical trials have demonstrated promising success in devascularizing targeted regions with minimal side effects [9, 10, 11, 12, 13, 14]. Magnetic resonance image (MRI)-guidance offers several advantages for FLA over guidance from other imaging modalities, including superior soft-tissue contrast for visualizing tumours and anatomy [15, 16, 17, 18], real-time temperature monitoring [19], and dynamic contrast-enhanced (DCE) confirmation of ablation regions [10]. These advantages motivate the development of new prostate-specific MRI-compatible needle guidance methods.

Due to its constricted work-space and strong magnetic gradients, the bore of an MRI scanner poses unique challenges to physicians performing prostate interventions when the prostate is near the scanner's isocenter. Traditionally, needles are guided through a static plastic template consisting of a grid of regularly spaced holes. Early MR-guided prostate interventions were performed using an open-scanner architecture [20, 21, 22, 23, 24], which allowed improved access to the patient, but sacrificed image quality due to the lower field strength. Some studies developed specialized templates to perform prostate biopsies using higher field strength closed-bore scanners for guidance [25, 26], but still required patients to be outside the bore for needle insertions, introducing an elevated risk for undesirable prostate motion. Cepek *et al.* developed a manually actuated system, which allows the needle guide to be positioned while the patient is inside the scanner bore [27, 28]; however, the physician was still required to work within a confined space and could not view the images while operating the system. Many groups have developed pneumatically actuated systems, which can be remotely operated from the MRI control suite [29, 30, 31, 32, 33, 34]. Pneumatically actuated systems require a bulky network of pumps and hoses, which are separated at an appropriate distance from the scanner. Su *et al.* presented a general-purpose MRI compatible concentric tube continuum robot using

piezoelectric motors for the guidance of a curved, steerable cannula [35]. Another system employed piezoelectric actuators for in-bore transrectal prostate interventions [36]; however, the transrectal approach conveys a higher risk of adverse clinical consequences, such as sepsis and rectal bleeding, compared with a transperineal approach [37, 38]. Goldenberg *et al.* reported on a piezoelectric device for prostate ablations including remote control of trocar penetration and retraction [39]. This design eliminates haptic feedback for the physician, makes the system more difficult to sterilize, and complicates the insertion process since motors must be deactivated during imaging.

We hypothesize that a remotely actuated transperineal system will reduce MR-guided prostate FLA procedure times while maintaining or increasing needle guidance accuracy, and could potentially be adapted to other needle biopsies and alternative energy modalities, requiring transperineal delivery of needles. The system will be used to hold a desired position and angle of the needle templates as the physician manually inserts needles. Importantly, retaining manual needle insertion will improve patient safety via haptic feedback through needle forces for the physician and simplify the sterilization process. Such a system should be small enough to fit inside the MRI scanner bore with the patient, while not noticeably degrading image quality or presenting any adverse safety risks. Another important feature is the ability to angle needles to reach targets behind the pubic arch. This paper introduces an experimental prototype of a novel mechatronic system for guidance and delivery of FLA needles, which satisfies the preceding criteria. The design and kinematics of the system are described, MR-compatibility is tested, and the accuracy of the needle guidance is evaluated in benchtop experiments and in an in-bore 3T MRI environment.

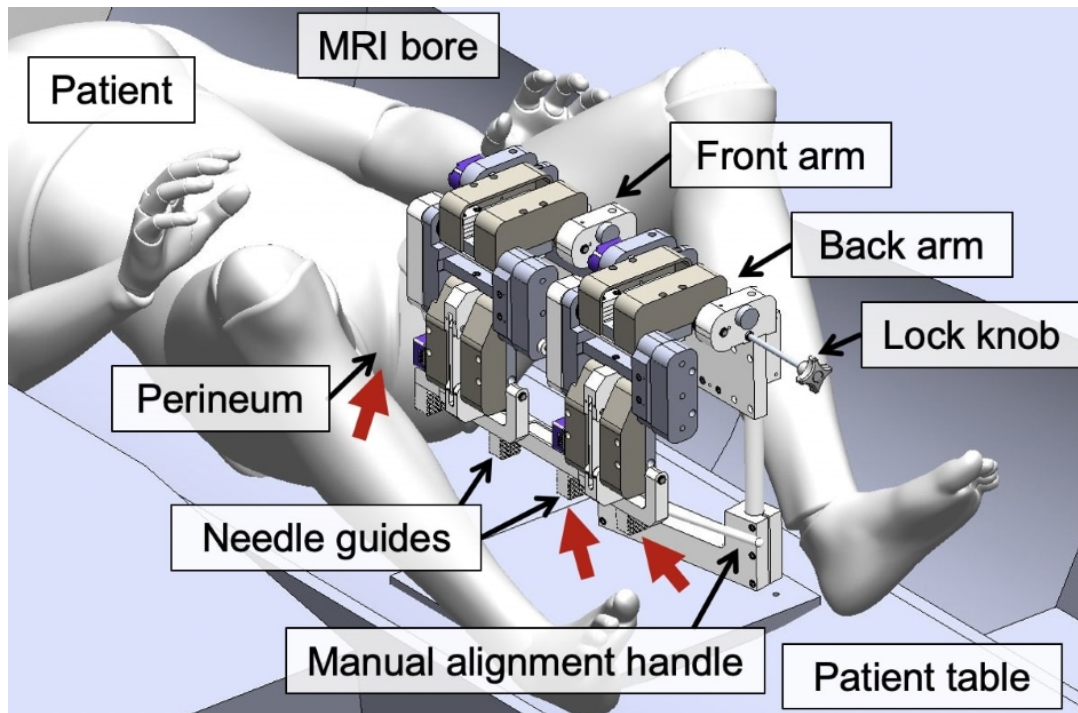


Figure 3.1: Computer-aided design (CAD) isometric model of the MRI-compatible mechatronic needle guidance system for prostate focal laser ablation (FLA) needle intervention. Encoders are identified by purple casings. Motors are hidden inside the device. Red arrows indicate where the needles are inserted: first through the guide at the rear of the system, then through the rest of the needle guides, and finally into the perineum.

3.2 Methods

3.2.1 Mechatronic System Design

The complete mechatronic system consists of a remotely actuated needle trajectory alignment device, an electronic control box, and a computer and monitor to interface with system control and image visualization software. The trajectory alignment device, shown in Fig. 3.1, is placed between the patient's legs within the bore of the MRI scanner with the needle guide positioned against the patient's perineum, while the patient lays in the dorsal recumbent position. The control box and computer are located in the scanner control room, where custom software is used to register the device coordinate system with the scanner coordinate system, visualize MR images, select target regions within the prostate, and control the motors to align the needle template with the desired trajectory.

Mechanical Design

The trajectory alignment device consists of four collinear needle guidance templates with 5×5 needle position holes, suspended from two main arms (Fig. 3.2). Two independently controlled arms were used to facilitate angulation of the needle template while maintaining a clear view of the patient's perineum. Each arm is comprised of two links connected with rotational joints, allowing for two degree-of-freedom (DOF) for planar motion perpendicular to the axis of needle insertion, vertical and horizontal translation at the end of the arm. The arms have a $6 \times 6 \text{ cm}^2$ range of motion, which corresponds to the width of a conventional fixed needle guidance template used in prostate brachytherapy. A set of adjustable plastic leaf springs on each arm provides a counterbalancing force against the weight of the arm to reduce the torque load on the motors. The needle guide is attached to the front arm via a dual-axis rotational joint, and to the rear arm via a dual axis rotational joint combined with an orthogonal sliding joint. The needle guide can therefore be remotely maneuvered through 4 DOFs: vertical translation, horizontal translation, pitch, and yaw. This allows the physician to select and set a needle trajectory from the console in the scanner control room. Once in position, the arms can be locked independently or concurrently using the knob on the rear of the system, which rotates through four positions: both arms unlocked, only front arm locked, both arms locked, only rear arm locked. An alignment handle attached to the rear of the system can be used if the physician needs to position the template manually, e.g. in case of motor failure, and the locking mechanism can be used to position each arm individually. Importantly, needle insertion is manually performed by the expert physician, as a safety measure via haptic feedback and to simplify sterilization of the system. During insertion, the needle can be rotated about its axis as it passes through the templates, providing a fifth DOF.

The system is constructed entirely of non-ferromagnetic materials. The black plastic components seen in Fig. 3.2 are composed of polyoxymethylene (Delrin®, DuPont, USA) and the light brown components are composed of polyether ether ketone (PEEK). Metallic components are composed of brass or aluminum. The electrical junction box mounted on the side of the

system is clad in an aluminum skin Faraday cage to shield the wires from electromagnetic interference, and all of the connectors are wrapped in copper tape. The length of the system along its longest dimension is 55.5 cm and its mass is $10.0 \text{ kg} \pm 5\%$. The width of the system with the arms fully extended is 30.5 cm and its height with the arms fully raised is 42.2 cm, which are both less than the diameter of the scanner bore, enabling it to fit within the bore while placed on the patient table.

Forward kinematics are used to calculate the position (p^n) and direction (\hat{v}^n) of the needle guide from the joint angles of the front and rear arms. The solutions to the forward kinematics equations inform the physician of the system's current pose during operation. Inverse kinematics are used to calculate the joint angles required to reach the desired position and direction of the needle guide. With these equations, the system can reach a desired pose based on the physician's treatment plan. The comprehensive derivation of these equations is given in Appendix A.

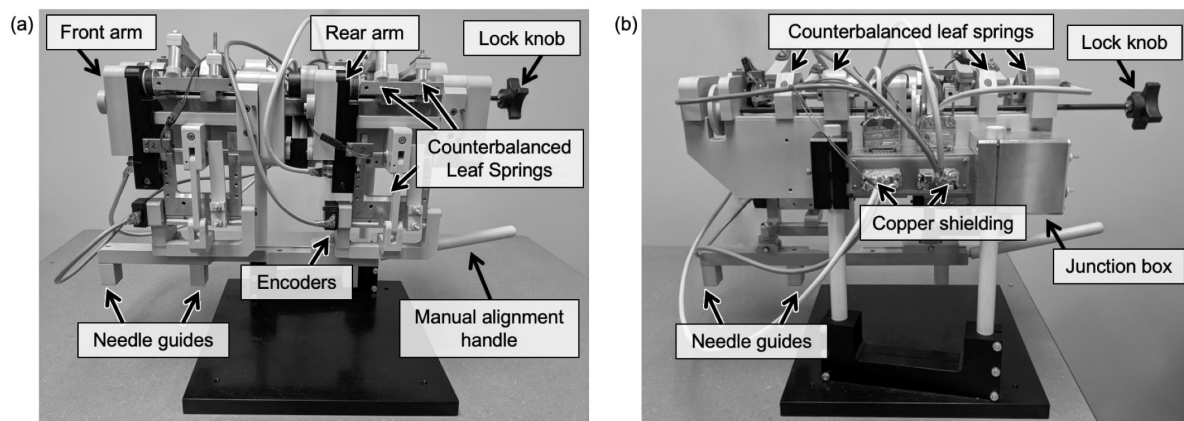


Figure 3.2: (a) Side View. The trajectory of the needle as it passes through the guides is determined by the poses of the front and rear arms. The arms are controlled using piezoelectric motors and the position is measured using optical encoders (two motor/encoder pairs are hidden in the top of the system). Each arm is counterbalanced to aid the motors against gravity. (b) Reverse Side View. The alignment handle and lock knob allow for manual positioning and locking of the needle guides. Electrical connections are shielded against RF interference using an aluminum junction box and copper tape.

Electrical Components

Each link is actuated using an MR-compatible rotary piezoelectric motor (LR50, PiezoMotor, Uppsala, Sweden), which generates $50 \text{ mN} \cdot \text{m}$ of torque. The speed of the axle rotation is proportional to the frequency of the waveform supplied by the motor controller, which is in the 0–2500 Hz range. These frequencies operate outside of the frequencies used in MR scanners and should not produce appreciable interference, nevertheless, all the signal wires connected to the motors are shielded using grounded aluminum or copper foil.

Each motor is controlled using a PMD101 (PiezoMotor, Uppsala, Sweden) driver, which is capable of stepping the motors in $0.1 \mu\text{rad}$ increments. The four controllers are housed in a metal control box positioned inside the scanner control room. Shielded DB25 connector cables connect the control box with the system's junction box through the waveguides on the scanner room's penetration panel. The controllers function in a closed-loop operation to reach the angles calculated using the inverse kinematic equations without overshoot using quadrature optical encoders to provide the necessary feedback. These encoders output a 5 V square wave containing frequency components that could cause interference with the scanner's RF signals. However, the system should not be in motion during image acquisitions, so the encoder feedback will not be present. To guard against the MR signals corrupting the encoder counts, the signal wires are shielded in the same manner as the motor wires. Furthermore, the encoder counts are saved in software before each acquisition and restored after image acquisition if any corruption has occurred.

User Interface

Custom software running on a computer connected to the control box is responsible for displaying images, collecting operator input, registering coordinate systems (Section 3.2.4), and calculating kinematics (Appendix A). A python module written for 3D Slicer (www.slicer.org) imports images from the MRI computer via FTP transfer. In the module, 3D MRI images of the registration fiducial can be segmented semi-automatically by delineating spheres with a bound-

ing box (Section 3.2.4) and the transform between the system and scanner coordinate systems can be calculated based on the location of the four spheres. Following registration, the module can be used to select two target points on anatomical images for the needle entry and tip. A text-based user interface acts as a liaison to the motor controllers and communicates with each one concurrently via USB interface using the D2XX API (Future Technology Devices International Ltd, Glasgow, United Kingdom). Commands can be issued to move the needle guide to the desired position, read the current position, stop the motors, and park the motors for needle insertion and imaging (parked motors apply braking pressure and save their encoder values). Additionally, the system can be commanded to move to its home position for registration, or to move to a trajectory, which passes through two points (the selected entry point for the needle to penetrate the perineum, and the location of the targeted tumour) identified in the 3D MRI image.

Clinical Workflow Integration

While clinical trials have not yet begun, this section provides context for the intended use of the system. Several papers have previously described the clinical workflow of prostate FLA using a conventional needle template [13, 11, 14]. Before the procedure begins, components that come into direct contact with the patient - the needle templates, needle guide support, and manual alignment handle - are detached and sterilized using ethylene oxide gas. The rest of the system is draped with a sterile plastic sheet to remove it from the sterile field. At the time of the procedure, the system is affixed to the patient table (between where the patient's legs would be) with the registration fiducial (see Fig. 3.5) attached in order to register the system co-ordinates with the MR scanner co-ordinates. Following scanning of the fiducial, it can be detached and the image is loaded into software for processing (Section 3.2.4). The system is then removed from the table so the patient can be positioned head-first and the system is re-affixed in the same spot. During the procedure, the physician selects an entry point for the needle to penetrate the patient's perineum and a target point where the lesion is located, based

on pre-operative plans and intra-operative imaging. The system is used to remotely align the needle guide so that the trajectory of the needle passes through these two points. Once the system is in position, the software parks the motors. New MR images can be acquired any time that the motors are parked. To perform needle insertion, the physician enters the scanner room and locks the system using the manual locking handle, which applies more braking torque than the parked motors alone. A tungsten trocar sheathed inside a PEEK catheter can then be manually advanced through the perineum via holes on the needle template, and the trocar can be freely rotated in case steering is required. The trocar is replaced with a fluid-filled closed-end catheter to confirm placement with imaging and then with a laser fiber in a plastic coaxial cooling sheath for ablation. Depending on the size of the targeted lesion, two or more laser fibers may be required. These can be held in position simultaneously using the extra holes on the needle template.

3.2.2 MRI Compatibility Testing

To be safely used in the MRI environment, our guidance system should not be affected by the electromagnetic fields and degrade the quality of MR images [40]. To verify this criteria, tests were performed in accordance with the American Society for Testing and Materials (ASTM) standards [41]. An ASTM classification of ‘MR conditional’ was sought, which indicates that the system is safe to be used in the MR environment during specific acquisition sequences. The standard stipulates that the system must not cause image distortions or substantial reduction of signal-to-noise ratio (SNR), and must not experience a substantial force, torque, vibration, heating, or electrical interference from the magnetic fields during the chosen sequences. All tests were performed on a 3T MRI scanner (Discovery MR750, GE Healthcare, Chicago, IL) using the sequences described in Table 3.1, which are adapted from the PI-RADS v2 [42] guidelines to verify compatibility with mpMRI.

Table 3.1: Image acquisition parameters for distortion and SNR measurements. A 3T Discovery MR750 scanner by GE Healthcare (Chicago, IL) was used.

Weighting	Pulse Sequence	FOV (mm ²)	Matrix (pixels ²)	Slice Thickness (mm)	T _R (ms)	T _E (ms)	Flip Angle (°)
T1	GRE	140x140	256x256	3.0	100	4	30
T2	FSE	180x180	256x256	3.0	3000	90	90
DWI	FSE EPI	180x180	256x256	3.0	3000	90	90

Effects of MRI on System

With any object introduced into the MR environment, there is a concern for interaction with the strong magnetic gradients, which are present. Although our system is constructed entirely from non-ferromagnetic materials to limit such interactions, compliance testing was still performed to protect the patient and operator safety and to ensure that the system will still function properly. The ASTM standard for magnetically induced force [43] is that it should be less than the force on the system due to gravity, and the torque [44] should be less than the product of the system's length along the longest dimension and the force on the system due to gravity. These standards were developed for passive medical implants, which are sufficiently stringent for our system since it will only be used external to the body and touching the surface of the skin at most. Since the device will always be used in the same orientation relative to the scanner bore, with the needle guide parallel to the bore, all tests were performed in this orientation.

The ASTM Low Friction Surface Method [44] was used to verify that induced force and torque were within the required bounds. An acrylic sheet with markings to outline the base of the system was selected as the low friction surface. The angle of repose was measured by placing the system on the sheet outside of the MR environment and slowly lifting one side of the sheet until the system began sliding due to gravity. The coefficient of static friction can be calculated using

$$\mu = \tan \theta \quad (3.1)$$

where θ is the angle between the sheet and the level surface of the tabletop. Next, the system was placed on the sheet inside the scanner bore at an orientation and distance from the isocenter representative of the intended use scenario. After completing the image acquisition sequence, the position of the system was compared with the markings on the sheet to check for any displacement or rotation. The test was considered a success if no motion was detected, and the induced force was bounded by

$$F_{\text{magnetic}} < \mu mg \quad (3.2)$$

where m is the mass of the system and g is the acceleration due to gravity. The induced torque is bounded by

$$\tau_{\text{magnetic}} < L\mu mg \quad (3.3)$$

where L is the length of the system along its longest dimension. If any sliding of the system's base over the sheet is detected, then the test is a failure and modifications to the system would be required.

Induced heating was monitored using an infrared thermometer to measure the temperature of system surfaces before and after image acquisitions. Electrical interference was assessed by comparing encoder counts before and after image acquisitions, and ensuring that motor controllers still functioned normally after the acquisition.

Effects of System on Images

The ASTM standard test was performed to evaluate the degradation of the MR image quality due our guidance system [45]. Axial and coronal T1- and T2-weighted images of a fluid-filled (1% by volume aqueous solution of a gadolinium-based contrast agent (Gadovist, 1.0 mmol/mL)) grid phantom at the scanner's isocenter were acquired in four scenarios with increasing likelihood of decreased image quality:

1. No system present (baseline).
2. The system present at a typical distance from the isocenter (10 cm), but not connected or powered.
3. The system present and connected, but not powered.
4. The system present, connected, and powered.

The mechatronic system was always placed in its orientation of normal use. To maximize the effects of image distortion, a low bandwidth (195 Hz/pixel) was used for each scan. Distortion was assessed using a qualitative visual inspection of subtraction images between the baseline and other three scenarios, and by measuring the dimensions of the phantom ten times in each image and comparing the means using an unpaired *t*-test.

The in-bore effects of the guidance system on MR image SNR were evaluated according to the National Electrical Manufacturers Association (NEMA) standard [46]. Axial images were acquired in the same four scenarios listed above using a high bandwidth (977 Hz/pixel). The signal was determined by measuring the mean voxel intensity in a $30 \times 30 \times 10$ voxel subregion near the middle of the images where fluid was present. The noise was determined by measuring the standard deviation of voxel intensities in an identically-sized subregion outside the phantom and multiplying by a correction factor of 1.5 to approximate a Gaussian distribution from the magnitude image [46].

3.2.3 Open-air Targeting Accuracy

Prior to testing the system in an MR environment for MR image-guidance and tracking, its ability to reach virtual target positions and trajectory accuracy in free space was first determined. Three-dimensional (3D) position measurements were performed using an optical tracking system (Polaris Vicra, Northern Digital Inc., Ontario, Canada), which employs stereo infrared cameras and an illuminator (Fig. 3.4(a)) to calculate the position of the tip of a stylus outfitted

with three non-collinear infrared-reflective spheres (Fig. 3.4(b)) with a volumetric RMS accuracy of 0.25 mm over its usable workspace [47]. Each measurement was made by using one hand to hold the stylus in place until at least 40 image frames of measurement were recorded (2 sec duration at 20 frames per second) by the optical tracker. The mean 3D position across 40 frames was used as the actual measurement.

Registration of Mechatronic System and Optical Tracker Coordinate Systems

The transformation between the optical tracker coordinate system and the mechatronic system coordinate system was computed using a stylus to trace a plane, a line, and a point on three faces of the largest plastic component of the needle guidance device (see Fig. 3.3), parallel with its axes, and collecting them into the sets P_{plane} , P_{line} , and P_{point} with centroids c_{plane} , c_{line} , and c_{point} respectively. These sets were used to reconstruct the system's coordinate system $(\hat{x}_d, \hat{y}_d, \hat{z}_d)$ as follows. The singular value decomposition (SVD) operation of an $m \times n$ matrix M provides the eigenvalues and eigenvectors in the form

$$M = U\Sigma V^T \quad (3.4)$$

Σ is an $m \times n$ diagonal matrix where the diagonal elements are the non-negative real singular values (eigenvalues) of M , U contains the left-singular vectors of M and V contains the right singular vectors (eigenvectors) of M . By filling the rows of M with the elements of $P_{plane} - c_{plane}$, the best fit for the normal to the plane is contained in the right singular vector corresponding to the smallest singular value. This normal to the plane was used as \hat{x}_d . Next, the direction vector (\hat{z}'_d) of the line was fitted by similarly filling the rows of M with the elements of $P_{line} - c_{line}$ and selecting the right singular vector corresponding to the largest singular value. Then, \hat{y}_d and \hat{z}_d were calculated using the vector cross product as

$$\hat{y}_d = \hat{z}'_d \times \hat{x}_d, \quad \hat{z}_d = \hat{x}_d \times \hat{y}_d \quad (3.5)$$

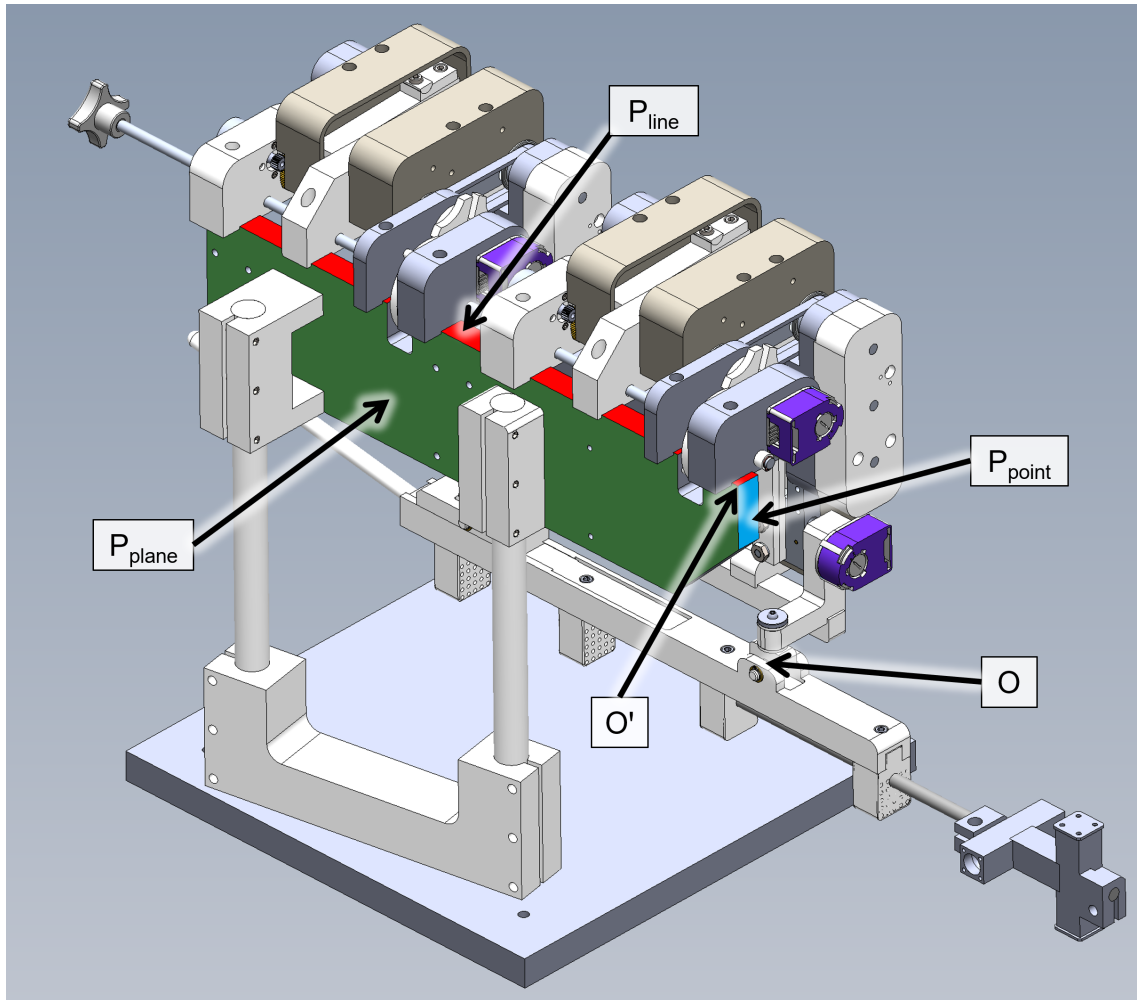


Figure 3.3: Three orthogonal surfaces used for registering the system with the optical tracker's coordinate system. Points for the set P_{plane} were collected by tracing the stylus over the green surface, P_{line} was collected from the red surface, and P_{point} was collected from the blue surface. The three surfaces intersect at the point O' , which is a fixed displacement from the system's origin at O .

Three planar equations were generated by solving for d' in the equation

$$\begin{bmatrix} \hat{x}_d \cdot c_{plane} \\ \hat{y}_d \cdot c_{line} \\ \hat{z}_d \cdot c_{point} \end{bmatrix} + \begin{bmatrix} d'_1 \\ d'_2 \\ d'_3 \end{bmatrix} = \begin{bmatrix} 0 \\ 0 \\ 0 \end{bmatrix}$$

The point O' at which the three planes intersect was determined by solving the linear system

$$\begin{bmatrix} \hat{x}_d \\ \hat{y}_d \\ \hat{z}_d \end{bmatrix} \begin{bmatrix} O'_1 \\ O'_2 \\ O'_3 \end{bmatrix} = \begin{bmatrix} d'_1 \\ d'_2 \\ d'_3 \end{bmatrix} \quad (3.6)$$

O' was then translated a fixed distance based on the system geometry to the origin O at the end of the front arm, which was used in Eq. 3.6 to calculate d to shift the three planes to the system's origin. This way, transforming a point $P_{tracker}$ from the optical tracker's coordinate system to the system's coordinate system was performed using

$$P_{system} = \begin{bmatrix} \hat{x}_d \\ \hat{y}_d \\ \hat{z}_d \end{bmatrix} \begin{bmatrix} P_{tracker,1} \\ P_{tracker,2} \\ P_{tracker,3} \end{bmatrix} + \begin{bmatrix} d_1 \\ d_2 \\ d_3 \end{bmatrix} \quad (3.7)$$

which represents the orthogonal distance from $P_{tracker}$ to each of the three planes of the system's coordinate system.

Needle Guidance Accuracy Evaluation

A regular virtual 5×5 grid of points in space with 7.5 mm separation was created to cover the 2D plane of motion for the front arm. On the plane of motion of the rear arm, one virtual point was placed at each corner (15 mm horizontally and vertically from the center) of the arm's range of motion and a fifth point was placed in the center. Each combination of points for the front and rear arm generated 125 different trajectories for the needle guide, covering the

system's range of motion. For each trajectory, the required angle of the motors was calculated using the inverse kinematics of the system and the desired position of the needle tip, and the direction of the needle was calculated using the forward kinematics (see Appendix A).

The actual position and direction of the needle guide was measured as the line of best fit between four lines through the templates. This was accomplished by inserting the tip of the optical tracker's stylus into the four corner holes on three of the templates. Let $P^{i,j}$ be the set of points collected at hole $i = 1, 2, 3, 4$ on template $j = 1, 2, 3$, then the centroid c^i is calculated for each set of roughly co-linear points $\{P^{i,1}, P^{i,2}, P^{i,3}\}$ along a line of holes in the template. Each line is shifted to the same origin and collected into the superset $P = \{P^{i,j} - c^i \mid i = 1, 2, 3, 4 \text{ and } j = 1, 2, 3\}$. Using the SVD method described in Section 3.2.3 by filling the rows of M with the elements of P , the direction of the line \mathbf{v}'_{needle} is fitted as the right singular vector corresponding to the largest singular value. The position of the line p'_{needle} was taken as the average of the four centroids c^i .

Before measuring the targeting error, the bias in the system was first removed using measurements made on 85 of the trajectories. The inverse kinematics Eqs. A.6 and A.7 were used to calculate the positions of the end effectors of the front and rear arms. The error was calculated as the x- and y- displacement between the expected and measured positions of the end effectors. The components of error were plotted against the expected x and y positions of the end effectors, and four 3D planes were fit to the data using linear regression to model the bias. Since the bias is a constant and predictable error due to factors such as manufacturing variations, it can be compensated for by adjusting the target points based on the bias model. In the system control software, the bias for each arm was calculated as the elevation of the plane at the desired position and was subtracted.

For the remaining 40 trajectories, the measured trajectory of the needle guide was compared with the expected trajectory \mathbf{v}_{needle} and p_{needle} as calculated using the forward kinematics equations. Both positions were projected along the direction vector to a typical prostate FLA insertion depth of 10 cm from the front of the needle guide. The following error metrics are

based on those used by Cepek *et al.* [27]. The needle guidance error of each trajectory was defined as the Euclidean distance between the expected and measured positions of the virtual needle tip.

$$E_{openair} = \|p_{needle} - p'_{needle}\| \quad (3.8)$$

The one-sided 95% prediction interval of $E_{openair}$ was calculated to provide an upper limit for the needle tip targeting error in 95% of cases. The angular error was defined as the angle between the expected direction of the needle and the measured direction

$$A_{openair} = \arccos \frac{\mathbf{v}_{needle} \cdot \mathbf{v}'_{needle}}{\|\mathbf{v}_{needle}\| * \|\mathbf{v}'_{needle}\|} \quad (3.9)$$

The standard error of measurements made using the optical tracker was estimated as follows. Let P_i be a set of j points collected from a single template hole with centroid c_i . The variation of all points measured using the optical tracker was collected into a single set

$$P = \{\|P_{i,j} - c_i\| \mid \forall i, \forall j\} \quad (3.10)$$

Let s be the standard deviation of P , then the standard error was then estimated as

$$SE = \frac{s}{\sqrt{40}} \quad (3.11)$$

3.2.4 MRI Targeting Accuracy

Targeting accuracy of the system in the MR environment can be degraded due to MR image distortion and registration errors. To test the errors of the system's needle guide using MR imaging, a fiducial attachment was affixed to the front of the system, which housed four MR-visible spheres with an interior reservoir volume of 0.64 cm^3 each (Fig. 3.5), each filled with a 1% by volume aqueous solution of a gadolinium-based contrast agent (Gadovist, 1.0

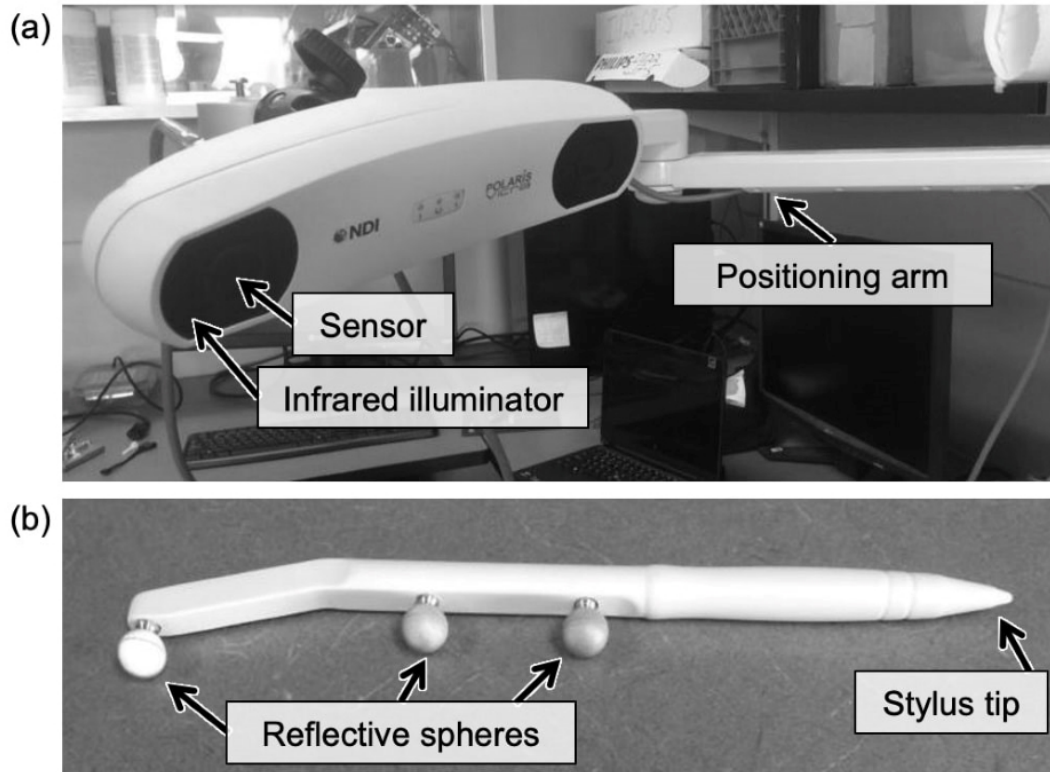


Figure 3.4: NDI Medical Polaris Vicra Optical Tracking System. (a) Arrangement of stereo cameras tuned to the same infrared frequency emitted by the infrared illuminator. (b) Tracking stylus contains three reflective spheres. The position of the tip can be calculated based on the tracked positions of the spheres and the known geometry of the stylus, as long as all three spheres are facing both cameras and are not occluded.

mmol/mL). Two of the spheres were separated vertically by 5.0 cm and two were separated horizontally by 5.0 cm. The spheres were localized using three gradient echo (GRE) images using a 3T MRI scanner (Discovery MR750, GE Healthcare, Chicago, IL): two axial images with the phase-encoding direction swapped, and a sagittal image with phase-encoding in the superior-inferior direction. Coordinates were only measured in the phase-encoding direction to reduce distortion due to main field inhomogeneity. The acquisition parameters were: field-of-view 360 mm x 360 mm, matrix dimensions 256 pixels x 256 pixels, slice thickness 3.0 mm, repetition time 270 ms, echo time 4 ms, flip angle 25.00°, bandwidth 195 Hz/px.

To localize each sphere (e.g. Fig. 3.6), the images were filtered using a spherical averaging filter of radius 2 voxels (2.8 mm) to reduce image noise. After selecting a bounding box

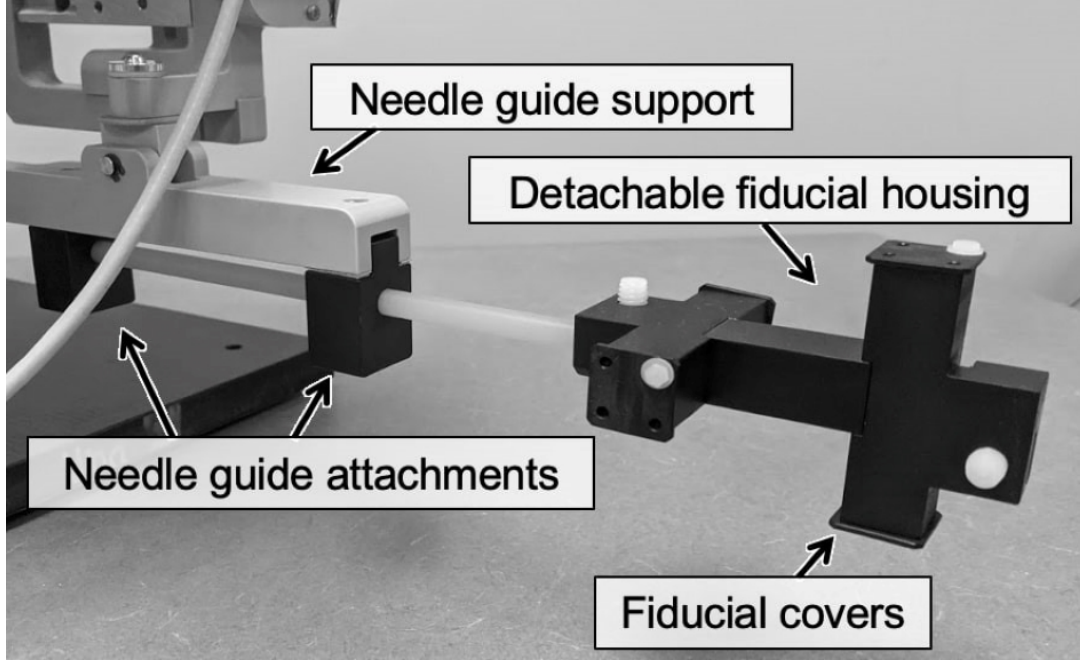


Figure 3.5: Attachable fiducial component containing four MR-visible spheres arranged in two orthogonal lines. The component can be quickly interchanged with the needle templates to perform system registration before procedures.

around a sphere, the region-of-interest (ROI) was thresholded such that the volume of the voxels remaining after thresholding matched the known volume of fluid inside the sphere. The intensity-weighted centroid after thresholding was then calculated as:

$$c = \frac{\sum_{i=1}^l \sum_{j=1}^m \sum_{k=1}^n I(i, j, k) * f(i, j, k)}{\sum_{i=1}^l \sum_{j=1}^m \sum_{k=1}^n I(i, j, k)} \quad (3.12)$$

where l , m , and n are the dimensions of the ROI, $I(i, j, k)$ is the intensity of the voxel at index (i, j, k) , and $f(i, j, k)$ is a function which maps the voxel index to a coordinate in the patient space using the acquisition parameters. The x -coordinate of c was obtained from the axial image with phase-encoding in the left-right direction, the y -coordinate from the axial image with phase-encoding in the anterior-posterior direction, and the z -coordinate from the sagittal image.

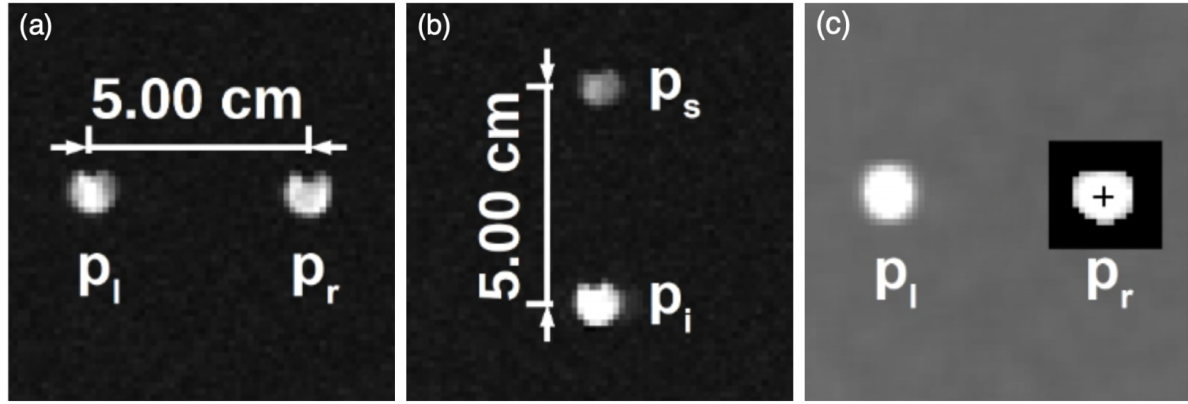


Figure 3.6: Axial gradient-echo image of fluid-filled spheres used in the attachable registration fiducial. (a) Original image of horizontal fiducials. (b) Original image of vertical fiducials. (c) Filtered image with the region of interest thresholded. Localized centroid delineated by a cross.

Registration of Mechatronic System and Scanner Coordinate Systems

Due to the variation in patient size and positions, MR landmark positions, and the need to remove the system from the scanner bore between procedures, a quick, accurate, and robust method for registration of the system coordinate system to the MR image coordinate system is required. This was accomplished by acquiring three images of the fiducial arrangement in the system's "base" pose (see Appendix A) and using the locations of the four spheres to construct the system's axes as

$$\hat{x}_d = \frac{p_r - p_l}{\|p_r - p_l\|} \quad (3.13a)$$

$$\hat{z}_d = \frac{(p_a - p_p) \times \hat{x}_d}{\|(p_a - p_p) \times \hat{x}_d\|} \quad (3.13b)$$

$$\hat{y}_d = \hat{x}_d \times \hat{z}_d \quad (3.13c)$$

where p_l , p_r , p_a , p_p are respectively the centroids of the leftmost, rightmost, most anterior, and most posterior fiducials in the images. To find the origin, the point O' was calculated as the intersection of the line $p_r - p_l$ and the line along \hat{z}_d which intersects both $p_r - p_l$ and $p_s - p_i$ by solving

$$p_l + t * \hat{x}_d = O' \quad (3.14a)$$

$$p_i + u * \hat{y}_d = O' + v * \hat{z}_d \quad (3.14b)$$

Since the distance from O' to origin of the device's coordinate system was known, O was found by translating O' by this distance along \hat{z}_d and was used in Eq. 3.6 to find d . Points in the scanner's coordinate system were translated to the system's coordinate system using Eq. 3.7.

Needle Guidance Accuracy Testing

The system's ability to reach a virtual target position with a planned trajectory in the scanner bore was determined using 25 of the trajectories defined in Section 3.2.3, selected to cover the system's entire range of motion. The trajectory of the needle guide measured on the GRE images is defined as

$$t^n = p^n + \hat{v}^n s \quad (3.15)$$

where p^n is calculated using the same method as O' in Eq. 3.14 and \hat{v}^n is calculated using the same method as \hat{z}_d in Eq. 3.13b. Let the desired needle trajectory be denoted by $t^d = p^d + \hat{v}^d s$ where p^d is the virtual target point for the needle tip at a depth of 10 cm from the front of the needle guide and let $t^k = p^k + \hat{v}^k s$ be the trajectory of the needle guide calculated using the forward kinematics with the joint angles measured using the encoders, where p^k has also been projected to a depth of 10 cm. Since needle insertion is accomplished manually by the physician and targeting errors in the insertion direction can be corrected by withdrawing or advancing the needle without requiring reinsertion, needle guidance error was calculated as the shortest distance from the needle axis to the target point. Let the error function be

$$E(p, t) = |(p - p') - \hat{v} * [(p - p') \cdot \hat{v}]| \quad (3.16)$$

where p is the desired point and $t = p' + \hat{v}s$ is the measured trajectory. Three errors were measured: first, the total error from the target point to the needle trajectory

$$E_{total} = E(p^d, t^n) \quad (3.17)$$

Second, the error from the desired point to the trajectory calculated using the encoder values

$$E_{encoder} = E(p^d, t^k) \quad (3.18)$$

Third, the error from the needle tip point calculated using encoder values to the needle trajectory measured on MRI

$$E_{MRI} = E(p^k, t^n) \quad (3.19)$$

The one-sided 95% prediction interval of each error was also calculated. The angular error was measured between the desired direction of the needle and the measured direction

$$A_{total} = \arccos \frac{\mathbf{v}^n \cdot \mathbf{v}^d}{\|\mathbf{v}^n\| * \|\mathbf{v}^d\|} \quad (3.20)$$

3.3 Results

3.3.1 MRI Compatibility

No appreciable heating above ambient temperatures was detected. The angle of repose on the low friction surface was 9.5° , which corresponds to a coefficient of static friction of 0.17 (Eq. 3.1). No motion of the system relative to the low friction surface occurred during magnetic pulse sequences, therefore the magnetically induced torque was less than 9.25 Nm and the induced force was less than 16.67 N. Electronic interference was detected in the form of randomly incrementing or decrementing encoder counts, up to hundreds of counts per acquisition,

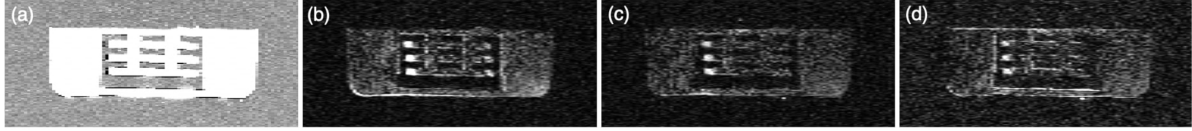


Figure 3.7: Low bandwidth (195 Hz/pixel) T1w gradient-echo images acquired during the distortion test. Absolute difference images (b)-(d) are subtracted from baseline image (a). (a) System absent. (b) System present. (c) System connected. (d) System powered. The window of intensities for each image has a range of 1,000.

during pulse sequences, but the motor controllers otherwise functioned normally during and after the sequences.

Results of the distortion test are shown in Table 3.2. Representative difference images from the distortion test are shown in Fig. 3.7. The absolute value difference images reveal no notable distortions due to the presence of the system, which is confirmed by measuring the distance across the dimensions of the phantom. The average dimensions of the phantom differed by no more than 0.17 mm (less than 1 voxel) from baseline (system absent), or at most 0.4% of the total length. None of the mean dimensions in the presence of the system differed significantly ($p < 0.05$) from the baseline mean dimensions. Table 3.3 summarizes the results of the signal-to-noise ratio test. In the worst case, with the system present and powered, the SNR decreased by 9.25% compared with the baseline in the T1-weighted image.

Table 3.2: Summary of distortion measurements. Voxel dimensions $1.17 \text{ mm} \times 1.17 \text{ mm} \times 0.94 \text{ mm}$ in the T1w image and $1.17 \text{ mm} \times 1.17 \text{ mm} \times 0.94 \text{ mm}$ in the T2w and DWI images.

Sequence	System Status	Width (mm)		Depth (mm)		Height (mm)	
		Mean	SD	Mean	SD	Mean	SD
T1w	Absent	68.27	0.24	76.44	0.23	38.36	0.23
	Present, Unconnected	68.26	0.16	76.45	0.22	38.38	0.18
	Present, Connected	68.27	0.32	76.45	0.37	38.29	0.36
	Present, Powered	68.28	0.27	76.52	0.29	38.37	0.45
T2w	Absent	68.25	0.17	76.25	0.17	38.46	0.17
	Present, Unconnected	68.17	0.23	76.14	0.25	38.43	0.20
	Present, Connected	68.28	0.23	76.27	0.21	38.29	0.29
	Present, Powered	68.25	0.21	76.08	0.21	38.34	0.38

Table 3.3: Summary of SNR measurements.

Sequence		System Status			
		Absent	Present, Unconnected	Present, Connected	Present, Powered
T1w	SNR (dB)	22.11	21.81	21.76	20.07
	Change (%)	-	-1.39	-1.58	-9.25
T2w	SNR (dB)	25.32	25.09	25.01	24.54
	Change (%)	-	-0.92	-1.23	-3.09

3.3.2 Open Air Accuracy

After calibrating the front and rear arms to remove biases (see Fig. 3.8 for an example bias model), the mean positioning error of the virtual needle tip at a depth of 10 cm was 0.80 ± 0.36 mm with a one-sided 95% prediction interval of 1.40 mm. The scatter plot of the vertical and horizontal components of needle positioning error is given on a Cartesian axis in Fig. 3.9, alongside the cumulative distribution function of $E_{openair}$, which represents the percentage of needle tip positioning errors below a given value. The median positioning error was 0.83 mm and 67.5% of the errors were less than 1.0 mm. The mean angular error in the shaft of the virtual needle was $0.14 \pm 0.06^\circ$ with the cumulative distribution function shown in Fig. 3.10. The standard error of measurements made using the optical tracking system was estimated to be 0.016 mm using Eq. 3.11.

3.3.3 Needle Guidance Error in the MRI Bore

In the MR bore, the mean targeting error of the virtual needle at the tip (Eq. 3.17) was $E_{total} = 2.11 \pm 1.05$ mm, with a one-sided 95% prediction interval of 3.84 mm. The scatter plot and cumulative distribution function of the targeting error is shown in Figure 3.11. The mean of the left-right error was not statistically significantly different from zero ($p = 0.68$) according to a one-sample t -test, but the anterior-posterior mean error was statistically significantly different from zero ($p = 0.04$), with a 95% confidence interval of 0.03 to 1.48. The mean error due to

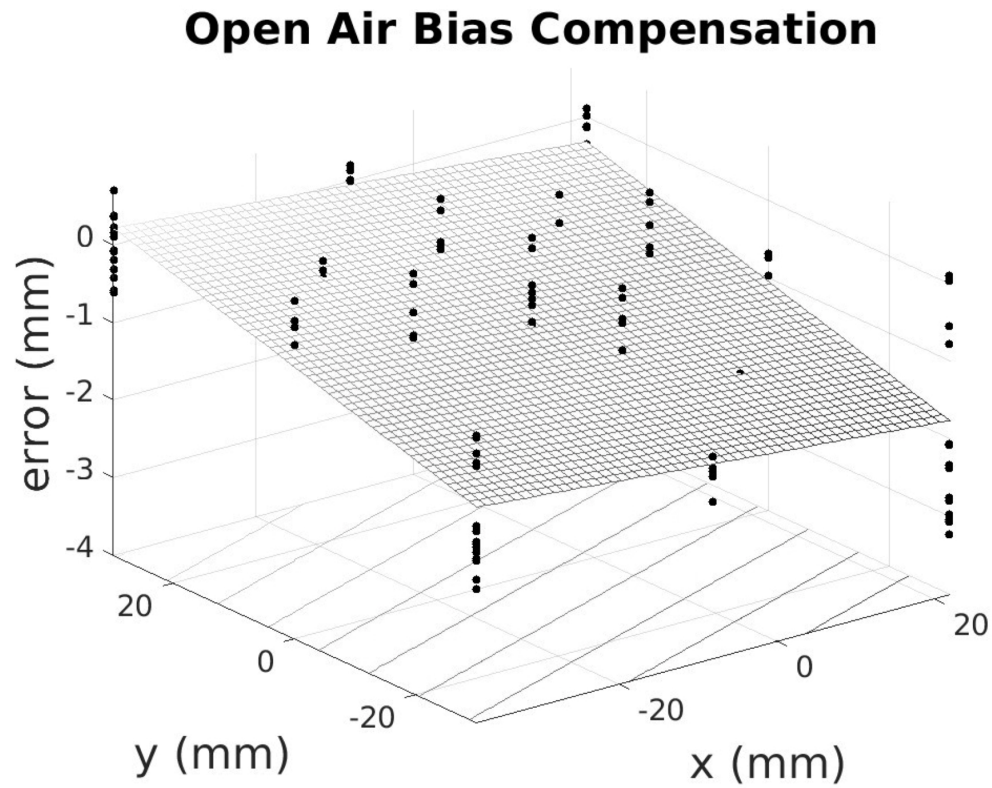


Figure 3.8: 3D plane fitted to the horizontal component of error in the position of the front arm generated from the set of 85 trajectories used for bias compensation. The equation of the plane along with a plane similarly fitted to the vertical component of error was used to determine and compensate for the systematic bias present in the system. The same procedure was used to compensate for bias in the rear arm.

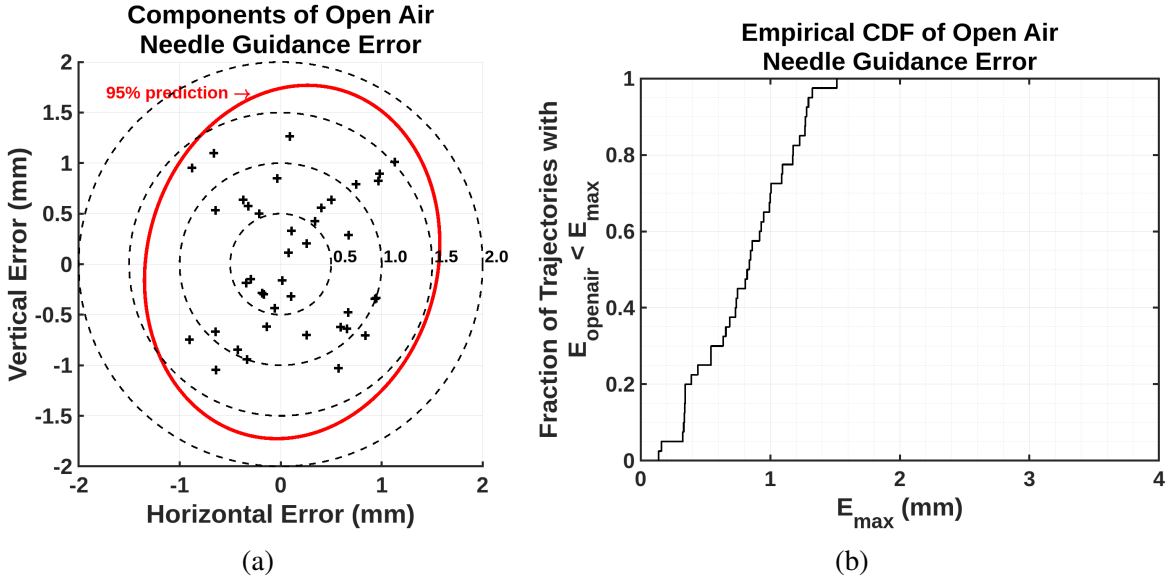


Figure 3.9: Targeting error from open-air experiment measured using 40 trajectories. (a) Components of the error separated into horizontal and vertical directions, where the origin corresponds to the target point for each trajectory at a depth of 10 cm calculated using the forward kinematics. Dashed circles are shown to indicate error magnitudes of 0.5, 1.0, and 1.5 mm. (b) Cumulative distribution of targeting error, representing the percentage of trajectories with the error less than E_{max} .

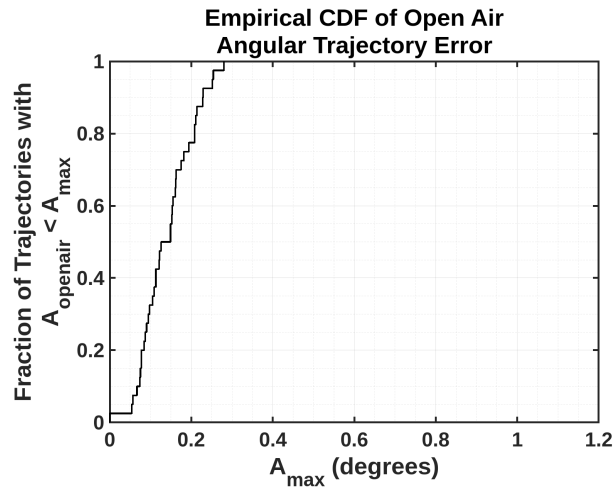


Figure 3.10: Cumulative distribution of angular error from an open-air experiment on 40 trajectories, representing the percentage of trajectories with the error less than A_{max} .

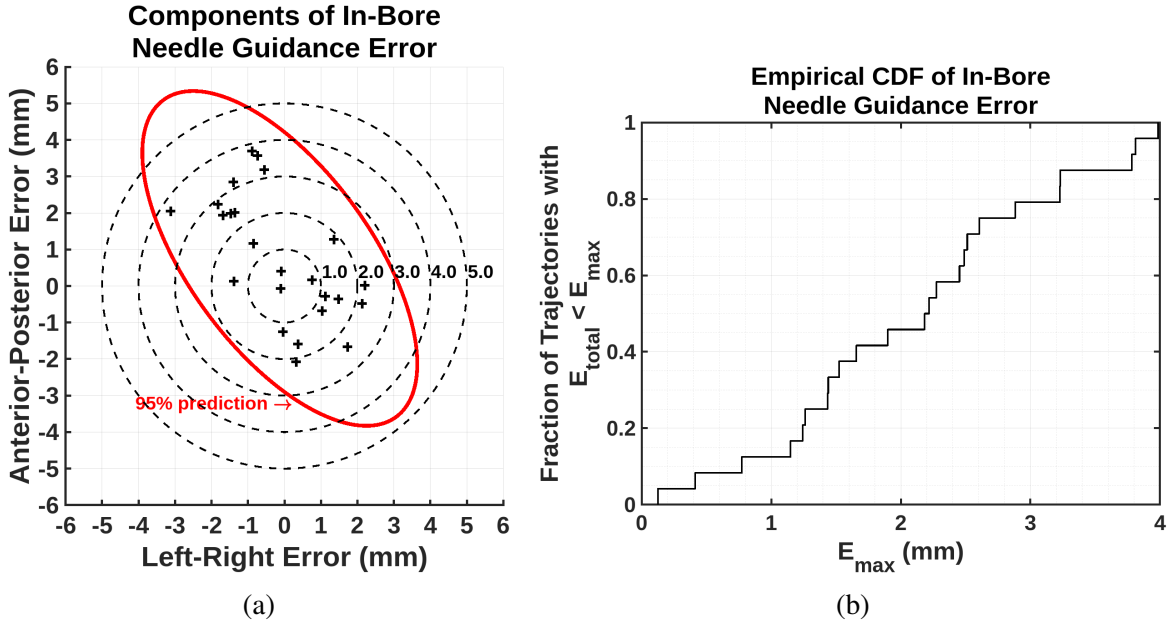


Figure 3.11: Targeting error from MRI virtual targeting experiment using 25 trajectories. a) Components of error separated into left-right and superior-inferior directions, where the origin corresponds to the target point for each trajectory at a depth of 10 cm calculated using the forward kinematics. Dashed circles are shown to indicate error magnitudes of 0.5, 1.0, and 1.5 mm. b) Cumulative distribution of targeting error, representing the percentage of trajectories with error less than E_{max} .

positioning of the motors (Eq. 3.18) was $E_{encoder} = 0.14 \pm 0.06$ mm, and the mean error between the kinematics calculated using the encoder values and the measured position of the needle guide (Eq. 3.19) was $E_{MRI} = 2.18 \pm 1.06$ mm. The mean angular error between the desired trajectory and measured trajectory of the needle guide (Eq. 3.20) was $A_{total} = 0.49 \pm 0.26^\circ$, the cumulative distribution of which is shown in Figure 3.12.

3.4 Discussion

Based on the results of the MRI compatibility tests, our image-guided interventional device is ‘MR-conditional’ [41], confirming safe use while a patient would occupy the scanner bore with the mpMRI imaging protocols tested in this study. Our results showed that no appreciable heating, force, torque, or image distortion was induced. The subtraction images did not indicate any susceptibility artifacts (i.e., local variations in voxel intensity) or artifacts due to induced

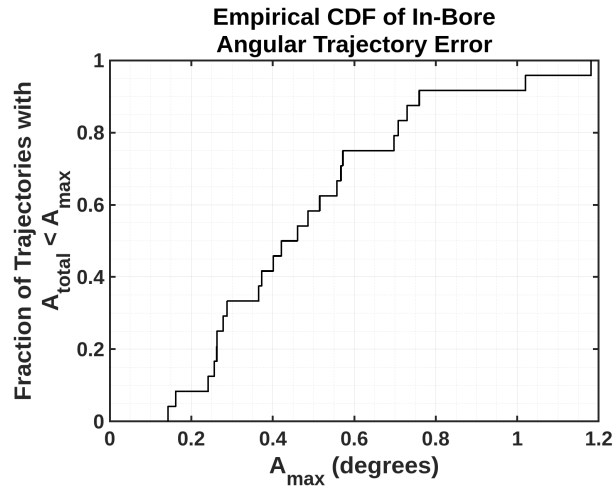


Figure 3.12: Cumulative distribution of angular error from MRI virtual targeting experiment on 25 trajectories, representing the percentage of trajectories with error less than A_{\max} .

inhomogeneity in the magnetic field (e.g., spatial distortion, banding, or blurring). Changes in susceptibility were likely localized around the metal components of the system outside of the imaging field-of-view. SNR reduction was non-negligible at 9.25% in the T1-weighted image while the system was powered, which was likely caused by the presence of the system inducing inhomogeneity in the main magnetic field; however, this can be mitigated by turning off the motor controllers during image acquisitions, which will limit the SNR reduction to 1.58% in T1-weighted images and 1.23% in T2-weighted images. Engaging the locking mechanism during imaging will ensure that no motion of the arms occurs while the system is not powered. Furthermore, the count of each encoder can be saved prior to image acquisition and restored following, which eliminates the observed interference with the encoder values. Turning off the controllers during imaging is a simple imposition compared with removing the system from the scanner bore, which would require the registration procedure to be performed again, and can be integrated into procedure workflows in a straightforward manner.

In the MR scanner bore, the system was predicted to have a needle guidance error of less than 3.84 mm in 95% of cases in hitting a virtual target at a depth of 10 cm. In the context of focal ablation, this error should be sufficient to completely ablate a targeted region, since a 5 mm margin of healthy tissue is typically also included in the planned ablation region [48].

However, this targeting error neglects the effects of needle deflection as it penetrates tissue. Previous work has quantified error due to needle deflection in tissue-mimicking phantoms as 1.10 mm [27], that increases the error to 3.99 mm when added in quadrature, and possibly higher in prostate tissue, which tends to be inhomogeneous and anisotropic. The error is also sufficiently low for our system to be used to guide needles for prostate biopsies, since the smallest clinically significant radius for a tumour is 5 mm [49, 50] and the total error at the tip did not exceed 5 mm in any of the cases. However, sources of error should still be examined for areas which could be improved, and the effects of needle deflection should be investigated further.

Compared with open-air accuracy, in-bore accuracy includes the effects of fiducial localization, image distortions, and registration error. Since the total open-air targeting error was relatively low (prediction interval of 1.40 mm), these effects had a large impact on in-bore accuracy. Our MR compatibility tests found image distortion to be low and are further mitigated by using measurements in the phase-encoding direction only, but fiducial localization is a contributor to registration error. Therefore, inaccurate registration is the most likely cause of high targeting error in our experiments. This is consistent with finding a bias in the anterior-posterior component of error since registration biases will manifest in every trajectory measured. The fiducial arrangement used is susceptible to localization error, since only one fiducial is used to localize the endpoint of each axis. Furthermore, the apparatus must be manually aligned with the system axes, which may also contribute to registration error. Considering this, a more robust registration method using more tracking spheres with wider separation should be investigated. The common z -frame fiducial arrangement was not used for this study as it has been demonstrated to be sensitive to image distortions [51]. Analysis of the bias, by subtracting the means within the confidence interval of 0.03 to 1.48, revealed that it could be contributing as much as 0.5 mm to the prediction interval of the error.

Open-air targeting accuracy is affected by errors in kinematics, manufacturing tolerances, encoder resolution, registration errors with the optical tracking system, and manual leveling of

the system's arms to find the 'home' position. Leveling of the system's arms was suspected to be the major contributor to the bias, which had to be compensated for, since the 'home' position was the starting point for all trajectories. A minor contributor to bias may have been manufacturing tolerances, especially in the upper parallelogram structure of the system, since the kinematics assume the sides of that structure always remain perfectly vertical and a small deviation in the length of any of the sides will cause that assumption to be violated. However, components were manufactured to tolerances of approximately 0.01 mm and thus were not considered a major source of error. Encoder resolution was quantified as $E_{encoder} = 0.14 \pm 0.06$ mm which only explains a small contribution to the error. The standard error of measurements from the optical tracker was estimated to be 0.016 mm which is also a very small contribution to error. Although the angular error appears very low ($0.49 \pm 0.26^\circ$), this results in an average displacement of 1.56 mm when projected out to the needle tip at 10.0 cm and could be caused by misalignment of the system's axes with the MRI or tracker axes.

The system described in this paper was designed as an experimental prototype. The study was limited to virtual evaluation of needle guidance accuracy; however full evaluation will require a clinical trial. Before use with human subjects, a more robust registration system must be implemented, which can be easily integrated into the clinical workflow. Furthermore, the effects of needle deflection should be accounted for by experimenting with needles penetrating tissue-mimicking phantoms in the MR bore.

3.5 Conclusion

An image-guided mechatronic trajectory alignment system for delivering needles to prostate lesions during focal therapies in the bore of an MR scanner was designed with remote actuation capabilities. MR-compatibility testing demonstrated no adverse safety risks when using the system in the MR environment, and no degradation of acquired image quality when proper protocols are observed. The mechatronic system was able to align the needle guide to virtual

targets at typical procedure insertion depths with an accuracy of 3.84 mm, within 95% confidence. There is potential to improve this accuracy using a more robust registration method and system ‘homing’ method, which will be investigated in future studies, in addition to phantom trials of needle guidance accuracy to quantify the contributions of needle deflection.

3.6 Acknowledgements

The authors are grateful for the funding support from the Ontario Institute of Cancer Research (OICR), the Canadian Institutes for Health Research (CIHR), and the Natural Sciences and Engineering Research Council of Canada (NSERC).

3.7 Conflict of interest

The authors have no relevant conflicts of interest to disclose.

3.8 Data Availability Statement

The data that support the findings of this study are available from the corresponding author upon reasonable request.

Bibliography

- [1] J. F. Anderson, D. A. Swanson, L. B. Levy, D. A. Kuban, A. K. Lee, R. Kudchadker, J. Phan, T. Bruno, and S. J. Frank, “Urinary Side Effects and Complications After Permanent Prostate Brachytherapy: The MD Anderson Cancer Center Experience,” *Urology*, vol. 74, no. 3, pp. 601–605, 2009.
- [2] A. U. Frey, J. Sønksen, and M. Fode, “Neglected side effects after radical prostatectomy: A systematic review,” *The Journal of Sexual Medicine*, vol. 11, no. 2, pp. 374–385, 2014.
- [3] J. Hugosson, J. Stranne, and S. V. Carlsson, “Radical retropubic prostatectomy: A review of outcomes and side-effects,” *Acta Oncologica*, vol. 50, no. SUPPL. 1, pp. 92–97, 2011.
- [4] N. N. Stone and R. G. Stock, “Complications following permanent prostate brachytherapy,” *European Urology*, vol. 41, no. 4, pp. 427–433, 2002.
- [5] L. Klotz, L. Zhang, A. Lam, R. Nam, A. Mamedov, and A. Loblaw, “Clinical results of long-term follow-up of a large, active surveillance cohort with localized prostate cancer,” *Journal of Clinical Oncology : Official Journal of the American Society of Clinical Oncology*, vol. 28, pp. 126–31, jan 2010.
- [6] F. Fang, N. L. Keating, L. A. Mucci, H.-O. Adami, M. J. Stampfer, U. Valdimarsdóttir, and K. Fall, “Immediate risk of suicide and cardiovascular death after a prostate cancer diagnosis: cohort study in the United States,” *Journal of the National Cancer Institute*, vol. 102, pp. 307–314, mar 2010.
- [7] H. U. Ahmed, L. Dickinson, S. Charman, S. Weir, N. McCartan, R. G. Hindley, A. Freeman, A. P. Kirkham, M. Sahu, R. Scott, C. Allen, J. Van der Meulen, and M. Emberton, “Focal Ablation Targeted to the Index Lesion in Multifocal Localised Prostate Cancer: a Prospective Development Study,” *European urology*, vol. 68, pp. 927–936, dec 2015.
- [8] H. U. Ahmed, “The index lesion and the origin of prostate cancer,” *New England Journal of Medicine*, vol. 361, no. 17, pp. 1704–1706, 2009.
- [9] S. Natarajan, S. Raman, A. M. Priester, J. Garritano, D. J. Margolis, P. Lieu, M. L. Macairan, J. Huang, W. Grundfest, and L. S. Marks, “Focal Laser Ablation of Prostate Cancer: Phase I Clinical Trial,” *Journal of Urology*, vol. 196, no. 1, pp. 68–75, 2016.
- [10] U. Lindner, N. Lawrentschuk, R. A. Weersink, S. R. H. Davidson, O. Raz, E. Hlasny, D. L. Langer, M. R. Gertner, T. Van der Kwast, M. A. Haider, and J. Trachtenberg, “Focal laser ablation for prostate cancer followed by radical prostatectomy: validation of focal therapy and imaging accuracy,” *European Urology*, vol. 57, no. 6, pp. 1111–1114, 2010.
- [11] O. Raz, M. A. Haider, S. R. H. Davidson, U. Lindner, E. Hlasny, R. A. Weersink, M. R. Gertner, W. Kucharczyk, S. A. McCluskey, and J. Trachtenberg, “Real-time magnetic resonance imaging-guided focal laser therapy in patients with low-risk prostate cancer,” *European Urology*, vol. 58, no. 1, pp. 173–177, 2010.

- [12] S. E. Eggener, A. Yousuf, S. Watson, S. Wang, and A. Oto, "Phase II evaluation of magnetic resonance imaging guided focal laser ablation of prostate cancer," *Journal of Urology*, vol. 196, no. 6, pp. 1670–1675, 2016.
- [13] U. Lindner, R. A. Weersink, M. A. Haider, M. R. Gertner, S. R. H. Davidson, M. Atri, B. Wilson, A. Fenster, and J. Trachtenberg, "Image guided photothermal focal therapy for localized prostate cancer: phase I trial," *The Journal of Urology*, vol. 182, no. 4, pp. 1371–1377, 2009.
- [14] A. Oto, I. Sethi, G. Karczmar, R. J. McNichols, M. K. Ivancevic, W. M. Stadler, S. Watson, and S. E. Eggener, "MR imaging-guided focal laser ablation for prostate cancer: phase I trial," *Radiology*, vol. 267, pp. 932–940, June 2013.
- [15] Ö. Algan, G. E. Hanks, and A. H. Shaer, "Localization of the prostatic apex for radiation treatment planning," *International Journal of Radiation Oncology, Biology, Physics*, vol. 33, no. 4, pp. 925–930, 1995.
- [16] P. Kozlowski, S. D. Chang, R. Meng, B. Mädler, R. Bell, E. C. Jones, and S. L. Goldenberg, "Combined prostate diffusion tensor imaging and dynamic contrast enhanced MRI at 3T—quantitative correlation with biopsy.," *Magnetic Resonance Imaging*, vol. 28, pp. 621–8, jun 2010.
- [17] C. M. A. Hoeks, J. J. O. Barentsz, T. Hambrock, D. Yakar, D. M. Somford, S. W. T. P. J. Heijmink, T. W. J. Scheenen, P. C. Vos, H. Huisman, I. M. van Oort, J. A. Witjes, A. Heerschap, and J. J. Fütterer, "Prostate cancer: multiparametric MR imaging for detection, localization, and staging," *Radiology*, vol. 261, no. 1, pp. 46–66, 2011.
- [18] S. Rais-Bahrami, M. M. Siddiqui, B. Turkbey, L. Stamatakis, J. Logan, A. N. Hoang, A. Walton-Diaz, S. Vourganti, H. Truong, J. Kruecker, M. J. Merino, B. J. Wood, P. L. Choyke, and P. A. Pinto, "Utility of multiparametric magnetic resonance imaging suspicion levels for detecting prostate cancer," *Journal of Urology*, vol. 190, no. 5, pp. 1721–1727, 2013.
- [19] R. J. Stafford, A. Shetty, A. M. Elliott, S. A. Klumpp, R. J. McNichols, A. Gowda, J. D. Hazle, and J. F. Ward, "Magnetic resonance guided, focal laser induced interstitial thermal therapy in a canine prostate model.," *The Journal of Urology*, vol. 184, pp. 1514–20, oct 2010.
- [20] A. V. D'Amico, R. Cormack, C. M. Tempany, S. Kumar, G. Topulos, H. M. Kooy, and C. N. Coleman, "Real-time magnetic resonance image-guided interstitial brachytherapy in the treatment of select patients with clinically localized prostate cancer.," *International Journal of Radiation Oncology, Biology, Physics*, vol. 42, no. 3, pp. 507–515, 1998.
- [21] A. V. D'Amico, C. M. Tempany, R. Cormack, N. Hata, M. Jinzaki, K. Tuncali, M. Weinstein, J. P. Richie, and P. Richie, "Transperineal magnetic resonance image guided prostate biopsy.," *The Journal of Urology*, vol. 164, no. 2, pp. 385–387, 2000.

- [22] R. A. Cormack, A. V. D'Amico, N. Hata, S. Silverman, M. Weinstein, and C. M. Tempany, "Feasibility of transperineal prostate biopsy under interventional magnetic resonance guidance," *Urology*, vol. 56, no. 4, pp. 663–664, 2000.
- [23] B. Fei, J. L. Duerk, D. T. Boll, J. S. Lewin, and D. L. Wilson, "Slice-to-volume registration and its potential application to interventional MRI-guided radio-frequency thermal ablation of prostate cancer," *IEEE Transactions on Medical Imaging*, vol. 22, no. 4, pp. 515–525, 2003.
- [24] N. Hata, M. Jinzaki, D. Kacher, R. Cormack, D. Gering, a. Nabavi, S. G. Silverman, a. V. D'Amico, R. Kikinis, F. a. Jolesz, and C. M. Tempany, "MR imaging-guided prostate biopsy with surgical navigation software: device validation and feasibility.," *Radiology*, 2001.
- [25] R. C. Susil, K. Camphausen, P. Choyke, E. R. McVeigh, G. S. Gustafson, H. Ning, R. W. Miller, E. Atalar, C. N. Coleman, and C. Ménard, "System for prostate brachytherapy and biopsy in a standard 1.5 T MRI scanner," *Magnetic Resonance in Medicine*, vol. 52, no. 3, pp. 683–687, 2004.
- [26] C. Ménard, R. C. Susil, P. Choyke, G. S. Gustafson, W. Kammerer, H. Ning, R. W. Miller, K. L. Ullman, N. Sears Crouse, S. Smith, E. Lessard, J. Pouliot, V. Wright, E. McVeigh, C. N. Coleman, and K. Camphausen, "MRI-guided HDR prostate brachytherapy in standard 1.5T scanner," *International Journal of Radiation Oncology Biology Physics*, vol. 59, no. 5, pp. 1414–1423, 2004.
- [27] J. Cepek, B. A. Chronik, U. Lindner, J. Trachtenberg, S. R. H. Davidson, J. Bax, and A. Fenster, "A system for MRI-guided transperineal delivery of needles to the prostate for focal therapy," *Medical Physics*, vol. 40, no. 1, p. 012304, 2013.
- [28] J. Cepek, U. Lindner, S. Ghai, A. S. Louis, S. R. H. Davidson, M. R. Gertner, E. Hlasny, M. S. Sussman, A. Fenster, and J. Trachtenberg, "Mechatronic system for in-bore MRI-guided insertion of needles to the prostate: An in vivo needle guidance accuracy study," *Journal of Magnetic Resonance Imaging*, vol. 42, no. 1, pp. 48–55, 2015.
- [29] S. E. Song, N. B. Cho, G. Fischer, N. Hata, C. Tempany, G. Fichtinger, and I. Iordachita, "Development of a pneumatic robot for MRI-guided transperineal prostate biopsy and brachytherapy: New approaches," in *Proceedings - IEEE International Conference on Robotics and Automation*, (Anchorage, AK, USA), pp. 2580–2585, IEEE, 2010.
- [30] S. P. DiMaio, S. Pieper, K. Chinzei, N. Hata, S. J. Haker, D. F. Kacher, G. Fichtinger, C. M. Tempany, and R. Kikinis, "Robot-assisted needle placement in open MRI: System architecture, integration and validation," *Computer Aided Surgery*, vol. 12, no. 1, pp. 15–24, 2007.
- [31] G. S. Fischer, I. Iordachita, C. Csoma, J. Tokuda, S. P. DiMaio, C. M. Tempany, N. Hata, and G. Fichtinger, "MRI-compatible pneumatic robot for transperineal prostate needle placement," *IEEE/ASME Transactions on Mechatronics*, vol. 13, no. 3, pp. 295–305, 2008.

- [32] M. R. Van Den Bosch, M. R. Moman, M. Van Vulpen, J. J. Battermann, E. Duiveman, L. J. Van Schelven, H. De Leeuw, J. J. Lagendijk, and M. A. Moerland, "MRI-guided robotic system for transperineal prostate interventions: Proof of principle," *Physics in Medicine and Biology*, vol. 55, no. 5, 2010.
- [33] S. Zangos, C. Herzog, K. Eichler, R. Hammerstingl, A. Lukoschek, S. Guthmann, B. Gutmann, U. J. Schoepf, P. Costello, and T. J. Vogl, "MR-compatible assistance system for puncture in a high-field system: device and feasibility of transgluteal biopsies of the prostate gland," *European Radiology*, vol. 17, no. 4, pp. 1118–1124, 2007.
- [34] M. G. Schouten, J. Ansems, W. K. J. Renema, D. Bosboom, T. W. J. Scheenen, and J. J. Fütterer, "The accuracy and safety aspects of a novel robotic needle guide manipulator to perform transrectal prostate biopsies," *Medical Physics*, vol. 37, pp. 4744–4750, sep 2010.
- [35] H. Su, D. C. Cardona, W. Shang, A. Camilo, G. A. Cole, D. C. Rucker, R. J. Webster, and G. S. Fischer, "A MRI-guided concentric tube continuum robot with piezoelectric actuation: A feasibility study," in *Proceedings - IEEE International Conference on Robotics and Automation*, (Saint Paul, MN, USA), pp. 1939–1945, IEEE, 2012.
- [36] A. Krieger, I. Iordachita, S. Song, N. B. Cho, P. Guion, G. Fichtinger, and L. L. Whitcomb, "Development and preliminary evaluation of an actuated MRI-compatible robotic device for MRI-guided prostate intervention," in *2010 IEEE International Conference on Robotics and Automation*, pp. 1066–1073, 2010.
- [37] J. Xiang, H. Yan, J. Li, X. Wang, H. Chen, and X. Zheng, "Transperineal versus transrectal prostate biopsy in the diagnosis of prostate cancer: a systematic review and meta-analysis," *World Journal of Surgical Oncology*, vol. 17, no. 1, p. 31, 2019.
- [38] J. P. Grummet, M. Weerakoon, S. Huang, N. Lawrentschuk, M. Frydenberg, D. A. Moon, M. O'Reilly, and D. Murphy, "Sepsis and 'superbugs': should we favour the transperineal over the transrectal approach for prostate biopsy?," *BJU international*, vol. 114, pp. 384–388, sep 2014.
- [39] A. A. Goldenberg, J. Trachtenberg, Y. Yi, R. Weersink, M. S. Sussman, M. Haider, L. Ma, and W. Kucharczyk, "Robot-assisted MRI-guided prostatic interventions," *Robotica*, vol. 28, no. 2, pp. 215–234, 2010.
- [40] N. Yu, R. Gassert, and R. Riener, "Mutual interferences and design principles for mechatronic devices in magnetic resonance imaging," *International Journal of Computer Assisted Radiology and Surgery*, vol. 6, no. 4, pp. 473–488, 2011.
- [41] T. O. Woods, "MRI Safety and Compatibility of Implants and Medical Devices," in *Stainless Steels for Medical and Surgical Applications* (G. L. Winters and M. J. Nutt, eds.), pp. 82–90, West Conshohocken, PA: ASTM International, jan 2003.
- [42] American College of Radiology, "PI-RADS™ Prostate Imaging – Reporting and Data System, Version 2," tech. rep., American College of Radiology, 2015.

- [43] ASTM International, “ASTM F2052-15, Standard Test Method for Measurement of Magnetically Induced Displacement Force on Medical Devices in the Magnetic Resonance Environment,” tech. rep., ASTM International, West Conshohocken, PA, 2015.
- [44] ASTM International, “ASTM F2213-17, Standard Test Method for Measurement of Magnetically Induced Torque on Medical Devices in the Magnetic Resonance Environment,” tech. rep., ASTM International, West Conshohocken, PA, 2017.
- [45] ASTM International, “ASTM F2119-07(2013), Standard Test Method for Evaluation of MR Image Artifacts from Passive Implants,” tech. rep., ASTM International, West Conshohocken, PA, 2013.
- [46] National Electrical Manufacturers Association, “NEMA Standards Publication MS 1-2008 (R2014): Determination of Signal-to-Noise Ratio (SNR) in Diagnostic Magnetic Resonance Imaging,” tech. rep., NEMA, Rosslyn, VA, 2008.
- [47] NDI Medical, *Medical Polaris Spectra and Vicra*, 2020 (accessed Sept 2, 2020). <https://www.ndigital.com/medical/products/polaris-family/{#}specifications>.
- [48] E. Knull, A. Oto, S. Eggener, D. Tessier, S. Guneyli, A. Chatterjee, and A. Fenster, “Evaluation of tumor coverage after MR-guided prostate focal laser ablation therapy,” *Medical Physics*, vol. 46, pp. 800–810, feb 2019.
- [49] J. I. Epstein, P. C. Walsh, M. Carmichael, and C. B. Brendler, “Pathologic and Clinical Findings to Predict Tumor Extent of Nonpalpable (Stage T1 c) Prostate Cancer,” *JAMA*, vol. 271, pp. 368–374, feb 1994.
- [50] G. Ploussard, J. I. Epstein, R. Montironi, P. R. Carroll, M. Wirth, M.-O. Grimm, A. S. Bjartell, F. Montorsi, S. J. Freedland, A. Erbersdobler, and T. H. van der Kwast, “The Contemporary Concept of Significant Versus Insignificant Prostate Cancer,” *European Urology*, vol. 60, no. 2, pp. 291–303, 2011.
- [51] J. Cepek, B. A. Chronik, and A. Fenster, “The effects of magnetic field distortion on the accuracy of passive device localization frames in MR imaging,” *Medical Physics*, vol. 41, no. 5, p. 052301, 2014.

Chapter 4

Toward Mechatronic MRI-Guided Focal Laser Ablation of the Prostate: Robust Registration for Improved Needle Delivery

4.1 Introduction

Despite recent modifications to screening guidelines to reduce overdiagnosis [1], prostate cancer (PCa) remains the most common non-skin cancer in men in the USA [2]. Although the most prevalent, PCa is the second leading cause of cancer death in men and has a five-year net survival rate of 98% for all stages combined [2]. Many cases, particularly non-life-threatening early-stage cases, which remain low grade and local, would be overtreated if definitive therapies such as radical prostatectomy or radiation therapy were used. These treatments elevate the risk for erectile dysfunction or urinary incontinence [3], causing men to increasingly opt for active surveillance instead [4, 5]. Focal therapies [6, 7, 8, 9, 10, 11, 12] are a compromise between active surveillance and whole gland therapies by retaining some oncologic control with minimal side effects.

Focal laser ablation (FLA) therapy [13, 14, 15, 16, 17, 10] destroys lesions thermally with laser energy delivered via diffuser-tipped needle fibers placed in the center of the lesion. The success of FLA is dependent on proper patient selection criteria [18, 19], diligent treatment planning [19], and accurate needle guidance [20]. Magnetic resonance imaging (MRI) of-

fers several advantages for the guidance of prostate FLA [21] compared with other imaging modalities. Multi-parametric MRI (mpMRI) has demonstrated effectiveness in detecting, staging, and localizing clinically significant PCa [22, 23, 24, 25, 26, 27], and also provides superior contrast and resolution for visualizing surrounding anatomy (important for healthy tissue sparing). MR thermometry [28] enables the generation of temperature maps in near-real-time to monitor temperature changes as the energy applicator is activated [29, 16, 10]. Finally, dynamic contrast-enhanced (DCE) MRI can exploit the immediate devascularization of ablation regions to visualize the extent of tissue destruction [30, 31].

Highly accurate delivery of needles to lesions is critical for the therapeutic success of FLA but guiding needles to prostate targets within the MR environment poses unique challenges. The limited diameter of the scanner bore restricts access to the patient, and strong electromagnetic fields make the use of any ferromagnetic materials hazardous. Furthermore, radio-frequency signals generated for image acquisition may interfere with or receive interference from inadequately shielded electronics in proximity to the scanner. The first MR-guided prostate interventions used an open-bore MRI scanner [32, 33, 34, 35, 36] for easier access to place a traditional fixed-grid needle template between the patient's legs. Other studies [37, 38] used closed-bore MRI scanners to acquire higher resolution images for guidance, but required the patient to be withdrawn from the bore for needle insertion. This increased procedure times and increased the risk of patient motion. A number of groups have implemented pneumatically actuated systems [39, 40, 41, 42, 43, 44], allowing the physician to guide ablation needles from outside the scanner bore without moving the patient. However, pneumatic actuators are difficult to control precisely and require large pumps and tubes. Two systems using piezoelectric (non-magnetic) motors for actuation have been developed. The first system [45] requires a transrectal approach to the prostate which carries a higher risk for complications compared with the transperineal approach [46]. The other system [47] is fully remotely actuated, including advancing and withdrawing the needles, which provides no haptic feedback for the physician. A manually actuated system, which allowed the physician to align the needle templates with an

intended trajectory using handles extending outside of the scanner bore, demonstrated clinical feasibility [48, 49]. This system still required the physician to exit the scanner room to view the images used for guidance during needle alignment, and thus a system capable of remotely aligning the needle templates may further improve procedure times.

A mechatronic MR-compatible needle guidance system was previously developed [50], which overcomes these challenges while maintaining a clinically acceptable level of needle guidance accuracy. The system is sufficiently compact to be placed in the bore with the patient; thus, the patient bed does not need to be retracted between image acquisition and needle insertion. Electric motors and encoders allow the needle trajectory to be set remotely, while manual needle insertion is retained for haptic feedback for the physician and for patient safety. Angulation of the needle is possible for the treatment of large prostates. Preliminary results in the previous work demonstrated the MR compatibility and safety of the system and measured the accuracy of needle guidance in the open air, outside and inside the MR environment. This work presents an improved multi-fiducial arrangement for robust registration of the system and scanner coordinate systems and measurements of needle guidance accuracy to virtual targets in tissue-mimicking prostate phantoms.

4.2 Methods

4.2.1 Mechatronic System Description

A complete description of the mechatronic system has been previously published [50] (see Sec. 3.2.1), and is summarized here. The system consists of a needle trajectory alignment device, which is positioned between the legs of a patient lying in the dorsal recumbent position in the MR scanner bore, an electronic control box positioned in the scanner's control room, and software running on a computer in the scanner's control room. The alignment device uses two dual-link arms to position a suspended needle template against the patient's perineum and is constructed entirely of non-ferromagnetic materials (Fig. 4.1). Actuating torque is provided

by four piezoelectric motors connected to the control box through the scanner room's penetration panel. Four optical encoders provide feedback. The needle template can be moved in four degrees of freedom: horizontal and vertical translation, pitch, and yaw. Each arm has a 60 mm x 60 mm range of motion, which corresponds to the coverage of a conventional prostate brachytherapy needle guidance template while also angulating the needle. The software is integrated with 3D Slicer (www.slicer.org, version 4.10) to visualize the needle trajectory overlaid on MR images from the scanner and to select target alignment points. This allows a physician to prepare a needle path from the control suite while the patient remains in the MR bore, reducing the potential for patient motion between scans and improving ergonomics for the physician. Importantly, insertion of the needle is still performed manually, which provides haptic feedback for the physician, improving patient safety and simplifying sterilization of the system. In case it is required, full manual control of the system is possible using the lock knob and alignment handle located on the rear of the system. A shielded junction box on the side of the system prevents interference between the system's electrical signals and the scanner's electromagnetic fields. MRI-compatibility of the system was previously demonstrated, as well as its ability to align to virtual targets in the open air [50].

4.2.2 Graphical User Interface

A graphical user interface (GUI) has been implemented in 3D Slicer (Fig. 4.2) allowing full control over the system without needing the command-line interface used previously. This facilitates ease-of-use for operators not familiar with the command prompt and provides direct visualization of the chosen needle trajectory overlaid on MR images from the scanner. Images are transferred from the scanner computer either via file-transfer protocol through the network or physically on USB storage media. The GUI is written as a Python plugin for Slicer's Extension Wizard module and uses the D2XX driver library (FTDI Limited, Glasgow, UK) to communicate via USB with the electronic control box. The plugin allows the user to register the system with the scanner coordinates by semi-automatically segmenting the registration

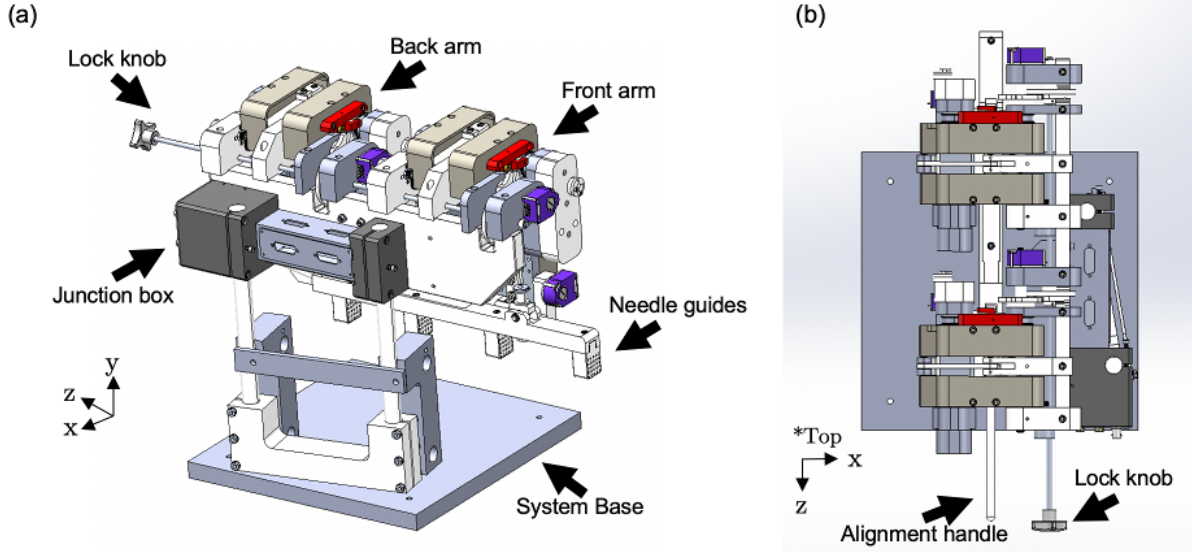


Figure 4.1: Isometric (a) and top-down (b) views of computer-aided design (CAD) model of the previously developed MRI-compatible mechatronic system for prostate focal laser ablation (FLA) needle guidance. The system's front (identified by the needle guides arrow) is placed against the patient's perineum. After alignment with chosen targets, needles are inserted through the needle guides, starting at the back of the system and into the perineum.

fiducials from a series of MR images (Section 4.2.4) and calculating the transform between the coordinate systems (Section 4.2.4). The plugin provides full control over the motor controllers, including calibrating, moving, and parking (for scanning). Following calibration, movement commands can be given manually or by selecting a target for the needle tip and for the needle entry point on an MR image and allowing the software to automatically align the needle template's trajectory with the chosen points. The plugin also projects the actual trajectory of the needle template (as measured by the encoders) in real-time onto the MR image to visualize the system's position.

4.2.3 MR Image Acquisition

All MR images in the following sections were acquired on a 3T MRI scanner (Discovery MR750, GE Healthcare, Chicago, IL) by a trained operator (D.T.) using a T1-weighted sequence from the PI-RADS v2 [51] Guidelines for imaging prostate cancer, as this was previously found to represent the worst-case performance scenario for the system [50]. The

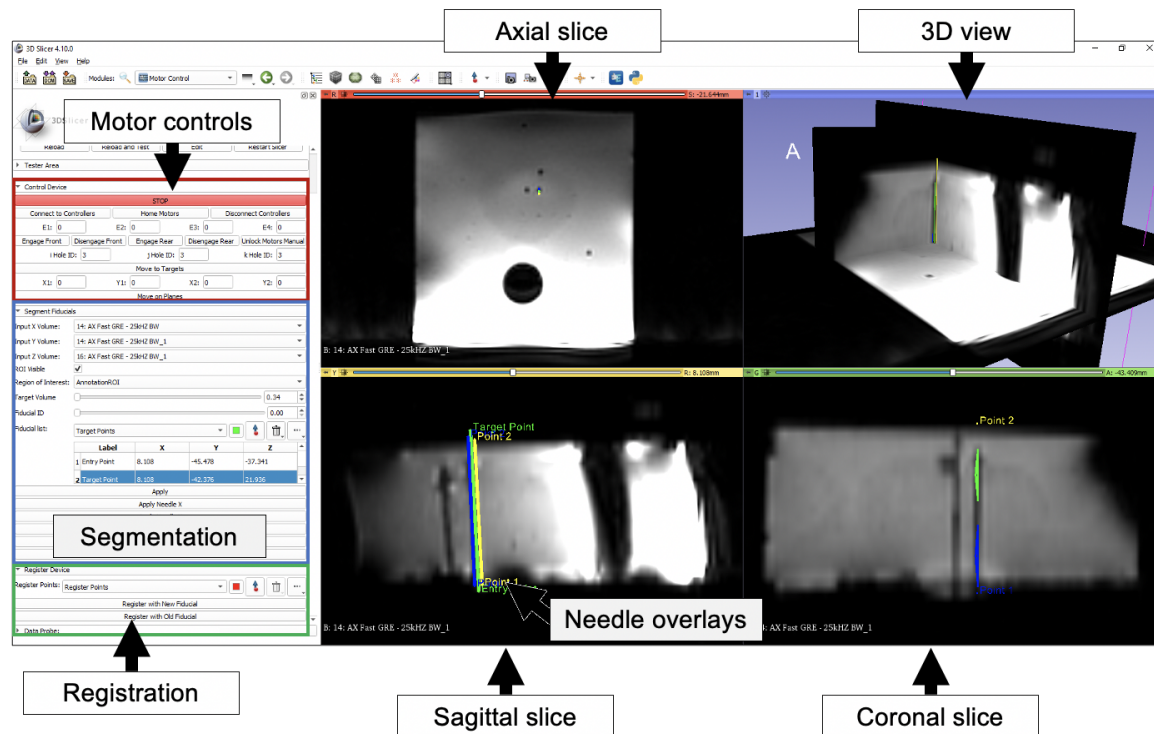


Figure 4.2: Screenshot of the Python scripted module created within Slicer software. The panel on the left is divided into three sections. The first section is used to control the motors, the second is used for segmenting fiducials and needle tracks, and the third is used to register the image with the mechatronic system's coordinate system using the segmented fiducials. The visualization panels show, clockwise from the top right: 3D view of the orthogonal imaging planes, coronal imaging plane, sagittal imaging plane, axial imaging plane. The images have been overlaid with lines created using VTK (Visualization ToolKit), which show the current needle trajectory, the targeted needle trajectory, and the needle trajectory segmented from the image. The motors can also be moved by adjusting the targeted needle trajectory on the image.

sequence parameters are given in Table 4.1.

Table 4.1: Acquisition parameters for images of the registration fiducials and prostate phantom, acquired on 3T Discovery MR750 scanner by GE Healthcare (Chicago, IL).

Weighting	Pulse Sequence	FOV (mm ²)	Matrix (pixels ²)	Slice Thickness (mm)	T _R (ms)	T _E (ms)	Flip Angle (°)
T1	Fast Gradient Echo	220x220	256x256	3.0	270	4	25

4.2.4 Registration of the Mechatronic System and MR Images

The coordinate systems of the scanner and the needle guidance system must first be registered to use MR images to select target points for the needle guidance system and to visualize the needle's trajectory over the MR images. A landmark-based rigid registration algorithm was implemented to use three T1-weighted images of the fiducials with the phase-encoding direction aligned with a different axis in each image. Coordinates were only measured in the phase-encoding direction to minimize the image distortion effects caused by main field inhomogeneity.

Registration Fiducial Assembly

In the previous work [50], a fiducial assembly containing four fluid-filled spheres (Fig. 4.3) was used for registration with the MR coordinate system. The design of this assembly made it susceptible to fiducial localization error as only four spheres were used, and it was only held in place by one shaft, making it difficult to align the anterior-posterior and left-right axes precisely. Furthermore, it was affixed in place of the needle templates, making it difficult to exchange them easily during a procedure. Therefore, an improved multi-fiducial structure was designed and built (Fig. 4.4). This design contains thirty-six spheres with an internal radius of 6.35 mm (volume of 1.07 cm³), filled with a 1% by volume aqueous solution of gadolinium-based contrast agent (Gadovist, 1.0 mmol/mL) to enhance MR-visibility. These spheres are arranged in 3 layers parallel to the coronal imaging plane. Each layer housed twelve spheres

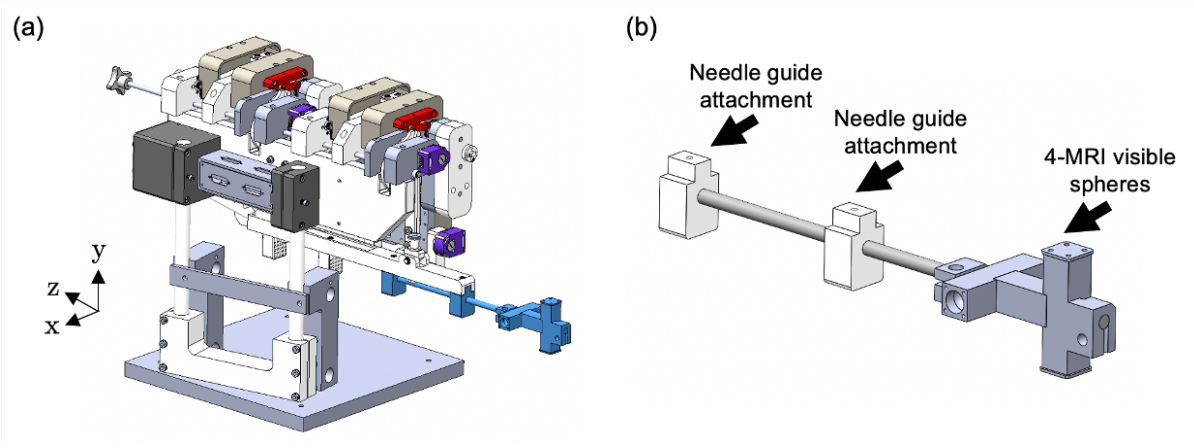


Figure 4.3: a) Previous four-sphere fiducial assembly (in blue) shown attached to the rest of the system. Note that the assembly takes the place of the needle templates, making it difficult to attach and detach as part of the clinical workflow. b) Close-up view of the previous fiducial assembly. The use of only four spheres limits the registration accuracy.

covering a volume of 7.3 cm x 7.3 cm x 5.0 cm between the centroids of the furthest spheres. Combining more fiducials distributed over a wider volume decreases the effect of fiducial localization error on the target registration error, [52] improving registration accuracy. The fiducial structure is attached to the system by two fiberglass rods and a plastic tension rod, which hold the new arrangement more securely than the previous arrangement, and it can be easily removed using two thumb screws. Thus, it can be quickly attached for system registration and removed for needle insertion.

Fiducial Localization

The location of each fiducial in the image was determined using a semi-automated segmentation algorithm. User input to the algorithm is required to place a bounding box surrounding the entire arrangement. The intensity-weighted centroid of voxels inside the bounding box was calculated using Eq. 4.1:

$$c = \frac{\sum_{i=1}^l \sum_{j=1}^m \sum_{k=1}^n I(i, j, k) * (i, j, k)}{\sum_{i=1}^l \sum_{j=1}^m \sum_{k=1}^n I(i, j, k)} \quad (4.1)$$

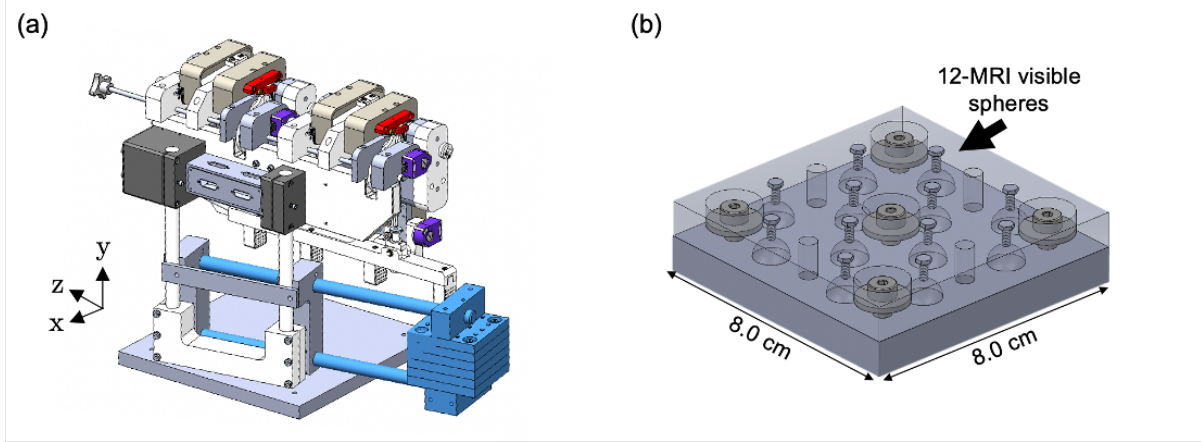


Figure 4.4: a) Improved multi-fiducial structure (in blue) shown attached to the rest of the system. The needle template remains in place, making it less disruptive to the clinical workflow. b) Close-up view of one layer of the improved multi-fiducial design. The layer contains twelve hollowed-out spheres filled with MR-visible fluid, and two more layers are stacked on top.

where l , m , and n are the dimensions of the ROI and $I(i, j, k)$ is the intensity of the voxel at index (i, j, k) . This centroid was used to initialize a seed point for each fiducial sphere, based on their known distances from the center of the entire multi-fiducial arrangement. The initialization was further refined by clustering each voxel in the region of interest with the nearest seed point according to 3D Euclidean distance. The voxel within each cluster with the highest intensity value was then used as the new seed point.

A region-growing algorithm was then applied to each seed point to segment the fiducials. Beginning with the voxel at the seed point, the six orthogonally-neighboring voxels are added to a list, which is ordered based on the intensity of the voxels. During each iteration of the algorithm, the brightest voxel from the list is removed and added to the region, and then its six orthogonal neighbors are added to the list. The algorithm terminates when the desired size of the region (the volume of the fiducial) is reached. The intensity-weighted centroid of all voxels in the region was computed using Eq. 4.1 and used as the fiducial point. This process was repeated on each of the three images with different phase-encoding directions to compile the (i, j, k) coordinates of the fiducials.

Transform

The rigid transformation between the mechatronic system and scanner's coordinate systems is given by Eq. 4.2:

$$p_{image} = R * p_{system} + T \quad (4.2)$$

where p_{image} is a point in the image space, p_{system} is a point in the mechatronic system's space, R is a rotation matrix, and T is a translation matrix. The rotation and translation matrices were calculated using a linear least-squares method, [53] which minimized the sum of squared displacements between corresponding landmarks in the two coordinate systems.

Given a set of n landmarks P_{image} in the image space and P_{system} in the mechatronic system space, the method begins by translation each set of points to be centered at their respective origins (Eq. 4.3a and Eq. 4.3b):

$$P'_{image} = P_{image} - \frac{1}{n} * \sum_{i=0}^{n-1} P_{image}[i] \quad (4.3a)$$

$$P'_{system} = P_{system} - \frac{1}{n} * \sum_{i=0}^{n-1} P_{system}[i] \quad (4.3b)$$

The translated landmarks were then used to construct an intermediate matrix (Eq. 4.4):

$$H = P'_{system} * (P'_{image})^T \quad (4.4)$$

The singular value decomposition (SVD) of H (of dimensions $n \times n$) factorizes H into three matrices U , Σ , and V such that:

$$H = U\Sigma V^T \quad (4.5)$$

where U and V are $n \times n$ unitary matrices and Σ is a $n \times n$ diagonal matrix, the diagonal entries of which are the singular values of H . The SVD was computed using the method given

in [54], which involves reducing the matrix to bidiagonal form using Householder reflections [55], followed by the application of an iterative QR algorithm [56, 57, 58]. The rotation (Eq. 4.6a) and translation (Eq. 4.6b) matrices were then constructed:

$$R = VU^T \quad (4.6a)$$

$$T = \frac{1}{n} * \sum_{i=0}^{n-1} P_{image}[i] - R * \frac{1}{n} * \sum_{i=0}^{n-1} P_{system}[i] \quad (4.6b)$$

4.2.5 Phantom Design

Mechatronics-assisted MRI-guided needle positioning accuracy was quantified with agar-based tissue-mimicking prostate phantoms. The phantom design was adopted from D'Souza *et al.* [59]. These phantoms were fabricated from a mixture of 35 g agar, 80 ml glycerol, and 1 L distilled water. Agar was selected because it possesses similar T1 and T2 relaxation values to human tissue and is stiffer than gelatin [60]. Since gelatin requires a similar force to penetrate as human prostate tissue [61], the agar phantom provides a more difficult challenge and gives an upper bound for the needle guidance error estimate. The agar was mixed using a method similar to that of Rickey *et al.* [62], and was poured into a rectangular plexiglass box to create the background. A 3D prostate mold was constructed with an internal volume of 50 cc, based on contours from an MR prostate image of a patient enrolled in a previous clinical study. To create contrast from the background material, the prostate mold was filled with an agar solution that was first cooled to 55 °C and then mixed with 50% volume unsweetened condensed milk, 0.15 g of ethylenediaminetetraacetic acid tetrasodium (EDTA) salt hydrate, and 0.08 g of CuCl₂ (Sigma-Aldrich, St. Louis, Missouri, USA) [59]. The prostate was positioned 10.0 cm from the surface of the phantom, which corresponds to the anatomical distance from the perineum to the prostate (see Fig. 4.5a).

The needle assembly (Fig. 4.5b) used for all insertion tests was a custom design previously used for MR-guided prostate FLA trials [48]. A tungsten trocar with a three-sided symmetrical

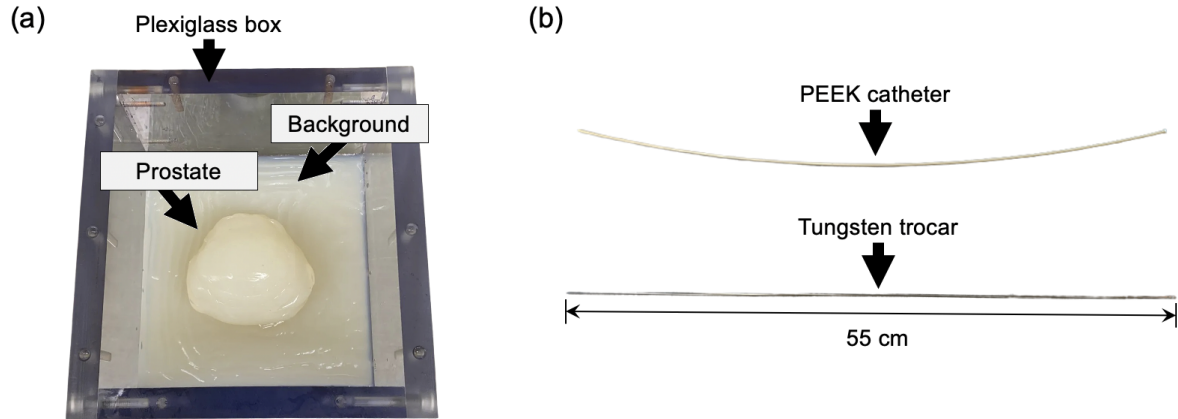


Figure 4.5: a) Tissue-mimicking prostate phantom. An agar and condensed milk prostate moulded from anatomical data is embedded in agar background material. The phantom has similar T1 and T2 relaxation times and stiffness characteristics to human prostate tissue. b) Custom tungsten trocar and PEEK catheter used for all needle insertion tests.

bevel tip is housed inside a polyetheretherketone (PEEK) open-ended catheter. The trocar and catheter are both non-magnetic and thus safe for use in the MR scanner bore. Visualization of the needle path was accomplished by withdrawing the entire assembly and imaging the remaining air-filled void within the phantom (Sec. 4.2.6).

4.2.6 Needle Track Segmentation

The trajectories of the needles were measured by imaging the air-filled tracks (see Fig. 4.6) left behind after the needles were inserted and withdrawn. Semi-automatic segmentation was used to determine which voxels comprised the needle track. User input was required to place a 2D bounding box around a single needle track on a slice near the entry point of the needle into the phantom. Pixels within the bounding box were thresholded with an iteratively decreasing threshold, only keeping pixels with intensities below the threshold until the darkest pixels with a total area equal to the known cross-sectional area of the needle remained. The 2D intensity-weighted centroid after thresholding was then calculated as:

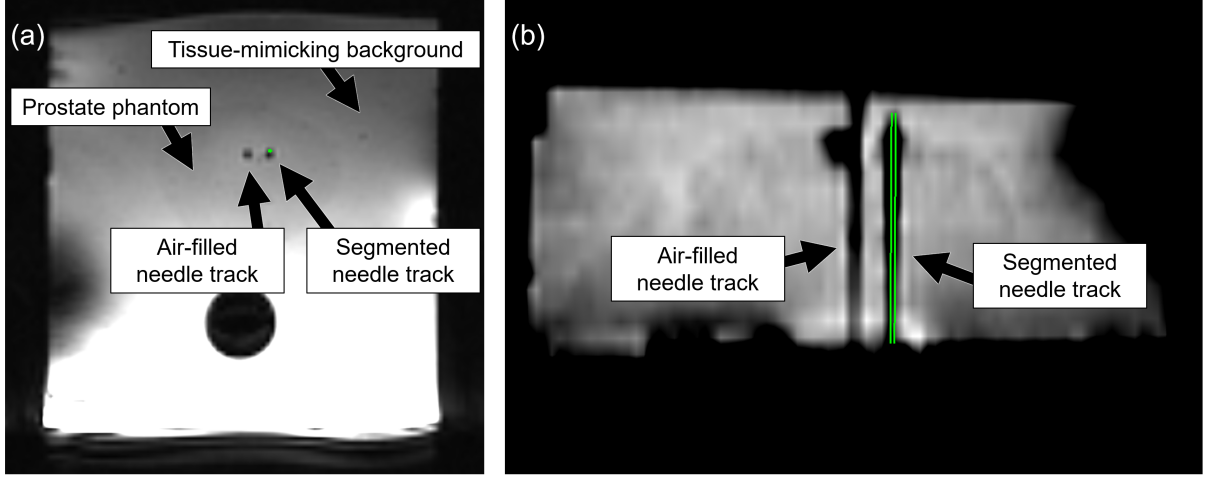


Figure 4.6: Example axial (a) and coronal (b) images of air tracks left behind after withdrawing the needle assembly from the tissue-mimicking prostate phantom. The air tracks were clearly visible for all insertions. The semi-automatic segmentation of one of the needle tracks is shown overlaid in green.

$$c = \frac{\sum_{i=1}^m \sum_{j=1}^m I(i, j) * f(i, j)}{\sum_{i=1}^m \sum_{j=1}^n I(i, j)} \quad (4.7)$$

where m and n are the pixel dimensions of the bounding box, $I(i, j)$ is the intensity of the pixel at index (i, j) , and $f(i, j)$ is a function that maps the pixel index to a coordinate in the patient space using the acquisition parameters. The x -coordinate of c was obtained from the axial image with phase-encoding in the left-right direction, and the y -coordinate was obtained from the axial image with phase-encoding in the anterior-posterior direction. This process was repeated on a slice near the virtual target point of the needle to obtain both endpoints of the needle track, p_{entry}^n and p_{target}^n . Then the trajectory of the needle, parameterized by s , was defined as:

$$t_n = p_{target}^n + s * \hat{v}_n, \quad \hat{v}_n = \frac{p_{target}^n - p_{entry}^n}{\|p_{target}^n - p_{entry}^n\|} \quad (4.8)$$

An example of a segmented needle trajectory is showing in Fig. 4.6.

Validation of Semi-Automatic Segmentation

The semi-automatic segmentation described in the previous section was validated using manual segmentation of the needle tracks as the ground truth. Two trained operators (E.K. and C.P.) placed points as close as possible to the center of the needle tracks on the slice where the needle entered the phantom and the slice where the virtual target was located. This was done on two images with the phase-encoding directions in the right-left and anterior-posterior directions. X-axis components of the four points (two from each operator) were taken from the right-left phase-encoded image, and Y-axis components were taken from the anterior-posterior phase-encoded image. A line was fit to the four points using linear regression and was used as the ground truth of the trajectory of the needle track. This process was performed for 25 trajectories. The needle guidance error metrics described in Sec. 4.2.7 were recalculated using these ground truth trajectories and were compared with the needle guidance errors calculated using the semi-automatic segmentation of the needle trajectories.

4.2.7 Needle Targeting Accuracy

The system's accuracy in aligning its needle guide with a desired needle trajectory was quantified using 44 pairs of virtual entry and target points within the prostate phantom and covering the system's range of motion. The desired trajectory (parameterized by s) was defined as:

$$t_d = p_{target}^d + s * \hat{v}_d, \quad \hat{v}_d = \frac{p_{target}^d - p_{entry}^d}{\|p_{target}^d - p_{entry}^d\|} \quad (4.9)$$

where p_{entry}^d is the desired entry point of the needle and p_{target}^d is the desired target of the needle tip, which are both selected on an image. The desired trajectory was transformed to the mechatronic system's coordinate space, and the inverse kinematics of the system was used to find the arm joint angles required to move the needle guides into position. Once the system was in position, the predicted trajectory of the needle was calculated using the system's forward kinematics and transformed back to the image space. Let the trajectory calculated using the

forward kinematics be defined as:

$$t_p = p^p + s * \hat{v}_p \quad (4.10)$$

p_{target}^p is the closest point to p_{target}^d along \hat{v}_p and was calculated using:

$$p_{target}^p = p_{target}^d - \{(p_{target}^d - p^p) - [(p_{target}^d - p^p) \cdot \hat{v}_p] * \hat{v}_p\} \quad (4.11)$$

The trocar was then slowly advanced into the phantom, a minimum of 10 cm, and withdrawn to leave an air-filled track. The track was imaged using the T1-weighted sequence described in Sec. 4.2.3, and the actual needle trajectory was measured as described in Sec. 4.2.6 and defined as t_n in Eq. 4.8. All target points were chosen at a depth of 10 cm from the front of the needle guide, as this represents a typical clinical insertion depth.

Needle guidance error was calculated as the shortest distance from the needle axis to the target point. Let the error function be:

$$E(p, t) = \|(p - p') - \hat{v} * [(p - p') \cdot \hat{v}]\| \quad (4.12)$$

where p is the reference point and $t = p' + \hat{v}s$ is the actual trajectory. The first error measured was the distance error from the desired target point to the measured needle trajectory and represents the total needle guidance error:

$$E_{total} = E(p_{target}^d, t_n) \quad (4.13)$$

The second error measured was the distance from the desired target point to the predicted needle trajectory:

$$E_{encoders} = E(p_{target}^d, t_p) \quad (4.14)$$

The third error measured was the distance from the predicted target point to the measured

needle trajectory:

$$E_{MRI} = E(p_{target}^p, t_n) \quad (4.15)$$

The final error metric was the angle between the desired needle trajectory and the measured needle trajectory:

$$A_{total} = \arccos \frac{\mathbf{v}_n \cdot \mathbf{v}_d}{\|\mathbf{v}_n\| * \|\mathbf{v}_d\|} \quad (4.16)$$

Comparison with Previous Registration Method

To validate the new registration method, seven needle insertions were performed after registering with the previous four-sphere registration fiducial assembly [50]. Nylon thumb screws were used to attach the previous assembly in place of the needle templates so that it could be easily removed and the templates reattached without disturbing the position of the mechatronic system. The needle tracks were imaged and segmented as described in Sec. 4.2.6, and E_{total} and A_{total} were calculated as described in the previous section. These results were compared with the results measured using the new registration fiducial structure.

4.2.8 Statistical Analysis

All statistical tests were performed with a statistical significance level of 0.05 ($p < 0.05$) corresponding to a 95% confidence value. Tests for normality were performed using the Shapiro-Wilk test. The means of each component of E_{total} in the left-right and anterior-posterior directions were tested for statistically significant difference from zero using a one-sample Student's t-test if the data was normal; otherwise, the median was tested using a Wilcoxon signed-rank test. The distribution of E_{total} and A_{total} resulting from manual segmentation of the needle tracks was compared with E_{total} and A_{total} calculated using semi-automatic segmentation of the same subset of needle tracks, using a paired Student's t-test if the data was normal. Otherwise, a

Wilcoxon signed-rank test was used. The distribution of E_{total} and A_{total} gathered using the previous registration fiducial assembly was compared with E_{total} and A_{total} from the corresponding needle tracks registered with the new registration fiducial arrangement, using a Welch's unequal variances t-test if the data was normal. Otherwise, a Mann Whitney U test was used. Since E_{total} and A_{total} are absolute measures of error, the one-sided 95% prediction interval of each error metric was also calculated using the bounds given in Eq. 4.17. Note that since a one-sided interval was desired, a value for z from the Student's t distribution corresponding to a 90% prediction interval was used, and only the upper bound was taken. All statistics were computed in GraphPad Prism 9.0.

The equation for a prediction interval is given by

$$[\mu - z\sigma, \mu + z\sigma], \quad \sigma = s * \sqrt{1 + \frac{1}{n}} \quad (4.17)$$

where μ is the sample mean, the z -score is chosen for the desired level of probability, s is the sample standard deviation, and n is the sample size [63]. A 2D 95% two-sided confidence ellipsoid of the Left-Right and Anterior-Posterior components of needle guidance error centered on the mean 2D needle guidance error was computed in Matlab using principal component analysis (PCA). The square roots of the eigenvalues calculated using PCA were used as the standard deviation of the data along the eigenvectors. The ellipse was constructed using the eigenvectors as the axes, scaled by the standard deviation multiplied by the z -score corresponding to the desired confidence level, dimensionality, and degrees of freedom of the data. The ellipse was then translated to the mean of the needle guidance error sample. This ellipsoid represents the area which is 95% likely to contain the true value of the mean needle guidance error.

4.3 Results

4.3.1 Needle Targeting Accuracy

The distributions of E_{total} and A_{total} were found to differ significantly from an equivalent normal distribution using the Shapiro-Wilk test ($p = 0.0002$ and $p = 0.0009$, respectively); therefore, medians and interquartile ranges (IQR) are reported for the data, and non-parametric statistical tests were used.

The median positioning error of the needle tracks aiming for virtual targets in the tissue-mimicking phantoms at a depth of 10 cm (E_{total} , Eq. 4.13) was 1.02 mm with an interquartile range of 0.42 - 2.94 mm. The upper limit of the one-sided 95% prediction interval of E_{total} was 4.13 mm. The $E_{encoders}$ was found to have a median (IQR) of 0.11 mm (0.07 - 0.14 mm), with an upper limit of the one-sided 95% prediction interval of 0.21 mm. E_{MRI} was found to have a median (IQR) of 1.05 mm (0.43 - 3.01 mm) and an upper limit of the one-sided 95% prediction interval of 4.17 mm. The angular error, A_{total} , had a median (IQR) of 0.0097 rad (0.0057 - 0.015 rad) and an upper limit of the one-sided 95% prediction interval of 0.022 rad. The cumulative distribution functions (CDFs) of E_{total} and A_{total} are given in Fig. 4.7.

Decomposing E_{total} into its spatial components failed to show a significant difference from a median of 0.0 mm for either the left-right ($p = 0.82$) or the anterior-posterior ($p = 0.64$) directions using the Wilcoxon signed-rank test. A scatter plot of the spatial components of needle guidance error is given on a Cartesian axis in Fig. 4.8. The approximately spherical shape of the 95% confidence ellipse indicates low correlation between the components of needle guidance error.

4.3.2 Comparison with Previous Registration Method

The median (IQR) positioning error found after using the previous registration fiducial assembly to register the mechatronic system with the image space was 1.87 mm (1.77 - 2.14 mm). This was found to be significantly different ($p = 0.0012$) from the median (IQR) positioning

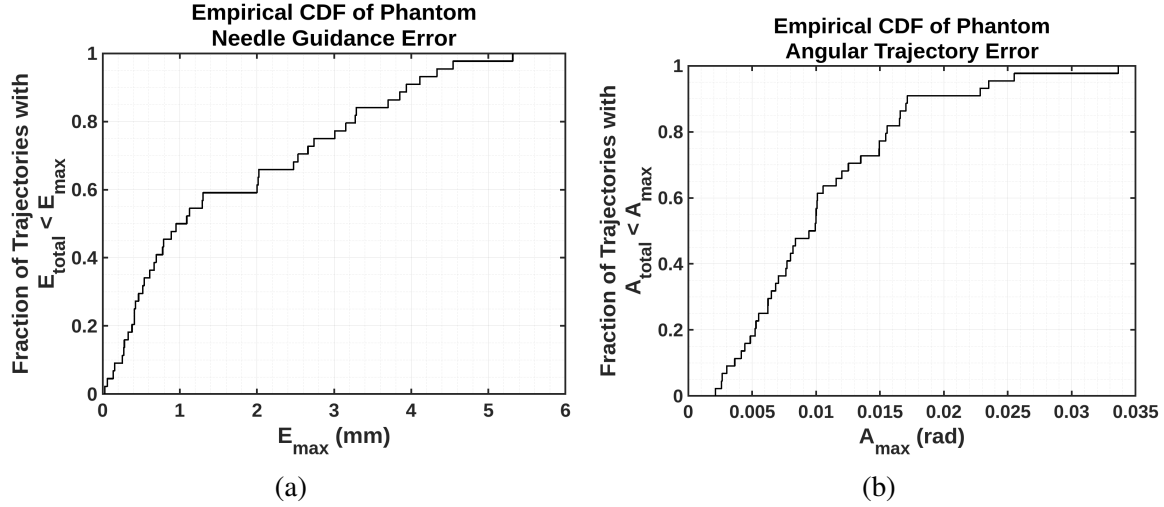


Figure 4.7: Cumulative distribution functions of needle guidance errors in tissue-mimicking prostate phantoms measured using 44 trajectories. The CDF plots the percentage of trajectories with error less than the value on the x-axis. (a) CDF of E_{total} , representing the shortest Euclidean distance between the measured needle trajectory and the targeted point. 50% of the errors were less than 1.0 mm. (b) CDF of A_{total} , representing the angle between the intended needle trajectory and the measured needle trajectory. 61% of the errors were less than 0.01 rad.

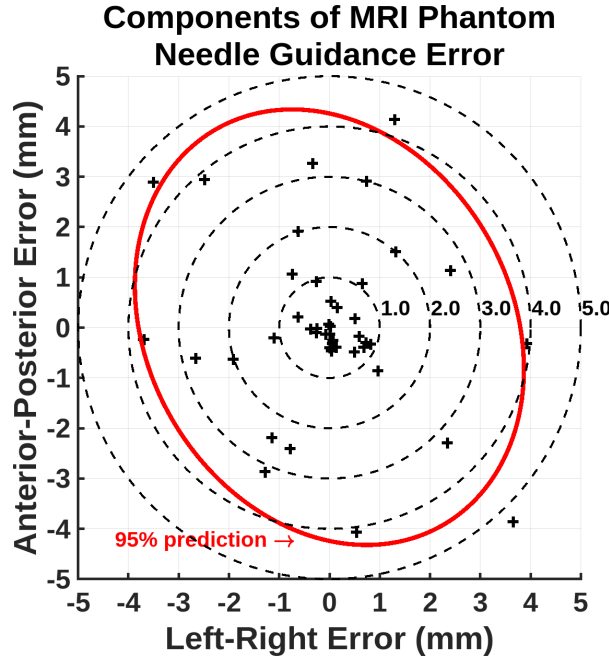


Figure 4.8: Spatial components of targeting error in prostate phantoms measured using 44 trajectories. E_{total} was separated into left-right and anterior-posterior directions, where the origin corresponds to the target point for each trajectory at a depth of 10 cm calculated using the forward kinematics. Dashed circles are shown to indicate error magnitudes in steps of 1 mm. The 95% confidence ellipsoid represents the area which is 95% likely to contain the true value of the means of the components of needle guidance error.

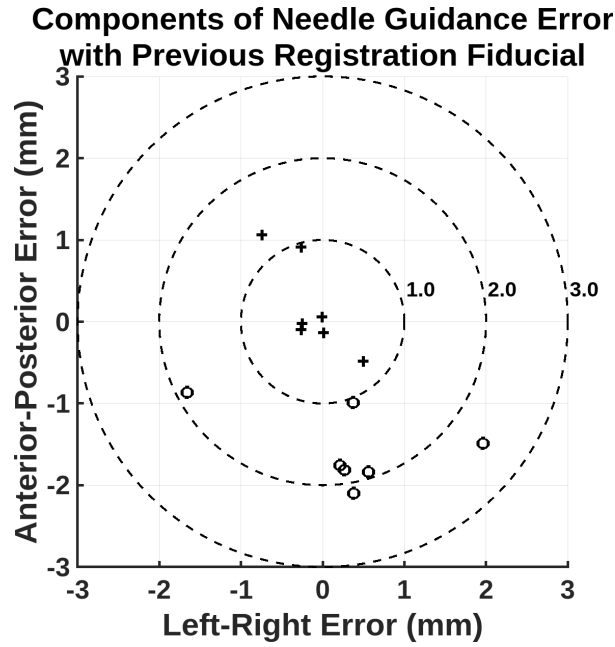


Figure 4.9: Comparison of the left-right and anterior-posterior components of targeting error using the new and previous registration fiducial arrangements on 7 trajectories. The origin corresponds to the target point for each trajectory at a depth of 10 cm calculated using the forward kinematics. Dashed circles are shown to indicate error magnitudes in steps of 1 mm. ‘+’ marks indicate errors using the new registration method, and ‘o’ marks indicate errors using the previous registration method.

error of 0.28 mm (0.14 - 0.95 mm) found using the new registration fiducial arrangement on the same trajectories. The components of the errors found using both methods are shown in Fig. 4.9. The median error from the previous registration assembly differed significantly from 0 mm in the anterior-posterior direction ($p = 0.016$), but no significant difference was detected in the left-right direction ($p = 0.22$). The median (IQR) angular error from the previous registration fiducial assembly was 0.012 rad (0.009 - 0.018 rad) and from the new registration assembly was 0.010 rad (0.008 - 0.012 rad). No significant difference was found between the medians of the angular errors ($p = 0.26$).

4.3.3 Validation of Semi-Automatic Needle Segmentation

The median (IQR) positioning error found after using manual segmentation of the needle tracks and recalculating E_{total} was 1.79 mm (0.42 - 3.24 mm), compared with a median (IQR) of

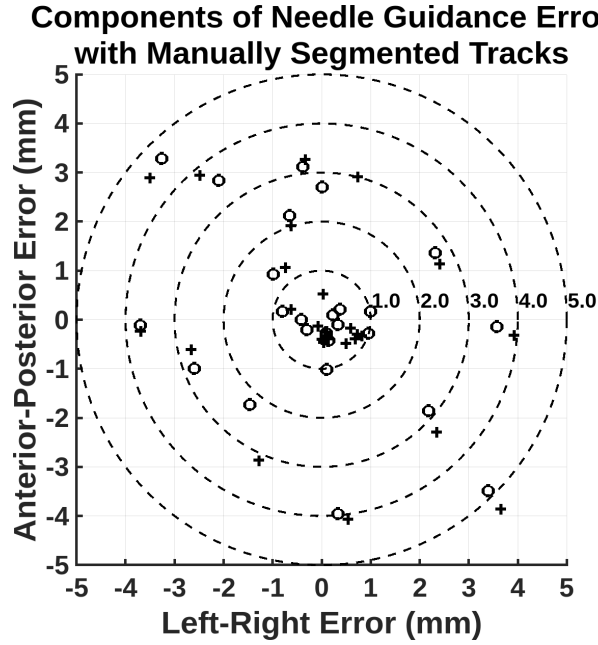


Figure 4.10: Comparison of the left-right and anterior-posterior components of targeting error using manual and semi-automatic needle track segmentation on 26 trajectories. The origin corresponds to the target point for each trajectory at a depth of 10 cm calculated using the forward kinematics. Dashed circles are shown to indicate error magnitudes in steps of 1 mm. ‘+’ marks indicate errors using semi-automatic segmentation, and ‘o’ marks indicate errors using manual segmentation.

1.66 mm (0.59 - 3.39 mm) calculated using semi-automatic segmentation on the same needle tracks. The distributions of positioning errors calculated using each method of segmentation are shown in Fig. 4.10. Recalculating angular error A_{total} using manual segmentation resulted in a median (IQR) of 0.012 rad (0.006 - 0.016 rad), compared with 0.010 rad (0.007 - 0.016 rad) calculated using semi-automatic segmentation. The Wilcoxon matched-pairs signed-rank test failed to detect any significant difference between the methods for E_{total} ($p = 0.15$) or A_{total} ($p = 0.52$).

4.4 Discussion

Focal therapy is increasingly reported as a minimally invasive option for managing localized low- to intermediate-grade PCa [16, 64, 15, 65, 66, 67]; however, effective needle guidance

methods remain an ongoing area of research and development. Although long-term survival data indicates higher overall survival rates for patients treated using radiotherapy (particularly in intermediate-grade PCa) [68], it is often accompanied by a decline in quality of life [69]. Comparatively, FLA offers improved functional incomes, with clinical trials reporting no significant loss of erectile or urinary function after FLA [15, 70]. Outcomes of FLA may be improved by reducing residual cancer after treatment, which is partially caused by inaccurate delivery of needles to targeted lesions [71], leading to more successful long-term oncologic control. This paper described a prototype of an improved mechatronic system capable of aligning needle templates with targets identified on MR images and its testing for guiding needles to targets in agar phantoms. Quantification of errors in aligning the needle templates to targets assessed the system's capabilities in its primary function of guiding needles to MR-identified prostate lesions. Our results showed that the system could place a needle in tissue-mimicking phantoms with a median (IQR) positioning error of 1.02 mm (0.42 - 2.94 mm) and within 4.13 mm or less at a typical insertion depth of 10.0 cm in 95% of attempts. This error was measured perpendicular to the axis of needle insertion. Since the system only aligns the needle guides with the desired trajectory and the physician still performs the needle insertion manually, errors in needle placement accuracy, which are parallel to the needle insertion direction, can be easily corrected simply by advancing or withdrawing the needle. Errors perpendicular to the axis of needle insertion are much more difficult to correct, requiring complete reinsertion of the needle, which increases procedure times and trauma to the patient. Therefore, perpendicular errors were considered much more consequential, and parallel errors were neglected for this study. In cases where multiple needle insertions are required, our semi-automatic segmentation algorithm allows a single needle track to be selected by tightening the bounding box to include only the desired track.

Given that a 5 mm margin of healthy tissue surrounding the target is usually included in the ablation region, the system's accuracy achieved in this work is sufficient to guide needles for their intended use in prostate FLA procedures. However, the healthy tissue margin included

in the ablation region is meant to compensate for the possibility of mpMRI to underestimate prostate tumor volumes [72, 73, 74], and therefore should not be treated as a "buffer zone" for mitigating errors in needle placement. Minimizing error is especially imperative when targeting lesions proximal to functional structures such as the urethra, rectum, or neurovascular bundles, which should not be ablated. In these cases, MR thermometry may be used in stationary tissues to monitor the heating progression carefully and protect nearby structures [28]. When targeting larger lesions, multiple holes in the system's needle template can be used to insert several thermal ablation applicators simultaneously to enlarge the ablation region. Needles inserted through adjacent template holes tend to deflect similarly [48]; therefore, the successful placement of the first needle can be used to guide subsequent insertions. Although the tumor volume is not the only grading criteria used for PCa, tumors less than 0.5 cm^3 in volume (approximately 0.5 cm in radius) are generally considered clinically insignificant [75, 76, 77]. Thus, the system could also be used to guide biopsy needles and successfully sample at least 95% of lesions with a radius of 0.5 cm or greater.

The needle guidance accuracy measured in this study includes errors due to many factors. Kinematic errors were minimal as components of the system were manufactured to tolerances of approximately 0.05 mm. Encoder resolution was also a minimal error contributor as the selected encoders generated 4,096 counts per revolution or an angular resolution of about 0.0015 rad. Propagating this resolution from all four encoders through the forward kinematics of the system results in a maximum potential error of 0.22 mm at the needle tip. Our results found $E_{encoders}$ to have a median of 0.11 mm (IQR of 0.07 - 0.14 mm), representing the closest practical needle trajectory that the guidance software was able to calculate to the desired trajectory. There was also some error in the 'base' pose of the system from which all the relative kinematics calculations were based. In this pose, all system arms were adjusted to be either parallel or perpendicular to the system's base. Previously [50], this adjustment was made using an ordinary spirit level, but the 'base' position was re-calibrated for this study using a height gauge with an accuracy of $\pm 0.0127 \text{ mm}$. Over the 73.0 mm length of each arm, this

corresponds to an angular accuracy of 0.000 35 rad, which is an order of magnitude smaller than the errors due to encoder resolution.

More substantial sources of error include effects from image distortion, fiducial localization error (FLE), registration error, and needle deflection. MR-compatibility tests previously found image distortion due to the presence of the system in the scanner bore to be low, and it was further mitigated by performing all measurements in the phase-encoding direction only. FLE was introduced due to image distortion and resolution limitations of the MR images and was further exacerbated by the imperfect filling of all fiducial spheres in the arrangement with liquid. The new design of the fiducial arrangement both increased the number of fiducials from four to thirty-six and distributed the fiducials more widely across the imaging volume compared with the former design, which minimized the impact of FLE on registration error according to work by *Fitzpatrick* [52]. Evaluating the system's accuracy in tissue-mimicking phantoms, thereby including errors due to needle deflection, was another major focus of this paper. Previously, needle deflection in agar-based phantoms was estimated to be approximately 1.1 mm after 10.0 cm of insertion [48]. Since the 95% prediction interval of needle guidance error found in tissue-mimicking phantoms in this work was similar to that found previously in open-air (3.84 mm), while also including needle deflection, the new registration fiducial design must have reduced registration errors. It should be noted that the phantoms represent an idealized scenario for needle deflection. While they were designed with a similar stiffness to human prostate tissue, they were mostly homogeneous with isotropic material properties. Higher needle deflection, up to 2.8 mm at a depth of 6.0 cm, was measured *in vivo* [78], where complex anatomy presents anisotropic and heterogeneous tissues. However, the majority of needle deflection occurs during initial penetration [48], allowing this error to be predicted and compensated for if MRI visible needles are used, such as the custom trocar and catheter designed for our system. An optimal method of correcting for needle deflection remains an ongoing area of research.

The median needle guidance error in phantoms using the previous fiducial assembly to

register the system with MR images was 1.87 mm, significantly different from the median of 0.28 mm using the new fiducial assembly on the same needle trajectories. This also indicates that the new assembly was successful in reducing registration errors. Furthermore, bias in the anterior-posterior direction was detected when using the previous fiducial assembly, which may have been due to a registration error. No such biases were detected with the new assembly. Mechanical bias was compensated for as described previously [50]. In the previous open-air in-bore experiments, the median needle guidance error on the same trajectories was 1.28 mm. Assuming needle deflection is independent of other errors, it can be added in quadrature between the open-air experiments and phantom experiments, yielding an approximation of 1.36 mm for needle deflection, which is consistent with the results cited in the paragraph above. Our phantom design used two materials with different stiffness values but was otherwise homogeneous. This work presents a complete system for MR-guided prostate FLA needle guidance and comprehensive pre-clinical quantification of its error. The system should next be validated for accuracy and usefulness in a clinical setting where more complex tissue properties and potential patient motion will be encountered.

4.5 Conclusion

The needle guidance accuracy of an image-guided mechatronic trajectory alignment system for transperineal needle delivery to prostate lesions during focal therapies in the bore of an MR scanner with remote actuation capabilities was quantified in tissue-mimicking prostate phantoms. A new registration method was developed, allowing the mechatronic system to align the trajectory of the needle templates to virtual targets at typical clinical insertion depths with an accuracy of 4.13 mm, within 95% confidence. This represents the total ability of the system to target a lesion under idealized conditions and demonstrates potential utility for accurate delivery of FLA to small localized prostate lesions. The system's efficacy should be validated next in a clinical setting.

4.6 Acknowledgments

The authors gratefully acknowledge financial support from the Ontario Institute of Cancer Research (OICR), the Canadian Institutes for Health Research (CIHR), and the Natural Sciences and Engineering Research Council (NSERC) of Canada.

Conflict of interest

The authors have no relevant conflicts of interest to disclose.

Bibliography

- [1] V. A. Moyer, "Screening for Prostate Cancer: U.S. Preventive Services Task Force Recommendation Statement," *Annals of Internal Medicine*, vol. 157, pp. 120–134, jul 2012.
- [2] R. L. Siegel, K. D. Miller, H. E. Fuchs, and A. Jemal, "Cancer Statistics, 2021," *CA: A Cancer Journal for Clinicians*, vol. 71, pp. 7–33, jan 2021.
- [3] J. L. Donovan, F. C. Hamdy, J. A. Lane, M. Mason, C. Metcalfe, E. Walsh, J. M. Blazeby, T. J. Peters, P. Holding, S. Bonnington, T. Lennon, L. Bradshaw, D. Cooper, P. Herbert, J. Howson, A. Jones, N. Lyons, E. Salter, P. Thompson, S. Tidball, J. Blaikie, C. Gray, P. Bollina, J. Catto, A. Doble, A. Doherty, D. Gillatt, R. Kockelbergh, H. Kynaston, A. Paul, P. Powell, S. Prescott, D. J. Rosario, E. Rowe, M. Davis, E. L. Turner, R. M. Martin, D. E. Neal, and P. S. Group*, "Patient-Reported Outcomes after Monitoring, Surgery, or Radiotherapy for Prostate Cancer," *The New England journal of medicine*, vol. 375, pp. 1425–1437, oct 2016.
- [4] M. R. Cooperberg and P. R. Carroll, "Trends in Management for Patients With Localized Prostate Cancer, 1990-2013," *JAMA*, vol. 314, pp. 80–82, jul 2015.
- [5] P. R. Womble, J. E. Montie, Z. Ye, S. M. Linsell, B. R. Lane, and D. C. Miller, "Contemporary use of initial active surveillance among men in Michigan with low-risk prostate cancer.," *European urology*, vol. 67, pp. 44–50, jan 2015.
- [6] M. Perera, N. Krishnananthan, U. Lindner, and N. Lawrentschuk, "An update on focal therapy for prostate cancer," *Nature Reviews Urology*, vol. 13, no. 11, pp. 641–653, 2016.
- [7] M. Valerio, H. U. Ahmed, M. Emberton, N. Lawrentschuk, M. Lazzeri, R. Montironi, P. L. Nguyen, J. Trachtenberg, and T. J. Polascik, "The Role of Focal Therapy in the Management of Localised Prostate Cancer: A Systematic Review," *European Urology*, vol. 66, no. 4, pp. 732–751, 2014.
- [8] A. H. Hou, K. F. Sullivan, and E. D. Crawford, "Targeted focal therapy for prostate cancer: a review," *Current Opinion in Urology*, vol. 19, no. 3, 2009.
- [9] C. T. Iberti, N. Mohamed, and M. A. Palese, "A review of focal therapy techniques in prostate cancer: clinical results for high-intensity focused ultrasound and focal cryoablation.," *Reviews in urology*, vol. 13, no. 4, pp. 196–202, 2011.
- [10] T. Lee, N. Mendhiratta, D. Sperling, and H. Lepor, "Focal laser ablation for localized prostate cancer: principles, clinical trials, and our initial experience.," *Reviews in urology*, vol. 16, no. 2, pp. 55–66, 2014.
- [11] G. Bozzini, P. Colin, P. Nevoux, A. Villers, S. Mordon, and N. Betrouni, "Focal therapy of prostate cancer: energies and procedures," *Urologic Oncology: Seminars and Original Investigations*, vol. 31, no. 2, pp. 155–167, 2013.
- [12] S. Marshall and S. Taneja, "Focal therapy for prostate cancer: The current status," *Prostate International*, 2015.

- [13] J. G. Bomers, E. B. Cornel, J. J. Fütterer, S. F. Jenniskens, H. E. Schaafsma, J. O. Barentsz, J. P. Sedelaar, C. A. Hulsbergen-van de Kaa, and J. A. Witjes, “MRI-guided focal laser ablation for prostate cancer followed by radical prostatectomy: correlation of treatment effects with imaging,” *World Journal of Urology*, vol. 35, no. 5, pp. 703–711, 2017.
- [14] U. Lindner, N. Lawrentschuk, R. A. Weersink, S. R. H. Davidson, O. Raz, E. Hlasny, D. L. Langer, M. R. Gertner, T. Van der Kwast, M. A. Haider, and J. Trachtenberg, “Focal laser ablation for prostate cancer followed by radical prostatectomy: validation of focal therapy and imaging accuracy,” *European Urology*, vol. 57, no. 6, pp. 1111–1114, 2010.
- [15] S. E. Eggener, A. Yousuf, S. Watson, S. Wang, and A. Oto, “Phase II evaluation of magnetic resonance imaging guided focal laser ablation of prostate cancer,” *Journal of Urology*, vol. 196, no. 6, pp. 1670–1675, 2016.
- [16] A. Oto, I. Sethi, G. Karczmar, R. J. McNichols, M. K. Ivancevic, W. M. Stadler, S. Watson, and S. E. Eggener, “MR imaging-guided focal laser ablation for prostate cancer: phase I trial,” *Radiology*, vol. 267, pp. 932–940, jun 2013.
- [17] S. Natarajan, S. Raman, A. M. Priester, J. Garritano, D. J. Margolis, P. Lieu, M. L. Macairan, J. Huang, W. Grundfest, and L. S. Marks, “Focal Laser Ablation of Prostate Cancer: Phase I Clinical Trial,” *Journal of Urology*, vol. 196, no. 1, pp. 68–75, 2016.
- [18] M. R. Abern, M. Tsivian, and T. J. Polascik, “Focal Therapy of Prostate Cancer: Evidence-based Analysis for Modern Selection Criteria,” *Current Urology Reports*, vol. 13, no. 2, pp. 160–169, 2012.
- [19] O. Rouvière, R. Souchon, R. Salomir, A. Gelet, J.-Y. Chapelon, and D. Lyonnet, “Transrectal high-intensity focused ultrasound ablation of prostate cancer: Effective treatment requiring accurate imaging,” *European Journal of Radiology*, vol. 63, pp. 317–327, sep 2007.
- [20] P. Colin, S. Mordon, P. Nevoux, M. F. Marqa, A. Ouzzane, P. Puech, G. Bozzini, B. Leroux, A. Villers, and N. Betrouni, “Focal Laser Ablation of Prostate Cancer: Definition, Needs, and Future,” *Advances in Urology*, vol. 2012, p. 589160, 2012.
- [21] G. Sommer, D. Bouley, H. Gill, B. Daniel, K. B. Pauly, and C. Diederich, “Focal ablation of prostate cancer: four roles for magnetic resonance imaging guidance,” *The Canadian journal of urology*, vol. 20, pp. 6672–6681, apr 2013.
- [22] N. B. Delongchamps, M. Rouanne, T. Flam, F. Beuvon, M. Liberatore, M. Zerbib, and F. Cornud, “Multiparametric magnetic resonance imaging for the detection and localization of prostate cancer: combination of T2-weighted, dynamic contrast-enhanced and diffusion-weighted imaging,” *BJU International*, vol. 107, pp. 1411–1418, may 2011.
- [23] D. L. Langer, T. H. van der Kwast, A. J. Evans, J. Trachtenberg, B. C. Wilson, and M. A. Haider, “Prostate cancer detection with multi-parametric MRI: Logistic regression analysis of quantitative T2, diffusion-weighted imaging, and dynamic contrast-enhanced MRI,” *Journal of Magnetic Resonance Imaging*, vol. 30, pp. 327–334, aug 2009.

- [24] B. Turkbey, H. Mani, V. Shah, A. R. Rastinehad, M. Bernardo, T. Pohida, Y. Pang, D. Daar, C. Benjamin, Y. L. McKinney, H. Trivedi, C. Chua, G. Bratslavsky, J. H. Shih, W. M. Linehan, M. J. Merino, P. L. Choyke, and P. A. Pinto, "Multiparametric 3T prostate magnetic resonance imaging to detect cancer: histopathological correlation using prostatectomy specimens processed in customized magnetic resonance imaging based molds.," *The Journal of urology*, vol. 186, pp. 1818–1824, nov 2011.
- [25] G. Murphy, M. Haider, S. Ghai, and B. Sreeharsha, "The expanding role of MRI in prostate cancer," *American Journal of Roentgenology*, vol. 201, no. 6, pp. 1229–1238, 2013.
- [26] C. M. A. Hoeks, J. J. O. Barentsz, T. Hambrock, D. Yakar, D. M. Somford, S. W. T. P. J. Heijmink, T. W. J. Scheenen, P. C. Vos, H. Huisman, I. M. van Oort, J. A. Witjes, A. Heerschap, and J. J. Fütterer, "Prostate cancer: multiparametric MR imaging for detection, localization, and staging," *Radiology*, vol. 261, no. 1, pp. 46–66, 2011.
- [27] J. V. Hegde, R. V. Mulkern, L. P. Panych, F. M. Fennessy, A. Fedorov, S. E. Maier, and C. M. C. Tempany, "Multiparametric MRI of prostate cancer: an update on state-of-the-art techniques and their performance in detecting and localizing prostate cancer.," *Journal of magnetic resonance imaging : JMRI*, vol. 37, pp. 1035–1054, may 2013.
- [28] J. Yuan, C.-S. Mei, L. P. Panych, N. J. McDannold, and B. Madore, "Towards fast and accurate temperature mapping with proton resonance frequency-based MR thermometry.," *Quantitative imaging in medicine and surgery*, vol. 2, no. 1, pp. 21–32, 2012.
- [29] U. Lindner and J. Trachtenberg, "MRI-guided laser ablation for localized prostate cancer," in *Imaging and focal therapy of early prostate cancer* (T. J. Polascik, ed.), pp. 297–307, New York, NY, USA: Springer International Publishing, 2013.
- [30] A. Boyes, K. Tang, M. Yaffe, L. Sugar, R. Chopra, and M. Bronskill, "Prostate tissue analysis immediately following magnetic resonance imaging guided transurethral ultrasound thermal therapy.," *The Journal of urology*, vol. 178, pp. 1080–1085, sep 2007.
- [31] H.-L. M. Cheng, M. A. Haider, M. J. Dill-Macky, J. M. Sweet, J. Trachtenberg, and M. R. Gertner, "MRI and contrast-enhanced ultrasound monitoring of prostate microwave focal thermal therapy: an in vivo canine study.," *Journal of magnetic resonance imaging : JMRI*, vol. 28, pp. 136–143, jul 2008.
- [32] A. V. D'Amico, R. Cormack, C. M. Tempany, S. Kumar, G. Topulos, H. M. Kooy, and C. N. Coleman, "Real-time magnetic resonance image-guided interstitial brachytherapy in the treatment of select patients with clinically localized prostate cancer.," *International Journal of Radiation Oncology, Biology, Physics*, vol. 42, no. 3, pp. 507–515, 1998.
- [33] A. V. D'Amico, C. M. Tempany, R. Cormack, N. Hata, M. Jinzaki, K. Tuncali, M. Weinstein, J. P. Richie, and P. Richie, "Transperineal magnetic resonance image guided prostate biopsy.," *The Journal of Urology*, vol. 164, no. 2, pp. 385–387, 2000.

- [34] R. A. Cormack, A. V. D'Amico, N. Hata, S. Silverman, M. Weinstein, and C. M. Tempany, "Feasibility of transperineal prostate biopsy under interventional magnetic resonance guidance," *Urology*, vol. 56, no. 4, pp. 663–664, 2000.
- [35] B. Fei, J. L. Duerk, D. T. Boll, J. S. Lewin, and D. L. Wilson, "Slice-to-volume registration and its potential application to interventional MRI-guided radio-frequency thermal ablation of prostate cancer," *IEEE Transactions on Medical Imaging*, vol. 22, no. 4, pp. 515–525, 2003.
- [36] N. Hata, M. Jinzaki, D. Kacher, R. Cormak, D. Gering, a. Nabavi, S. G. Silverman, a. V. D'Amico, R. Kikinis, F. a. Jolesz, and C. M. Tempany, "MR imaging-guided prostate biopsy with surgical navigation software: device validation and feasibility.," *Radiology*, 2001.
- [37] R. C. Susil, K. Camphausen, P. Choyke, E. R. McVeigh, G. S. Gustafson, H. Ning, R. W. Miller, E. Atalar, C. N. Coleman, and C. Ménard, "System for prostate brachytherapy and biopsy in a standard 1.5 T MRI scanner," *Magnetic Resonance in Medicine*, vol. 52, no. 3, pp. 683–687, 2004.
- [38] C. Ménard, R. C. Susil, P. Choyke, G. S. Gustafson, W. Kammerer, H. Ning, R. W. Miller, K. L. Ullman, N. Sears Crouse, S. Smith, E. Lessard, J. Pouliot, V. Wright, E. McVeigh, C. N. Coleman, and K. Camphausen, "MRI-guided HDR prostate brachytherapy in standard 1.5T scanner," *International Journal of Radiation Oncology Biology Physics*, vol. 59, no. 5, pp. 1414–1423, 2004.
- [39] S. E. Song, N. B. Cho, G. Fischer, N. Hata, C. Tempany, G. Fichtinger, and I. Iordachita, "Development of a pneumatic robot for MRI-guided transperineal prostate biopsy and brachytherapy: New approaches," in *Proceedings - IEEE International Conference on Robotics and Automation*, (Anchorage, AK, USA), pp. 2580–2585, IEEE, 2010.
- [40] S. P. DiMaio, S. Pieper, K. Chinzei, N. Hata, S. J. Haker, D. F. Kacher, G. Fichtinger, C. M. Tempany, and R. Kikinis, "Robot-assisted needle placement in open MRI: System architecture, integration and validation," *Computer Aided Surgery*, vol. 12, no. 1, pp. 15–24, 2007.
- [41] G. S. Fischer, I. Iordachita, C. Csoma, J. Tokuda, S. P. DiMaio, C. M. Tempany, N. Hata, and G. Fichtinger, "MRI-compatible pneumatic robot for transperineal prostate needle placement," *IEEE/ASME Transactions on Mechatronics*, vol. 13, no. 3, pp. 295–305, 2008.
- [42] M. R. Van Den Bosch, M. R. Moman, M. Van Vulpen, J. J. Battermann, E. Duiveman, L. J. Van Schelven, H. De Leeuw, J. J. Lagendijk, and M. A. Moerland, "MRI-guided robotic system for transperineal prostate interventions: Proof of principle," *Physics in Medicine and Biology*, vol. 55, no. 5, 2010.
- [43] S. Zangos, C. Herzog, K. Eichler, R. Hammerstingl, A. Lukoschek, S. Guthmann, B. Gutmann, U. J. Schoepf, P. Costello, and T. J. Vogl, "MR-compatible assistance system for

- punction in a high-field system: device and feasibility of transgluteal biopsies of the prostate gland,” *European Radiology*, vol. 17, no. 4, pp. 1118–1124, 2007.
- [44] M. G. Schouten, J. Ansems, W. K. J. Renema, D. Bosboom, T. W. J. Scheenen, and J. J. Fütterer, “The accuracy and safety aspects of a novel robotic needle guide manipulator to perform transrectal prostate biopsies,” *Medical Physics*, vol. 37, pp. 4744–4750, sep 2010.
- [45] A. Krieger, I. Iordachita, S. Song, N. B. Cho, P. Guion, G. Fichtinger, and L. L. Whitcomb, “Development and preliminary evaluation of an actuated MRI-compatible robotic device for MRI-guided prostate intervention,” in *2010 IEEE International Conference on Robotics and Automation*, pp. 1066–1073, 2010.
- [46] J. Xiang, H. Yan, J. Li, X. Wang, H. Chen, and X. Zheng, “Transperineal versus transrectal prostate biopsy in the diagnosis of prostate cancer: a systematic review and meta-analysis,” *World Journal of Surgical Oncology*, vol. 17, no. 1, p. 31, 2019.
- [47] A. A. Goldenberg, J. Trachtenberg, Y. Yi, R. Weersink, M. S. Sussman, M. Haider, L. Ma, and W. Kucharczyk, “Robot-assisted MRI-guided prostatic interventions,” *Robotica*, vol. 28, no. 2, pp. 215–234, 2010.
- [48] J. Cepek, B. A. Chronik, U. Lindner, J. Trachtenberg, S. R. H. Davidson, J. Bax, and A. Fenster, “A system for MRI-guided transperineal delivery of needles to the prostate for focal therapy,” *Medical Physics*, vol. 40, no. 1, p. 012304, 2013.
- [49] J. Cepek, U. Lindner, S. Ghai, A. S. Louis, S. R. H. Davidson, M. R. Gertner, E. Hlasny, M. S. Sussman, A. Fenster, and J. Trachtenberg, “Mechatronic system for in-bore MRI-guided insertion of needles to the prostate: An in vivo needle guidance accuracy study,” *Journal of Magnetic Resonance Imaging*, vol. 42, no. 1, pp. 48–55, 2015.
- [50] E. Knull, J. S. Bax, C. K. S. Park, D. Tessier, and A. Fenster, “Design and validation of an mri-compatible mechatronic system for needle delivery to localized prostate cancer,” *Medical Physics*, vol. 48, no. 9, pp. 5283–5299, 2021.
- [51] A. C. of Radiology, “PI-RADS™ Prostate Imaging – Reporting and Data System, Version 2,” tech. rep., American College of Radiology, 2015.
- [52] J. Fitzpatrick, J. West, and C. Maurer, “Predicting error in rigid-body point-based registration,” *IEEE Transactions on Medical Imaging*, vol. 17, no. 5, pp. 694–702, 1998.
- [53] K. S. Arun, T. S. Huang, and S. D. Blostein, “Least-Squares Fitting of Two 3-D Point Sets,” *IEEE Transactions on Pattern Analysis and Machine Intelligence*, vol. PAMI-9, no. 5, pp. 698–700, 1987.
- [54] W. H. Press, S. A. Teukolsky, W. T. Vetterling, and B. P. Flannery, *Numerical recipes in C (2nd ed.): the art of scientific computing*. Cambridge University Press, 2 ed., 1992.
- [55] A. S. Householder, “Unitary Triangularization of a Nonsymmetric Matrix,” *J. ACM*, vol. 5, pp. 339–342, oct 1958.

- [56] J. G. F. Francis, “The QR Transformation A Unitary Analogue to the LR Transformation—Part 1,” *The Computer Journal*, vol. 4, pp. 265–271, jan 1961.
- [57] J. G. F. Francis, “The QR Transformation—Part 2,” *The Computer Journal*, vol. 4, pp. 332–345, jan 1962.
- [58] V. N. Kublanovskaya, “On some algorithms for the solution of the complete eigenvalue problem,” *USSR Computational Mathematics and Mathematical Physics*, vol. 1, no. 3, pp. 637–657, 1962.
- [59] W. D. D’Souza, E. L. Madsen, O. Unal, K. K. Vigen, G. R. Frank, and B. R. Thomadsen, “Tissue mimicking materials for a multi-imaging modality prostate phantom,” *Medical Physics*, vol. 28, pp. 688–700, apr 2001.
- [60] T. J. Hall, M. Bilgen, M. F. Insana, and T. A. Krouskop, “Phantom materials for elastography,” *IEEE Transactions on Ultrasonics, Ferroelectrics, and Frequency Control*, vol. 44, no. 6, pp. 1355–1365, 1997.
- [61] U. Lindner, N. Lawrentschuk, R. A. Weersink, O. Raz, E. Hlasny, M. S. Sussman, S. R. Davidson, M. R. Gertner, and J. Trachtenberg, “Construction and Evaluation of an Anatomically Correct Multi-Image Modality Compatible Phantom for Prostate Cancer Focal Ablation,” *The Journal of Urology*, vol. 184, pp. 352–357, jul 2010.
- [62] D. W. Rickey, P. A. Picot, D. A. Christopher, and A. Fenster, “A wall-less vessel phantom for Doppler ultrasound studies,” *Ultrasound in Medicine and Biology*, vol. 21, pp. 1163–1176, jan 1995.
- [63] S. Geisser, “Confidence regions for future realizations,” in *Predictive Inference: An Introduction*, ch. 2.1, pp. 6–10, London: Chapman & Hall, 1993.
- [64] O. Raz, M. A. Haider, S. R. H. Davidson, U. Lindner, E. Hlasny, R. A. Weersink, M. R. Gertner, W. Kucharczyk, S. A. McCluskey, and J. Trachtenberg, “Real-time magnetic resonance imaging-guided focal laser therapy in patients with low-risk prostate cancer,” *European Urology*, vol. 58, no. 1, pp. 173–177, 2010.
- [65] A. Napoli, M. Anzidei, C. De Nunzio, G. Cartocci, V. Panebianco, C. De Dominicis, C. Catalano, F. Petrucci, and C. Leonardo, “Real-time magnetic resonance-guided high-intensity focused ultrasound focal therapy for localised prostate cancer: preliminary experience,” *European Urology*, vol. 63, no. 2, pp. 395–398, 2013.
- [66] H. U. Ahmed, R. G. Hindley, L. Dickinson, A. Freeman, A. P. Kirkham, M. Sahu, R. Scott, C. Allen, J. Van der Meulen, and M. Emberton, “Focal therapy for localised unifocal and multifocal prostate cancer: A prospective development study,” *The Lancet Oncology*, vol. 13, no. 6, pp. 622–632, 2012.
- [67] U. Lindner, R. A. Weersink, M. A. Haider, M. R. Gertner, S. R. H. Davidson, M. Atri, B. Wilson, A. Fenster, and J. Trachtenberg, “Image guided photothermal focal therapy for localized prostate cancer: phase I trial,” *The Journal of Urology*, vol. 182, no. 4, pp. 1371–1377, 2009.

- [68] X. Zhou, K. Jin, S. Qiu, D. Jin, X. Liao, X. Tu, X. Zheng, J. Li, L. Yang, and Q. Wei, "Comparative Effectiveness of Radiotherapy versus Focal Laser Ablation in Patients with Low and Intermediate Risk Localized Prostate Cancer," *Scientific Reports*, vol. 10, no. 1, p. 9112, 2020.
- [69] R. C. Chen, R. Basak, A.-M. Meyer, T.-M. Kuo, W. R. Carpenter, R. P. Agans, J. R. Broughman, B. B. Reeve, M. E. Nielsen, D. S. Usinger, K. C. Spearman, S. Walden, D. Kaleel, M. Anderson, T. Stürmer, and P. A. Godley, "Association Between Choice of Radical Prostatectomy, External Beam Radiotherapy, Brachytherapy, or Active Surveillance and Patient-Reported Quality of Life Among Men With Localized Prostate Cancer," *JAMA*, vol. 317, pp. 1141–1150, mar 2017.
- [70] E. Walser, A. Nance, L. Ynalvez, S. Yong, J. S. Aoughsten, E. J. Eyzaguirre, and S. B. Williams, "Focal Laser Ablation of Prostate Cancer: Results in 120 Patients with Low-to Intermediate-Risk Disease," *Journal of vascular and interventional radiology : JVIR*, vol. 30, pp. 401–409.e2, mar 2019.
- [71] M. Ahdoot, A. H. Lebastchi, B. Turkbey, B. Wood, and P. A. Pinto, "Contemporary treatments in prostate cancer focal therapy," *Current opinion in oncology*, vol. 31, pp. 200–206, may 2019.
- [72] J. Le Nobin, A. B. Rosenkrantz, A. Villers, C. Orczyk, F. M. Deng, J. Melamed, A. Mikheev, H. Rusinek, and S. S. Taneja, "Image Guided Focal Therapy for Magnetic Resonance Imaging Visible Prostate Cancer: Defining a 3-Dimensional Treatment Margin Based on Magnetic Resonance Imaging Histology Co-Registration Analysis," *Journal of Urology*, vol. 194, no. 2, pp. 364–370, 2015.
- [73] M. Piert, P. R. Shankar, J. Montgomery, L. P. Kunju, V. Rogers, J. Siddiqui, T. Rajendiran, J. Hearn, A. George, X. Shao, and M. S. Davenport, "Accuracy of tumor segmentation from multi-parametric prostate MRI and F-choline PET / CT for focal prostate cancer therapy applications," *European Journal of Nuclear Medicine and Molecular Imaging*, vol. 8, no. 23, pp. 1–14, 2018.
- [74] E. Gibson, G. S. Bauman, C. Romagnoli, D. W. Cool, M. Bastian-Jordan, Z. Kassam, M. Gaed, M. Moussa, J. A. Gómez, S. E. Pautler, J. L. Chin, C. Crukley, M. A. Haider, A. Fenster, and A. D. Ward, "Toward prostate cancer contouring guidelines on magnetic resonance imaging: dominant lesion gross and clinical target volume coverage via accurate histology fusion," *International Journal of Radiation Oncology, Biology, Physics*, vol. 96, no. 1, pp. 188–196, 2016.
- [75] T. A. Stamey, F. S. Freiha, J. E. McNeal, E. A. Redwine, A. S. Whittemore, and H. P. Schmid, "Localized prostate cancer. Relationship of tumor volume to clinical significance for treatment of prostate cancer.," *Cancer*, vol. 71, pp. 933–938, feb 1993.
- [76] G. Ploussard, J. I. Epstein, R. Montironi, P. R. Carroll, M. Wirth, M.-O. Grimm, A. S. Bjartell, F. Montorsi, S. J. Freedland, A. Erbersdobler, and T. H. van der Kwast, "The Contemporary Concept of Significant Versus Insignificant Prostate Cancer," *European Urology*, vol. 60, no. 2, pp. 291–303, 2011.

- [77] A. Matoso and J. I. Epstein, “Defining clinically significant prostate cancer on the basis of pathological findings,” *Histopathology*, vol. 74, pp. 135–145, jan 2019.
- [78] G. Wan, Z. Wei, L. Gardi, D. B. Downey, and A. Fenster, “Brachytherapy needle deflection evaluation and correction,” *Medical Physics*, vol. 32, no. 4, pp. 902–909, 2005.

Chapter 5

Conclusions and Future Work

Each chapter of this thesis presented an important step towards developing a remotely actuated, MRI-compatible mechatronic needle guidance system capable of accurately and consistently delivering MR-guided focal laser ablation therapy.

In Chapter 2, the overlap between ablation zones and targeted lesions was quantified on pre- and intra-operative MR images, using non-rigid image registration. The lesions extended at least partially beyond the boundary of the ablation zone in 52% of cases, and the other cases did not achieve a minimum ablation margin of 5 mm around the lesions. The results from this chapter motivated the development of an MRI-compatible needle guidance system to improve targeting accuracy in Chapter 3.

The system described in Chapter 3 is the main contribution of this thesis. A mechatronic needle guidance system for MRI-guided prostate FLA was constructed entirely of non-ferromagnetic materials, with actuation controlled by piezoelectric motors and optical encoders. The system has 4 DOF to align the needle template to targets chosen on MRI, with needle insertion still performed manually by the physician. Rigorous MR-compatibility testing demonstrated no adverse safety risks when using the system in the MRI environment, and image quality was not degraded by the presence of the system when proper protocols were observed. Open-air mean positioning error at the needle tip was 0.80 ± 0.36 mm with a one-sided 95% prediction interval of 1.40 mm. In the MR bore, the mean positioning error at the needle tip was 2.11 ± 1.05 mm with a one-sided 95% prediction interval of 3.84 mm, which

was deemed sufficient for prostate FLA therapy although errors due to needle deflection were not included in the accuracy measurements.

Chapter 4 focused on accounting for the effects of needle deflection by evaluating the accuracy of the system in tissue-mimicking prostate phantoms. To maintain an acceptable level of accuracy, an improved registration method was developed for aligning the needle guidance system with the MRI coordinate system. This allowed the system to guide needles to virtual targets at typical clinical insertion depths with a predicted accuracy of within 4.13 mm, in 95% of future attempts. This represents the total accuracy of the system under idealized conditions and demonstrates the potential utility for accurate delivery of FLA therapy to localized prostate lesions.

We created a remotely actuated system that is capable of accurately delivering needles transperineally to the prostate for FLA therapy, which can also be adapted to other procedures. Its unobtrusive hanging arm design provides more access to the patient than existing systems, and integrating miniature manual needle insertion templates retains haptic feedback for physicians without jeopardizing patient safety. We envision that the system will undergo clinical trials where it will be able to accurately guide needles to lesions in the prostate, reduce FLA procedure times, and maintain patient safety. These objectives will optimize FLA as a technique for the control of localized prostate cancer with minimal treatment-related side effects, allowing it to be meaningfully compared with competing energy modalities for focal therapy.

5.1 Limitations and Future Work

In Chapter 2, the accuracy of the results are limited by segmentation variability and the method of registration. Delineation of the tumour itself is highly variable between clinicians [1] and was not accounted for in this study. The prostate surfaces used for the registration algorithm were difficult to contour in the base and apex regions where contrast is poor, and suffered from low resolution on the DCE images used to visualize the ablation zone. Furthermore, TPS

registration is a surface-based registration algorithm which does not model the internal biomechanical properties of the prostate, and may affect the deformation field since prostate shape can change for a number of reasons between imaging sessions. [2, 3] Future studies should focus on analysing the effects that inter-observer variability in the segmentation of tumours and prostates has on image registration, and incorporating the biomechanical properties of the prostate into non-rigid registration algorithms, perhaps using finite element modelling. [4, 5, 6, 7] Deep learning techniques have shown good potential for segmentation of the prostate on T2W images and identifying lesions on DWI in less than a second. [8, 9] More work needs to be done in adapting deep learning for automated deformable MR-MR prostate registration and motion compensation, and in obtaining larger, more diverse data sets for training of the machine learning models.

In Chapters 3 and 4, the major limitation of the results was that the estimates of needle guidance accuracy were obtained in an idealized experimental setting. While every attempt was made to match the material properties of bulk prostate tissue, the phantoms used were mostly homogeneous with isotropic material properties. To reach a target in a real prostate, the needle must penetrate multiple layers of heterogeneous tissues with complex anisotropic properties. Needle deflection in agar-based phantoms has been estimated at approximately 1.1 mm after 10.0 cm of insertion, [10] compared with up to 2.8 mm of deflection at a depth of 6.0 cm that was measured *in vivo* during prostate biopsy and brachytherapy procedures. [11] One promising study reported that the majority of needle deflection occurs during initial penetration, [10] suggesting that it may be possible to predict the effects of needle deflection before the total insertion depth is reached. Phantoms are also inanimate objects that do not move, whereas a patient may move voluntarily or involuntarily for a number of reasons.

In order to fully account for needle deflection and patient motion, our system should proceed to clinical FLA trials, where its effect on needle guidance accuracy, procedure times, and treatment-related morbidity can be quantified. Future research should attempt to implement a model which predicts and compensates for needle deflection in transperineal prostate interven-

tions and mitigates the impact of patient motion on targeting accuracy. In addition to automated prostate and lesion segmentation, deep learning tools may also be useful for these tasks. Deep learning-based needle segmentation could monitor the needle's trajectory in real time and aid in guiding the needle to the tumour target, even if the patient moves. Furthermore, the potential of inserting multiple needles through the guidance templates at once for coverage of larger lesions should be studied, as well as the benefits of using a steerable cannula to help guide the needle to the target. This research may further improve the accuracy of the system for needle guidance and improve the efficacy of FLA for control of localized PCa.

Bibliography

- [1] G. M. Villeirs, K. Van Vaerenbergh, L. Vakaet, S. Bral, F. Claus, W. J. De Neve, K. L. Verstraete, and G. O. De Meerleer, “Interobserver delineation variation using CT versus combined CT + MRI in intensity-modulated radiotherapy for prostate cancer,” *Strahlentherapie und Onkologie*, vol. 181, pp. 424–430, jul 2005.
- [2] M. van Herk, A. Bruce, A. P. G. Kroes, T. Shouman, A. Touw, and J. V. Lebesque, “Quantification of organ motion during conformal radiotherapy of the prostate by three dimensional image registration,” *International Journal of Radiation Oncology, Biology, Physics*, vol. 33, no. 5, pp. 1311–1320, 1995.
- [3] A. M. Nichol, K. K. Brock, G. A. Lockwood, D. J. Moseley, T. Rosewall, P. R. Warde, C. N. Catton, and D. A. Jaffray, “A magnetic resonance imaging study of prostate deformation relative to implanted gold fiducial markers,” *International Journal of Radiation Oncology, Biology, Physics*, vol. 67, no. 1, pp. 48–56, 2007.
- [4] J. M. Hensel, C. Ménard, P. W. M. Chung, M. F. Milosevic, A. Kirilova, J. L. Moseley, M. A. Haider, and K. K. Brock, “Development of multiorgan finite element-based prostate deformation model enabling registration of endorectal coil magnetic resonance imaging for radiotherapy planning,” *International Journal of Radiation Oncology, Biology, Physics*, vol. 68, no. 5, pp. 1522–1528, 2007.
- [5] B. Marami, S. Sirouspour, S. Ghoul, J. Cepek, S. R. H. Davidson, D. W. Capson, J. Trachtenberg, and A. Fenster, “Elastic registration of prostate MR images based on estimation of deformation states,” *Medical Image Analysis*, vol. 21, no. 1, pp. 87–103, 2015.
- [6] A. Bharatha, M. Hirose, N. Hata, S. K. Warfield, M. Ferrant, K. H. Zou, E. Suarez-Santana, J. Ruiz-Alzola, A. D’Amico, R. A. Cormack, R. Kikinis, F. A. Jolesz, and C. M. Tempany, “Evaluation of three-dimensional finite element-based deformable registration of pre- and intraoperative prostate imaging,” *Medical Physics*, vol. 28, no. 12, pp. 2551–2560, 2001.
- [7] A. Mohamed, C. Davatzikos, and R. Taylor, “A combined statistical and biomechanical model for estimation of intra-operative prostate deformation,” in *Medical Image Computing and Computer-Assisted Intervention — MICCAI 2002* (T. Dohi and R. Kikinis, eds.), vol. 2489, pp. 452–460, Springer, Berlin, Heidelberg, 2002.
- [8] H. Li, C. H. Lee, D. Chia, Z. Lin, W. Huang, and C. H. Tan, “Machine Learning in Prostate MRI for Prostate Cancer: Current Status and Future Opportunities,” 2022.
- [9] B. Turkbey and M. A. Haider, “Deep learning-based artificial intelligence applications in prostate MRI: brief summary,” *The British Journal of Radiology*, vol. 95, p. 20210563, dec 2021.
- [10] J. Cepek, B. A. Chronik, U. Lindner, J. Trachtenberg, S. R. H. Davidson, J. Bax, and A. Fenster, “A system for MRI-guided transperineal delivery of needles to the prostate for focal therapy,” *Medical Physics*, vol. 40, no. 1, p. 012304, 2013.

- [11] G. Wan, Z. Wei, L. Gardi, D. B. Downey, and A. Fenster, “Brachytherapy needle deflection evaluation and correction,” *Medical Physics*, vol. 32, no. 4, pp. 902–909, 2005.

Appendix A

Mechatronic System Kinematics

The variables used in the kinematic equations are defined in Figure A.1. To simplify the equations, the pose of the needle guide is calculated with respect to a “home” position, which is defined as the pose created when the top links on the system are horizontal and the bottom links are vertical. This is the pose that was used to register the system co-ordinate system to the MRI co-ordinate system. Forward kinematic equations are used to calculate the position (p^n) and direction ($\hat{\mathbf{v}}^n$) of the needle guide. The first step in the forward kinematics is to compute the position of the end of each arm (see Figure A.1b). For the front arm, θ_1 and θ_2 will be θ_{Ft} and θ_{Fb} respectively (measured from the encoders), and for the rear arm, θ_1 and θ_2 will be θ_{Rt} and θ_{Rb} respectively. The displacement (x_2, y_2) of the end effector from the home position is given by

$$x_2 = L_1 \cos \theta_1 + L_2 \sin \left(\theta_2 - \frac{\pi}{2} \right) - L_1 \quad (\text{A.1a})$$

$$y_2 = L_1 \sin \theta_1 + L_2 \cos \left(\theta_2 - \frac{\pi}{2} \right) + L_2 \quad (\text{A.1b})$$

Once the position of the end of the front arm (x_F, y_F) and rear arm (x_R, y_R) are computed, the trajectory of the needle guide ($\hat{\mathbf{v}}^n$) can be calculated with the known constant distance between the two arms D using

$$\mathbf{v}^n = (x_F - x_R, y_F - y_R, D) \quad (\text{A.2a})$$

$$\hat{\mathbf{v}}^n = \frac{\mathbf{v}^n}{\|\mathbf{v}^n\|} \quad (\text{A.2b})$$

The position of the needle tip (p^n) can be calculated using

$$\begin{aligned} \alpha_x &= h_x * \frac{-\hat{\mathbf{v}}_x^n}{\|(\hat{\mathbf{v}}_x^n, \hat{\mathbf{v}}_z^n)\|}, & \alpha_y &= h_y * \frac{-\hat{\mathbf{v}}_y^n}{\|(\hat{\mathbf{v}}_y^n, \hat{\mathbf{v}}_z^n)\|} \\ \beta_x &= h_x * \frac{\hat{\mathbf{v}}_z^n}{\|(\hat{\mathbf{v}}_x^n, \hat{\mathbf{v}}_z^n)\|}, & \beta_y &= h_y * \frac{\hat{\mathbf{v}}_z^n}{\|(\hat{\mathbf{v}}_y^n, \hat{\mathbf{v}}_z^n)\|} \\ p_x^n &= x_F + \beta_x + \alpha_y * \frac{\hat{\mathbf{v}}_x^n}{\|(\hat{\mathbf{v}}_x^n, \hat{\mathbf{v}}_z^n)\|} + \hat{\mathbf{v}}_x^n * h_z \end{aligned} \quad (\text{A.3a})$$

$$p_y^n = y_F + \beta_y + \hat{\mathbf{v}}_y^n * h_z \quad (\text{A.3b})$$

$$p_z^n = \alpha_x + \alpha_y * \frac{\hat{\mathbf{v}}_z^n}{\|(\hat{\mathbf{v}}_x^n, \hat{\mathbf{v}}_z^n)\|} + \hat{\mathbf{v}}_z^n * h_z \quad (\text{A.3c})$$

where h_x and h_y are the horizontal and vertical displacements, respectively, of the selected hole location with respect to the system's origin, and h_z is the depth of needle insertion with respect to the system's origin.

Inverse kinematic equations are used to calculate the values of the four encoders given a needle entry point (p^e) and tip position p^t (or any two points along the needle's axis). The trajectory of the needle is defined as

$$\hat{\mathbf{v}}^n = \frac{p^t - p^e}{\|p^t - p^e\|} \quad (\text{A.4})$$

To calculate the position of the arm end effectors, the following intermediate variables were used:

$$\alpha_x = \begin{cases} 0, \|(\hat{\mathbf{v}}_x^n, \hat{\mathbf{v}}_z^n)\| = 0 \\ h_x * \frac{-\hat{\mathbf{v}}_x^n}{\|(\hat{\mathbf{v}}_x^n, \hat{\mathbf{v}}_z^n)\|}, \text{ otherwise} \end{cases}, \quad \alpha_y = \begin{cases} 0, \|(\hat{\mathbf{v}}_y^n, \hat{\mathbf{v}}_z^n)\| = 0 \\ h_y * \frac{-\hat{\mathbf{v}}_y^n}{\|(\hat{\mathbf{v}}_y^n, \hat{\mathbf{v}}_z^n)\|}, \text{ otherwise} \end{cases} \quad (\text{A.5a})$$

$$\beta_x = \begin{cases} h_x, \|(\hat{\mathbf{v}}_x^n, \hat{\mathbf{v}}_z^n)\| = 0 \\ h_x * \frac{\hat{\mathbf{v}}_z^n}{\|(\hat{\mathbf{v}}_x^n, \hat{\mathbf{v}}_z^n)\|}, \text{ otherwise} \end{cases}, \beta_y = \begin{cases} h_y, \|(\hat{\mathbf{v}}_y^n, \hat{\mathbf{v}}_z^n)\| = 0 \\ h_y * \frac{\hat{\mathbf{v}}_z^n}{\|(\hat{\mathbf{v}}_y^n, \hat{\mathbf{v}}_z^n)\|}, \text{ otherwise} \end{cases} \quad (\text{A.5b})$$

$$z^0 = \begin{cases} \alpha_x \alpha_y, \|(\hat{\mathbf{v}}_x^n, \hat{\mathbf{v}}_z^n)\| = 0 \\ \alpha_x + \alpha_y * \frac{\hat{\mathbf{v}}_z^n}{\|(\hat{\mathbf{v}}_x^n, \hat{\mathbf{v}}_z^n)\|}, \text{ otherwise} \end{cases} \quad (\text{A.5c})$$

$$t = \frac{z^0 - p_z^t}{\hat{\mathbf{v}}_z^n}, \quad u = \frac{-D}{\hat{\mathbf{v}}_z^n} \quad (\text{A.5d})$$

$$x' = p_x^t + \hat{\mathbf{v}}_x^n * t, \quad y' = p_y^t + \hat{\mathbf{v}}_y^n * t \quad (\text{A.5e})$$

The position of the end of the front arm becomes

$$x_F = x' - \beta_x - \alpha_y * \frac{\hat{\mathbf{v}}_x^n}{\|(\hat{\mathbf{v}}_x^n, \hat{\mathbf{v}}_z^n)\|}, \quad y_F = y' - \beta_y \quad (\text{A.6})$$

And the position of the end of the rear arm becomes

$$x_R = x_F + \hat{\mathbf{v}}_x^n * u, \quad y_R = y_F + \hat{\mathbf{v}}_y^n * u \quad (\text{A.7})$$

Once the position of the end of the arm is known, the values of the joint angles for each arm can be calculated using

$$\theta_2 = \arccos \frac{x^2 + y^2 - L_1^2 - L_2^2}{2 * L_1 * L_2} \quad (\text{A.8a})$$

$$\theta_1 = \arctan \frac{y * (L_1 + L_2 * \cos \theta_B) - x * L_2 * \sin \theta_B}{x * (L_1 + L_2 * \cos \theta_B) + y * L_2 * \sin \theta_B} + \frac{\pi}{2} \quad (\text{A.8b})$$

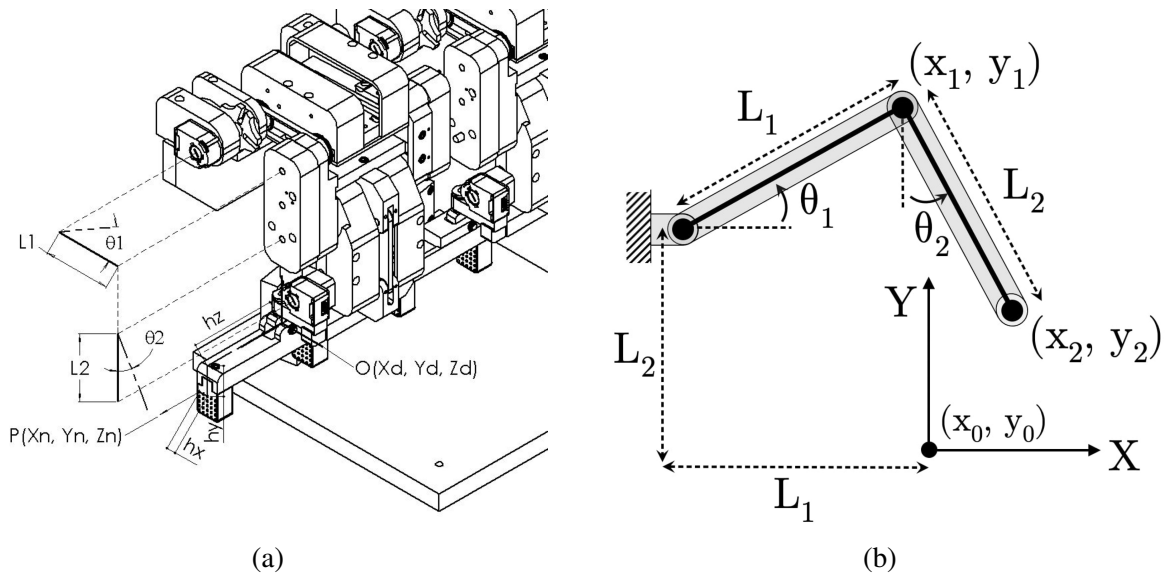


Figure A.1: System kinematics. a Variables used in the kinematic equations. θ_1 and θ_2 are the angles of the links, measured by encoders on each arm, used to calculate the pose, (p^n) and (\hat{v}^n) , of the needle guide in the forwards kinematics. Conversely, in the inverse kinematics, the pose of the needle guide is used to calculate the angles of the links. O is the origin of the system's coordinate system. b Simplified diagram of the two-link 2D kinematic chain. The origin (x_0, y_0) is placed at the location of (x_2, y_2) in the “base” pose (both θ_1 and θ_2 are zero), so that the kinematics provide the displacement of the end effector from the base pose. h_x , h_y , and h_z are the fixed displacements of the hole in the needle guide from the end-effector of the front arm.

Appendix B

Permissions

B.1 Permission to reproduce previously published material in Chapters 2, 3, and 4

JOHN WILEY AND SONS LICENSE TERMS AND CONDITIONS

Apr 29, 2023

This Agreement between Mr. Eric Knull ("You") and John Wiley and Sons ("John Wiley and Sons") consists of your license details and the terms and conditions provided by John Wiley and Sons and Copyright Clearance Center.

License Number 5538101347073

License date Apr 29, 2023

Licensed Content
Publisher John Wiley and Sons

Licensed Content
Publication Medical Physics

Licensed Content
Title Evaluation of tumor coverage after MR-guided prostate focal laser
ablation therapy

Licensed Content
Author Aaron Fenster, Aritrick Chatterjee, Serkan Guneyli, et al

Licensed Content
Date Dec 7, 2018

Licensed Content
Volume 46

Licensed Content
Issue 2

Licensed Content
Pages 11

Type of use Dissertation/Thesis

Requestor type Author of this Wiley article

Format Print and electronic

Portion Full article

Will you be
translating? No

Title NOVEL MAGNETIC RESONANCE IMAGING-COMPATIBLE
MECHATRONIC NEEDLE GUIDANCE SYSTEM FOR PROSTATE
FOCAL LASER ABLATION THERAPY

Institution name The University of Western Ontario

Expected
presentation date Jul 2023

Mr. Eric Knull
1151 Richmond Street North

Requestor Location
London, ON N6A 5B7
Canada
Attn: Mr. Eric Knull

Publisher Tax ID EU826007151

Total 0.00 CAD

Terms and Conditions

TERMS AND CONDITIONS

This copyrighted material is owned by or exclusively licensed to John Wiley & Sons, Inc. or one of its group companies (each a "Wiley Company") or handled on behalf of a society with which a Wiley Company has exclusive publishing rights in relation to a particular work (collectively "WILEY"). By clicking "accept" in connection with completing this licensing transaction, you agree that the following terms and conditions apply to this transaction (along with the billing and payment terms and conditions established by the Copyright Clearance Center Inc., ("CCC's Billing and Payment terms and conditions"), at the time that you opened your RightsLink account (these are available at any time at <http://myaccount.copyright.com>).

Terms and Conditions

- The materials you have requested permission to reproduce or reuse (the "Wiley Materials") are protected by copyright.
- You are hereby granted a personal, non-exclusive, non-sub licensable (on a stand-alone basis), non-transferable, worldwide, limited license to reproduce the Wiley Materials for the purpose specified in the licensing process. This license, **and any CONTENT (PDF or image file) purchased as part of your order**, is for a one-time use only and limited to any maximum distribution number specified in the license. The first instance of republication or reuse granted by this license must be completed within two years of the date of the grant of this license (although copies prepared before the end date may be distributed thereafter). The Wiley Materials shall not be used in any other manner or for any other purpose, beyond what is granted in the license. Permission is granted subject to an appropriate acknowledgement given to the author, title of the material/book/journal and the publisher. You shall also duplicate the copyright notice that appears in the Wiley publication in your use of the Wiley Material. Permission is also granted on the understanding that nowhere in the text is a previously published source acknowledged for all or part of this Wiley Material. Any third party content is expressly excluded from this permission.
- With respect to the Wiley Materials, all rights are reserved. Except as expressly granted by the terms of the license, no part of the Wiley Materials may be copied, modified, adapted (except for minor reformatting required by the new Publication), translated, reproduced, transferred or distributed, in any form or by any means, and no derivative works may be made based on the Wiley Materials without the prior permission of the respective copyright owner. **For STM Signatory Publishers clearing permission under the terms of the [STM Permissions Guidelines](#) only, the terms of the license are extended to include subsequent editions and for editions in other languages, provided such editions are for the work as a whole in situ and does not involve the separate exploitation of the permitted figures or extracts,** You may not alter, remove or suppress in any manner any copyright, trademark or other notices displayed by the Wiley Materials. You may not license, rent, sell, loan, lease, pledge, offer as security, transfer or assign the Wiley Materials on a stand-alone basis, or any of the rights granted to you hereunder to any other person.
- The Wiley Materials and all of the intellectual property rights therein shall at all times

remain the exclusive property of John Wiley & Sons Inc, the Wiley Companies, or their respective licensors, and your interest therein is only that of having possession of and the right to reproduce the Wiley Materials pursuant to Section 2 herein during the continuance of this Agreement. You agree that you own no right, title or interest in or to the Wiley Materials or any of the intellectual property rights therein. You shall have no rights hereunder other than the license as provided for above in Section 2. No right, license or interest to any trademark, trade name, service mark or other branding ("Marks") of WILEY or its licensors is granted hereunder, and you agree that you shall not assert any such right, license or interest with respect thereto

- NEITHER WILEY NOR ITS LICENSORS MAKES ANY WARRANTY OR REPRESENTATION OF ANY KIND TO YOU OR ANY THIRD PARTY, EXPRESS, IMPLIED OR STATUTORY, WITH RESPECT TO THE MATERIALS OR THE ACCURACY OF ANY INFORMATION CONTAINED IN THE MATERIALS, INCLUDING, WITHOUT LIMITATION, ANY IMPLIED WARRANTY OF MERCHANTABILITY, ACCURACY, SATISFACTORY QUALITY, FITNESS FOR A PARTICULAR PURPOSE, USABILITY, INTEGRATION OR NON-INFRINGEMENT AND ALL SUCH WARRANTIES ARE HEREBY EXCLUDED BY WILEY AND ITS LICENSORS AND WAIVED BY YOU.
- WILEY shall have the right to terminate this Agreement immediately upon breach of this Agreement by you.
- You shall indemnify, defend and hold harmless WILEY, its Licensors and their respective directors, officers, agents and employees, from and against any actual or threatened claims, demands, causes of action or proceedings arising from any breach of this Agreement by you.
- IN NO EVENT SHALL WILEY OR ITS LICENSORS BE LIABLE TO YOU OR ANY OTHER PARTY OR ANY OTHER PERSON OR ENTITY FOR ANY SPECIAL, CONSEQUENTIAL, INCIDENTAL, INDIRECT, EXEMPLARY OR PUNITIVE DAMAGES, HOWEVER CAUSED, ARISING OUT OF OR IN CONNECTION WITH THE DOWNLOADING, PROVISIONING, VIEWING OR USE OF THE MATERIALS REGARDLESS OF THE FORM OF ACTION, WHETHER FOR BREACH OF CONTRACT, BREACH OF WARRANTY, TORT, NEGLIGENCE, INFRINGEMENT OR OTHERWISE (INCLUDING, WITHOUT LIMITATION, DAMAGES BASED ON LOSS OF PROFITS, DATA, FILES, USE, BUSINESS OPPORTUNITY OR CLAIMS OF THIRD PARTIES), AND WHETHER OR NOT THE PARTY HAS BEEN ADVISED OF THE POSSIBILITY OF SUCH DAMAGES. THIS LIMITATION SHALL APPLY NOTWITHSTANDING ANY FAILURE OF ESSENTIAL PURPOSE OF ANY LIMITED REMEDY PROVIDED HEREIN.
- Should any provision of this Agreement be held by a court of competent jurisdiction to be illegal, invalid, or unenforceable, that provision shall be deemed amended to achieve as nearly as possible the same economic effect as the original provision, and the legality, validity and enforceability of the remaining provisions of this Agreement shall not be affected or impaired thereby.
- The failure of either party to enforce any term or condition of this Agreement shall not

constitute a waiver of either party's right to enforce each and every term and condition of this Agreement. No breach under this agreement shall be deemed waived or excused by either party unless such waiver or consent is in writing signed by the party granting such waiver or consent. The waiver by or consent of a party to a breach of any provision of this Agreement shall not operate or be construed as a waiver of or consent to any other or subsequent breach by such other party.

- This Agreement may not be assigned (including by operation of law or otherwise) by you without WILEY's prior written consent.
- Any fee required for this permission shall be non-refundable after thirty (30) days from receipt by the CCC.
- These terms and conditions together with CCC's Billing and Payment terms and conditions (which are incorporated herein) form the entire agreement between you and WILEY concerning this licensing transaction and (in the absence of fraud) supersedes all prior agreements and representations of the parties, oral or written. This Agreement may not be amended except in writing signed by both parties. This Agreement shall be binding upon and inure to the benefit of the parties' successors, legal representatives, and authorized assigns.
- In the event of any conflict between your obligations established by these terms and conditions and those established by CCC's Billing and Payment terms and conditions, these terms and conditions shall prevail.
- WILEY expressly reserves all rights not specifically granted in the combination of (i) the license details provided by you and accepted in the course of this licensing transaction, (ii) these terms and conditions and (iii) CCC's Billing and Payment terms and conditions.
- This Agreement will be void if the Type of Use, Format, Circulation, or Requestor Type was misrepresented during the licensing process.
- This Agreement shall be governed by and construed in accordance with the laws of the State of New York, USA, without regards to such state's conflict of law rules. Any legal action, suit or proceeding arising out of or relating to these Terms and Conditions or the breach thereof shall be instituted in a court of competent jurisdiction in New York County in the State of New York in the United States of America and each party hereby consents and submits to the personal jurisdiction of such court, waives any objection to venue in such court and consents to service of process by registered or certified mail, return receipt requested, at the last known address of such party.

WILEY OPEN ACCESS TERMS AND CONDITIONS

Wiley Publishes Open Access Articles in fully Open Access Journals and in Subscription journals offering Online Open. Although most of the fully Open Access journals publish open access articles under the terms of the Creative Commons Attribution (CC BY) License only, the subscription journals and a few of the Open Access Journals offer a choice of Creative Commons Licenses. The license type is clearly identified on the article.

The Creative Commons Attribution License

The [Creative Commons Attribution License \(CC-BY\)](#) allows users to copy, distribute and transmit an article, adapt the article and make commercial use of the article. The CC-BY license permits commercial and non-

Creative Commons Attribution Non-Commercial License

The [Creative Commons Attribution Non-Commercial \(CC-BY-NC\)License](#) permits use, distribution and reproduction in any medium, provided the original work is properly cited and is not used for commercial purposes.(see below)

Creative Commons Attribution-Non-Commercial-NoDerivs License

The [Creative Commons Attribution Non-Commercial-NoDerivs License](#) (CC-BY-NC-ND) permits use, distribution and reproduction in any medium, provided the original work is properly cited, is not used for commercial purposes and no modifications or adaptations are made. (see below)

Use by commercial "for-profit" organizations

Use of Wiley Open Access articles for commercial, promotional, or marketing purposes requires further explicit permission from Wiley and will be subject to a fee.

Further details can be found on Wiley Online Library <http://olabout.wiley.com/WileyCDA/Section/id-410895.html>

Other Terms and Conditions:

v1.10 Last updated September 2015

Questions? customercare@copyright.com.

JOHN WILEY AND SONS LICENSE TERMS AND CONDITIONS

Apr 29, 2023

This Agreement between Mr. Eric Knull ("You") and John Wiley and Sons ("John Wiley and Sons") consists of your license details and the terms and conditions provided by John Wiley and Sons and Copyright Clearance Center.

License Number 5538101046083

License date Apr 29, 2023

Licensed Content
Publisher John Wiley and Sons

Licensed Content
Publication Medical Physics

Licensed Content
Title Design and validation of an MRI-compatible mechatronic system for
needle delivery to localized prostate cancer

Licensed Content
Author Eric Knull, Jeffrey Scott Bax, Claire Keun Sun Park, et al

Licensed Content
Date Jul 21, 2021

Licensed Content
Volume 48

Licensed Content
Issue 9

Licensed Content
Pages 17

Type of use Dissertation/Thesis

Requestor type Author of this Wiley article

Format Print and electronic

Portion Full article

Will you be
translating? No

Title NOVEL MAGNETIC RESONANCE IMAGING-COMPATIBLE
MECHATRONIC NEEDLE GUIDANCE SYSTEM FOR PROSTATE
FOCAL LASER ABLATION THERAPY

Institution name The University of Western Ontario

Expected
presentation date Jul 2023

Mr. Eric Knull
1151 Richmond Street North

Requestor Location
London, ON N6A 5B7
Canada
Attn: Mr. Eric Knull

Publisher Tax ID EU826007151

Total 0.00 CAD

Terms and Conditions

TERMS AND CONDITIONS

This copyrighted material is owned by or exclusively licensed to John Wiley & Sons, Inc. or one of its group companies (each a "Wiley Company") or handled on behalf of a society with which a Wiley Company has exclusive publishing rights in relation to a particular work (collectively "WILEY"). By clicking "accept" in connection with completing this licensing transaction, you agree that the following terms and conditions apply to this transaction (along with the billing and payment terms and conditions established by the Copyright Clearance Center Inc., ("CCC's Billing and Payment terms and conditions"), at the time that you opened your RightsLink account (these are available at any time at <http://myaccount.copyright.com>).

Terms and Conditions

- The materials you have requested permission to reproduce or reuse (the "Wiley Materials") are protected by copyright.
- You are hereby granted a personal, non-exclusive, non-sub licensable (on a stand-alone basis), non-transferable, worldwide, limited license to reproduce the Wiley Materials for the purpose specified in the licensing process. This license, **and any CONTENT (PDF or image file) purchased as part of your order**, is for a one-time use only and limited to any maximum distribution number specified in the license. The first instance of republication or reuse granted by this license must be completed within two years of the date of the grant of this license (although copies prepared before the end date may be distributed thereafter). The Wiley Materials shall not be used in any other manner or for any other purpose, beyond what is granted in the license. Permission is granted subject to an appropriate acknowledgement given to the author, title of the material/book/journal and the publisher. You shall also duplicate the copyright notice that appears in the Wiley publication in your use of the Wiley Material. Permission is also granted on the understanding that nowhere in the text is a previously published source acknowledged for all or part of this Wiley Material. Any third party content is expressly excluded from this permission.
- With respect to the Wiley Materials, all rights are reserved. Except as expressly granted by the terms of the license, no part of the Wiley Materials may be copied, modified, adapted (except for minor reformatting required by the new Publication), translated, reproduced, transferred or distributed, in any form or by any means, and no derivative works may be made based on the Wiley Materials without the prior permission of the respective copyright owner. **For STM Signatory Publishers clearing permission under the terms of the [STM Permissions Guidelines](#) only, the terms of the license are extended to include subsequent editions and for editions in other languages, provided such editions are for the work as a whole in situ and does not involve the separate exploitation of the permitted figures or extracts,** You may not alter, remove or suppress in any manner any copyright, trademark or other notices displayed by the Wiley Materials. You may not license, rent, sell, loan, lease, pledge, offer as security, transfer or assign the Wiley Materials on a stand-alone basis, or any of the rights granted to you hereunder to any other person.
- The Wiley Materials and all of the intellectual property rights therein shall at all times

remain the exclusive property of John Wiley & Sons Inc, the Wiley Companies, or their respective licensors, and your interest therein is only that of having possession of and the right to reproduce the Wiley Materials pursuant to Section 2 herein during the continuance of this Agreement. You agree that you own no right, title or interest in or to the Wiley Materials or any of the intellectual property rights therein. You shall have no rights hereunder other than the license as provided for above in Section 2. No right, license or interest to any trademark, trade name, service mark or other branding ("Marks") of WILEY or its licensors is granted hereunder, and you agree that you shall not assert any such right, license or interest with respect thereto

- NEITHER WILEY NOR ITS LICENSORS MAKES ANY WARRANTY OR REPRESENTATION OF ANY KIND TO YOU OR ANY THIRD PARTY, EXPRESS, IMPLIED OR STATUTORY, WITH RESPECT TO THE MATERIALS OR THE ACCURACY OF ANY INFORMATION CONTAINED IN THE MATERIALS, INCLUDING, WITHOUT LIMITATION, ANY IMPLIED WARRANTY OF MERCHANTABILITY, ACCURACY, SATISFACTORY QUALITY, FITNESS FOR A PARTICULAR PURPOSE, USABILITY, INTEGRATION OR NON-INFRINGEMENT AND ALL SUCH WARRANTIES ARE HEREBY EXCLUDED BY WILEY AND ITS LICENSORS AND WAIVED BY YOU.
- WILEY shall have the right to terminate this Agreement immediately upon breach of this Agreement by you.
- You shall indemnify, defend and hold harmless WILEY, its Licensors and their respective directors, officers, agents and employees, from and against any actual or threatened claims, demands, causes of action or proceedings arising from any breach of this Agreement by you.
- IN NO EVENT SHALL WILEY OR ITS LICENSORS BE LIABLE TO YOU OR ANY OTHER PARTY OR ANY OTHER PERSON OR ENTITY FOR ANY SPECIAL, CONSEQUENTIAL, INCIDENTAL, INDIRECT, EXEMPLARY OR PUNITIVE DAMAGES, HOWEVER CAUSED, ARISING OUT OF OR IN CONNECTION WITH THE DOWNLOADING, PROVISIONING, VIEWING OR USE OF THE MATERIALS REGARDLESS OF THE FORM OF ACTION, WHETHER FOR BREACH OF CONTRACT, BREACH OF WARRANTY, TORT, NEGLIGENCE, INFRINGEMENT OR OTHERWISE (INCLUDING, WITHOUT LIMITATION, DAMAGES BASED ON LOSS OF PROFITS, DATA, FILES, USE, BUSINESS OPPORTUNITY OR CLAIMS OF THIRD PARTIES), AND WHETHER OR NOT THE PARTY HAS BEEN ADVISED OF THE POSSIBILITY OF SUCH DAMAGES. THIS LIMITATION SHALL APPLY NOTWITHSTANDING ANY FAILURE OF ESSENTIAL PURPOSE OF ANY LIMITED REMEDY PROVIDED HEREIN.
- Should any provision of this Agreement be held by a court of competent jurisdiction to be illegal, invalid, or unenforceable, that provision shall be deemed amended to achieve as nearly as possible the same economic effect as the original provision, and the legality, validity and enforceability of the remaining provisions of this Agreement shall not be affected or impaired thereby.
- The failure of either party to enforce any term or condition of this Agreement shall not

constitute a waiver of either party's right to enforce each and every term and condition of this Agreement. No breach under this agreement shall be deemed waived or excused by either party unless such waiver or consent is in writing signed by the party granting such waiver or consent. The waiver by or consent of a party to a breach of any provision of this Agreement shall not operate or be construed as a waiver of or consent to any other or subsequent breach by such other party.

- This Agreement may not be assigned (including by operation of law or otherwise) by you without WILEY's prior written consent.
- Any fee required for this permission shall be non-refundable after thirty (30) days from receipt by the CCC.
- These terms and conditions together with CCC's Billing and Payment terms and conditions (which are incorporated herein) form the entire agreement between you and WILEY concerning this licensing transaction and (in the absence of fraud) supersedes all prior agreements and representations of the parties, oral or written. This Agreement may not be amended except in writing signed by both parties. This Agreement shall be binding upon and inure to the benefit of the parties' successors, legal representatives, and authorized assigns.
- In the event of any conflict between your obligations established by these terms and conditions and those established by CCC's Billing and Payment terms and conditions, these terms and conditions shall prevail.
- WILEY expressly reserves all rights not specifically granted in the combination of (i) the license details provided by you and accepted in the course of this licensing transaction, (ii) these terms and conditions and (iii) CCC's Billing and Payment terms and conditions.
- This Agreement will be void if the Type of Use, Format, Circulation, or Requestor Type was misrepresented during the licensing process.
- This Agreement shall be governed by and construed in accordance with the laws of the State of New York, USA, without regards to such state's conflict of law rules. Any legal action, suit or proceeding arising out of or relating to these Terms and Conditions or the breach thereof shall be instituted in a court of competent jurisdiction in New York County in the State of New York in the United States of America and each party hereby consents and submits to the personal jurisdiction of such court, waives any objection to venue in such court and consents to service of process by registered or certified mail, return receipt requested, at the last known address of such party.

WILEY OPEN ACCESS TERMS AND CONDITIONS

Wiley Publishes Open Access Articles in fully Open Access Journals and in Subscription journals offering Online Open. Although most of the fully Open Access journals publish open access articles under the terms of the Creative Commons Attribution (CC BY) License only, the subscription journals and a few of the Open Access Journals offer a choice of Creative Commons Licenses. The license type is clearly identified on the article.

The Creative Commons Attribution License

The [Creative Commons Attribution License \(CC-BY\)](#) allows users to copy, distribute and transmit an article, adapt the article and make commercial use of the article. The CC-BY license permits commercial and non-

Creative Commons Attribution Non-Commercial License

The [Creative Commons Attribution Non-Commercial \(CC-BY-NC\)License](#) permits use, distribution and reproduction in any medium, provided the original work is properly cited and is not used for commercial purposes.(see below)

Creative Commons Attribution-Non-Commercial-NoDerivs License

The [Creative Commons Attribution Non-Commercial-NoDerivs License](#) (CC-BY-NC-ND) permits use, distribution and reproduction in any medium, provided the original work is properly cited, is not used for commercial purposes and no modifications or adaptations are made. (see below)

Use by commercial "for-profit" organizations

Use of Wiley Open Access articles for commercial, promotional, or marketing purposes requires further explicit permission from Wiley and will be subject to a fee.

Further details can be found on Wiley Online Library <http://olabout.wiley.com/WileyCDA/Section/id-410895.html>

Other Terms and Conditions:

v1.10 Last updated September 2015

Questions? customercare@copyright.com.

JOHN WILEY AND SONS LICENSE TERMS AND CONDITIONS

Apr 29, 2023

This Agreement between Mr. Eric Knull ("You") and John Wiley and Sons ("John Wiley and Sons") consists of your license details and the terms and conditions provided by John Wiley and Sons and Copyright Clearance Center.

License Number 5538110023677

License date Apr 29, 2023

Licensed Content
Publisher John Wiley and Sons

Licensed Content
Publication Medical Physics

Licensed Content
Title Toward mechatronic MRI-guided focal laser ablation of the prostate:
Robust registration for improved needle delivery

Licensed Content
Author Eric Knull, Claire Keun Sun Park, Jeffrey Bax, et al

Licensed Content
Date Jan 19, 2023

Licensed Content
Volume 50

Licensed Content
Issue 3

Licensed Content
Pages 15

Type of use Dissertation/Thesis

Requestor type Author of this Wiley article

Format Print and electronic

Portion Full article

Will you be
translating? No

Title NOVEL MAGNETIC RESONANCE IMAGING-COMPATIBLE
MECHATRONIC NEEDLE GUIDANCE SYSTEM FOR PROSTATE
FOCAL LASER ABLATION THERAPY

Institution name The University of Western Ontario

Expected
presentation date Jul 2023

Mr. Eric Knull
1151 Richmond Street North

Requestor Location
London, ON N6A 5B7
Canada
Attn: Mr. Eric Knull

Publisher Tax ID EU826007151

Total 0.00 CAD

Terms and Conditions

TERMS AND CONDITIONS

This copyrighted material is owned by or exclusively licensed to John Wiley & Sons, Inc. or one of its group companies (each a "Wiley Company") or handled on behalf of a society with which a Wiley Company has exclusive publishing rights in relation to a particular work (collectively "WILEY"). By clicking "accept" in connection with completing this licensing transaction, you agree that the following terms and conditions apply to this transaction (along with the billing and payment terms and conditions established by the Copyright Clearance Center Inc., ("CCC's Billing and Payment terms and conditions"), at the time that you opened your RightsLink account (these are available at any time at <http://myaccount.copyright.com>).

Terms and Conditions

- The materials you have requested permission to reproduce or reuse (the "Wiley Materials") are protected by copyright.
- You are hereby granted a personal, non-exclusive, non-sub licensable (on a stand-alone basis), non-transferable, worldwide, limited license to reproduce the Wiley Materials for the purpose specified in the licensing process. This license, **and any CONTENT (PDF or image file) purchased as part of your order**, is for a one-time use only and limited to any maximum distribution number specified in the license. The first instance of republication or reuse granted by this license must be completed within two years of the date of the grant of this license (although copies prepared before the end date may be distributed thereafter). The Wiley Materials shall not be used in any other manner or for any other purpose, beyond what is granted in the license. Permission is granted subject to an appropriate acknowledgement given to the author, title of the material/book/journal and the publisher. You shall also duplicate the copyright notice that appears in the Wiley publication in your use of the Wiley Material. Permission is also granted on the understanding that nowhere in the text is a previously published source acknowledged for all or part of this Wiley Material. Any third party content is expressly excluded from this permission.
- With respect to the Wiley Materials, all rights are reserved. Except as expressly granted by the terms of the license, no part of the Wiley Materials may be copied, modified, adapted (except for minor reformatting required by the new Publication), translated, reproduced, transferred or distributed, in any form or by any means, and no derivative works may be made based on the Wiley Materials without the prior permission of the respective copyright owner. **For STM Signatory Publishers clearing permission under the terms of the [STM Permissions Guidelines](#) only, the terms of the license are extended to include subsequent editions and for editions in other languages, provided such editions are for the work as a whole in situ and does not involve the separate exploitation of the permitted figures or extracts,** You may not alter, remove or suppress in any manner any copyright, trademark or other notices displayed by the Wiley Materials. You may not license, rent, sell, loan, lease, pledge, offer as security, transfer or assign the Wiley Materials on a stand-alone basis, or any of the rights granted to you hereunder to any other person.
- The Wiley Materials and all of the intellectual property rights therein shall at all times

remain the exclusive property of John Wiley & Sons Inc, the Wiley Companies, or their respective licensors, and your interest therein is only that of having possession of and the right to reproduce the Wiley Materials pursuant to Section 2 herein during the continuance of this Agreement. You agree that you own no right, title or interest in or to the Wiley Materials or any of the intellectual property rights therein. You shall have no rights hereunder other than the license as provided for above in Section 2. No right, license or interest to any trademark, trade name, service mark or other branding ("Marks") of WILEY or its licensors is granted hereunder, and you agree that you shall not assert any such right, license or interest with respect thereto

- NEITHER WILEY NOR ITS LICENSORS MAKES ANY WARRANTY OR REPRESENTATION OF ANY KIND TO YOU OR ANY THIRD PARTY, EXPRESS, IMPLIED OR STATUTORY, WITH RESPECT TO THE MATERIALS OR THE ACCURACY OF ANY INFORMATION CONTAINED IN THE MATERIALS, INCLUDING, WITHOUT LIMITATION, ANY IMPLIED WARRANTY OF MERCHANTABILITY, ACCURACY, SATISFACTORY QUALITY, FITNESS FOR A PARTICULAR PURPOSE, USABILITY, INTEGRATION OR NON-INFRINGEMENT AND ALL SUCH WARRANTIES ARE HEREBY EXCLUDED BY WILEY AND ITS LICENSORS AND WAIVED BY YOU.
- WILEY shall have the right to terminate this Agreement immediately upon breach of this Agreement by you.
- You shall indemnify, defend and hold harmless WILEY, its Licensors and their respective directors, officers, agents and employees, from and against any actual or threatened claims, demands, causes of action or proceedings arising from any breach of this Agreement by you.
- IN NO EVENT SHALL WILEY OR ITS LICENSORS BE LIABLE TO YOU OR ANY OTHER PARTY OR ANY OTHER PERSON OR ENTITY FOR ANY SPECIAL, CONSEQUENTIAL, INCIDENTAL, INDIRECT, EXEMPLARY OR PUNITIVE DAMAGES, HOWEVER CAUSED, ARISING OUT OF OR IN CONNECTION WITH THE DOWNLOADING, PROVISIONING, VIEWING OR USE OF THE MATERIALS REGARDLESS OF THE FORM OF ACTION, WHETHER FOR BREACH OF CONTRACT, BREACH OF WARRANTY, TORT, NEGLIGENCE, INFRINGEMENT OR OTHERWISE (INCLUDING, WITHOUT LIMITATION, DAMAGES BASED ON LOSS OF PROFITS, DATA, FILES, USE, BUSINESS OPPORTUNITY OR CLAIMS OF THIRD PARTIES), AND WHETHER OR NOT THE PARTY HAS BEEN ADVISED OF THE POSSIBILITY OF SUCH DAMAGES. THIS LIMITATION SHALL APPLY NOTWITHSTANDING ANY FAILURE OF ESSENTIAL PURPOSE OF ANY LIMITED REMEDY PROVIDED HEREIN.
- Should any provision of this Agreement be held by a court of competent jurisdiction to be illegal, invalid, or unenforceable, that provision shall be deemed amended to achieve as nearly as possible the same economic effect as the original provision, and the legality, validity and enforceability of the remaining provisions of this Agreement shall not be affected or impaired thereby.
- The failure of either party to enforce any term or condition of this Agreement shall not

constitute a waiver of either party's right to enforce each and every term and condition of this Agreement. No breach under this agreement shall be deemed waived or excused by either party unless such waiver or consent is in writing signed by the party granting such waiver or consent. The waiver by or consent of a party to a breach of any provision of this Agreement shall not operate or be construed as a waiver of or consent to any other or subsequent breach by such other party.

- This Agreement may not be assigned (including by operation of law or otherwise) by you without WILEY's prior written consent.
- Any fee required for this permission shall be non-refundable after thirty (30) days from receipt by the CCC.
- These terms and conditions together with CCC's Billing and Payment terms and conditions (which are incorporated herein) form the entire agreement between you and WILEY concerning this licensing transaction and (in the absence of fraud) supersedes all prior agreements and representations of the parties, oral or written. This Agreement may not be amended except in writing signed by both parties. This Agreement shall be binding upon and inure to the benefit of the parties' successors, legal representatives, and authorized assigns.
- In the event of any conflict between your obligations established by these terms and conditions and those established by CCC's Billing and Payment terms and conditions, these terms and conditions shall prevail.
- WILEY expressly reserves all rights not specifically granted in the combination of (i) the license details provided by you and accepted in the course of this licensing transaction, (ii) these terms and conditions and (iii) CCC's Billing and Payment terms and conditions.
- This Agreement will be void if the Type of Use, Format, Circulation, or Requestor Type was misrepresented during the licensing process.
- This Agreement shall be governed by and construed in accordance with the laws of the State of New York, USA, without regards to such state's conflict of law rules. Any legal action, suit or proceeding arising out of or relating to these Terms and Conditions or the breach thereof shall be instituted in a court of competent jurisdiction in New York County in the State of New York in the United States of America and each party hereby consents and submits to the personal jurisdiction of such court, waives any objection to venue in such court and consents to service of process by registered or certified mail, return receipt requested, at the last known address of such party.

WILEY OPEN ACCESS TERMS AND CONDITIONS

Wiley Publishes Open Access Articles in fully Open Access Journals and in Subscription journals offering Online Open. Although most of the fully Open Access journals publish open access articles under the terms of the Creative Commons Attribution (CC BY) License only, the subscription journals and a few of the Open Access Journals offer a choice of Creative Commons Licenses. The license type is clearly identified on the article.

The Creative Commons Attribution License

The [Creative Commons Attribution License \(CC-BY\)](#) allows users to copy, distribute and transmit an article, adapt the article and make commercial use of the article. The CC-BY license permits commercial and non-

Creative Commons Attribution Non-Commercial License

The [Creative Commons Attribution Non-Commercial \(CC-BY-NC\)License](#) permits use, distribution and reproduction in any medium, provided the original work is properly cited and is not used for commercial purposes.(see below)

Creative Commons Attribution-Non-Commercial-NoDerivs License

The [Creative Commons Attribution Non-Commercial-NoDerivs License](#) (CC-BY-NC-ND) permits use, distribution and reproduction in any medium, provided the original work is properly cited, is not used for commercial purposes and no modifications or adaptations are made. (see below)

Use by commercial "for-profit" organizations

Use of Wiley Open Access articles for commercial, promotional, or marketing purposes requires further explicit permission from Wiley and will be subject to a fee.

Further details can be found on Wiley Online Library <http://olabout.wiley.com/WileyCDA/Section/id-410895.html>

Other Terms and Conditions:

v1.10 Last updated September 2015

Questions? customercare@copyright.com.

Curriculum Vitae

Name:	Eric Knull
Post-Secondary Education and Degrees:	<p>PhD Candidate, Medical Imaging, Biomedical Engineering The University of Western Ontario 2013 - Present Supervisor: Dr. Aaron Fenster</p> <p>Bachelor of Science, Computer Science, Honors Specialization The University of Western Ontario 2010 - 2013 Graduated with distinction</p> <p>Bachelor of Engineering Science, Electrical Engineering The University of Western Ontario 2008 - 2012 Graduated with distinction</p>
Honours and Awards:	<p>Western Graduate Research Scholarship 2013-2022</p> <p>Cancer Research and Technology Transfer Trainee 2014-2015</p> <p>NSERC CGS-M 2013-2014</p> <p>Szilard Award in Theoretical Computer Science 2013</p> <p>NSERC Undergraduate Student Research Award 2011 & 2012</p> <p>Nortel Network Scholarship for Distinction in Engineering 2010-2012</p>

**Related Work
Experience:**

Dean's Honour List
2008-2013

UWO Continuing Admission Scholarship
2008-2012

Graduate Teaching Assistant, The University of Western Ontario
Supervised tutorials and labs, marked assignments, and tutored students in the following courses: Programming Fundamentals for Engineers, Professional Communication for Engineers, and Introduction to Electrical Engineering for Mechanical Engineers
2013 - 2017

Student Researcher, Robarts Imaging Research Laboratories
Used Xbox Kinect with hand tracking algorithms to create hands-free interface for surgeons to manipulate 3D images during operations.
Supervised by Dr. Aaron Fenster
2011 - 2012

Publications and Presentations:

Articles in Refereed Journals

Knoll, E., Park, C. K. S., Bax, J., Tessier, D., & Fenster, A. (2023). Toward mechatronic MRI-guided focal laser ablation of the prostate: Robust registration for improved needle delivery. *Medical Physics*, 50(3), 1259–1273. ***Medical Physics Editor's Choice**

Park, C. K. S., Xing, S., Papernick, S., Orlando, N., **Knoll, E.**, Toit, C. Du, Bax, J. S., Gardi, L., Barker, K., Tessier, D., & Fenster, A. (2022). Spatially tracked whole-breast three-dimensional ultrasound system toward point-of-care breast cancer screening in high-risk women with dense breasts. *Medical Physics*, 49(6), 3944–3962. ***KAMPINA Best Paper Award**

Knoll, E., Bax, J. S., Park, C. K. S., Tessier, D., & Fenster, A. (2021). Design and validation of an MRI-compatible mechatronic system for needle delivery to localized prostate cancer. *Medical Physics*, 48(9), 5283–5299.

Park, C. K. S., Bax, J. S., Gardi, L., **Knoll, E.**, & Fenster, A. (2021). Development of a mechatronic guidance system for targeted ultrasound-guided biopsy under high-resolution positron emission mammography localization. *Medical Physics*, 48(4), 1859–1873. ***Medical Physics Editor's Choice and Journal Cover, Lucille and Norton Wolf Publication Award, and COMP Sylvia Fedoruk Prize in Medical Physics**

Knoll, E., Oto, A., Eggener, S., Tessier, D., Guneyli, S., Chatterjee, A., & Fenster, A. (2019). Evaluation of tumor coverage after MR-guided prostate focal laser ablation therapy. *Medical Physics*, 46(2), 800–810.

Refereed Conference Proceedings

Knoll, E., Park, C. K., Bax, J., Tessier, D., & Fenster, A. (2022). Robust registration and phantom validation of mechatronics-assisted MRI-guided needle delivery for prostate focal laser ablation therapy. *Proc. SPIE 12034, Medical Imaging 2022: Image-Guided Procedures, Robotic Interventions, and Modeling*, 120342K.

Knoll, E., Park, C. K., Bax, J., Tessier, D., & Fenster, A. (2021). MRI-compatible mechatronic needle guidance system for focal thermal laser ablation in localized prostate cancer, *Proc. SPIE 11598, Medical Imaging 2021: Image-Guided Procedures, Robotic Interventions, and Modeling*, 1159804.

Oral Presentations

Knoll, E.*, Park, C. K., Bax, J., Tessier, D., & Fenster, A. (2022). Mechatronics-assisted needle delivery system for MRI-guided focal laser ablation of localized prostate cancer. *Imaging Network Ontario - IMNO, 19th Annual Symposium*. Virtual, March 24, 2021.

Selected Posted Presentations

Knoll, E., Park, C. K.*, Bax, J., Tessier, D., & Fenster, A. (2022). Robust registration and phantom validation of mechatronics-assisted MRI-guided needle delivery for prostate focal laser ablation therapy. International Society for Optics and Photonics - SPIE. San Diego, April 4, 2022.

Knoll, E.*, Park, C. K., Bax, J., Tessier, D., & Fenster, A. (2022). Minimally invasive therapy in prostate cancer: A needle-guidance system for MRI-guided prostate focal laser ablation. OICR Translational Research Conference. Virtual, March 25-26, 2021.

Knoll, E.*, Oto, A., Eggener, S., Tessier, D., Guneyli, S., Chatterjee, A., & Fenster, A. 2018. Overlap between tumours and ablation zones after MR-guided prostate focal laser ablation therapy. CARO-COMP-CAMRT Joint Scientific Meeting. Montreal, QC, September 12-15, 2018.

Knoll, E.*, Kakani, N., & Fenster, A. 2018. Hand gesture control system for manipulation of images during three-dimensional ultrasound guidance. Imaging Network Ontario - IMNO, 13th Annual Symposium. London, ON, March 30-31, 2015.

Published Abstracts

Knoll, E., Park, C. K., Bax, J., Tessier, D., & Fenster, A. (2021). MO-A-TRACK 6-04: Mechatronics-Assisted MRI-Guided Focal Laser Ablation of the Prostate: A Phantom Study, Proceedings of the American Association of Physicists in Medicine Annual Meeting, Medical Physics, 48(6).